Examining the Charge Storage Mechanisms of Nanoscale Nickel Hydroxide

Joseph H L Hadden

A thesis presented for the degree of Doctor of Philosophy and the Diploma of Imperial College London

I, Joseph H L Hadden, confirm that the work presented in this thesis is my own. Where information has been derived from other sources, I confirm that this has been indicated.

Signed:

Date:

The copyright of this thesis rests with the author and is made available under a Creative Commons Attribution Non-Commercial No Derivatives license. Researchers are free to copy, distribute or transmit the thesis on the condition that they attribute it, that they do not use it for commercial purposes and that they do not alter, transform or build upon it. For any reuse or redistribution, researchers must make clear to others the license terms of this work

Abstract

The aim of this work was to develop mechanistic understanding, as well as techniques to study the charging and discharging behaviour of a material which has controversially been described as either a battery or a pseudocapacitor electrode material. Nickel hydroxide, $Ni(OH)_2$, was chosen as the material of choice due to its long history as a secondary battery cathode material, as well as recent interest in it as a high rate supercapacitor. This recent interest is mainly due to advances in nanoscaling the material architecture.

After a review of the literature (Chapter 1) and a summation of the methods used in this thesis (Chapter 2), the experimental work began by studying the specific capacitance (Cap_s), the specific capacity (C_s) and the areal capacity (C_A) of nickel hydroxide nanoparticles in aqueous 1.0 mol dm^{-3} potassium hydroxide electrolyte. Particles were fabricated using hydrothermal methods, in the diameter range of 3–450 nm (Chapter 3). All metrics were consistent with surface only charging down to a critical diameter of around 20 nm at which point there was a deviation. This suggested the novel idea that a charging "skin", which was interacting below this diameter, was preventing further charging.

This charging "skin" was investigated using ToF-SIMS with isotopic labelling (Chapter 4) to follow the uptake of deuterium ions during charging cycling. Ingress of deuterium into the material was dependent on charge cycling number, and the depth was found to approximately match that observed in the nanoparticle study.

The impedance behaviour of the $Ni(OH)_2$ was studied in order to separate the different contributions of non-Faradaic double layer capacitance, surface Faradaic pseudocapacitance, and intercalation reactions to the charge storage (Chapter 5). Studying the capacitance at different DC potentials and frequencies allowed these mechanisms to be deconvoluted, while the best fitting circuit model gave insight into the porous structure of the electrode. Using a semi-infinite pore model, the porous electrode data would not map onto the flat electrode data, showing the diffusion into the pores does not follow a semi-infinite model, as often assumed in literature.

The evidence gathered suggests that the charging mechanism of $Ni(OH)_2$ is a complex combination of both capacitive surface dependant charging and intercalation into the bulk of the structure.

Acknowledgements

The research for this thesis was carried out in the Department of Materials, Imperial College London from October 2015 to October 2018. I would like to thank my supervisors, Prof Jason Riley and Prof Mary Ryan, for their guidance and assistance during the project.

Special mention to Dr. Sarah Fearn, Mr Richard Sweeny, Dr Victoria Bemmer, and Dr Mahmoud Ardakani, and Dr Anna Regoutz for their training and assistance in the operation of the analytical equipment in the department.

I would also like to thank my parents, Andy and Carole, for their support throughout my research life and providing a great platform for my career. Finally, I'd like to thank Ellie Roberts for her support while this work was undertaken.

Table of Contents

Abstract **3**

Acknowledgements **4**

Table of Contents **5**

List of Figures **9**

List of Tables **18**

List of Abbreviations **20**

List of Symbols **22**

Chapter 1 – Introduction and Literature Review **25**

1.1 The Importance of Charge Storage Device Research 25

1.2 Batteries and Supercapacitors 26

1.3 Energy and Power Densities 28

1.4 Mechanisms of Charge Storage 29

1.4.1 Electrical Double Layer Capacitors 29

1.4.2 Pseudocapacitors 31

1.4.3 Intercalation Batteries 33

1.5 Materials for Charge Storage Devices 34

1.5.1 Inert Double Layer Materials 34

1.5.2 Redox Active Pseudocapacitive Materials 35

1.5.3 Secondary Battery Materials 37

1.5.4 Electrolytes 39

1.6 Physical and Electronic Properties of Nickel Hydroxide 40

1.6.1 Structure of Nickel Hydroxide Polymorphs 41

1.6.2 Electrochemical Properties of Nickel Hydroxide 42

1.7 Battery or Supercapacitor Material? – The Controversy 44

1.8 References 48

Chapter 2 – Experimental Methodologies **51**

2.1 Synthesis Methodologies ……. 51

2.2 Structural and Elemental Characterisation Methods …… 51

2.2.1 Scanning Electron Microscopy …… 51

2.2.2 Transmission Electron Microscopy …… 55

2.2.3 Energy Dispersive X-ray Spectroscopy …… 55

2.2.4 X-ray Photoelectron Spectroscopy …… 56

2.2.5 X-ray Diffraction …… 57

2.2.6 Small Angle X-ray Scattering …… 59

2.2.7 Dynamic Light Scattering …… 60

2.2.8 Nitrogen Adsorption/Desorption …… 61

2.2.9 Atomic Force Microscopy …… 61

2.2.10 Light Microscopy …… 62

2.3 Time of Flight Secondary Ion Mass Spectrometry …… 62

2.4 Electrochemical Characterisation …… 63

2.4.1 Electrochemical Cell Set-Up …… 63

2.4.2 Cyclic Voltammetry …… 64

2.4.3 Galvanostatic Charge/Discharge …… 65

2.4.4 Electrochemical Impedance Spectroscopy …… 66

2.4.5 Calculating Charge Storage Metrics …… 67

2.5 References …… 68

Chapter 3 – The Charging Behaviour of Nickel Hydroxide Nanoparticles …… 70

3.1 Introduction …… 70

3.2 Initial Synthesis Methods …… 73

3.2.1 Wet Chemical precipitation …… 73

3.2.2 Multiphase Synthesis …… 75

3.2.3 Sonochemical Synthesis …… 76

3.2.4 Hydrothermal Synthesis …… 77

3.2.5 Comparison of Synthesis Methods …… 78

3.3 Synthesis Method …… 78

3.4 Materials Characterisation …… 81

3.4.1 Synthesis Mechanism 81
3.4.2 Chemical Composition of Hydrothermal Products 82
3.4.3 Phase, Size and Morphologies of $Ni(OH)_2$ Particles 83
3.4.4 Nanoparticle Specific Surface Area 91
3.5 Electrochemical Characterisation of $Ni(OH)_2$ Nanoparticles 93
3.5.1 Optimisation of Electrodes 93
3.5.2 Cyclic Voltammetry of $Ni(OH)_2$ Nanoparticles 95
3.5.3 Galvanostatic Charge/Discharge of $Ni(OH)_2$ Nanoparticles 98
3.6 Specific Capacity and Capacitance of $Ni(OH)_2$ Nanoparticles 99
3.7 Capacity Per Unit Area of $Ni(OH)_2$ Nanoparticles 103
3.8 Conclusions 104
3.9 References 105

Chapter 4 – ToF-SIMS Depth Profiling of Nickel Hydroxide 108
4.1 Introduction 108
4.2 Electrochemical Deposition Rational 110
4.3 Determination of Reaction Parameters 111
4.3.1 Selection of Starting Conditions 112
4.3.2 Substrate Selection 112
4.3.3 Effect of Deposition Time 114
4.3.4 Effect of Deposition Temperature 115
4.3.5 Effect of Ni^{2+} Concentration 115
4.3.6 Effect of Deposition Potential 117
4.3.7 Final Synthesis Procedure 119
4.4 Structural Characterisation of Electrodeposited $Ni(OH)_2$ 119
4.5 Electrochemical Characterisation of Electrodeposited $Ni(OH)_2$ 124
4.6 Manufacture of Non-Porous $Ni(OH)_2$ Electrode 125
4.6.1 Wax Deposition 125
4.6.2 Wax Grinding 126
4.6.3 Structural Characterisation 127
` 4.6.4 Electrochemical Characterisation 128
4.7 Time of Flight Secondary Ion Mass Spectrometry 129

4.7.1 ToF-SIMS of Porous Electrodeposited $Ni(OH)_2$ 129
4.7.2 ToF-SIMS of Non-Porous Electrodes 133
4.8 Conclusions 135
4.9 References 136

Chapter 5 – Impedance Analysis of Electrodeposited Nickel Hydroxide 138
5.1 Introduction 138
5.2 Synthesis Method and Preparation of Impermeable $Ni(OH)_2$ Films 140
5.3 Structural Characterisation of Electrodeposited $Ni(OH)_2$ 141
5.4 Electrochemical Characterisation of Electrodeposited $Ni(OH)_2$ 142
5.5 Determination of Perturbation Potential 143
5.6 Impedance of Porous $Ni(OH)_2$ Coated Electrodes at 0.0 V DC 145
5.7 Variation of Impedance with DC Potential in Porous $Ni(OH)_2$ Electrodes 149
5.8 Impedance of Non-Porous $Ni(OH)_2$ Coated Electrodes 157
5.9 Mapping of Porous Impedance Data onto Flat Impedance Data 162
5.10 Conclusions 164
5.11 References 165

Chapter 6 – Conclusions and Outlook 167
6.1 Summary of Research Chapters 167
6.2 Future Work 169
6.2.1 Chapter 3 169
6.2.2 Chapter 4 170
6.2.3 Chapter 5 171
6.2.4 *In-operando* Measurements 171
6.3 References 173

Appendices 174

Dissemination of Research 192

List of Figures

Chapter 1

Figure 1.1 Global primary electricity generation by fuel type 2017, drawn from data taken from the BP Statistical Review of World Energy 2018[1] 25

Figure 1.2 Ragone plot showing the specific energy and power of various electrochemical storage devices. Figure was redrawn from data taken from source[2] 28

Figure 1.3 Schematic representation of the electrical double layer formed at the electrode surface (not to scale) 30

Figure 1.4 Schematic of an electrical double layer capacitor, redrawn from source3 (not to scale) 31

Figure 1.5 Schematic of a typical redox pseudocapacitor, redrawn from source3 (not to scale) 32

Figure 1.6 Schematic of Li-ion battery, showing intercalation graphitic carbon anode and transition metal oxide cathode during discharge. Reprinted with permission (see Appendix 1) from Xu, K., Nonaqueous Liquid Electrolytes for Lithium-Based Rechargeable Batteries. Chemical Reviews 2004, 104 (10), 4303-4418. Copyright (2019) American Chemical Society 38

Figure 1.7 Ball and stick rendering of the β-$Ni(OH)_2$ unit cell, in (a) Ni (001) and (b) Ni (111) projections. Figures made using crystallographic data from the American Mineralogist Crystal Structure Database 41

Figure 1.8 Interstratification of α- and β-$Ni(OH)_2$ showing intercalated water and anions.(not to scale) 42

Figure 1.9 Phase changes on charging of nickel hydroxide (a) charging, (b) discharging, (c) over-charging, and (d) chemical ageing 43

Figure 1.10 Expected electrochemical response for different types of charge storage electrode measured using CV (a/c/e) and galvanostatic discharge (b/d/f) (a/b) EDLC electrode material (c/d) pseudocapacitor electrode material (e/f) battery electrode material 45

Figure 1.11 Example CV for Ni(OH)2 nanospheres ~50 nm diameter at various scan rates. . Reprinted with permission (see Appendix 2) from Li, H. B.; Yu, M. H.; Wang, F. X.; Liu, P.; Liang, Y.; Xiao, J.; Wang, C. X.; Tong, Y. X.; Yang, G. W., Amorphous nickel hydroxide nanospheres

with ultrahigh capacitance and energy density as electrochemical pseudocapacitor materials. Nature Communications 2013, 4, 1894. Copyright (2013) Macmillan Publishers Limited….. 46
Figure 1.12 Expected changes in charge storage with particle size using battery-like and pseudocapacitive mechanisms …… 47

Chapter 2

Figure 2.1 Simplified schematic of scanning electron microscope, not to scale. Some features have been omitted/not duplicated for simplicity …….. 52
Figure 2.2 Scanning electron micrograph of uncoated $Ni(OH)_2$ nanoparticles with analysis grid overlay …… 54
Figure 2.3 EDX analysis method applied to each sample of $Ni(OH)_2$ nanoparticles …….. 56
Figure 2.4 Peak fitting of XRD data using Origin Software …….. 58
Figure 2.5 Schematic of electrochemical cell set up for analysis (not to scale) …… 63
Figure 2.6 Electrochemical cycling of $Ni(OH)_2$ coated Ni foil electrode at 50 mV s^{-1} (a) Increase in electrochemical activity over first 10 cycles (b) Stability of electrode over 200 cycles ……. 65

Chapter 3

Figure 3.1 a) SEM micrograph of nickel hydroxide produced using wet chemical precipitation methods using potassium hydroxide as the reacting base. b) nickel hydroxide produced using wet chemical precipitation methods using ammonium hydroxide as the reacting base. Both exhibit banding due to lack of charge conductive coating and poor contact with SEM stub.. 74
Figure 3.2 a) SEM micrograph of nickel hydroxide produced using multiphase synthesis methods using sodium ethoxide via an organometallic precursor. b) SEM micrograph of nickel hydroxide produced using multiphase synthesis methods using CTAB based emulsions to form nanoscale aqueous environments …….. 76
Figure 3.3 SEM micrograph of nickel hydroxide nanoplates produced using a sonochemical synthesis method, without conductive coating …….. 76
Figure 3.4 a) SEM micrograph of nickel hydroxide produced using hydrothermal synthesis methods and sodium citrate surfactant at 80°C b) SEM micrograph of nickel hydroxide produced using hydrothermal synthesis methods at 80°C with no surfactant …….. 78

Figure 3.5 Energy dispersive X-ray spectroscopy of the intermediate of reduction assisted synthesis. Samples drop-cast directly onto aluminium stub for analysis. EDX performed at 10 kV accelerating voltage …… 81
Figure 3.6 Energy dispersive X-ray spectroscopy of final product of hydrothermal reactions. Samples drop-cast directly onto aluminium stub for analysis. EDX performed at 10 kV accelerating voltage…… 82
Figure 3.7 X-ray photoelectron spectra of $Ni(OH)_2$ samples using Al Kα X-rays (hv = 1486.86 eV) with C1s peak set to a binding energy of 285 eV (a) Survey spectrum (pass energy 200 eV, dwell time 25 ms) (b) O 1s and (c) Ni 2P spectra. The high-resolution Ni(2p) and O(1s) spectra were obtained at a pass energy of 20 eV, and a dwell time of 50 ms …… 83
Figure 3.8 Scanning Electron Microscopy (a-d) SEM images of $Ni(OH)_2$ synthesised at various temperatures (150°C, 120°C, 80°C, 60°C) using 0.2 M surfactant and non-reduction assisted syntheses (samples 11,10,8,6). Images taken by directly drop-casting onto aluminium stub with no further metal coating …… 85
Figure 3.9 TEM images of particles synthesised at 60°C using 2.0 M surfactant and reductant assisted synthesis (a) before ozonolysis and (b) after ozonolysis. Images taken by dispersing in methanol and drop casting onto carbon grid …… 86
Figure 3.10 TEM image of edge on particles synthesised at 60°C using 0.2 M surfactant in a non-reductant assisted synthesis. Images taken by dispersing in methanol and drop casting onto carbon grid …… 86
Figure 3.11 DLS results for hydrothermally synthesised samples of $Ni(OH)_2$ nanoparticles using different experimental conditions. Samples shown; (1) 60°C + RA + 2 M surfactant (4) 60°C + nRA + 2 M surfactant (6) 60°C + nRA + 0.2 M surfactant (8) 80°C + nRA + 0.2 M surfactant. All samples collected while dispersed in water at room temperature with no further surfactant to aid dispersion …… 86
Figure 3.12 X-ray diffractograms of nickel hydroxide samples deposited on to Si wafer produced using low surfactant syntheses. Analysis conditions described in Section 2.2.5 ... 87
Figure 3.13 X-ray diffractograms of nickel hydroxide samples deposited on to Si wafer produced using high surfactant syntheses. Analysis conditions described in Section 2.2.5 … 88
Figure 3.14 XRD diffractogram of Sample (9) produced at 100°C using nRA low surfactant synthesis before and after 50 cycles of cyclic voltammetry between 0.0 V and 0.7 V at a scan rate of 50 mV s^{-1}. Samples deposited onto Si wafer before analysis …… 89

Figure 3.15 N_2 Adsorption/Desorption analysis of $Ni(OH)_2$ samples (a) 450 nm diameter particles (b) 3 nm diameter particles 92
Figure 3.16 Comparison of Ni foil prior to deposition vs lowest capacity sample, sample 11, at a mass loading of 1 mg cm^{-2}. Both scans taken at 100 mV s^{-1} 93
Figure 3.17 CV comparison of the effect of ozonolysis on $Ni(OH)_2$ nanoparticles. (a) Sample 2 - product of synthesis using high concentration of surfactant (b) Sample 8 - Product of synthesis using low concentration of surfactant. CV taken at a scan rate of 50 mV s^{-1} 94
Figure 3.18 Effect of mass loading of sample 6 on specific capacity measured using CV at a scan rate of 10 mV s^{-1} 95
Figure 3.19 Cyclic Voltammogram of product of synthesis 1, 3 nm diameter $Ni(OH)_2$ nanoparticles at various scan rates. Full methodology for electrochemical analysis can be found in section 2.4.2 96
Figure 3.20 Cyclic Voltammogram of product of synthesis 6, 56 nm diameter $Ni(OH)_2$ nanoparticles at various scan rates. Full methodology for electrochemical analysis can be found in Section 2.4.2 96
Figure 3.21 Cyclic Voltammogram of product of synthesis 11, 300 nm diameter $Ni(OH)_2$ nanoparticles at various scan rates. Full methodology for electrochemical analysis can be found in Section 2.4.2 97
Figure 3.22 Randles-Sevcik plots of $Ni(OH)_2$ nanoplates showing reduction peak current's dependence on the square root of scan rate. (a) 3 nm particles (b) 56 nm particles (c) 300 nm particles 98
Figure 3.23 Galvanostatic charging of $Ni(OH)_2$ nanoparticles (a) sample 3 at various current densities (b) comparison of charging behaviour for extreme particle sizes, sample 1 and sample 10 98
Figure 3.24 Comparing the effect of scan rate on specific capacitance on particles of various diameters 99
Figure 3.25 Variation of specific capacity, as calculated from CV data at 10 mV s^{-1}, with particle diameter. Calculation of particle size from SEM data and error calculation can be found in Section 2.2.1 100
Figure 3.26 Variation in specific capacity after 1 hours of UV generated ozone treatment .. 100

Figure 3.27 Proposed schematic of nickel hydroxide nanoparticle charging, showing electrochemically active material in black and inactive/unreacted material in green. (a) Large particles with diameter >20 nm and (b) Nanoparticles with diameter 20 nm or below …….. 101
Figure 3.28 Variation of specific capacitance, as calculated from CV data at 10 mV s^{-1}, with particle diameter. Calculation of particle size from SEM data and error calculation can be found in Section 2.2.1 …… 102
Figure 3.29 Variation of capacity per unit area, as calculated from CV data at 10 mV s^{-1}, with particle diameter. Calculation of particle size from SEM data and error calculation can be found in Section 2.2.1 …… 103

Chapter 4

Figure 4.1 SEM micrographs of electrodeposited $Ni(OH)_2$ on Ni foil. Deposition run at -0.7 V for 5 mins at room temperature. Electrolyte was 0.100 mol dm^{-3} $Ni(NO_3)_2$. Full details of electrochemical set up can be found in Section 2.4.1 …….. 112
Figure 4.2 Structure of flat smooth substrate, (a) side view (b) isometric view, showing Ni current collector (stripes), Si (100) wafer (black), Cr layer (grey), Au layer (gold), and conductive silver paint (diamond) (layer thicknesses not to scale) …….. 113
Figure 4.3 SEM micrographs of electrodeposited $Ni(OH)_2$ on Au/Cr sputter coated Si (100) wafer. Deposition run at -0.7 V for 5 mins at room temperature. Electrolyte was 0.100 mol dm^{-3} $Ni(NO_3)_2$. Full details of electrochemical set up can be found in Section 2.4.1…… 113
Figure 4.4 SEM micrographs of electrodeposited $Ni(OH)_2$ on Au/Cr sputter coated Si (100) wafer. Deposition run at -0.7 V for 10 mins at room temperature. Electrolyte was 0.100 mol dm^{-3} $Ni(NO_3)_2$. Full details of electrochemical set up can be found in Section 2.4.1…… 114
Figure 4.5 Dry mass of deposited $Ni(OH)_2$ on Au/Cr sputter coated Si (100) wafer electrode vs deposition time. Deposition run at -0.7 V at room temperature. Electrolyte was 0.100 mol dm^{-3} $Ni(NO_3)_2$. Full details of electrochemical set up can be found in Section 2.4.1. Error bars were calculated as the standard error of 3 experiments at the same deposition time…… 114

Figure 4.6 SEM micrographs of electrodeposited $Ni(OH)_2$ on Au/Cr sputter coated Si (100) wafer. Deposition run at -0.7 V for 5 mins at 60°C. Electrolyte was 0.100 mol dm^{-3} $Ni(NO_3)_2$. Full details of electrochemical set up can be found in Section 2.4.1…… 115
Figure 4.7 SEM micrographs of electrodeposited $Ni(OH)_2$ on Au/Cr sputter coated Si (100) wafer. Deposition run at -0.7 V for 5 mins at room temperature. $Ni(NO_3)_2$ electrolyte concentration was varied (a/b) 0.200 mol dm^{-3} (c/d) 0.300 mol dm^{-3} (e/f) 0.400 mol dm^{-3}. Full details of electrochemical set up can be found in Section 2.4.1…… 116
Figure 4.8 SEM micrographs of electrodeposited $Ni(OH)_2$ on Au/Cr sputter coated Si (100) wafer. Deposition was run for 5 mins at room temperature. $Ni(NO_3)_2$ electrolyte concentration was 0.100 mol dm^{-3}. Deposition potential was varied (a/b) -0.9 V (c/d) -1.1 V (e/f) -1.3 V. Full details of electrochemical set up can be found in Section 2.4.1…… 118
Figure 4.9 Typical current vs time plot of deposition procedure. Deposition was run for 5 mins at room temperature. $Ni(NO_3)_2$ electrolyte concentration was 0.100 mol dm^{-3}. Deposition potential was -0.9 V. Full details of electrochemical set up can be found in Section 2.4.1…. 120
Figure 4.10 XPS survey spectrum of electrodeposited $Ni(OH)_2$ on Au/Cr coated Si wafer. Deposition was run for 5 mins at room temperature. $Ni(NO_3)_2$ electrolyte concentration was 0.100 mol dm^{-3}. Deposition potential was -0.9 V. Full details of electrochemical set up can be found in Section 2.4.1…… 120
Figure 4.11 High resolution XPS spectra of key peaks of electrodeposited $Ni(OH)_2$ (a) C1s (b) Ni2p (c) O1s. Deposition was run for 5 mins at room temperature. $Ni(NO_3)_2$ electrolyte concentration was 0.100 mol dm^{-3}. Deposition potential was -0.9 V. Full details of electrochemical set up can be found in Section 2.4.1…… 121
Figure 4.12 EDX analysis of electrodeposited $Ni(OH)_2$. Deposition was run for 5 mins at room temperature. $Ni(NO_3)_2$ electrolyte concentration was 0.100 mol dm^{-3}. Deposition potential was -0.9 V. Full details of electrochemical set up can be found in Section 2.4.1…… 122
Figure 4.13 X-ray diffractogram of Au/Cr coated Si (100) wafer before and after electrodeposition of $Ni(OH)_2$. Deposition was run for 5 mins at room temperature. $Ni(NO_3)_2$ electrolyte concentration was 0.100 mol dm^{-3}. Deposition potential was -0.9 V. Full details of electrochemical set up can be found in Section 2.4.1…… 122
Figure 4.14 (a) N_2 Adsorption/Desorption analysis of electrodeposited $Ni(OH)_2$ samples (b) Pore size distribution by DFT analysis. Full BET analysis conditions can be found in Section 2.2.8. Deposition was run for 5 mins at room temperature. $Ni(NO_3)_2$ electrolyte concentration

was 0.100 mol dm^{-3}. Deposition potential was -0.9 V. Full details of electrochemical set up can be found in Section 2.4.1…….. 123
Figure 4.15 Cyclic voltammetry of electrodeposited $Ni(OH)_2$ film at various scan rates. Deposition was run for 5 mins at room temperature. $Ni(NO_3)_2$ electrolyte concentration was 0.100 mol dm^{-3}. Deposition potential was -0.9 V. Full details of electrochemical set up can be found in Section 2.4.1. All electrochemical measurements made using a three-cell set up and in 1.0 mol dm^{-3} KOH, see Section 2.4 for full conditions…… 124
Figure 4.16 Galvanostatic charge/discharge of the electrodeposited $Ni(OH)_2$ film at 1 A g^{-1}. Deposition was run for 5 mins at room temperature. $Ni(NO_3)_2$ electrolyte concentration was 0.100 mol dm^{-3}. Deposition potential was -0.9 V. Full details of electrochemical set up can be found in Section 2.4.1. All electrochemical measurements made using a three-cell set up and in 1.0 mol dm^{-3} KOH, see Section 2.4 for full conditions…….. 125
Figure 4.17 Wax deposition set up, prepared in house for this work…….. 126
Figure 4.18 Light Microscopy of wax coated electrodeposited $Ni(OH)_2$ electrodes (a) before grinding and (b) after grinding …….. 127
Figure 4.19 N_2 Adsorption/Desorption analysis of electrodeposited $Ni(OH)_2$ samples after paraffin wax deposition and grinding. Full BET analysis conditions can be found in Section 2.2.8. Deposition was run for 5 mins at room temperature. $Ni(NO_3)_2$ electrolyte concentration was 0.100 mol dm^{-3}. Deposition potential was -0.9 V. Full details of electrochemical set up can be found in Section 2.4.1 …….. 127
Figure 4.20 Atomic force micrograph of the electrodeposited $Ni(OH)_2$ electrode after wax coating, but prior to grinding …… 128
Figure 4.21 Cyclic voltammetry of electrodeposited $Ni(OH)_2$ film at 10 mV s^{-1} after wax deposition and grinding. Full details of electrochemical set up can be found in Section 2.4.1. All electrochemical measurements made using a three-cell set up and in 1.0 M KOH, see Section 2.4 for full conditions …… 128
Figure 4.22 Galvanostatic charging of electrodeposited $Ni(OH)_2$ film at 1 A g^{-1} of active material, before and after wax deposition and grinding. Full details of electrochemical set up can be found in Section 2.4.1. All electrochemical measurements made using a three-cell set up and in 1.0 M KOH, see Section 2.4 for full conditions …… 129

Figure 4.23 ToF-SIMS analysis of electrodeposited $Ni(OH)_2$ film on Au/Cr coated Si (100) wafer (a) short time scale (b) long time scale. Traces taken using analysis conditions described in Section 2.3. H^- not shown due to large magnitude of signal, around 10^5 counts 130
Figure 4.24 Relative measured intensity of D^- in electrodeposited $Ni(OH)_2$ electrode vs sputter time after various cycle numbers in deuterated alkaline electrolyte at 10 mV s^{-1}. Signal is normalised to $NiOH^-$ 131
Figure 4.25 Reaction schematic for the charging and discharging of $Ni(OH)_2$ in deuterated electrolyte. Deuterium loading into the sample is given as % D 132
Figure 4.26 Variation of relative deuterium ion intensity with cycle number. Average value calculated from Figure 4.24 is plotted along with theoretically derived uptake based on mechanism shown in Figure 4.25. Error bars calculated as standard error in intensity between 50 and 200 sputter seconds 132
Figure 4.27 ToF-SIMS plots of deuterium ion intensity (normalised to $NiOH^-$) verses sputter time for waxed and unwaxed samples after 1 cycle of charging and discharging at 10 mV s^{-1}. The uncoated sample is much nosier due to lower overall deuterium ion intensity. Full procedural details for ToF-SIMS analysis can be found in Section 2.3 133
Figure 4.28 AFM studies of ToF-SIMS sputter crater (a/b) AFM of sputter crater, showing 10-pixel linear profiles used to calculate crater depth (white) spaced every 10 µm. (c) Average heights across three linear profiles shown in (a) giving experimental profile and step height calculated from data 134
Figure 4.29 ToF-SIMS plots of deuterium ion intensity verses sputter depth. Comparison of D^- ion intensity and $NiOH^-$ ion intensity in a wax coated and ground sample after 1 cycle of charging and discharging at 10 mV s^{-1}. Full procedural details for ToF-SIMS analysis can be found in Section 2.3 135

Chapter 5

Figure 5.1 Equivalent circuit diagrams used in the characterisation of energy storage materials (a) Randles Cell (b) Combined EDL and Faradaic capacitances 139
Figure 5.2 The *b*-value analysis of $Ni(OH)_2$ coated electrodes over multiple syntheses. Samples produced using the standard potentiostatic electrodeposition procedure at -0.9 V, -1.1 V and -1.3 V. Different syntheses shown using different shaped points. Inset is fitting parameters for one of the data sets 142

Figure 5.3 Nyquist plot at various perturbation potentials at 0.0 V DC potential 144
Figure 5.4 Nyquist plots of $Ni(OH)_2$ coated electrode at 0.0 V DC potential and a perturbation potential of 10 mV (a) Whole frequency range (b) High frequency range only 145
Figure 5.5 Bode Plots of $Ni(OH)_2$ coated electrodes at 0.0 V DC potential and 10 mV perturbation 146
Figure 5.6 Equivalent circuit for the modelling of $Ni(OH)_2$ coated electrodes 147
Figure 5.7 Fitting of equivalent circuit model to experimental data for $Ni(OH)_2$ coated electrodes at 0.0 V DC potential and 10 mV perturbation (a) Nyquist plot (b) Bode Plots ... 148
Figure 5.8 Nyquist plot of $Ni(OH)_2$ coated electrodes at various DC potentials and 10 mV AC perturbation, high frequency region only 149
Figure 5.9 Nyquist plot of $Ni(OH)_2$ coated electrodes at various DC potentials and 10 mV AC perturbation (a) 0.0 V – 0.3 V (b) 0.4 V – 0.7 V 150
Figure 5.10 Fitting of equivalent circuit model to experimental data for Ni(OH)2 coated electrodes at 0.7 V DC potential and 10 mV perturbation (a) Nyquist plot (b) Bode Plots.... 151
Figure 5.11 Variation in capacitive equivalent circuit component values with applied DC potential for Ni(OH)2 coated electrodes charging from 0.0 V to 0.7 V and 10 mV AC perturbation potential calculated using equivalent circuit in Figure 5.6 152
Figure 5.12 Bode plots of $Ni(OH)_2$ coated electrodes at various DC potentials 0.0 V – 0.7 V and 10 mV AC perturbation (a) variation of $|Z|$ (b) variation of θ 153
Figure 5.13 Capacitance analysis of $Ni(OH)_2$ coated electrodes at various DC potentials 0.0 V – 0.7 V and 10 mV AC perturbation vs frequency 154
Figure 5.14 Impedance response of $Ni(OH)_2$ coated electrodes at various DC potentials and 10 mV AC perturbation (a) Nyquist plot 0.7 V – 0.4 V (b) Nyquist plot 0.3 V – 0.0 V (c) Bode plot showing variation of $|Z|$ with frequency (d) Bode plot showing variation of θ with frequency 156
Figure 5.15 Representation of (a) flat and (b) porous electrodes using RC circuit elements C_{INT}, the interfacial capacitance and R_P, the pore resistance 158
Figure 5.16 Equivalent circuit for the modelling of the $Ni(OH)_2$ coated electrodes after deposition and grinding of a porosity blocking wax layer 158
Figure 5.17 Nyquist representation of impedance data for $Ni(OH)_2$ coated electrodes after deposition and grinding of a porosity blocking wax layer at various DC potentials and 10 mV AC perturbation (a/b) charging (c/d) discharging 159

Figure 5.18 Bode representation of impedance data for $Ni(OH)_2$ coated electrodes after deposition and grinding of a porosity blocking wax layer at various DC potentials and 10 mV AC perturbation (a/b) charging (c/d) discharging 160
Figure 5.19 Capacitance analysis of $Ni(OH)_2$ coated electrodes after deposition and grinding of a porosity blocking wax layer at various DC potentials 0.0 V – 0.7 V and 10 mV AC perturbation vs frequency 161
Figure 5.20 Equivalent circuit model of an infinitely small of pore showing potential drop as current moves down pore in *x* direction 162
Figure 5.21 Nyquist representation of the impedance response of porous $Ni(OH)_2$ coated electrode at various DC potentials and 10 mV AC perturbation squared, high frequency region magnified in insert 164

List of Tables

Chapter 2

Table 2.1 Particle diameters of $Ni(OH)_2$ nanoparticles shown in Figure 2.2 measured using ImageJ software. N/M indicates particle at the intersection was not measurable 54

Chapter 3

Table 3.1: Initial results of synthesis methods to produce Ni(OH)2 nanoparticles 79
Table 3.2: Full list of reaction conditions for hydrothermal syntheses of nickel hydroxide nanoplates 80
Table 3.3: List of particle diameters as measured by SEM/TEM for hydrothermal syntheses of nickel hydroxide nanoplates. Standard error in particle diameter was calculated using the method laid out in Section 2.2.1 84
Table 3.4: List of particle diameters as measured by DLS for hydrothermal syntheses of nickel hydroxide nanoplates. Standard error in particle diameter was calculated using the Zetasizer software 87

Table 3.5: List of particle diameters as measured by XRD for hydrothermal syntheses of nickel hydroxide nanoplates. Standard error in particle size was calculated using the three largest peaks in each diffractogram …… 90
Table 3.6: List of particle diameters as measured by SAXS for hydrothermal syntheses of nickel hydroxide nanoplates. Error in particle size was calculated using PANalytical software and the interquartile range …….. 90
Table 3.7: Comparison of particle sizes measured by electron microscopy and specific surface areas for hydrothermal syntheses of nickel hydroxide nanoplates. Standard error in particle diameter was calculated using the method laid out in Section 2.2.8. Error in specific surface area is given as error in DFT analysis provided by Quantachrome software …… 91

Chapter 5

Table 5.1 Circuit component values for $Ni(OH)_2$ coated electrodes at 0.0 V DC potential and 10 mV perturbation potential calculated using equivalent circuit in Figure 5.6 …… 148
Table 5.2 Circuit component values for Ni(OH)2 coated electrodes at 0.7 V DC potential and 10 mV perturbation potential calculated using equivalent circuit in Figure 5.6…….. 151
Table 5.3 Capacitive circuit component values for $Ni(OH)_2$ coated electrodes at various DC potentials discharging from 0.7 V to 0.0 V and 10 mV AC perturbation potential calculated using equivalent circuit in Figure 5.6 …….. 156

List of Abbreviations

AC	Alternating current
AFM	Atomic force microscopy
BE	Backscatter electron
BEs	Binding energies
BET	Brunauer-Emmett-Teller model
BJH	Barrett-Joyner-Halenda theory
CNT	Carbon nanotubes
CTAB	Cetyl trimethyl ammonium bromide
CV	Cyclic voltammetry
DC	Direct current
DFT	Density functional theory
DLS	Dynamic light scattering
ECP	Electrically conducting polymer
EDL	Electrical double layer
EDLC	Electrical double layer capacitor
EDX	Energy dispersive X-ray spectroscopy
EIS	Electrochemical impedance spectroscopy
FWHM	Full width half maximum
GCD	Galvanostatic charge/discharge
HER	Hydrogen evolution reaction
IHP	Inner Helmholtz plane
NiCd	Nickel cadmium
NiMH	Nickel metal hydride
NMC	Nickel manganese cobalt
nRA	Non-reduction assisted
OHP	Outer Helmholtz plane
PANI	Polyaniline
PEDOT	poly(3,4-ethylenedioxythiophene)

PPy	Polypyrrole
PTFE	Polytetrafluoroethylene
RA	Reduction assisted
SAXS	Small angle x-ray scattering
SE	Secondary electron
SEI	Solid electrolyte interface
SEM	Scanning electron microscopy
SSA	Specific surface area
TEM	Transmission electron microscopy
TML	Transmission line model
ToF-SIMS	Time of flight secondary ion mass spectrometry
XPS	X-ray photoelectron Spectroscopy
XRD	X-ray diffraction

List of Symbols

A	Area of active electrode surface in m^2
A^*	The cross section of the interface area in m^2
A_P	Area per particle in m^2
C	Capacitance in F
c	Concentration of electrolyte in mol dm^{-3}
C'	Real component of capacitance in F
C''	Imaginary component of capacitance in F
C_A	Capacity per unit area in mAh m^{-2}
Cap_s	Specific capacitance in F g^{-1}
C_D	Capacitance of the diffuse layer in F
C_{EDL}	Double Layer Capacitance in F
C_H	Capacitance of the IHP and the OHP in F
COD	Distance between the demagnified source image and the condenser lens in m
C_P	Faradaic capacitance in F
C_S	Specific capacity in mAh g^{-1}
C_{SC}	Space charge capacitance in F
D	Layer thickness from the electrode surface to the OHP (Chapter 1) / Diffusion coefficient (Chapter 5) in m
D_f	Diameter of the final SEM image spot size in m
D_i	Demagnified source image diameter at the beam crossover in m
E	Input potential in V
e	Potential at point in circuit in V
En	Energy of device in J
F	Faraday constant (96485 C mol^{-1})
f	Frequency in Hz
I	Current in A
I^0	Exchange current density
I_{max}	Peak current in A

K	Dimensionless Scherrer shape factor
L	Effective diffusion thickness in m
m	Mass of active electrode material in grams
n	Number of particles in sample
Pw	Power of device in Watts
R	Universal gas constant (8.314 J mol^{-1} K^{-1}) (Chapter 1) / Resistance in Ohms (Chapter 5)
r	Particle radius in m
R_{CT}	Charge Transfer resistance in Ohms
R_F	Faradaic resistance in Ohms
R_s	Internal Resistance (Chapter 1) / Series Resistance (Chapter 5) in Ohms
T	Temperature in kelvin
t	Time in seconds
V	Cell potential in V
WD	Working distance in m
W_o	Warburg open circuit element
W_s	Warburg short circuit element
W_{SI}	Semi infinite Warburg element
x	Displacement from pore opening in m
$\bar{x}$	Arithmetic mean
z	Charge of ions
Z	Impedance in Ω
Z'	Real component of impedance in Ω
Z''	Imaginary component of impedance in Ω
Z_{INT}	Interfacial impedance in Ω cm^2
$\alpha_{a/c}$	Dimensionless anodic and cathodic charge transfer coefficients
β	Peak broadening at the FWHM in radians (Chapter 2)
ε_0	Permittivity of free space (8.854×10^{-12} F m^{-1})
ε_r	Dielectric constant of the electrolyte in F m^{-1}
η	Overpotential in V
θ	Bragg angle in degrees (Chapter 2) / Phase difference (Chapter 5)

λ	wavelength in m
ν	Scan rate in mV s^{-1} unless otherwise stated
ρ	Density in g m^{-3} unless otherwise stated
σ	Standard deviation
τ	Mean size of the crystalline domains in m
ω	Angular frequency in radians per second

Chapter 1 - Introduction and Literature Review

1.1 The Importance of Charge Storage Device Research

Addressing the problem of global warming due to greenhouse gasses is one of the most pressing issues facing society today. If targets limiting global average temperatures to well below 2°C above preindustrial levels, as set out in the Paris agreement, are to be reached; there must be a large shift in the way energy is produced, stored, and used.[2]

The world's current electricity generation is heavily based on fossil fuels, as shown in Figure 1.1. The greenhouse gasses produced from the combustion of these fuels yearly amounts to over 35 billion metric tonnes of CO_2 released into the atmosphere per year.[5] While nuclear energy has shown promise, and some countries such as France produce around 70% of their electricity from nuclear, there is a large backlash around the world due to the perceived dangers of nuclear reactors.[6]

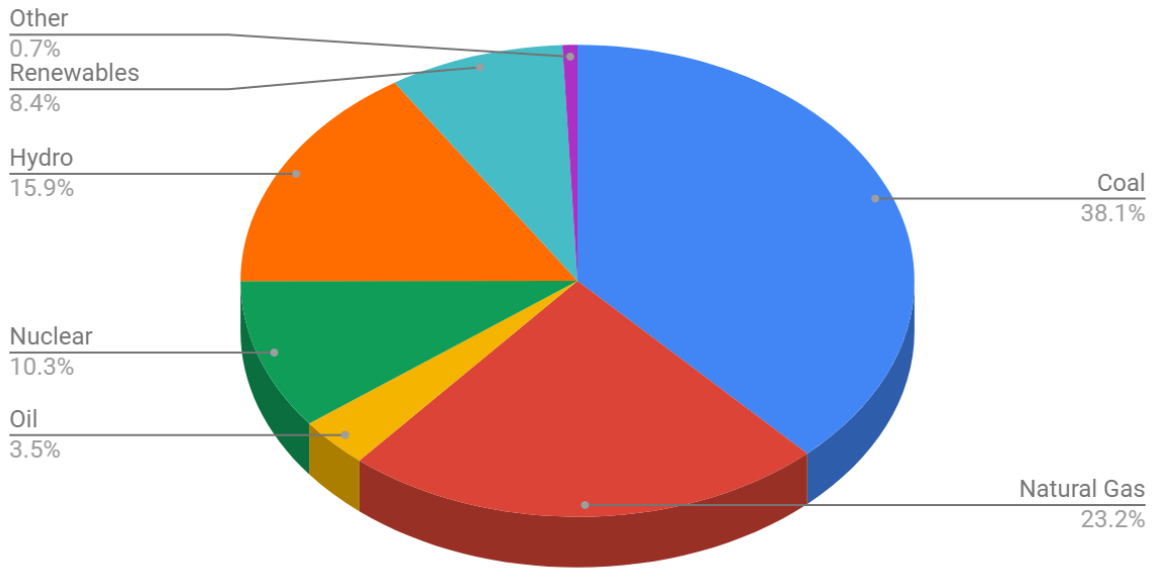


Figure 1.1 Global primary electricity generation by fuel type 2017, drawn from data taken from the BP Statistical Review of World Energy 2018[1]

Renewable energy sources, such as solar, wind and tidal energy, remain the cleanest choices for replacing fossil fuels. Over 2016 and 2017, the use of renewable energy sources in the UK increased by 19% to 99.3 TWh, accounting for approximately 10% of the energy consumed in the UK.[7]

The improvement of energy storage technologies is of vital importance, as society begins to depend more on renewable energy sources. These sources do not necessarily produce energy

at all times. This means excess energy must be stored, while stored energy is needed to compensate for times when energy production is low. Renewable energy sources represent just under 30% of energy generated in the UK, however the consumption was far lower since the excess could not be stored, meaning the flexibility of the network must be improved.[7]

In addition to grid storage, the use of high energy and power dense energy storage is necessary to cut emissions from transport networks. Electric cars such as the Nissan LEAF, the BAIC EC-series, or the Tesla Model S are becoming more and more common around the world. Batteries used in electric motor vehicles are improving year on year, but further improvement is required to match the convenience of a petrol- or diesel-powered vehicle.

A particular area of work is the range of the vehicle, which is limited by the gravimetric energy density. The specific energy of gasoline is approximately $1x10^4$ Wh kg^{-1}, exceeding the energy density of current secondary batteries, shown in Figure 1.2, by an order of magnitude.[1] Another problem faced by electric car users is the charging rate of the vehicles. An electric vehicle may require overnight charging compared to the mere minutes required to fill a fuel tank.

Portable charge storage is necessary for the continued development of consumer electronics. The requirements of portable electronic devices are extremely varied. Many devices require short pulsed power and current switching, which can not be achieved by slow charging and discharging devices.[8] In contrast to this, some devices require much higher energy density to be commercially viable

Finally, portable charge storage devices are also necessary to facilitate the development of off-grid energy storage. As of 2016, approximately 1.1 billion people worldwide had no access to electricity.[9] Energy access has be found to be intrinsically linked to quality of life in terms of health, education, food security, employment *etc*. Rapidly decreasing costs of renewable energy sources will help, but the energy generated must still be able to reach areas which are off-grid. The current Sustainable Development Goals report states that progress is falling short of targets to connect the entire world by 2030.[10]

1.2 Batteries and Supercapacitors

Batteries are the current standard in energy storage for both consumer and industrial electronic devices, due to their high energy density. Current battery technology however is

dangerous, expensive, and delivers poor performance in certain key areas. Most batteries suffer from low power densities, meaning many batteries must be used in series. As well as power density concerns, swelling during charging and discharging causes batteries to have a short usage lifetime as the materials degrade.[11]

Electrochemical capacitors, also known as supercapacitors, are an alternative type of energy storage device. Supercapacitors may be redox active devices similar to batteries, or store charge electrostatically, as discussed in Section 1.4.

Supercapacitors offer a middle ground between the high energy density of batteries or fuel cells and the high power density of traditional dielectric capacitors. Supercapacitors also exhibit rapid charge and discharge, and longer life times, since intercalation does not occur on charging meaning less electrode swelling.

Supercapacitors are typically lower resistance devices, meaning they function better at lower temperatures compared to batteries. At low temperatures, the kinetics of the chemical reactions in the battery slow down, causing high internal resistance. This makes batteries inefficient at low temperatures, whereas the internal resistance of supercapacitors does not reach battery levels even at temperatures as low as -40^{o}C.[12] Supercapacitors are considered much safer than batteries, due to the lower chance of overheating and as less toxic materials can be used in the devices.

The disadvantages of supercapacitors compared to batteries are the low energy densities and voltages produced, as well as the tendency of supercapacitors to self-discharge over time via charge redistribution, ohmic leakage and faradaic reactions with the electrolyte.[11-12] These are the areas of improvement which must be addressed in future research. Supercapacitors made of carbon or metal oxides also currently cost more to produce than batteries. However, this is not due to the inherent cost of the materials, only due to the fact that they are not yet produced in large quantities. Once large scale production is achieved, cost competitiveness would likely follow.

Supercapacitors are not necessarily a replacement for batteries. Since they have very different properties, they can be used in tandem with batteries to compensate for batteries' weaknesses. For applications with high power requirements, the life span and performance of a battery can be improved using a supercapacitor electrode as a hybrid device. The

supercapacitor produces a voltage damping effect, decreasing the large potential drop on the battery, and supplying power inversely proportional to its internal resistance. A low impedance supercapacitor can be charged in seconds with a low current during standby times between high current pulses.[4, 11-12]

1.3 Energy and Power Densities

As discussed in the Section 1.2, one of the key differences between batteries and supercapacitors is the energy and power densities produced by these devices. The energy and power densities of various energy storage devices are compared in Figure 1.2, the Ragone plot.

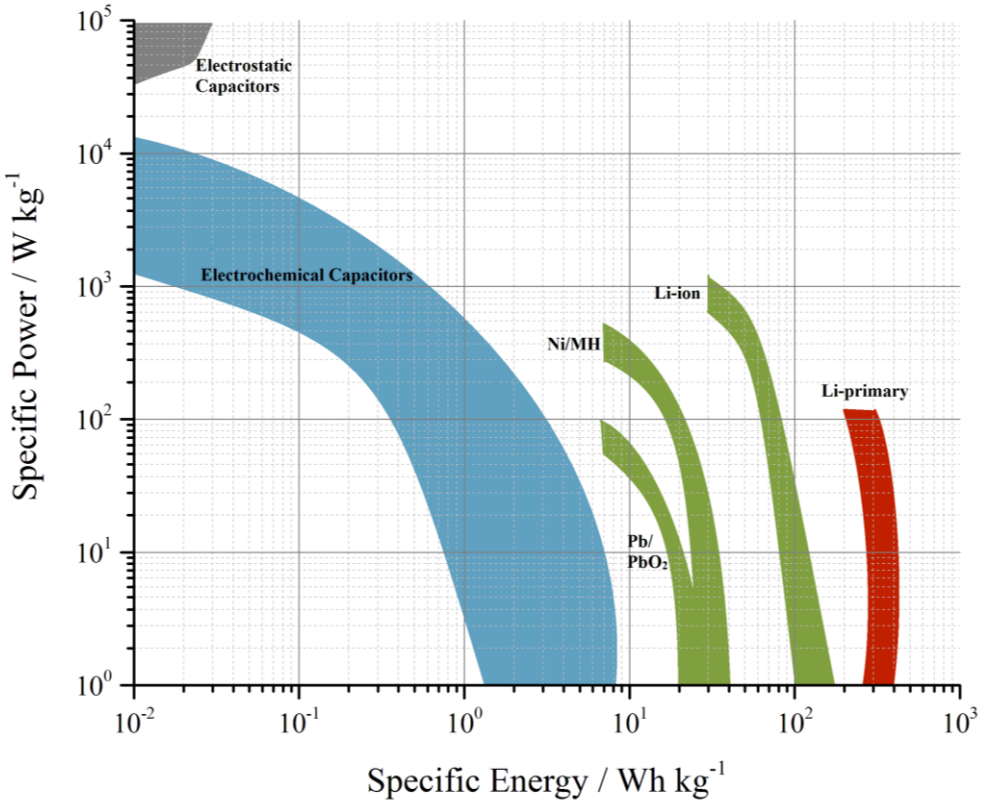


Figure 1.2 Ragone plot showing the specific energy and power of various electrochemical storage devices. Figure was redrawn from data taken from source[3]

Supercapacitors offer a wider range of performances compared to batteries due to the varying nature of the materials and storage mechanisms employed, as discussed in sections 1.4 and 1.5. The electrode materials, as well the electrolyte used, will have an effect on the properties of the device. The materials are required to have a wide potential window and be electrochemically stable, even at high voltages for some applications. A wider potential window is beneficial as the energy stored in the device, *En*, and the power of the device, *Pw*, are proportional to the square of the voltage, as shown in Equation (1.1) and Equation (1.2);

$$En = \tfrac{1}{2}CV^2 \quad (1.1)$$

$$Pw = V^2/4R_S \quad (1.2)$$

where C is the capacitance, V is the potential window, and R_S is the internal resistance of the device.

When attempting to maximise energy density in a supercapacitor or power density in a battery, it is important to not compromise the other properties of the device. For example, improving energy density in a supercapacitor is typically accompanied by a dramatic loss of power density. This risks turning a mediocre supercapacitor into a poor performing battery.

1.4 Mechanisms of Charge Storage

To allow improvements in the properties of charge storage devices, the mechanisms of charge storage must first be understood. Possible charge storage mechanisms include electrical double layer capacitance, pseudocapacitance, and intercalation redox as found in batteries.

1.4.1 Electrical Double Layer Capacitors

An electrical double layer capacitor (EDLC) makes use of the electrical double layer (EDL) formed at the interface between a charged surface, in this case the electrode, and an electrolyte solution. During charging, electrons are transferred between electrodes. This creates two charged electrode surfaces with either a deficiency or a surplus of electrons. Electrolyte cations move towards the negative cathode, while anions move towards the positive anode, forming an EDL at each electrode. The reverse processes take place during discharge. Charge is stored using the adsorption of electrolyte ions onto the active surface of the electrodes.

The double layer consists of two main layers, as shown in Figure 1.3. The innermost layer, the inner Helmholtz plane (IHP), is made up of partially desolvated ions adsorbed to the electrode surface. This layer may not be present if the free energy change on losing the water of solvation is not compensated for by that of ion adsorption, meaning adsorption is not energetically favourable. Following this is a layer of fully solvated ions called the outer Helmholtz plane (OHP). This layer, along with the IHP, has the effect of screening the surface charge “seen" by the rest of the bulk electrolyte.

The final layer, termed the diffuse layer, connects the OHP to the bulk, and is a region of high ionic concentration relative to the bulk for the ion with the counter charge to the electrode surface. This layer can still contribute to the EDL charge and capacitance, especially in the cases where electrolyte concentration is low. For high ionic concentration, the rapid decrease in potential as distance from the surface is increased means the total thickness of the double layer is *ca*. 1 nm, meaning it can be sufficiently modelled by the Helmholtz plane alone.[13]

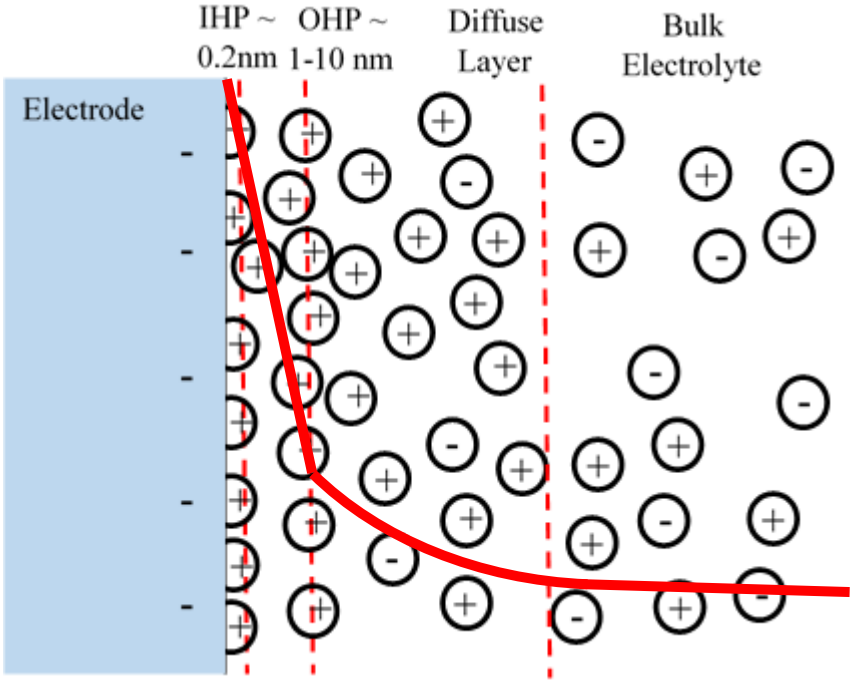


Figure 1.3 Schematic representation of the electrical double layer formed at the electrode surface (not to scale). Potential drop shown in red.

The electrostatic nature of charge storage requires no redox behaviour at the electrodes, meaning the electrodes can be classified as blocking electrodes for a perfect EDLC. The surface storage mechanism allows for very fast uptake of ions and prevents capacitor swelling during charging.

The double layer capacitance, C_{EDL}, can be expressed by Equation (1.3);[14]

$$1/C_{EDL} = 1/C_H + 1/C_D \quad (1.3)$$

where C_H is the capacitance of the IHP and the OHP, and C_D is the capacitance of the diffuse layer. C_H can be calculated according to Equation (1.4);[14]

$$C_H = \varepsilon_0\varepsilon_r(A/D) \quad (1.4)$$

where A is the area of the active electrode surface, ε_r is the dielectric constant of the electrolyte, ε_0 is the permittivity of free space, and D is the layer thickness from the electrode surface to the OHP. C_D can be calculated for a 1:1 electrolyte according to Equation (1.5);[14]

$$C_D = A^* F \frac{\sqrt{2z^2\epsilon_0\varepsilon_r c}}{RT} \cosh\frac{zFV}{2RT} \quad (1.5)$$

where A^* is the cross section of the interface area, F is the Faraday constant (96485 C mol^{-1}), z is the charge on the ions, c is the molar concentration of the electrolyte, V is the potential difference at the interface, R is the universal gas constant (8.314 J mol^{-1} K^{-1}), and T is the temperature in K.

This model is only accurate for materials with a near infinite density of states at the Fermi level, such as metals. For semiconductor materials, a third capacitance, known as the space-charge capacitance (C_{SC}) must also be included in Equation (1.3). Knowing the sources of capacitance in the system allows an EDLC to be modelled using an equivalent circuit.

Since the electrode in a perfect EDLC is not electrochemically active, but only provides a surface for double layer formation, the electrode material must have a high and accessible specific surface area (SSA). It must also be electrochemically stable and highly conductive. A schematic for this type of capacitor is shown in Figure 1.4.

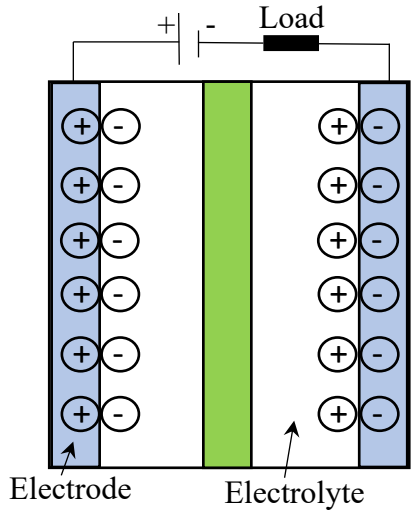


Figure 1.4 Schematic of an electrical double layer capacitor, redrawn from source[4] (not to scale)

1.4.2 Pseudocapacitors

Pseudocapacitors, also known as Faradaic supercapacitors, use redox active materials as the electrodes. During charging, reversible and non-rate limiting Faradaic reactions occur across the double layer on the electrode surface, shown in Figure 1.5. This process is similar to the

redox behaviour of a typical battery. As with EDLCs a high accessible SSA and good electrical conductivity are important for these materials.

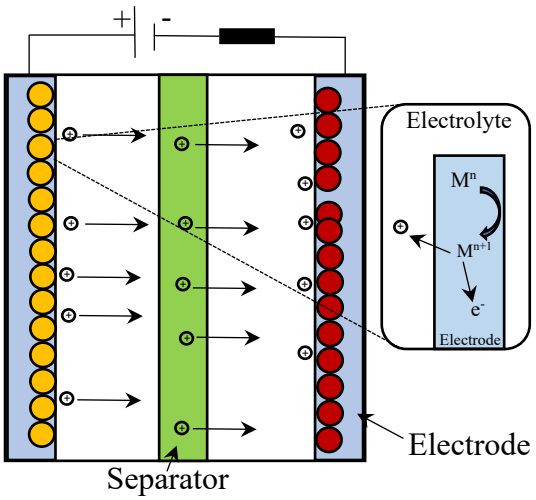


Figure 1.5 Schematic of a typical redox pseudocapacitor, redrawn from source[4] (not to scale)

Pseudocapacitors make use of different processes to store charge. The actual mechanism of charge storage depends on the electrode material and the electrolyte used. The mechanism shown in Figure 1.5 is known as redox pseudocapacitance, when ions are adsorbed electrochemically onto or just beneath the surface of the electrode, with an accompanying Faradaic charge transfer. This is the most common mechanism of pseudocapacitance and is the focus of this thesis. Less common mechanisms are underpotential deposition, such as lead onto a gold electrode surface,[15] and intercalation pseudocapacitance. Intercalation pseudocapacitance operates in a similar method to a battery, discussed in Section 1.4.3; however, there is no associated phase change. The similarity in this mechanism with battery chemistry demonstrates why it is often difficult to unambiguously state the mode of operation of a charge storage device.[14, 16]

Metal oxides in acidic solutions undergo partial reduction using aqueous protons and electrons from the electrodes to form hydroxides. The opposite will happen in basic electrolytes, where protons are removed during surface layer oxidation. This adsorption of protons and electrolyte counter ions is the source of capacitance.

Pseudocapacitance can be either intrinsic or extrinsic to a material. An intrinsic pseudocapacitor will display pseudocapacitance regardless of the material morphology and size. Examples of this type of pseudocapacitor are $RuO_2.xH_2O$, which is discussed further in Section 1.5. Extrinsic pseudocapacitive materials can act as pseudocapacitors, but only through appropriate material engineering. Extrinsic materials do not exhibit

pseudocapacitance in the bulk state due to phase transformations during ion storage limiting the reaction kinetics.[16-17] With these materials, increasing the surface area through nanostructuring leads to improved high-rate behaviour due to a decrease in diffusion distances.

The specific capacitance and energy density of a pseudocapacitor exceeds that of EDLCs by ten to a hundred times. However, since the mechanism of charge storage is similar to that of a battery, the devices share similar problems. These are a lack of stability after charge cycling and lower power density.

1.4.3 Intercalation Batteries

Battery type electrode materials make use of redox reactions to store electrochemical energy. There are several types of battery electrodes, the exploration of which is beyond the scope of this short review.

The underlying principle of modern battery operation is intercalation of an ion into the bulk of a "host" electrode structure. Intercalation of ions into the bulk of the structure allows for a large specific energy, utilising as much of the bulk of the electrode material as possible.

Host materials are stable crystal lattices. Pathways for "guest" ions, such as a lithium, are provided by their layered or tunnel structures. The redox reactions occur on the host lattice while mobile guest ions intercalate into, or deintercalate from, the host. Injecting or extracting electrons compensates for regional electroneutrality. During the whole charge/discharge cycle, the guest ion does *not* undergo a Faradaic reaction.

Phase changes during the intercalation of ions in the host material on charging will cause fatigue to the material. In some cases, swelling of the electrode is observed during deintercalation of the battery electrodes due to repulsion between oxygen in the cathode layered electrodes. In either case, this swelling will cause mechanical strain on the electrode material.

In addition, power density is limited by the rate at which ions can be deintercalated from the electrode lattice. The reaction is unique to the materials used as the anode and cathode in the battery, which is discussed further in Section 1.5.3.

1.5 Materials for Charge Storage Devices

The charge stored, lifetime, potential window, and other properties of charge storage devices all depend on the materials used to build the device. Improving the performance of current electrode materials allows new applications to be explored as well as potentially minimising the cost and environmental impact of the devices. Properties which are important to consider when designing charge storage materials are an SSA, in the order of 1000 $m^2\ g^{-1}$, the intra- and intermolecular connectivity of the materials, and the porosity of the material, allowing for electrolyte penetration into the structure.

1.5.1 Inert Double Layer Materials

Carbon materials have been shown to satisfy all considerations for an electrode material in an EDLC. The different morphologies of carbon give very different conductivities and capacitance values, ranging from 10 F g^{-1} to >250 F g^{-1}.

Carbon-based materials that have been studied include activated carbon granules (Cap_S = 40 F g^{-1}),[12] carbon nanotubes (CNT) (Cap_S = 80 F g^{-1}),[18] graphene nanosheets and their derivatives (Cap_S = 140 F g^{-1}),[19] and carbon aerogels (Cap_S = 160 F g^{-1}).[12] The different materials have also been used together to create hybrid morphologies of graphene and CNTs with Cap_S of over 290 F g^{-1}.[18,19]

These materials are good electrical conductors and have highly porous structures, giving rise to a large and accessible surface area. Activated carbon has a high outer surface area; however, many of the internal surfaces are not accessible by electrolyte ions.[3] Further loss of surface area can also occur due to aggregation of the material, preventing large areas from being accessible. This is particularly a problem for carbon structures in aqueous environments due to strong hydrophobic interactions. The highly porous structures can also collapse on drying due to van der Waals interactions, turning a high SSA graphene into compact graphitic carbon.[18]

Highly porous carbon networks contain micropores (<2 nm), mesopores (2-50 nm) and macropores (>50 nm).[20] Some studies have suggested that the smallest pores, < 1 nm,[3] are inaccessible to solvated ions due to the large, bulky solvation shell formed around the ion in solution, and therefore do not contribute to the EDL capacitance. However, increasing pore

size does not necessarily lead to an increase in capacitance, and pores much smaller than the solvated ions can lead to a large increase in capacitance by stabling desolvated ions.[20] High capacitances have been achieved using mesoporous carbon, which contains a large number of micropores. This suggests that at least partial desolvation of the ions occurs on adsorption, despite the large associated free energy change.[18-20] Carbon materials also have the advantage of being abundant, low cost, non-toxic, and highly stable with a wide range of operating temperatures. Activated carbons are produced by carbonisation followed by selective oxidation to increase SSA and pore volume. The sources of carbon in these cases can be natural materials such as biomass or synthesis polymers.

1.5.2 Redox Active Pseudocapacitive Materials

Due to their higher specific capacity, most new work in the area of supercapacitors uses redox active pseudocapacitive materials, either alone or with EDL high surface area carbon. The major classes of redox active electrodes are electrically conducting polymers (ECPs) and metal oxide materials.

ECPs such as polypyrrole (PPy) (Cap_s = 120 F g^{-1})[12,21], polyaniline (PANI) (Cap_s = 815 F g^{-1}),[12,14] and poly(3,4-ethylenedioxythiophene) (PEDOT) (Cap_s = 990 F g^{-1})[12] have been extensively studied as pseudocapacitive materials. ECPs are low cost, have a low environmental impact, and a high conductivity when undergoing redox reactions. The capacitance arises from the fast redox reactions related to the pi-conjugation in the polymer chains. ECPs can be either oxidised or reduced, resulting in p-type or n-type polymers respectively, with counter ions from the electrolyte maintaining the overall charge neutrality. Despite high capacitance values, typically higher than EDLC materials, ECPs are not used as electrode materials alone, due to their low mechanical strength. During charge cycling, volumetric changes caused by insertion of counter ions cause the material to break down and the capacitance to decrease. This degradation can be even more rapid if the device is overcharged.[12, 21] ECP materials are instead used as composites with a nanostructured carbon material such as graphene or CNTs.[21]

Due to their high energy densities and good electrochemical stability, metal oxides are widely regarded as the best prospect for supercapacitors. Ruthenium oxides (Cap_s = 1099-1300 F g^{-1}),[12,22-23] manganese oxides (Cap_s = 600 F g^{-1}),[12,24] iron oxides (Cap_s = 285 F g^{-}

^{1}),[25] cobalt oxides (Cap_s = 746 F g^{-1}),[12,26] and nickel oxides (Cap_s = 696 F g^{-1})[12,27-28] have all been shown to exhibit larger specific capacitance than pure EDLC materials and better electrochemical stability than ECPs.

Charge is stored by EDL capacitance and also through the redox reactions at the surface, and in the near surface bulk, of the materials. Transition metals, which have multiple accessible oxidation states at close energies to each other, are perfect for this application. Transition metals can exist in two or more oxidation states simultaneously and do not necessarily undergo irreversible morphological or phase changes during redox reactions. The oxides of these metals however tend to be resistive, so nanoscale morphologies such as thin films or nanoparticles on conductive metal current collectors are typically used.

The mechanism of pseudocapacitance requires an accessible surface so reduction and oxidation can occur. Therefore, transition metal oxide electrodes must also have a porous structure. As expected, increasing the SSA of metal oxide materials through nanostructuring can significantly improve the specific capacitance for similar reasons to the EDL materials.[14] The most studied systems to date are the ruthenium and manganese oxides, while other metals are still being explored.

Hydrated ruthenium oxide, $RuO_2.xH_2O$, is an intrinsic supercapacitor material which has been extensively studied due to the reversibility of redox reactions between its three oxidation states within a small 1.2 V potential window. It also shows high proton conductivity, thermal stability and electrical conductivity.

Specific capacitance values of over 1000 F g^{-1} for samples in aqueous electrolyte have been observed, with approximately 10% of this attributed to EDL capacitance and the rest to redox pseudocapacitance.[14, 22-23] The mechanism of pseudocapacitance is solution specific. In acid solutions for example, electroadsorption of aqueous protons on to the surface of ruthenium oxide is accompanied by rapid electron transfer. The ruthenium oxidation state changes between Ru(II) to Ru(IV), as shown in Equation (1.6).[14, 22]

$$RuO_2 + xH^+ + xe^- \rightarrow RuO_{2-x}(OH)_x \qquad (1.6)$$

The fraction of reduced metal oxide, x (where $0<x<2$), will vary continuously across the potential window, causing capacitance due to ion adsorption. Specific capacitance values for

these oxides will depend on the cation, in this case proton, exchange. This has been shown to be affected by the SSA, water presence, crystallinity, particle connectivity, and the electrolyte used.[22]

Despite impressive performance, RuO_2 capacitors are very expensive, and the materials are highly toxic. This means that alternative materials need to be found which can exhibit the same impressive specific capacitance and cycling stability as RuO_2. Research into cheaper alternatives, such as nickel oxides, is a promising area of development. Numerous studies using nickel oxide/hydroxide/oxyhydroxide have delivered high capacitance values similar to those found for ruthenium oxide based electrodes.[27, 29] This is only true when the material is engineered at the nanoscale, being an extrinsic pseudocapacitor. The electrochemical properties of $Ni(OH)_2$ are discussed further in Section 1.6.2.

1.5.3 Secondary Battery Materials

As discussed in Section 1.4.3, there are too many types of batteries to comprehensively review in this work. Lead-acid batteries, the oldest rechargeable or secondary battery and the most common, has been replaced in several applications by other technologies.[30-31] Two other common battery types are discussed to contextualise the work being done.

Lithium/Lithium Ion Batteries

One of the most common rechargeable battery types is the Li-ion battery[31] due to their high cell voltage, low rate of self-discharge and competitive power/energy densities.[32] Li-ions are highly suitable for energy storage due to their high electronegativity (~-3.0 V vs standard hydrogen electrode) and low atomic mass.[33] These properties lead to a high cell voltage and high theoretical specific capacity.

Lithium metal was originally used as an anode material, but ultimately failed due to Li dendrites growing on the surface during charging. These dendrites, referred to as such due to their needle-like morphology, not only reduce the amount of active lithium in the battery reducing the specific energy, but can also lead to short circuits, and explosion of the battery if the dendrites pierce the separator.

To prevent this, intercalation type electrodes using host-guest chemistry are utilised. Early host cathode materials were transition metal oxides or chalcogenides. Carbonaceous

materials such as graphite were employed as the anode intercalation host, in attempts to prevent the formation of Li dendrites.[34-35] Batteries employing such intercalation cathodes and anodes, nicknamed “rocking-chair batteries”, require the lithium ions to shuttle back and forth between the electrodes, shown in Figure 1.6.[32]

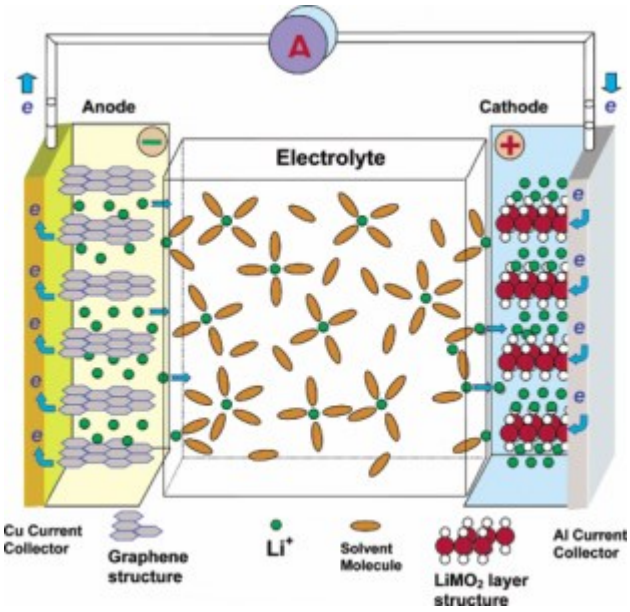


Figure 1.6 Schematic of Li-ion battery, showing intercalation graphitic carbon anode and transition metal oxide cathode during discharge. Reprinted with permission (see Appendix 1) from Xu, K., Nonaqueous Liquid Electrolytes for Lithium-Based Rechargeable Batteries. Chemical Reviews 2004, 104 (10), 4303-4418. Copyright (2019) American Chemical Society.

One feature of Li-ion batteries which has attracted a lot of experimental focus in recent years is the solid electrolyte interface (SEI). During the first charge cycle, the decomposition products of some electrolytes form a solid layer which covers and passivates both anode and cathode surfaces. An example of this is the formation of an SEI on graphitic electrodes by the breakdown of ethylene carbonate electrolytes.[32] This SEI acts as a passivating layer to prevent further electrolyte degradation, while remaining Li-ion conductive. The formation of the SEI and its mechanism of operation remain subjects of research despite numerous papers documenting the composition of the layer.

Nickel Hydroxide Based Secondary Batteries

Nickel hydroxide has been employed as a battery electrode for over 100 years. Representing 73% of non-lead acid rechargeable batteries used in Europe, common types of battery which use $Ni(OH)_2$ as an intercalation electrode material are nickel cadmium (NiCd) and nickel metal hydride (NiMH).[31]

NiCd secondary batteries were developed in the 1950s and dominated the market for portable applications.[31] On discharge, the cadmium anode reacts with electrolyte hydroxide

ions while the nickel oxyhydroxide is reduced back to nickel hydroxide. This is shown in Equations (1.7), (1.8), and (1.9). The overall cell reaction results in an average cell potential of 1.2 V.[36]

$$Discharge\ Cathode:\ NiOOH + H_2O + e^- \rightarrow Ni(OH)_2 + OH^- \quad (1.7)$$

$$Discharge\ Anode:\ Cd + 2OH^- \rightarrow Cd(OH)_2 + 2e^- \quad (1.8)$$

$$Discharge\ Cell\ Reaction:\ 2NiOOH + 2H_2O + Cd \rightarrow 2Ni(OH)_2 + Cd(OH)_2 \quad (1.9)$$

One major drawback for NiCd batteries is the environmental impact of the cadmium due to the material's toxicity. Despite efforts to improve battery recycling,[31] this toxicity has led to the replacement of NiCd batteries with NiMH alternatives. NiMH batteries are considered more environmentally friendly than NiCd, but have higher production costs.[31]

NiMH secondary batteries also use nickel hydroxide as the cathode on discharge, however the anode is now a hydrogen absorbing metal or alloy. Electrolytes typically contain potassium hydroxide and lithium hydroxide.[37] A similar cell reaction to NiCd batteries is shown in Equations (1.10), (1.11), and (1.12).

$$Discharge\ Cathode:\ NiOOH + H_2O + e^- \rightarrow Ni(OH)_2 + OH^- \quad (1.10)$$

$$Discharge\ Anode:\ MH + OH^- \rightarrow M + H_2O + e^- \quad (1.11)$$

$$Discharge\ Cell\ Reaction:\ NiOOH + MH \rightarrow Ni(OH)_2 + M \quad (1.12)$$

The *M* in the anode is typically an alloy made of nickel, manganese, and cobalt. Similar electrodes are also used in Li-ion batteries, known as an NMC electrode. The structure and electrochemistry of the $Ni(OH)_2$ electrode is discussed further in Section 1.6.

1.5.4 Electrolytes

The ions in the electrolyte must be present in high concentration and the solvated ionic radius of those ions must be small in order to exploit all available pores in the electrode structure. For example, solvated OH^- in aqueous solution has a radius of 0.3-0.4 nm depending on hydration number, meaning it can exploit nanoporous structures.[33] The electrolyte must also have suitable properties such as low viscosity and volatility. The cost of the electrolyte must be as low as possible, while maintaining the purity of the electrolyte.

Aqueous electrolytes, such as KOH or H_2SO_4, have high ionic strength and conductivities. For example, 1 mol dm^{-3} KOH has a conductivity of around 200 mS cm^{-1} at room temperature.[55] This compares favourably to organic electrolytes such as acetonitrile, which have conductivities in the range of 1 μS cm^{-1}.[56] Devices tuned for higher power densities tend to use aqueous electrolytes due to the small size and high concentration of the ions in solution. The low viscosity of water also allows for facile transport of ions through the solution. Aqueous electrolytes can be processed and used without the concern of stringent safety and environmental protection measures, that are associated with some organic electrolytes.

A major disadvantage of aqueous electrolytes is their small potential window, which is *ca.* 1.2 V.[14] Equations (1.1) and (1.2) show that this small potential window limits the energy and power densities of devices using aqueous electrolytes. This is the reason why organic electrolytes have been considered.

Organic electrolytes, such as acetonitrile or propylene carbonate, have a much larger potential window, up to 3.5 V,[14] and therefore have the possibility of reaching much higher energy densities, see Equation (1.1). Some of these organic solvents, particularly acetonitrile, can support high ionic strength solutions. They do, however, raise environmental and toxicity issues, so the greener propylene carbonate is preferred.[14] Organic electrolytes must be kept dry or the large potential window of the solvent will decrease.

Ionic liquids are solvent-free electrolytes with a potential window limited only by the electrochemical stability of the ions. Tailoring of the anion and the cation allows the design of high voltage supercapacitors.[38] By "melting" an ionic lattice, preferably at room temperature, into a liquid, an electrolyte is produced with an extremely high ionic concentration. In addition, the ions produced have no solvation shell. The major drawbacks to using these electrolytes are the low conductivity, approximately a few μS cm^{-1}, and high viscosity offered at room temperature. Most current applications are at high temperatures only.[38]

1.6 Physical and Electronic Properties of Nickel Hydroxide

As shown in Section 1.5.2 and 1.5.3, nickel hydroxide has long been used as an electrode in different types of electrochemical energy storage devices. Understanding the material

properties and its electrochemical behaviour is necessary before designing an experiment to measure its charge storage properties.

1.6.1 Structure of Nickel Hydroxide Polymorphs

Nickel hydroxide exhibits a large range of structures, with two polymorphs at the extreme ends, denoted the α- form and the β-form. Both the polymorphs are formed by hexagonal close packed lattices of hydroxyl ions, with hexagonal planar Ni(II) ions in an octahedrally coordinated environment. The $Ni(OH)_2$ layers then stack along the perpendicular z-axis. The interplanar spacing between these layers is the primary difference between the phases.

The β-$Ni(OH)_2$, shown in Figure 1.7, which occurs naturally, has a hexagonal close packed structure. The unit cell is primitive with the space group P-3m1, making the crystal isostructural with $Mg(OH)_2$ and metal halides such as CdI_2.[39] The interlayer distance in the β-form is *ca*. 4.6 Å, with the other two identical unit cell parameters of *ca*. 3.1 Å.[39]

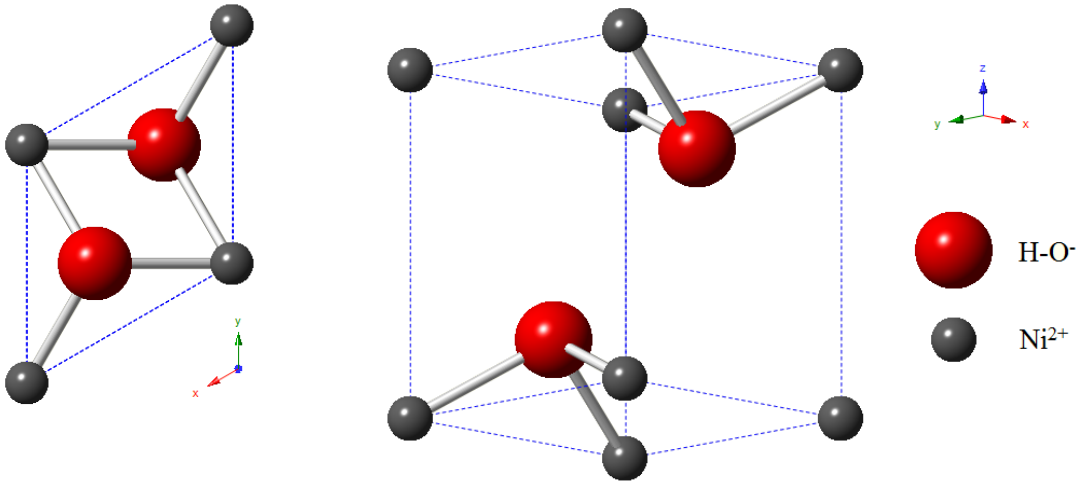


Figure 1.7 Ball and stick rendering of the β-$Ni(OH)_2$ unit cell, in (a) Ni (001) and (b) Ni (111) projections. Figures made using crystallographic data from the American Mineralogist Crystal Structure Database

While the β- form shows consistent stacking along the z-axis, the layers in the α- form exhibit several types of stacking faults. This phase is known as a turbostratic phase. The increased interlayer spacing allows the intercalation of water and other solvent anions into the structure. The formula for the α- phase is more accurately written $Ni(OH)_2.xH_2O$ with *x* varying from 0.4 to 0.7.[40-41] The amount of hydration can be estimated using thermogravimetric analysis. The interlayer distances can increase to *ca.* 8 Å if anions present from synthesis are intercalated into the structure.[39] If the water were close packed as suggested in the original analysis of the structure,[42] the interlayer spacing would not exceed 7.6 Å. The water is

thought, therefore, to be in an unbound state, allowing the layers to stack in random orientation and giving rise to the turbostratic phase.[39, 43]

Between the closely packed and fully separated phases of $Ni(OH)_2$ there are multiple other phases with various ion intercalation and stacking faults. These phases are sometimes termed β_{bc} where bc stands for badly crystallised. This terminology, however, offers little insight into the structural faults of the phase. Stacking faults are fairly common in these materials due to the relatively weak interlayer interactions. Regularly occurring faults include single layer rotations about the z-axis, single layer tilting with respect to the x-y plane, or translation within the x-y plane. Despite having hydroxyl groups orientated between layers, the spectroscopic evidence suggests there is very little interlayer hydrogen bonding, possibly due to the very electro-positive nickel ions.[43-44]

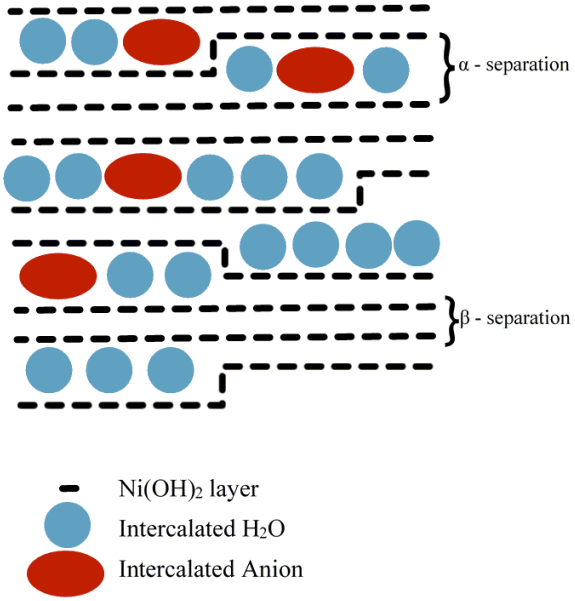


Figure 1.8 Interstratification of α- and β-Ni(OH)2 showing intercalated water and anions.(not to scale)

Samples containing both α- and β- layering have been identified,[45] with the structure shown in Figure 1.8. In these structures, some of the $Ni(OH)_2$ layers are separated by intercalated species, while others remain close packed. Rather than a simple mixture of α- and β- crystals, these materials show both structural motifs within the same crystal. These materials can be identified by the mixture of α- and β- diffraction patterns formed using X-ray diffraction.[41, 45-46]

1.6.2 Electrochemical Properties of Nickel Hydroxide

Nickel hydroxide is a p-type semi-conducting material, with a band gap in the range of 3-3.5 eV as measured by UV-Vis absorption spectra.[47] In basic electrolytes, the charge-discharge processes are given in Equation (1.13) and Equation (1.14).[42]

$$Charging: Ni(OH)_2 + OH^- \rightarrow NiOOH + H_2O + e^- \quad (1.13)$$

$$Discharging: NiOOH + H_2O + e^- \rightarrow Ni(OH)_2 + OH^- \quad (1.14)$$

The phase changes accompanying the charge-discharge processes are shown in Figure 1.9.[42] The cell reduction potential is measured at 0.291 V *vs* a Ag/AgCl reference electrode.[47]

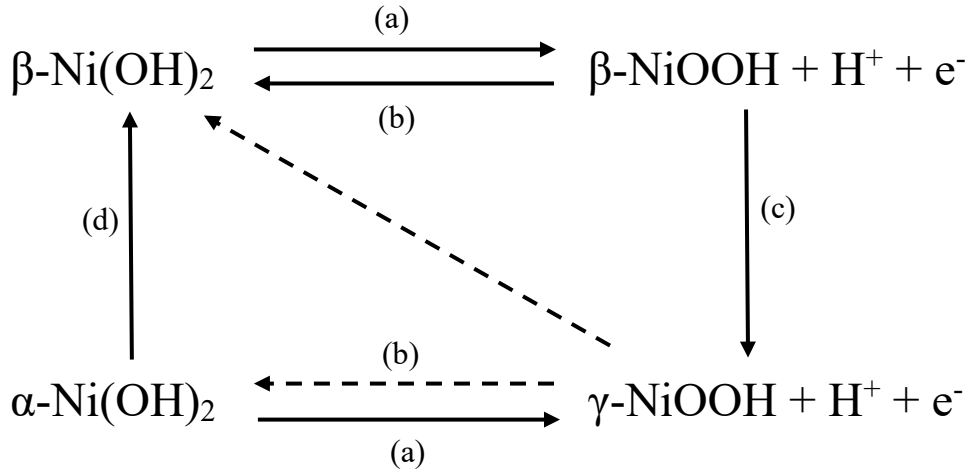


Figure 1.9 Phase changes on charging of nickel hydroxide (a) charging, (b) discharging, (c) over-charging, and (d) chemical ageing.

The extent of material utilisation is controlled by the intercalation of protons and electrons into the bulk of the material, allowing the surface to continue the reaction. While the reaction is represented as a formal $Ni^{2+/3+}$ redox, the nickel oxidation state has been found to be a mixture of between 2.0 to 3.7 within the charged material.[48] Consequently, the process is not a simple 1 e^- transfer, but rather dependent of the charging state and phase of the $Ni(OH)_2$.

The higher electrochemical activity of the intrinsically pseudocapacitive α-$Ni(OH)_2$ makes it a desirable electrode material. β-$Ni(OH)_2$ will also display pseudocapacitive properties, but only when engineered to the nanoscale, making it an extrinsic pseudocapacitor. The synthesis challenges of forming and maintaining the phase are discussed in Chapter 3.

The enhanced α-$Ni(OH)_2$ activity is due to several factors, such as the more open and accessible structure, the increased number of electrons transferred per nickel, and the increased electrochemical activity due to stacking faults. The first factor is intuitive. With a more open and porous structure, the intercalation of hydroxide ions and removal of water on charging is much faster.[47]

The high average Ni oxidation states of up to 3.7 are seen in γ-Ni(OOH) due to Ni^{4+} defects.[48] While this state is accessible using either $Ni(OH)_2$ polymorph, it is accessible at much lower potentials from α-$Ni(OH)_2$ compared to β-$Ni(OH)_2$. This means that while the maximum number of electrons transferred per reaction for the β-$Ni(OH)_2$/β-Ni(OOH) charging pair is 1, the α-$Ni(OH)_2$/γ-Ni(OOH) pair can reach up to 1.7 e^- transferred per reaction, resulting in a higher specific capacity.[45]

Stacking faults have been shown to lead to an increased interaction between the Ni ions, and the hydrogen of the bonded hydroxide groups. This interaction has been shown to destabilise the hydrogen, meaning the reaction between the hydrogen and solution hydroxide is much easier. This leads to an enhanced electrochemical activity compared to well-ordered β-$Ni(OH)_2$.[49]

As already mentioned, while pure α-$Ni(OH)_2$ has a very high theoretical capacitance, it is rarely used in supercapacitor devices. This is due to practical problems maintaining the α- form *in-operando.* To prevent the loss of the open structure due to chemical ageing, the inclusion of dopants into the $Ni(OH)_2$ structure has been used.

The most common dopant is cobalt, which will insert into the structure as cobalt hydroxide, $Co(OH)_2$.Cobalt will insert into the hydroxide ionic structure, but the larger ionic radius will cause stacking faults, such as those seen in α-$Ni(OH)_2$. As well as improving the electrochemical activity of the material, increasing the interlayer distance of the material reduces the mechanical stress on charging. Moving from the β-$Ni(OH)_2$ to the β-Ni(OOH) requires a slight increase in the interlayer distance.[46] This increase is much less going from α-$Ni(OH)_2$ to γ-Ni(OOH).[26-27] Reducing the material swelling means the cyclability of the material is improved, and high capacitances remain after more charge cycles.

The problem with these materials however is the leaching of the dopants from the structure by chemical ageing. This process, while slower than the α- to β-phase conversion in solution, is still a problem for device stability.[13]

1.7 Battery or Supercapacitor Material? – The Controversy

As already discussed in sections 1.5.2 and 1.5.3, nickel hydroxide has been studied and employed as both a battery and psuedocapacitive electrode. When defining a material as a

battery or pseudocapacitive electrode material, the electrochemical response must be considered.

The electrochemical response of an EDLC, psuedocapacitive, and battery-like electrode material is shown in Figure 1.10.

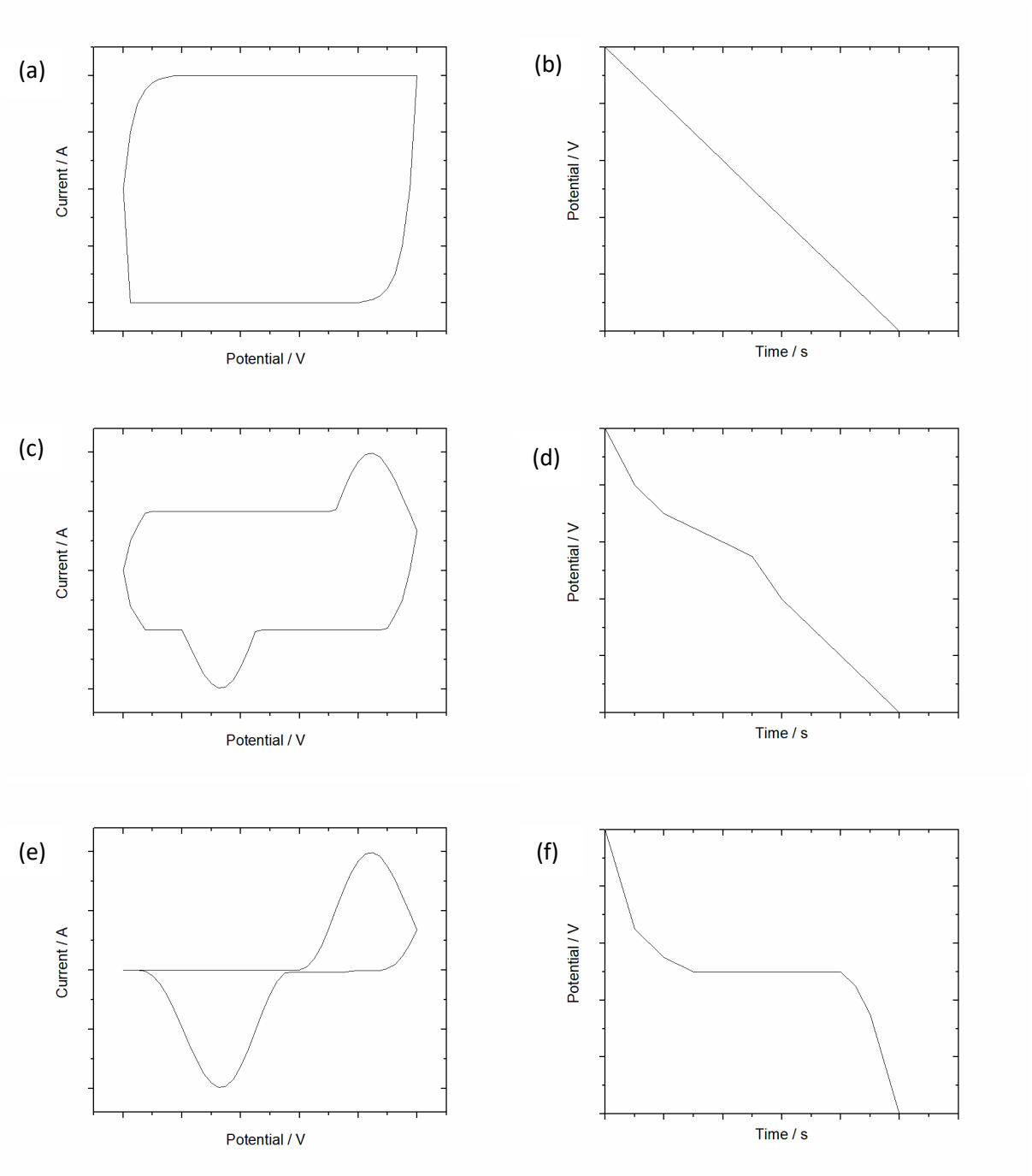


Figure 1.10 Expected electrochemical response for different types of charge storage electrode measured using CV (a/c/e) and galvanostatic discharge (b/d/f) (a/b) EDLC electrode material (c/d) pseudocapacitor electrode material (e/f) battery electrode material.

The capacitor response shows a constant current across the whole potential window giving a rectangular CV and a linear discharge response, Figure 1.10a and 1.10b. Conversely, a battery material will show sharp peaks in the CV, as well as a long charging plateau in discharging at the redox potential of the battery, Figure 1.10e and 1.10f.

Pseudocapacitor responses can be varied, depending on what mechanism of pseudocapacitance is at work, see Section 1.4.2. Since the pseudocapacitance is a combination of Faradaic redox reactions and non-Faradaic EDL capacitance, the CV will show the characteristics of both mechanisms, see Figure 1.10c. The discharge curve will not be completely linear as with an EDLC; however, it will not have a large potential plateau due to the constant current over the whole potential range, see Figure 1.10d.

Nickel hydroxide generally shows a battery like CV plot, with redox peaks corresponding to the oxidation and reduction of the material in the range of 0.3-0.5 V. An example CV and charge discharge curves are given in Figure 1.11. The discharge curve, however, is much more varied between studies, depending on particle size and morphology. Battery-like[29, 50-51] and pseudolinear[52-54] discharge curves have been reported in the literature.

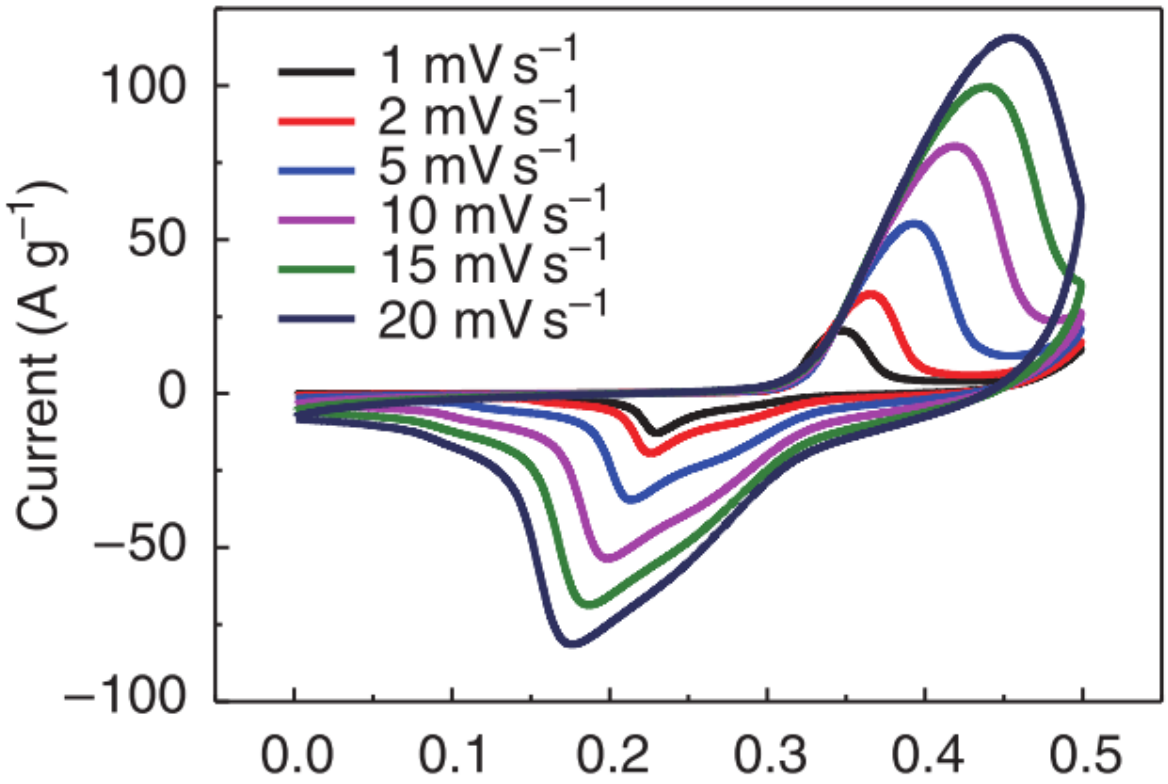


Figure 1.11 Example CV for $Ni(OH)_2$ nanospheres ~50 nm diameter at various scan rates. . Reprinted with permission (see Appendix 7) from Li, H. B.; Yu, M. H.; Wang, F. X.; Liu, P.; Liang, Y.; Xiao, J.; Wang, C. X.; Tong, Y. X.; Yang, G. W., Amorphous nickel hydroxide nanospheres with ultrahigh capacitance and energy density as electrochemical pseudocapacitor materials. Nature Communications 2013, 4, 1894. Copyright (2013) Macmillan Publishers Limited.[50]

Previous studies have shown an increase in charge stored per gram as nickel hydroxide particle size is reduced. If nickel hydroxide is an intercalation battery-type electrode material, it would be expected that the entirety of the bulk would be active, and the particle size would have no effect on the charge stored, assuming kinetics and diffusion were not a limiting factor. Conversely, if nickel hydroxide were a pure pseudocapacitive material, with surface based redox reactions the only charge storage mechanism, we would expect an increase in charge stored per gram with decreasing particle size. This is due to the expected increase in specific surface area as particle size is decreased. If this is the case, however, how is the battery like response for micron sized particles explained? The expected change in charge stored per gram with particle size is shown in Figure 1.12.

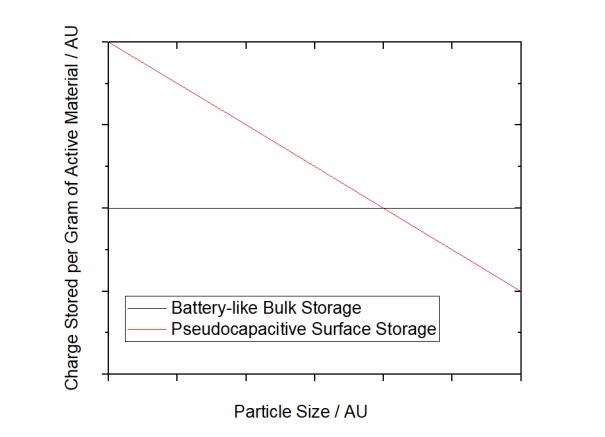


Figure 1.12 Expected changes in charge storage with particle size using battery-like and pseudocapacitive mechanisms

In this work, an attempt has been made to identify the contribution of these charging effects to the charge stored in nanostructured nickel hydroxide coated electrodes. It will be determined if the reality is either extreme end of the scale, or in fact a combination of both effects. Which effect dominates may be determined by the particle sizes and morphologies used. If both battery-like and pseudocapacitive charge storage are possible for the same material, there may be a point of crossover, where the dominant type of charging is replaced by another.

To investigate this hypothesis, the following experiments have been performed. Firstly, a series of $Ni(OH)_2$ nanoparticles of various particle sizes have been synthesised and characterised. Following this, the specific capacitance has been measured at various particle sizes and compared to the predictions shown in Figure 1.11.

Alternative methods for characterising the depth of charging without relying on *in-situ* measurements has also been investigated, using time of flight secondary ion mass spectrometry. The aim was to directly measure the depth of charging without needing to develop a synthesis procedure which would produce different sizes of nanoparticle.

Finally, the different components of the charging mechanism, which are normally electrochemically indistinguishable, have been investigated using electrochemical impedance spectroscopy. The contributions to the capacitance/capacity of the $Ni(OH)_2$ coated electrode have been separated into their Faradaic and non-Faradaic components, as well as studying the effects of porosity on the electrode response.

1.8 References

1. *Statistical Review of World Energy*; BP: 2018, 2018; p 48.
2. In *Adoption of the Paris Agreement*, 21st Conference of the Parties, Paris, United Nations: Paris, 2015.
3. Simon, P.; Gogotsi, Y., Materials for electrochemical capacitors. *Nat Mater* **2008,** *7* (11), 845-854.
4. Vangari, M.; Pryor, T.; Jiang, L., Supercapacitors: Review of Materials and Fabrication Methods. *Journal of Energy Engineering* **2013,** *139* (2), 72-79.
5. Boden, T. A.; Andres, R. J.; Marland, G. *Global, Regional, and National Fossil-Fuel CO2 Emissions*; Oak Ridge National Laboratory: Carbon Dioxide Information Analysis Center, 2017.
6. Nuclear Share of Electricity Generation in 2017. https://pris.iaea.org/PRIS/WorldStatistics/NuclearShareofElectricityGeneration.aspx (accessed 20/02/2019).
7. Digest of UK Energy Statistics 2018. Department for Business, Energy & Industrial Strategy: 2018.
8. Huggins, R. A., Supercapacitors and electrochemical pulse sources. *Solid State Ionics* **2000,** *134* (1–2), 179-195.
9. *Energy Access Outlook 2017*; International Energy Agency: 2017; pp 1-140.
10. *State of Electricity Access Report (SEAR) 2017*; The World Bank: 2017; pp 1-82.
11. Winter, M.; Brodd, R. J., What Are Batteries, Fuel Cells, and Supercapacitors? *Chemical Reviews* **2004,** *104* (10), 4245-4270.
12. Wang, G.; Zhang, L.; Zhang, J., A review of electrode materials for electrochemical supercapacitors. *Chemical Society Reviews* **2012,** *41* (2), 797-828.
13. Bard, A. J.; Faulkner, L. R., *Electrochemical Methods: Fundamentals and Applications*. Wiley: 2000.
14. Conway, B. E., *Electrochemical Supercapacitors: Scientific Fundamentals and Technological Applications*. Springer US: 1999.
15. Herrero, E.; Buller, L. J.; Abruña, H. D., Underpotential Deposition at Single Crystal Surfaces of Au, Pt, Ag and Other Materials. *Chemical Reviews* **2001,** *101* (7), 1897-1930.
16. Augustyn, V.; Simon, P.; Dunn, B., Pseudocapacitive oxide materials for high-rate electrochemical energy storage. *Energy & Environmental Science* **2014,** *7* (5), 1597-1614.
17. Gogotsi, Y.; Penner, R. M., Energy Storage in Nanomaterials – Capacitive, Pseudocapacitive, or Battery-like? *ACS Nano* **2018,** *12* (3), 2081-2083.

18. Cheng, Q.; Tang, J.; Ma, J.; Zhang, H.; Shinya, N.; Qin, L.-C., Graphene and carbon nanotube composite electrodes for supercapacitors with ultra-high energy density. *Physical Chemistry Chemical Physics* **2011,** *13* (39), 17615-17624.
19. Bharathidasan, P.; Kim, D.-W.; Devaraj, S.; Sivakkumar, S. R., Supercapacitive characteristics of carbon-based graphene composites. *Electrochimica Acta* **2016,** *204*, 146-153.
20. Salitra, G.; Soffer, A.; Eliad, L.; Cohen, Y.; Aurbach, D., Carbon Electrodes for Double-Layer Capacitors I. Relations Between Ion and Pore Dimensions. *Journal of The Electrochemical Society* **2000,** *147* (7), 2486-2493.
21. Woo, S.-W.; Dokko, K.; Kanamura, K., Composite electrode composed of bimodal porous carbon and polypyrrole for electrochemical capacitors. *Journal of Power Sources* **2008,** *185* (2), 1589-1593.
22. Kim, I.-H.; Kim, K.-B., Electrochemical Characterization of Hydrous Ruthenium Oxide Thin-Film Electrodes for Electrochemical Capacitor Applications. *Journal of The Electrochemical Society* **2006,** *153* (2), A383-A389.
23. Wang, P.; Liu, H.; Xu, Y.; Chen, Y.; Yang, J.; Tan, Q., Supported ultrafine ruthenium oxides with specific capacitance up to 1099 F g−1 for a supercapacitor. *Electrochimica Acta* **2016,** *194*, 211-218.
24. Tian, Y.; Liu, Z.; Xue, R.; Huang, L., An efficient supercapacitor of three-dimensional MnO2 film prepared by chemical bath method. *Journal of Alloys and Compounds* **2016,** *671*, 312-317.
25. Wang, L.; Yu, J.; Dong, X.; Li, X.; Xie, Y.; Chen, S.; Li, P.; Hou, H.; Song, Y., Three-Dimensional Macroporous Carbon/Fe3O4-Doped Porous Carbon Nanorods for High-Performance Supercapacitor. *ACS Sustainable Chemistry & Engineering* **2016,** *4* (3), 1531-1537.
26. Wang, R.; Yan, X., Superior asymmetric supercapacitor based on Ni-Co oxide nanosheets and carbon nanorods. *Scientific Reports* **2014,** *4*, 3712.
27. Vidotti, M.; Salvador, R. P.; de Torresi, S. I. C., Synthesis and characterization of stable Co and Cd doped nickel hydroxide nanoparticles for electrochemical applications. *Ultrasonics Sonochemistry* **2009,** *16* (1), 35-40.
28. Meyer, M.; Bee, A.; Talbot, D.; Cabuil, V.; Boyer, J. M.; Repetti, B.; Garrigos, R., Synthesis and dispersion of Ni(OH)2 platelet-like nanoparticles in water. *Journal of Colloid and Interface Science* **2004,** *277*, 309-315.
29. Lu, Z.; Chang, Z.; Zhu, W.; Sun, X., Beta-phased Ni(OH)2 nanowall film with reversible capacitance higher than theoretical Faradic capacitance. *Chemical Communications* **2011,** *47* (34), 9651-9653.
30. Ruetschi, P., Review on the lead—acid battery science and technology. *Journal of Power Sources* **1977,** *2* (1), 3-120.
31. Bernardes, A. M.; Espinosa, D. C. R.; Tenório, J. A. S., Recycling of batteries: a review of current processes and technologies. *Journal of Power Sources* **2004,** *130* (1), 291-298.
32. Xu, K., Nonaqueous Liquid Electrolytes for Lithium-Based Rechargeable Batteries. *Chemical Reviews* **2004,** *104* (10), 4303-4418.
33. Lide, D. R., *CRC Handbook of Chemistry and Physics, 89th Edition*. Taylor & Francis: 2008.
34. Whittingham, M. S., Chemistry of intercalation compounds: Metal guests in chalcogenide hosts. *Progress in Solid State Chemistry* **1978,** *12* (1), 41-99.
35. Mizushima, K.; Jones, P. C.; Wiseman, P. J.; Goodenough, J. B., LixCoO2 (0<x<-1): A new cathode material for batteries of high energy density. *Materials Research Bulletin* **1980,** *15* (6), 783-789.
36. Omar, N.; Firouz, Y.; Monem, M. A.; Samba, A.; Gualous, H.; Coosemans, T.; Van den Bossche, P.; Van Mierlo, J., Analysis of Nickel-Based Battery Technologies for Hybrid and Electric Vehicles. In *Reference Module in Chemistry, Molecular Sciences and Chemical Engineering*, Elsevier: 2014.
37. Sato, N.; Yagi, K., Thermal behavior analysis of nickel metal hydride batteries for electric vehicles. *JSAE Review* **2000,** *21* (2), 205-211.
38. Xie, H. J.; Gélinas, B.; Rochefort, D., Redox-active electrolyte supercapacitors using electroactive ionic liquids. *Electrochemistry Communications* **2016,** *66*, 42-45.

39. McEwen, R. S., Crystallographic studies on nickel hydroxide and the higher nickel oxides. *The Journal of Physical Chemistry* **1971,** *75* (12), 1782-1789.
40. Li, Z.; Han, J.; Fan, L.; Guo, R., In-situ controllable growth of α-Ni(OH)2 with different morphologies on reduced graphene oxide sheets and capacitive performance for supercapacitors. *Colloid and Polymer Science* **2016,** *294* (4), 681-689.
41. Coudun, C.; Grillon, F.; Hochepied, J.-F., Surfactant effects on pH-controlled synthesis of nickel hydroxides. *Colloids and Surfaces A: Physicochemical and Engineering Aspects* **2006,** *280* (1–3), 23-31.
42. Bode, H.; Dehmelt, K.; Witte, J., Zur kenntnis der nickelhydroxidelektrode—I.Über das nickel (II)-hydroxidhydrat. *Electrochimica Acta* **1966,** *11* (8), 1079-IN1.
43. Hall, D. S.; Lockwood, D. J.; Bock, C.; MacDougall, B. R., Nickel hydroxides and related materials: a review of their structures, synthesis and properties. *Proceedings of the Royal Society of London A: Mathematical, Physical and Engineering Sciences* **2014,** *471* (2174), 1-65.
44. Bantignies, J. L.; Deabate, S.; Righi, A.; Rols, S.; Hermet, P.; Sauvajol, J. L.; Henn, F., New Insight into the Vibrational Behavior of Nickel Hydroxide and Oxyhydroxide Using Inelastic Neutron Scattering, Far/Mid-Infrared and Raman Spectroscopies. *The Journal of Physical Chemistry C* **2008,** *112* (6), 2193-2201.
45. Rajamathi, M.; N. Subbanna, G.; Vishnu Kamath, P., On the existence of a nickel hydroxide phase which is neither alpha nor beta. *Journal of Materials Chemistry* **1997,** *7* (11), 2293-2296.
46. Van der Ven, A.; Morgan, D.; Meng, Y. S.; Ceder, G., Phase Stability of Nickel Hydroxides and Oxyhydroxides. *Journal of The Electrochemical Society* **2006,** *153* (2), A210-A215.
47. Hermet, P.; Gourrier, L.; Bantignies, J. L.; Ravot, D.; Michel, T.; Deabate, S.; Boulet, P.; Henn, F., Dielectric, magnetic, and phonon properties of nickel hydroxide. *Physical Review B* **2011,** *84* (23), 235211.
48. Corrigan, D. A.; Knight, S. L., Electrochemical and Spectroscopic Evidence on the Participation of Quadrivalent Nickel in the Nickel Hydroxide Redox Reaction. *Journal of The Electrochemical Society* **1989,** *136* (3), 613-619.
49. Delmas, C.; Tessier, C., Stacking faults in the structure of nickel hydroxide: a rationale of its high electrochemical activity. *Journal of Materials Chemistry* **1997,** *7* (8), 1439-1443.
50. Li, H. B.; Yu, M. H.; Wang, F. X.; Liu, P.; Liang, Y.; Xiao, J.; Wang, C. X.; Tong, Y. X.; Yang, G. W., Amorphous nickel hydroxide nanospheres with ultrahigh capacitance and energy density as electrochemical pseudocapacitor materials. *Nature Communications* **2013,** *4*, 1894.
51. Hu, G.; Li, C.; Gong, H., Capacitance decay of nanoporous nickel hydroxide. *Journal of Power Sources* **2010,** *195*, 6977-6981.
52. Wu, M. S.; Huang, Y. A.; Yang, C. H., Capacitive Behavior of Porous Nickel Oxide/Hydroxide Electrodes with Interconnected Nanoflakes Synthesized by Anodic Electrodeposition. *Journal of The Electrochemical Society* **2008,** *155* (11), A798-A805.
53. Inamdar, A. I.; Kim, Y.; Pawar, S. M.; Kim, J. H.; Im, H.; Kim, H., Chemically grown, porous, nickel oxide thin-film for electrochemical supercapacitors. *Journal of Power Sources* **2011,** *196* (4), 2393-2397.
54. Xing, S.; Wang, Q.; Ma, Z.; Wu, Y.; Gao, Y., Controlled synthesis of mesoporous β-Ni(OH)2 and NiO nanospheres with enhanced electrochemical performance. *Materials Research Bulletin* **2012,** *47* (9), 2120-2125.
55. Gilliam, R. J., A review of specific conductivities of potassium hydroxide solutions for various concentrations and temperatures. *International Journal of Hydrogen Energy* **2007**, 32, 359–364.
56. Barthel, J.; Iberl, L.; Rossmaier, J.; Gores, H. J.; Kaukal, B., Conductance of 1,1-electrolytes in acetonitrile solutions from −40° to 35°C. *Journal of Solution Chemistry* **1990,** *19* (4), 321-337.

Chapter 2 - Experimental Methodologies

This chapter is concerned with the methodologies employed in the material structural analysis and the determination of the electrochemical behaviour. In specific cases where deviations for the methods below were necessary, this is presented along with those cases in the relevant chapter. Specification of analysis conditions is vital in allowing the comparison of results across different experiments.

2.1 Synthesis Methodology

Since the synthesis methods used varied in each experiment, the specifics of each synthesis will be discussed in the separate chapters. Unless otherwise stated, reagents were purchased from Sigma-Aldrich (UK) and used as received without further purification.

All aqueous solutions were prepared and washed using ultra-pure water (>18.2 MΩ.cm). This was to ensure no large quantities of ions such as Ca^{2+} or Cl^{-} in the final products. Synthesis procedures were all repeated at least three times to ensure reproducibility.

2.2 Structural and Elemental Characterisation Methods

2.2.1 Scanning Electron Microscopy

Scanning electron microscopy (SEM) has been used to determine particle sizes and connectivity, as well as the morphology of the samples. The microscope used was a LEO Gemini 1525 FEG-SEM. The use of a field emission gun, rather than a tungsten filament or LaB_6, is necessary for resolving particles down to 10 nm in diameter. The machine schematic of a typical SEM is shown in Figure 2.1.

An accelerating voltage of 5 kV was used for all imaging. This voltage was chosen as a trade-off between the required resolution and the materials sensitivity to high energy electrons. As accelerating voltage is increased, the instrument resolution is also increased due to the shorter electron wavelength. The nickel hydroxide studied is easily charged and sensitive to high potentials however. At acceleration voltages above 5 kV, some damage from the beam into the material was noted after long exposure, due to burning off of the surfactant where used. In addition, charge build up on the sample made imaging very difficult at high accelerating potentials. To prevent this, the moderate energy of 5 kV was chosen.

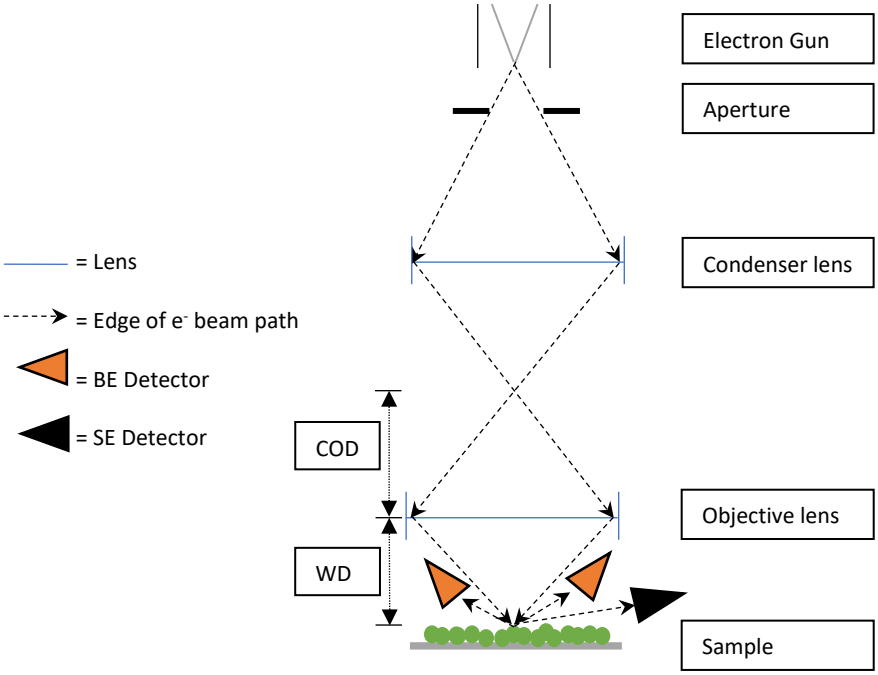


Figure 2.1 Simplified schematic of scanning electron microscope, not to scale. Some features have been omitted/not duplicated for simplicity

The chosen microscope was able to operate in both secondary electron (SE) and backscatter electron (BE) modes. Both modes were employed for this work as they offer distinct advantages. In SE mode electrons emitted from the sample due to excitation by the beam electrons are detected. Only electrons with sufficient energy to escape the sample surface can be detected. Since the technique is relatively surface sensitive and offers greater spatial resolution, it is used at high magnifications in this project to resolve small particles. The escape depth in BE mode is much deeper, giving a much larger depth range over which particles can be clearly resolved. In the cases of porous particulate structures, this is very advantageous. In addition, the intensity of back scattered electrons is proportional to atomic number. This means the particles comprised of heavy nickel will be easily distinguished from the aluminium stub, as well as any surface carbon or remaining solvent, in this mode.

To ensure continuity between experiments, the same magnifications were used for each sample in this work. An initial image at 1000 x magnification allowed the uniformity of the whole sample to be studied, then various micrographs at 10, 20, 50, 100 and 200 (where possible) k x magnification were taken.

The working distance of the samples was kept at 10 mm or below, to ensure a small beam size. Both electromagnetic lenses work to demagnify the electron beam. The diameter of the final image spot size, D_f, is given by Equation (2.1);

$$D_f = D_i \times (COD/WD) \quad (2.1)$$

where D_i is the demagnified source image diameter at the beam crossover below the condenser lens, *WD* is the working distance, and *COD* is the crossover distance between the demagnified source image and the condenser lens. D_i is determined by the emission source and the apertures passed through before the condenser lens. The strength of the condenser lens will determine the beam crossover point, so a stronger condenser lens will give a greater *COD*.

Since the distance between the condenser and the objective lens is fixed and the strength of the condenser lens is fixed, the only way to alter spot size as the end user is to alter the *WD*. According to Equation (2.1), as the *WD* is decreased, so is the final spot size.[1]

All samples were mounted on a conductive aluminium stub. This is necessary due to the mechanism by which samples are loaded into the machine. The consequences of this are the mounting method plays a role in determining the connectivity of the particles after drying. In this work, the samples were prepared by simple drop-casting directly onto the stub. The adhesion was found to be robust under high air flow, meaning no carbon tape was needed to secure the particles. This also had the added benefit of not adding an extra resistive element into the already resistive sample.

Since the samples were capacitive, charging was an issue during measurements. In some circumstances, it is common to add a conductive metallic layer such as chromium or gold to the sample. This prevents the build-up of charge from the electron gun. Since particle sizing was one of the major goals of using the SEM however, it was deemed inappropriate to use metallic coating. Typical metallic coats are 10-20 nm in thickness. Since the particles studied we of diameters down to 3 nm, a coating of this thickness would have vastly altered the particle size or masked the smaller particles in the sample.

To size the particles in the micrographs, a minimum of 3 micrographs were taken at each magnification. The final choice for which magnification to use in analysis was done based on

which ever magnification showed the clearest particles. Initial methods for digitally sizing the particles automatically were quickly abandoned. Edge-finding based image analysis gave an overestimate of average particle size due to larger and clearer particles being favoured.

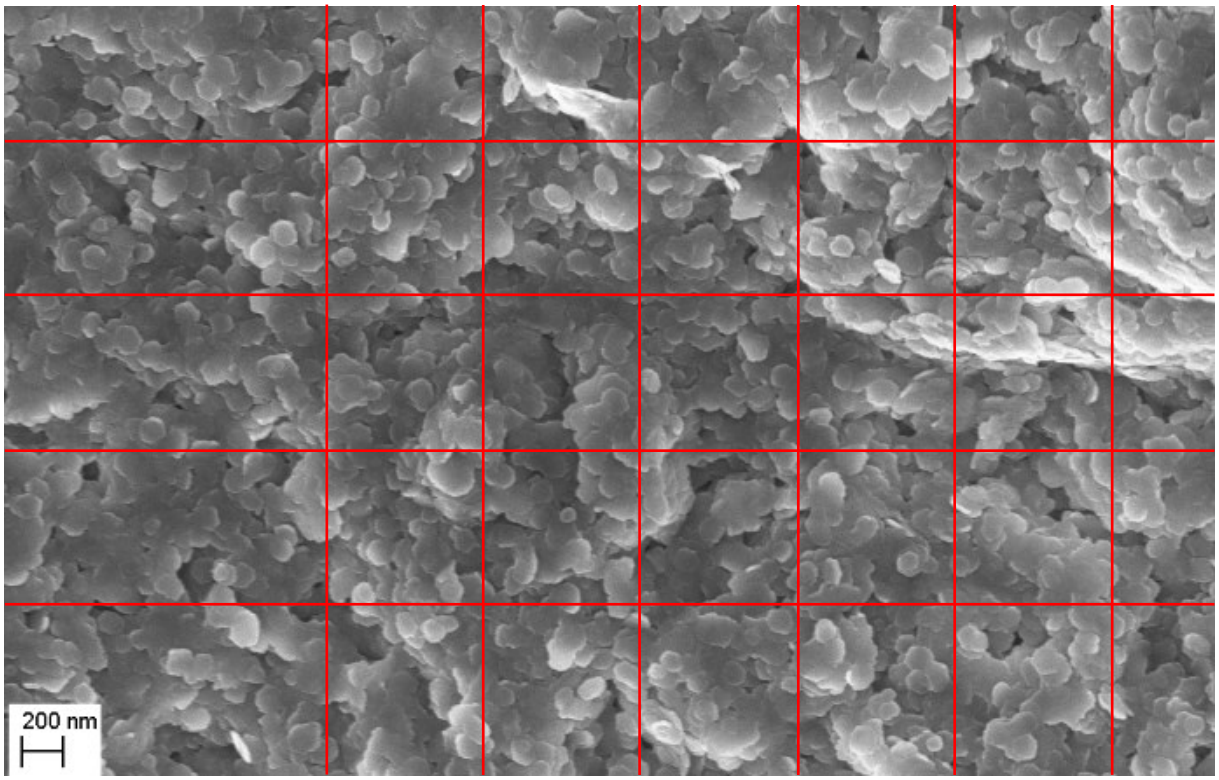


Figure 2.2 Scanning electron micrograph of uncoated $Ni(OH)_2$ nanoparticles with analysis grid overlay.

Instead, particles were sampled randomly using a grid overlay, as shown in Figure 2.2. At all intersections, any particle directly under the point of crossing was measured, giving 24 size measurements per micrograph. Increasing size and contrast allowed for even faint particles to be measured. If the crossover point was not usable, either there was no particle in that point or it crossed over multiple particles, the data point was discarded. The particle sizes were then measured and tabulated using ImageJ software. The arithmetic mean of these sizes was calculated and the standard error of the measurements was taken as the error in particle size. An example of this process is shown in Figure 2.2, Table 2.1 and the calculations below.

Table 2.1 Particle diameters of $Ni(OH)_2$ nanoparticles shown in Figure 2.2 measured using ImageJ software. N/M indicates particle at the intersection was not measurable.

Particle Diameters / nm					
150	134	115	59.2	N/M	133.2
108	116	107	97	141	138
133	92	153	108	146	102
N/M	87	117	113	153	116

The arithmetic mean ($\bar{x}$) was found to be 119 nm. The standard deviation in particle sizes (σ) was found to be 24 nm, which gave a standard error of 5 nm. Therefore, the final size of these particles was determined to be 119 ± 5 nm. This procedure was repeated for a further two micrographs to ensure the standard error converged before calculating a final average particle size.

2.2.2 Transmission Electron Microscopy

For particles below 20 nm in diameter, using SEM to determine particle diameter proved to be ineffective. This is due to approaching the resolution limit of the SEM. At this length scale, any blur related to bad focussing or the astigmatism in the microscope will be a large percentage of the size of the nanoparticles. Higher resolution size measurement by transmission electron microscopy (TEM) was performed in bright field mode with a JEOL 2100Plus with samples drop cast onto a carbon mesh.

The dry samples were dispersed in ethanol prior to drop casting. This was to allow fast drying of the solvent between deposition and analysis. Initial measurements were abandoned due to the mass loading on the carbon mesh being too high, making individual particles impossible to resolve. After several attempts, a dilution of 0.1 g dm^{-3} was found to deliver enough material without covering the carbon mesh completely.

Analysis was performed at an accelerating voltage of 200 kV. This higher voltage was possible since particles were only deposited at a monolayer thickness, preventing charge build up. Higher accelerating voltage would offer higher resolution, however the poor stability of the particles at higher voltages limited the analysis to 200 kV.

Particle diameter was measured using the same methodology as for scanning electron micrographs. Since the magnification was much higher, there were several cases where a single particle crossed multiple points. In these cases, the particle was only measured once.

2.2.3 Energy dispersive X-ray spectroscopy

Energy dispersive X-ray spectroscopy (EDX) was used to estimate the elemental ratio of Ni:O after syntheses. The analysis was also performed using a LEO Gemini 1525 FEG-SEM, with an accelerating voltage of 10 kV. This increased voltage relative to the imaging voltage was necessary to observe Ni peaks at around 7.5 keV. Analysis of the data was performed using

Inca software. As in the case of SEM analysis, all samples were mounted on a conductive aluminium stub and no metallic coating was used during analysis.

To ensure the EDX results taken were representative of the sample, five measurements were taken. If the sample was of a uniform morphology, these five points were evenly spaced over the micrograph, see Figure 2.3. If there was more than one distinct morphology observed, each different morphology was sampled three times.

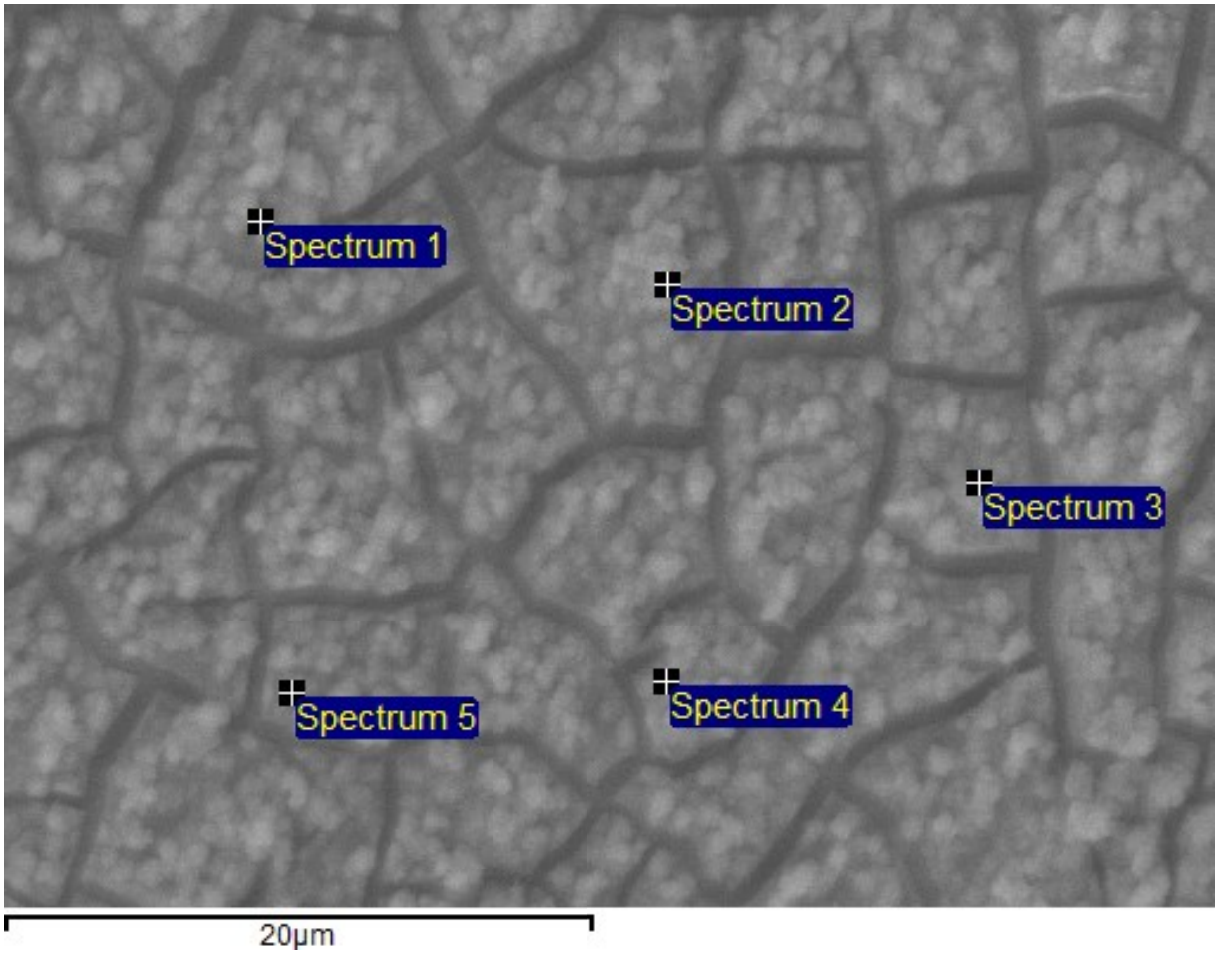


Figure 2.3 EDX analysis method applied to each sample of $Ni(OH)_2$ nanoparticles.

The spectra were taken, and quant-analysis performed to measure the atomic ratio of Ni to other common elements observed. The Ni:O ratio was of particular interest, as it could be used as an indication of the extent of oxidation of the Ni in the sample, assuming a constant contribution from the stub or residual solvent.

2.2.4 X-Ray Photoelectron Spectroscopy

X-ray photoelectron spectroscopy (XPS) was performed on a Thermo Scientific K-Alpha. Al-Kα X-rays were used as the source (hv = 1486.86 eV). The XPS analysis was not performed unless

an analysis chamber vacuum of < $5x10^{-8}$ mbar was achieved. For some samples, this was not possible even after 48 hours pre-analysis degassing in a vacuum oven and over two hours in the load lock at a pressure of < $5x10^{-7}$ mbar. Analysis of the resulting data was performed using Thermo Scientific Avantage software.

All binding energies (BEs) for the samples were referenced by setting the C(1s) peak to 285 eV. The BEs were measured with a precision of ± 0.3 eV, as stated by the manufacturer. Survey spectra were obtained using a 0.5 eV step size at a pass energy of 200 eV, and a dwell time of 25 ms. The high-resolution core level Ni(2p) and O(1s) spectra were obtained at a pass energy of 20 eV, and a dwell time of 50 ms. The step size for all core level spectra was 0.1 eV.

In the case of hydrothermally synthesised $Ni(OH)_2$ nanoparticles, the samples were drop cast onto Ni foil for analysis. This was to reduce the chance of exposing users of the facility to carcinogenic nickel hydroxide. Air was blown over the samples before transfer to the facility to ensure there was no loose particles on the surface. Samples were then dried in a vacuum oven at 80^{o}C for 24 hours prior to analysis. Due to the conductive nature of the substrate, no further conducting pathway was needed to prevent charging.

$Ni(OH)_2$ samples, synthesised using electrodeposition methods described in Chapter 4, were analysed on the Au/Cr sputter coated (001) Si wafer onto which they were deposited. An electronic connection between the metallic coating on the substrate and the mounting plate was made using silver conductive paint (RS, UK) before drying in a vacuum oven at 80^{o}C for 24 hours.

2.2.5 X-Ray Diffraction

X-ray diffraction (XRD) was performed with a Bruker D2 PHASER desktop diffractometer using Cu-Kα radiation. Analysis of the data was performed using X'Pert Highscore Plus and X'Pert Data viewer software. Diffraction patterns were matched to those obtained from the X'Pert data base for α- and β-$Ni(OH)_2$ phases, supplied by the IUCr. As in Section 2.2.4, nanoparticles were dispersed in water then drop cast onto a single crystal [100] Si wafer for analysis. Air was blown over the samples before transfer to the facility to ensure there was no loose particles on the surface.

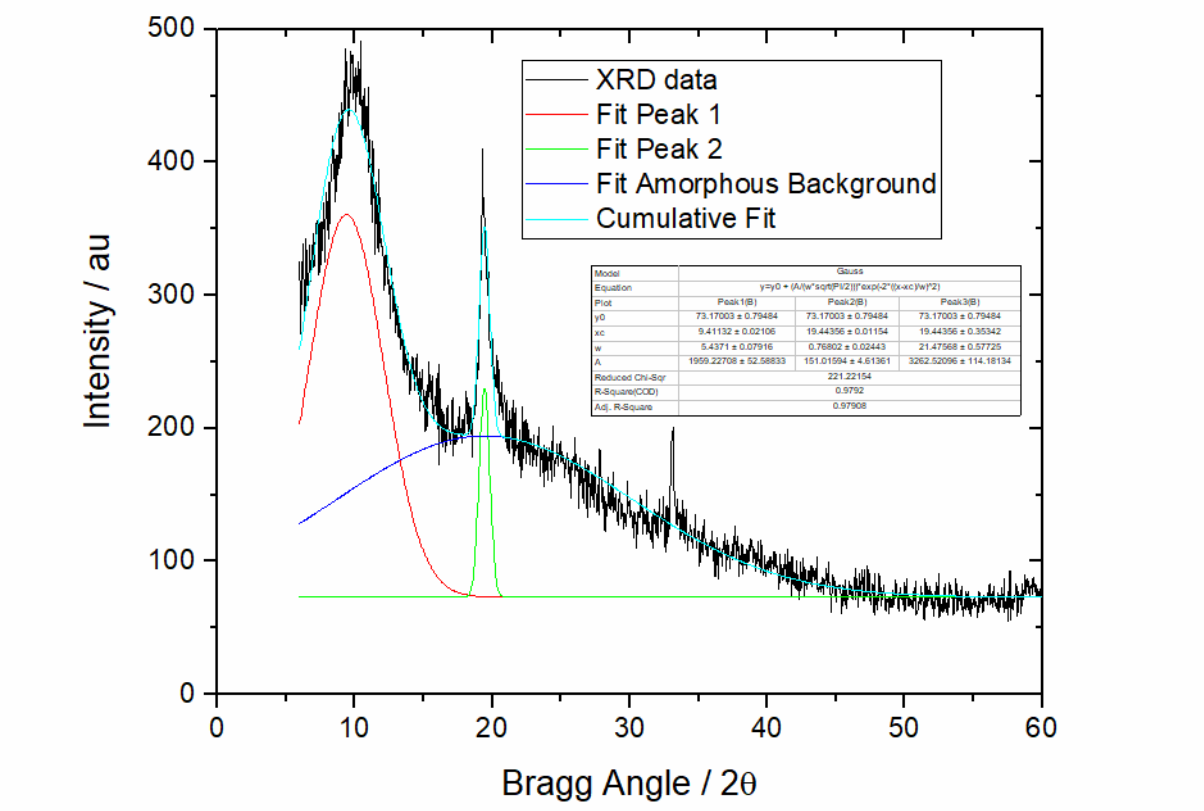
The diffraction pattern was collected at a scan rate of 0.1 degrees per second in 2θ ranging from 6° to 60°. This scan range was chosen to prevent damage to the detector. The lower limit of the scan range, 6°, is to ensure there is no chance of incident radiation hitting the detector. The upper limit is due to a reflective shoulder of intensity caused by the [100] Si wafer.

A scan rate of 0.1 degrees per second was chosen to give a data collection time of approximately 10 minutes. Shorter scans were found to give small signal to noise ratios, meaning less intense peaks were lost in the back ground. Longer scans did improve scan quality with respect to signal to noise. No further peaks were revealed, however, so it was decided that the ability to collect data for multiple samples in one session was more important than this small improvement in data quality.

Particle sizing can also be achieved using XRD and the Scherrer Equation (2.2);[2]

$$\tau = (K\lambda)/(\beta\cos\theta) \qquad (2.2)$$

where τ is the mean size of the crystalline domains in m, *K* is the dimensionless shape factor, λ is the X-ray wavelength in m (Cu-Kα = 1.54 Å), β is the peak broadening at the full width half maximum (FWHM) in radians, and θ is the Bragg angle in degrees.



Model	Gauss		
Equation	y=y0 + (A/(w*sqrt(PI/2)))*exp(-2*((x-xc)/w)^2)		
Plot	Peak1(B)	Peak2(B)	Peak3(B)
y0	73.17003 ± 0.79484	73.17003 ± 0.79484	73.17003 ± 0.79484
xc	9.41132 ± 0.02106	19.44356 ± 0.01154	19.44356 ± 0.35342
w	5.4371 ± 0.07916	0.76802 ± 0.02443	21.47568 ± 0.57725
A	1959.22708 ± 52.58833	151.01594 ± 4.61361	3262.52096 ± 114.18134
Reduced Chi-Sqr	221.22154		
R-Square(COD)	0.9792		
Adj. R-Square	0.97908		

Figure 2.4 Peak fitting of XRD data using Origin Software

Finding the FWHM of each peak meant fitting the data using Origin software. An example of this peak fitting is shown in Figure 2.4. Machine broadening was measured using a standard sample and found to be negligible due to the large FWHM exhibited by the peaks for particles < 200 nm in diameter.

The shape factor or Scherrer constant was set at 0.9, as this has become a standard in literature if the correct shape factor is unknown.[2-3] Shape factors have been reported in literature as having values ranging from around 0.6 to 2.0, which will obviously have a huge impact on the reported size of the crystallite.[3] An accepted literature shape factor was not found for this work, so the standard 0.9 was assumed. This may then explain any discrepancies between crystallite sizing between XRD and other analysis techniques. For larger particle sizes, there may have been multiple crystal domains per particle. This was not observed however for the small particles during TEM.

Assuming a crystal size is equivocal to particle size, the averages were calculated using three diffractograms taken from the same sample. The crystallite size was estimated by applying the Scherrer Equation to the three most intense peaks seen in the pattern, not including the peak relating to the substrate at around $2\theta = 33^{o}$. The error in the particle diameter was given as the standard error of these measurements. If there were less than three clear peaks in the spectrum, as seen in Figure 2.4, then fewer than three peaks were used. This approach assumes that crystallite dimensions will not vary based on the Miller indices of the peak and that the particles are randomly oriented in the sample. A full texture analysis would be required to confirm this.

2.2.6 Small Angle X-ray Scattering

Small angle X-ray scattering (SAXS) was performed using a ScatterX 78 attachment in low vacuum conditions on a PANalytical Empyrean diffractometer. The samples were analysed as colloidal dispersions in water at room temperature. Samples were prepared at a loading of 2-3 g dm^{-3}. Due to the necessity for a stable dispersion, only samples suspected of having diameters < 50 nm were studied.

Particle size was estimated using the PANalytical EasySAXS software, which converts the background corrected scattering curve, intensity vs the scattering vector, into the size distribution by volume. As well as the average particle diameter, the software also estimates

the upper and lower quartile range, which was then used to estimate the error in the sample sizes as a ±(Interquartile Range/2).

2.2.7 Dynamic Light Scattering

Dynamic Light Scattering (DLS) measurements were performed on a Malvern Zetasizer Nano series instrument and Zetasizer software. Concentrations for solutions were determined empirically by diluting until the software did not recommend a more dilute solution to avoid multiple scattering events. This concentration varied significantly depending on the stability of the particles in solutions. For particle size and zeta potential measurements, copper contacted folded capillary zeta cell DTS1070 cuvettes were used. Each measurement comprising of 10-20 runs was repeated three times. The number of runs was determined by the stability of the measurement, until the reading became stable.

The decay of the correlation function with time was observed at the start of each experiment. An unstable correlation function, particularly at short time scales, was a good indication of an unstable colloidal suspension. This could usually be corrected by dilution and then re-running the sample if the particle diameter was < 100 nm.

The machine was operated in back scattered mode for small particles, detecting at an angle of 175^{o} to the incident laser direction. Back scattered mode is chosen as the primary method of detection, since the laser has less volume through which to travel, decreasing the likelihood of multiple scattering events. If a measurement in back scattered mode was unsuccessful due to low signal, then it was repeated in forward scattered mode, detecting at an angle of 15^{o} to the incident laser direction.

Low signal was also caused by diluting the starting solution too much, at which point more solid needed to be added. Due to the nature of the software, particle sizes were calculated as the hydrodynamic radius of the particles. This is due to the calculation assuming spherical particles. The radius calculated is therefore that of a sphere with the same diffusion coefficient as the nanoparticles and the associated solvent system. This makes the technique insensitive to dimensions which have little to no effect on particle diffusion, such as nanoplate thickness. Additional complications due to particle flocculation and the weighting of the measurement towards larger particle sizes, giving an overestimate of average particle size.

2.2.8 Nitrogen Adsorption/Desorption

Nitrogen adsorption-desorption measurements were performed with a Quantachrome autosorb IQ at 77 K. The powder product was dried under vacuum at 100^{o}C for 24 hours prior to analysis. The dry mass of the nanoparticles was measured before degassing, and then again after the measurement, to ensure an accurate specific surface area. A minimum of 50 m^2 of material was used in analysis, as recommended by the manufacturer. Measurements of all substrates used, Ni foil and Si wafer, showed negligible specific surface area.

To ensure a representative and reproducible surface area and pore volume, multiple methods were trialled to analyse the data. The classical Brunauer-Emmett-Teller (BET) model was used to calculated specific surface area. The Barrett-Joyner-Halenda (BJH) method was used to calculate pore volume distribution in the sample. These classical methods were compared to results calculated using a density functional theory (DFT) model of cylindrical pores on silica.

It has been reported that the BET surface area analysis does not apply to micro/mesoporous materials such as the materials in this work.[4-5] The reproducibility of the measured specific surface area was poor for multiple samples from the same synthesis. The DFT method gave more reproducible results and generally lower specific surface areas compared to the BET method. The pore sizes calculated using the DFT method agreed well with those calculated using the BJH method, within the machine calculated error in the measurement.

2.2.9 Atomic Force Microscopy

Tapping mode atomic force microscopy (AFM) was performed using an Asylum MFP-3D classic at room temperature and pressure. No further preparation of the electrodeposited samples was performed aside from drying after deposition for 24 hours at 60^{o}C in a vacuum oven.

Intermittent contact mode was used to prevent damage to the sample surface. A PPP-NHCR tip (Nanosensors, Germany) was used at a tapping frequency of 0.5 Hz and a tapping amplitude of 1.5 V, as determined by the resonant frequency and stiffness of the cantilever.

Electrodeposited samples were studied using AFM before and after wax coating/polishing. The samples were initially very rough and gave very noisy profiles. These were improved considerably by the addition of wax coating and then polishing. Analysis of sputter crater depths was performed using Gwyddion software on 256 x 256 pixel AFM contour map. Step

heights were calculated using three 10 pixel line-averages approximately 20 µm apart, shown in Figure 4.28.

2.2.10 Light Microscopy

Bright field light microscopy was performed using an Olympus BX51 microscope, equipped with an Olympus UC30 digital camera. In Chapter 4, samples were imaged after wax deposition, and then again during grinding every 20 seconds until the desired finish was achieved. Images were taken at a magnification of 100 x to attempt to observe clusters of particles becoming visible through the wax layer.

The exposed surface area was calculated using ImageJ software in a similar method to particle diameter measured used in SEM, as discussed in Section 2.2.1.

2.3 Time of Flight Secondary Ion Mass Spectrometry

Time of flight secondary ion mass spectrometry (ToF-SIMS) was performed using an IONTOF ToF-SIMS V. Analysis was performed using IONTOF SurfaceLab 6 software. All data was taken and then re-run to ensure that any change to the position of peaks during analysis would not be reflected in the intensity of the signal.

Bi^+ was used as the primary analysis ion with a beam current of 1 pA. The beam was run in high-current bunched mode, with each pulse lasting 100 µs. Beam current was checked prior to each measurement using a Faraday cup. The sputter beam used was 1 keV Cs^+. A sputter current of 75 ± 3 nA was used to ensure consistency between experiments.

Due to the capacitive nature of the samples, charge build up was a problem throughout ToF-SIMS analysis. A charge compensating flood gun was used during all depth profiles. It was also necessary to run the depth profile as a non-interlaced analysis, giving the sample time to discharge between sputtering. A sputter time and pause time of 1 second was used. This had the disadvantage of causing very long analysis times.

An area of 100 μm^2 was analysed, in a sputter crater of 300 μm^2. Data were taken over a mass range from m/z = 0 to 200 for negative secondary ions. Calibration was performed using C^-, CH^-, CH_2^- CH_3^- O^-, OH^-, F^-, and $35Cl^-$. The differences between the expected and observed masses after calibration were less than 50 ppm.

2.4 Electrochemical Characterisation

2.4.1 Electrochemical Cell Set-Up

For electrochemical syntheses and analyses, all measurements were carried out using a three-electrode PTFE electrochemical cell, with combined working and working sense electrodes. A schematic of the cell can be seen in Figure 2.5. Experiments were performed using a Metrohm Autolab PGSTAT 12 at room temperature, using a Pt mesh flag counter electrode and a Radiometer Analytical Hg/HgO reference electrode (+0.098 V vs SHE).[6] Unless stated otherwise, all analysis was performed in 1.0 mol dm^{-3} potassium hydroxide electrolyte using General Purpose Electrochemical System (GPES) or Nova 2.1 software.

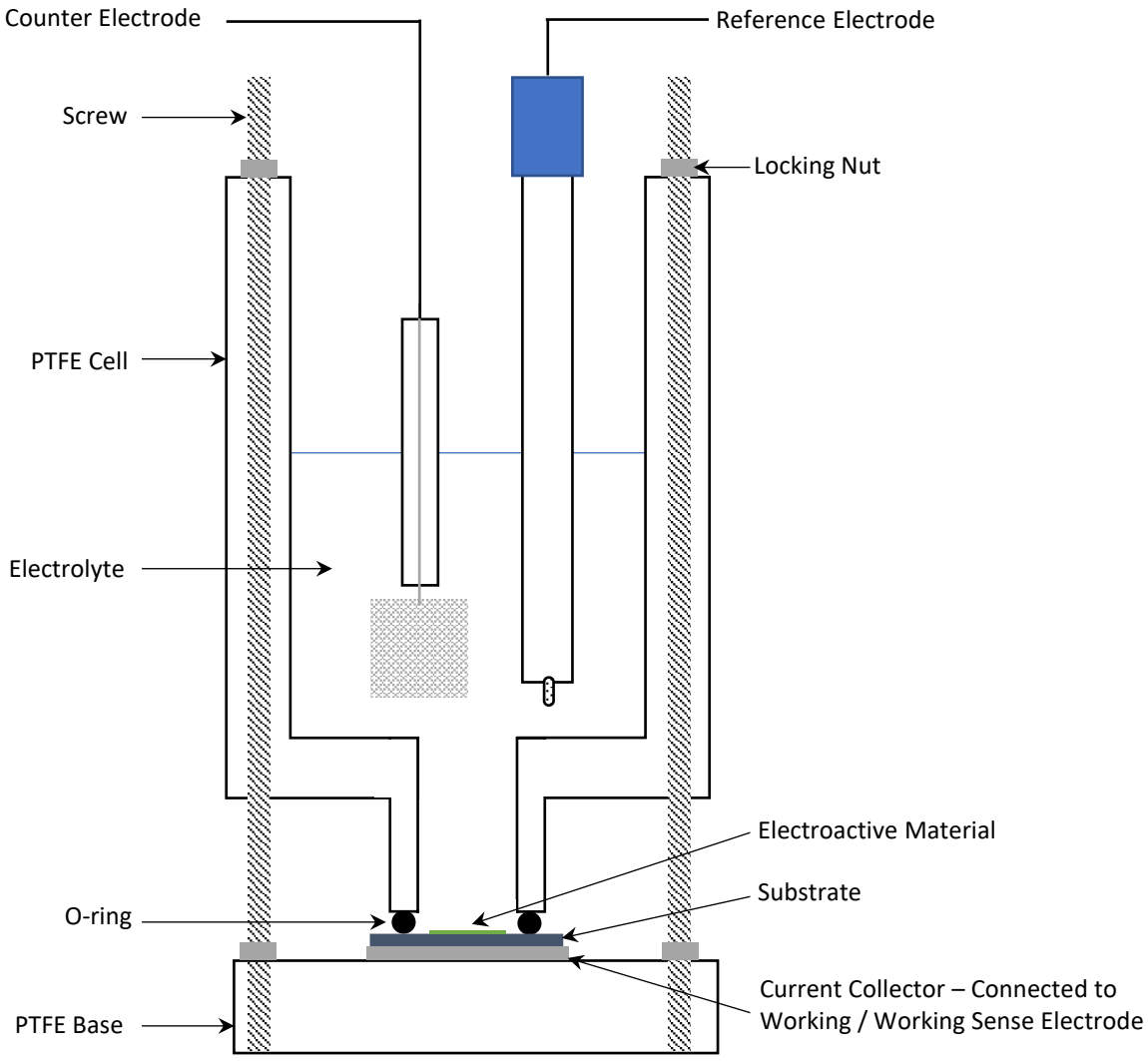


Figure 2.5 Schematic of electrochemical cell set up for analysis (not to scale).

2.4.2 Cyclic Voltammetry

Cyclic voltammetry (CV) was used to characterise the hydrothermal and electrodeposited products in chapters 3, 4, and 5, as well as to provide measurements for the specific capacity and specific capacitance of the samples. The methodology of calculating these charge storage metrics is discussed in Section 2.4.5.

As the potentiostat is a digital instrument with no true linear sweep capabilities, a small step sweep was used, with a step size of 0.0024 V. The protocol was set to give a data point at every step.

The potential region studied was from 0.0 V to 0.7 V. This potential window was determined based on the expected redox behaviour of the nickel hydroxide, oxidising on charging to the oxyhydroxide form at around 0.3-0.5 V, then reducing at 0.4-0.2 V on the reverse sweep.[7-9] The stability window of the electrolyte, 1.0 mol dm^{-3} KOH, was also a factor in determining the potential window. Nickel hydroxide has shown promise as an oxygen evolution catalyst in alkaline media, reducing the overpotential required for water splitting.[10] Therefore, the potential window was limited to a maximum potential of 0.7 V to ensure that degradation of the solvent did not occur.

The scan rates used were selected based on the values reported in literature. Studies of electrochemical capacitor type electrodes typically use very fast scan rates of between 10 – 100 mV s^{-1}.[7, 11] This is due to the rapid charging behaviour of the materials. In studies of battery-type electrodes however, scan rates are typically much lower, around 1 – 10 mV s^{-1}.[11-13]

In studies for the comparison of potential battery materials for commercial application, standard analysis scan rates are typically 0.1 mV s^{-1}.[12] Low scan rates of < 1 mV s^{-1} were not used in this work, since the aim was not to create a commercially viable battery/supercapacitor electrode. For most samples, intermediate scan rates of 10 and 50 mV s^{-1} were used. In cases where the variation in electrochemical behaviour with scan rate was being studied, this scan rate range was extended to 1 – 100 mV s^{-1}.

The number of scans used was varied depending on the aim of the experiment and behaviour of the material. In the case of electrochemical characterisation, it was found that except for

the first scan in the series, every other scan after shared the same electrochemical behaviour, so a minimum of ten scans were studied. This is due to the removal of surface adsorbed species on the first scan.

In measuring the specific capacitance or specific capacity, it was found that electrochemical aging played a large role in the performance of the material, see Section 3.4.3 and Figure 2.6a. All samples showed an initial increase in specific capacitance/capacity. The number of cycles was determined by how long the charge stored took to stabilise, typically around 50 – 80 cycles.

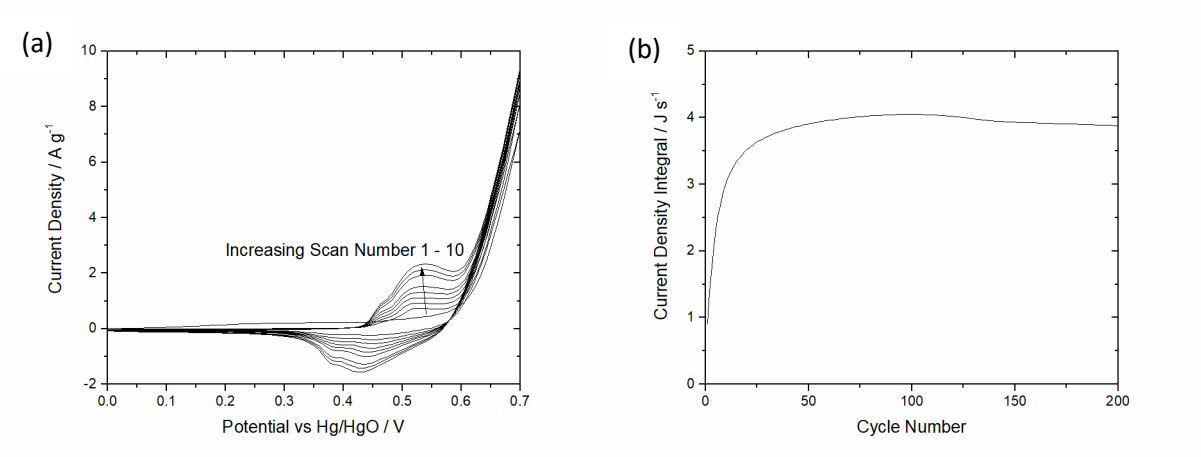


Figure 2.6 Electrochemical cycling of $Ni(OH)_2$ coated Ni foil electrode at 50 mV s^{-1} (a) Increase in electrochemical activity over first 10 cycles (b) Stability of electrode over 200 cycles.

In studying the electrochemical stability, 200 cycles were used. This is significantly less than the industry standard; however, since creating a commercially viable device was not the aim, this was deemed appropriate to demonstrate that no further phase changes would occur, see Figure 2.6b.

2.4.3 Galvanostatic Charge/Discharge

The charging and discharging behaviour of the $Ni(OH)_2$ nanoparticle coated electrodes was studied at a constant current magnitude. Galvanostatic charge/discharge (GCD) was performed at various current densities to simulate a range of applications.

As in the case for the CV studies, the variations in the study of supercapacitors and batteries were considered when planning the experimental conditions. Battery charging is typically measured using variations of the C rate, with 1 C being equivalent to complete charging in

one hour.[11, 13-14] Since supercapacitors charge quickly, most studies use current density in A g^{-1} or A cm^{-2} as the metric of study.[7, 15]

Since the charging rate of the $Ni(OH)_2$ coated electrodes was more comparable to a supercapacitor type time scale, minutes rather than hours, it was decided current density was a more appropriate metric. Studies typically use current densities varying from 0.1 – 10 A g^{-1}.[16] High current densities of 20 -70 A g^{-1} are used in applications studying the high rate performance of supercapacitors, however that was beyond the scope of this work.[8]

To compare the results to the CV data, the charge discharge was run between 0.0 and 0.7 V limits, however some samples did not charge to this potential limit. This is possibly due to water splitting in the electrolyte. As already discussed in Section 2.4.2, the aim of this work was not to establish the commercial viability of the material over thousands of charging cycles, and so long-term cycling is not included in the report.

In several papers studied, GCD is used to quantify the specific capacity/capacitance of electrochemical charge storage devices. In many cases, particularly for supercapacitors, the specific capacitance (Cap_s) is calculated using Equation (2.3);[17]

$$Cap_s = (I\Delta t)/(m\Delta V) \quad (2.3)$$

where I is the applied current, m is the mass of the active material, Δt is the duration of the charge/discharge, and ΔV is the change in potential. This Equation assumes a linear charge/discharge characteristic, the same as would be seen in a metallic capacitor. In devices using electrochemical redox as a mechanism of charge storage, such as pseudocapacitors and batteries, this linear behaviour may not hold over the whole potential range.[13] This means specific capacitances calculated this way tend to be over exaggerated compared to other methods. Due to this, the GCD was not used to quantify specific capacitance/capacity in this work, but rather to compare results qualitatively.

2.4.4 Electrochemical Impedance Spectroscopy

As discussed in Section 1.4, there are multiple mechanisms of charge storage at work in electrochemical devices. CV and GCD, while useful analyses, are not able to deconvolute the effects of these various mechanisms. To achieve this, electrochemical impedance spectroscopy (EIS) was used to study the electrodeposited $Ni(OH)_2$ on Ni foil. Unlike CV and

GCD, EIS was performed on a Solatron-Schlumberger SI1286 Electrochemical Interface, equipped with a Solartron SI1250 Frequency Response Analyser. Data was generated and analysed using Scribner ZPlot/ZView respectively.

The frequency range studied was 0.1 – 6.5x10^4 Hz. The upper limit was chosen as the largest achievable using the Solartron. The lower limit was chosen as this was found to be the most common low frequency limit in the literature.[18] In some cases, particularly samples with high resistivity, this range was reduced at the low frequency end due to the measurement being unstable.

Potentiostatic impedance spectra were recorded in the range 0.0 V to 0.7 V at 0.1 V intervals with a perturbation potential of 10 mV in order to observe the redox behaviour of the $Ni(OH)_2$. Measurements were taken every 0.1 V in this range, in the order of charging (0.0 V → 0.7 V) and then discharging (0.7 V → 0.0 V). This was to simulate the changes the material underwent during CV cycling. The AC perturbation potential chosen was 10 mV, see Section 5.5.

2.4.5 Calculating Charge Storage Metrics

Since the nature of the charge storage was unknown at the beginning of this work, both specific capacitance and specific capacity were studied as charge storage metrics. For reasons discussed in Section 2.4.3, the integral of the cyclic voltammogram was used as the sole method of calculation of charge stored.

The specific capacitance, Cap_s in F g^{-1}, of the system can be calculated using Equation (2.4);[8]

$$Cap_s = (1 / (2m(V_f-V_i)v)) \int_{Vi}^{Vf} I(dV) \quad (2.4)$$

where m is the mass of the active material, I is the current, V_f is the higher vertex potential, V_i is the lower vertex potential, and v is the scan rate. The factor of two is present to give an average specific capacitance from the charge and discharge capacitances.

The specific capacity, C_s in mA h g^{-1}, of the system can be calculated using Equation (2.5);[12]

$$C_s = (1 / (3.6m)) \int_{ti}^{tf} I(dt) \quad (2.5)$$

where m is the mass of the active material, I is the current, t_f is the time at which the current minimises following the redox peak, and t_i is the time at which the scan begins.

Initially, capacity was calculated over the whole scan range, as in the case for the capacitance. This eventually proved, however, to give unrealistically large values of specific capacity. For samples which show poor charge storage, such as Figure 2.6a, there is a large contribution to the integral area by the characteristic IV curve after the redox peak. By limiting the scan to just the range in which redox is occurring, this gives a more realistic measure of the specific capacity. The region of the charge curve between the oxidation peak and the limit of the scan data at 0.7 V was modelled using Origin software. The Equation of this line was differentiated and set equal to zero to find the minimum in the curve. This value was taken as the upper limit of the current vs time integral for analysis.

2.5 References

1. Hafner, B., *Scanning Electron Microscopy Primer*. 1 ed.; University of Minnesota: University of Minnesota, 2015; Vol. 1, p 29.
2. Hargreaves , J. S. J., Powder X-ray diffraction and heterogeneous catalysis *Crystallography Reviews* **2005,** *11* (1), 21-34.
3. Monshi, A.; Foroughi, M. R.; Monshi, M. R., Modified Scherrer Equation to Estimate More Accurately Nano-Crystallite Size Using XRD. *World Journal of Nano Science and Engineering* **2012,** *Vol.02No.03*, 7.
4. Tian, Y.; Wu, J., A comprehensive analysis of the BET area for nanoporous materials. *AIChE Journal* **2018,** *64* (1), 286-293.
5. Sing, K., The use of nitrogen adsorption for the characterisation of porous materials. *Colloids and Surfaces A: Physicochemical and Engineering Aspects* **2001,** *187-188*, 3-9.
6. J. Smith, T.; J. Stevenson, K., Reference Electrodes. In *Handbook of Electrochemistry*, G. Zoski, C., Ed. Elsevier: 2007; Vol. 1, pp 73-110.
7. Kiani, M. A.; Mousavi, M. F.; Ghasemi, S., Size effect investigation on battery performance: Comparison between micro- and nano-particles of β-Ni(OH)2 as nickel battery cathode material. *Journal of Power Sources* **2010,** *195* (17), 5794-5800.
8. Li, H. B.; Yu, M. H.; Wang, F. X.; Liu, P.; Liang, Y.; Xiao, J.; Wang, C. X.; Tong, Y. X.; Yang, G. W., Amorphous nickel hydroxide nanospheres with ultrahigh capacitance and energy density as electrochemical pseudocapacitor materials. *Nature Communications* **2013,** *4*, 1894.
9. Oliva, P.; Leonardi, J.; Laurent, J. F.; Delmas, C.; Braconnier, J. J.; Figlarz, M.; Fievet, F.; Guibert, A. d., Review of the structure and the electrochemistry of nickel hydroxides and oxy-hydroxides. *Journal of Power Sources* **1982,** *8* (2), 229-255.
10. Gao, M.; Sheng, W.; Zhuang, Z.; Fang, Q.; Gu, S.; Jiang, J.; Yan, Y., Efficient Water Oxidation Using Nanostructured α-Nickel-Hydroxide as an Electrocatalyst. *Journal of the American Chemical Society* **2014,** *136* (19), 7077-7084.
11. Ko, J. S.; Sassin, M. B.; Parker, J. F.; Rolison, D. R.; Long, J., Combining battery-like and pseudocapacitive charge storage in 3D MnOx@carbon electrode architectures for zinc-ion cells. *Sustainable Energy & Fuels* **2018,** *2* (3), 626-636.

12. Brisse, A.-L.; Stevens, P.; Toussaint, G.; Crosnier, O.; Brousse, T., Ni(OH)2 and NiO Based Composites: Battery Type Electrode Materials for Hybrid Supercapacitor Devices. *Materials* **2018,** *11* (7), 1178.
13. Gogotsi, Y.; Penner, R. M., Energy Storage in Nanomaterials – Capacitive, Pseudocapacitive, or Battery-like? *ACS Nano* **2018,** *12* (3), 2081-2083.
14. Wang, X.; Luo, H.; Parkhutik, P. V.; Millan, A.-C.; Matveeva, E., Studies of the performance of nanostructural multiphase nickel hydroxide. *Journal of Power Sources* **2003,** *115* (1), 153-160.
15. Xiao, H.; Qu, F.; Wu, X., Ultrathin NiO nanoflakes electrode materials for supercapacitors. *Applied Surface Science* **2016,** *360, Part A*, 8-13.
16. Li, Z.; Han, J.; Fan, L.; Guo, R., In-situ controllable growth of α-Ni(OH)2 with different morphologies on reduced graphene oxide sheets and capacitive performance for supercapacitors. *Colloid and Polymer Science* **2016,** *294* (4), 681-689.
17. Laheäär, A.; Przygocki, P.; Abbas, Q.; Béguin, F., Appropriate methods for evaluating the efficiency and capacitive behavior of different types of supercapacitors. *Electrochemistry Communications* **2015,** *60*, 21-25.
18. Wu, M. S.; Huang, Y. A.; Yang, C. H., Capacitive Behavior of Porous Nickel Oxide/Hydroxide Electrodes with Interconnected Nanoflakes Synthesized by Anodic Electrodeposition. *Journal of The Electrochemical Society* **2008,** *155* (11), A798-A805.

Chapter 3 – The Charging Behaviour of Nickel Hydroxide Nanoparticles

This chapter is concerned with an investigation of the nature of charging at the surface of nickel hydroxide nanoparticles immersed in potassium hydroxide. Several synthesis methods were trialled to identify a route to produce repeatably particles of the correct diameter and consistent morphology. Batches of nickel hydroxide nanoparticles were hydrothermally synthesised in the diameter range of 3–450 nm. Increased inter-particle resistance caused by the surfactants employed in the syntheses of small particle sizes was addressed using a post syntheses treatment of UV generated ozone to remove surfactant. Due to the ambiguity in the charging mechanism, the nature of charge storage was determined by studying the specific capacitance (Cap_s) and the specific capacity (C_s). The surface area of the particles was determined using N_2 adsorption and the areal capacity (C_A) of the materials was also studied. Cap_s and C_s were shown to increase with decreasing particle size, consistent with a surface-only charging mechanism due to the increase in specific surface area with decreasing particle size. This was only true, however, until a critical diameter of around 20 nm, at which point Cap_s and C_s began to decrease with decreasing particle size. C_A was found to be constant with decreasing particle size; however, this was only true down to a similar 20 nm critical diameter. Further reduction in particle size resulted in a decrease in all metrics. The mechanism suggested to explain these results is a charging "skin" in which charged material reaches a depth of around 10 nm. Once these two charging skins begin to interact, at a particle diameter of 20 nm, C_S and C_A both begin to decrease. The results obtained have implications in the design of $Ni(OH)_2$ electrodes in charge storage applications.

3.1 Introduction

The advancement of electrochemical energy storage devices, such as batteries and electrochemical pseudocapacitors, requires a detailed understanding of the charge and discharge mechanisms. As discussed in Section 1.7, materials that show battery-like properties in the bulk have been reported to exhibit pseudocapacitive behaviour at the nanoscale.[1] This phenomenon is known as extrinsic pseudocapacitance and is seen in several transition metal oxides/hydroxides.[2] The change in performance with material architecture has been linked to shortened diffusion and intercalation pathways in the nanomaterial. However, there is currently no consistent model which describes the material behaviour at all length scales.

In battery electrodes, it is accepted that the entire bulk of the material undergoes redox intercalation processes. In contrast, pseudocapacitor redox reactions occur purely at or just beneath the surface of the material, while the bulk remains inactive. What is meant by "at or just beneath the surface" is poorly defined and open to interpretation. This has led to controversy in the classification of materials as battery or psuedocapacitive.

Nickel hydroxide is a model extrinsic psuedocapacitive material, which has been reported as showing both battery-like and capacitor-like behaviours depending on the electrode structure and analysis conditions.[1, 3-7] It has been argued that as cyclic voltammograms of $Ni(OH)_2$ show distinct redox peaks the material should be classified solely as a Faradaic battery-like material rather than a pseudocapacitor.[8] $Ni(OH)_2$ has been used in battery electrodes for several years now and there is extensive research on the subject.[1, 9] Battery electrodes using $Ni(OH)_2$ have been reported with capacities of approximately 300 mA h g^{-1}.[1]

In response to this however, others have stated the rapid linear charge/discharge profiles of nanoscale $Ni(OH)_2$ are indicative of pseudocapacitive behaviour.[3, 7, 10-11] Supercapacitors using $Ni(OH)_2$ electrodes have been reported with specific capacitances of up to 3000 F g^{-1}.[10-11] The inclusion of $Ni(OH)_2$ in pulse electronics, and the potential of their use in transport, has sparked interest in several types of hybrid material and electrode designs.

The bulk redox behaviour of $Ni(OH)_2$ is discussed in detail in Section 1.6.2. On charging, the hydroxide oxidises to the oxyhydroxide form, as shown in Equation (3.1);

$$Ni(OH)_2 + OH^- \rightarrow NiOOH + H_2O + e^- \quad (3.1)$$

The phase changes which accompany the oxidation and reduction reactions have also been discussed.[9] Due to the confusion between battery and psuedocapacitive charging in the literature, the exact nature of the charge storage mechanism is still debated.[12]

To begin to answer the question as to why $Ni(OH)_2$ exhibits pseudocapacitive behaviour at the nanoscale exclusively, this chapter presents a study of the charging of $Ni(OH)_2$ over different particle sizes. To do this, it was necessary to identify a method of synthesis which could be altered to produce different sizes of $Ni(OH)_2$ particles with a similar morphology. The synthesis needed to be easily reproducible to allow for repeat measurements, as well as

producing the same phase composition. Finally, the synthesis had to produce enough high quality product that all materials and electrochemical characterisation can be carried out.

Several synthesis methods were trialled including wet chemical precipitation, sol-gel, sonochemical, and hydrothermal syntheses. All these methods have been previously shown to produce $Ni(OH)_2$ particles with dimensions on the nanoscale.[1, 13-16] The details of each of these methods are described in Section 3.2, along with the preliminary results. Hydrothermal synthesis was chosen as the optimum synthesis method due to the range of particle sizes produced and the small variation between repeat syntheses. Nanoplates of $Ni(OH)_2$ of various diameters, between 3–450 nm, were synthesised and the particles examined for their electrochemical properties.

These particles were used to study the charging behaviour of $Ni(OH)_2$ by comparing the specific capacity (C_s) and areal capacity (C_A) to the particle size. In order to address both existing schools of thought in the battery vs supercapacitor debate, the variation of specific capacitance (Cap_s) with particle size is also discussed. Most previous studies have relied on the Cap_s and C_s as a performance metric, while no studies were found which studied the C_A.

As particles get smaller, the particle surface area to volume ratio increases. This is normally given as the reason why specific capacitance generally increases for smaller particles. This model assumes a surface-only charging process, typical of a pseudocapacitor. For a pure pseudocapacitor, Cap_s should increase as particle size decreases whilst C_A should be constant over all particle sizes. For materials that exhibit battery like bulk charging, C_s should be constant as the entirety of the particles are electrochemically active. C_A should decrease with decreasing particle size due to the expected increase in specific surface area. If neither model can correctly predict the behaviour of the material over all length scales, it is hypothesised that there may be a crossover between battery like bulk charging, and surface only charging seen in pseudocapacitive systems. This chapter will explore any crossover of behaviour and develop a model which explains the results at all length scales.

3.2 Initial Synthesis Methods

Several synthesis methods were trialled to find one which met the necessary criteria. The method had to produce discrete particles with a low variation in size over different synthesis runs. Particles in the size range from <10 nm to >100 nm must be accessible, without changing significantly in morphology or requiring any harsh conditions which might further oxidise the product to NiO. The methods trialled were rejected for a variety of reasons, giving useful insight into tailoring future synthesis attempts. As the work was abandoned at various stages, results obtained from these methods do not follow the stringent methodology laid out in Section 2.2.

3.2.1 Wet chemical Precipitation

Chemical precipitation has the advantages of being an easy and cheap to run synthesis method. Typically, a solution of aqueous Ni^{2+} salt is heated and rapidly stirred. A basic solution is then either added dropwise for steady growth, or rapidly injected for a single nucleation event to produce small monodisperse particles. The reaction of the nickel and hydroxide ions causes nickel hydroxide to be precipitated, shown in Equation (3.2).

$$Ni^{2+}_{(aq)} + 2OH^{-}_{(aq)} \rightarrow Ni(OH)_{2(s)} \quad (3.2)$$

Control of the phase and particle size has been reported by varying the solution concentrations, the Ni(II) salt used, the base used, the temperature, and the pH of the solution.[17-19] Decreased pH and elevated temperatures have been shown to favour β-$Ni(OH)_2$ formation, however mixed phases are produced predominantly.[18, 20] The formation of this mixture of phases suggest that a similar process to the chemical aging described above occurs during synthesis, with the α-$Ni(OH)_2$ forming first and then aging to the β-$Ni(OH)_2$.[21]

As well as the phase, the particle size alters with temperature, with particles becoming larger as synthesis temperature increases. Alternatively, size can be mediated using a stabilising agent such as sodium citrate or sodium dodecyl sulphate. This also gives the added benefit of stabilising the colloidal suspension and allowing for easier deposition.[5, 15, 17]

Going forward, wet chemical precipitation had the potential advantage of allowing the easy production of mixed metal hydroxides. Common examples use other first row transition metals, such as manganese or cobalt. The ratio of inclusion into the lattice has been found to be stoichiometric, suggesting the dopant metal occupies the same site as the nickel. Complex

morphologies, such as layered structures or core shell nanoparticles have also been produced.[22]

Initial wet chemical precipitation results were obtained using the methodology established by Meyer *et al.*[23] Both ammonium hydroxide and potassium hydroxide were trialled as alkaline solutions with a molar ratio of base to nickel of two. As well as being inconsistent over multiple repeats, the particles sizes showed large variation within samples. SEM images can be seen in Figure 3.1.

Using potassium hydroxide as a base, a mixture of micron sized domains with flake like morphology was initially seen, Figure 3.1a. The particle size is difficult to determine due to the aggregation of the flakes into microscale domains. On repeating the experiment, a mix of some flakes, along with smaller more particulate structures around 30 – 50 nm were seen. Using ammonium hydroxide as a base, aggregate structures termed nanoflowers were produced, Figure 3.1b. The use of these structures would make quantifying particle size difficult. This is due to the ambiguity between the size of the nanoflowers, approximately 1-3 µm, and its constituent particles of approximately 100 nm.

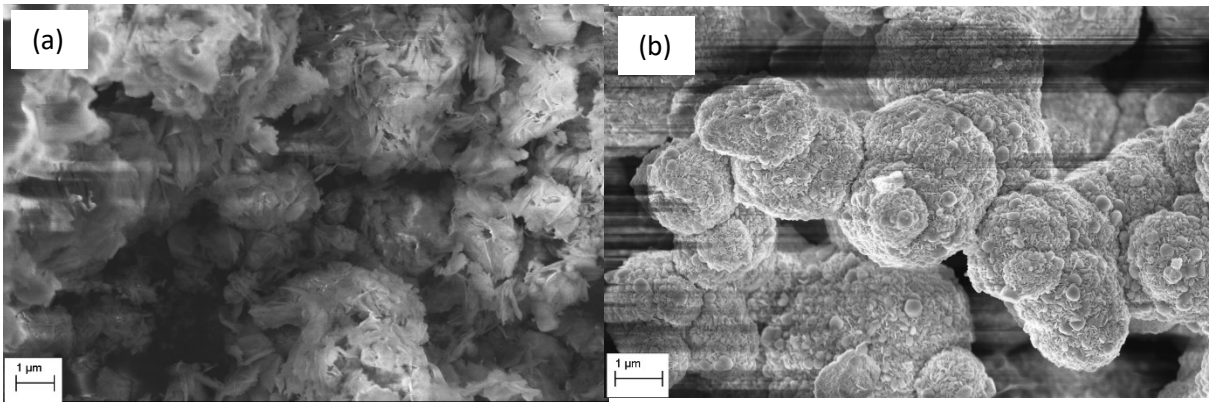


Figure 3.1 1) SEM micrograph of nickel hydroxide produced using wet chemical precipitation methods using potassium hydroxide as the reacting base. b) nickel hydroxide produced using wet chemical precipitation methods using ammonium hydroxide as the reacting base. Both exhibit banding due to lack of charge conductive coating and poor contact with SEM stub.

Further alteration of conditions using both bases gave unrepeatable results in terms of particle size and morphology. This is thought to be partially due to the inconsistent heating of the reaction vessel, as well as scratches and other marks which act as heterogeneous nucleation points on the glassware.

3.2.2 Multiphase Synthesis

Multiphase synthesis methods have been employed to control the size and distribution of nickel hydroxide nanoparticles. Nanoscale water environments are maintained using a surfactant such as cetyl trimethyl ammonium bromide (CTAB).[24] The nano-environment provided by such a method, such as a reverse micelle, allows for a narrow size range to be obtained. This size can also be controlled by the water to surfactant ratio.

One disadvantage of this technique is the separation step required to remove the product from the bulk solution, without causing aggregation of the product. These methods are sometimes referred to as sol-gel methods. A colloidal suspension of nanoparticles, such as those already described, is formed. This can then be gelled by physical aggregation caused by repeated washing with deionised water.[14] Three-dimensional interconnected gel networks have also been reported, forming from organometallic precursors. The formation of nickel hydroxide networks via the hydrolysis of nickel ethoxide is one example of this, shown in Equations (3.3) and (3.4).[14]

$$Ni^{2+}_{(aq)} + 2NaOCH_2CH_{3(aq)} \rightarrow Ni(OCH_2CH_3)_{2(aq)} + 2Na^{+}_{(aq)} \quad (3.3)$$

$$Ni(OCH_2CH_3)_{2(aq)} + 2H_2O_{(l)} \rightarrow Ni(OH)_{2(s)} + 2HOCH_2CH_{3(aq)} \quad (3.4)$$

The products may then be dried to form a xerogel or an aerogel, depending on drying conditions. These materials provide very high specific surface areas, however are brittle and can be damaged rapidly on charging.[25]

Initial syntheses were based on the work of Cheng *et al.* and Wu *et al*.[14, 24] Both methods produced very low yields, making them unlikely to be used further. While a 3D porous network would be a useful morphology for electrochemical energy storage, the continuous nature makes it unsuitable for this work. The product is shown in Figure 3.2a. The CTAB based microemulsion produced discrete particles. There was a large dispersity in the sample however and the sizes were not repeatable over multiple syntheses. An example of the $Ni(OH)_2$ produced by these CTAB microemulsions is shown in Figure 3.2b.

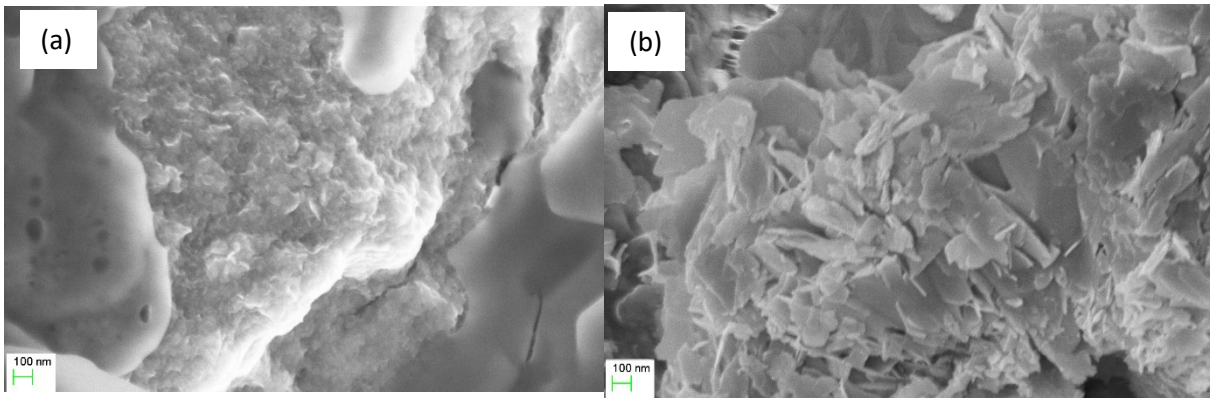


Figure 3.2 a) SEM micrograph of nickel hydroxide produced using multiphase synthetic methods using sodium ethoxide via an organometallic precursor. b) SEM micrograph of nickel hydroxide produced using multiphase synthetic methods using CTAB based emulsions to form nanoscale aqueous environments.

3.2.3 Sonochemical Synthesis

Sonochemical synthesis relies on the creation of microbubbles by an ultrasonic bath or horn. When these bubbles collapse, the energy released gives rise to small super-heated areas of solvent, providing the activation energy for the reaction.[13, 22] The small solvent domains mean the synthesis consistently produces very small particle sizes without the need for surfactants which can affect the product's electrochemical activity.

The initial synthesis was based on the method used originally by Vidotti *et al.* to create nanoplates of $Ni(OH)_2$.[22] One key difference however was the use of an ultrasonic bath, rather than a high power ultrasonic horn, which was not available. Initial results showed nanoplates of around 100-150 nm being produced, shown in Figure 3.3. These results were promising, giving an appropriate size range for the experiment and discrete particles. However, the yield of the reaction was very poor, returning only 1-2% of the mass of Ni^{2+}. Further increasing the concentration of Ni^{2+} resulted in a loss of particulate structure.

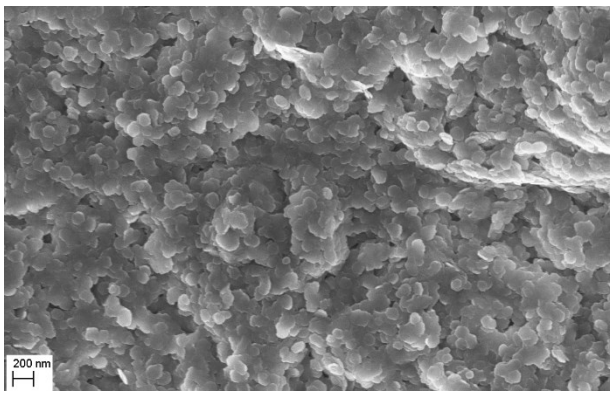


Figure 3.3 SEM micrograph of nickel hydroxide nanoplates produced using a sonochemical synthetic method, without conductive coating.

3.2.4 Hydrothermal Synthesis

Solvothermal methods have been used to great effect in producing large quantities of nanoparticles and nanoplates.[26-27] Hydrothermal methods are the most common among these, using water as a superheated solvent.[4-5, 10, 15] The method requires the reagents and solvent to be contained in an autoclave pressure vessel, which is then heated. During heating, the fixed volume of the vessel means that the pressure inside the vessel increases. This increased pressure above the solution increases the boiling point of the water, meaning the solvent remains liquid well above the normal boiling point of water. These high temperatures allow the synthesis of particles which were inaccessible using normal reflux syntheses. Results reported in the literature showed a wide range of $Ni(OH)_2$ particle sizes using mild conditions.[5, 15]

Due to the high temperatures and long reaction times, the thermodynamically favoured β-$Ni(OH)_2$ is usually the major product. The size distributions produced by these hydrothermal methods tends to be narrower compared to wet chemical precipitation; however, the average sizes are larger due to the higher temperatures typically used. The formation of α-$Ni(OH)_2$ is possible using lower temperatures or by adding an intercalating agent into the reaction.[3]

Initial syntheses, based on the method used by Xing *et al.*,[15] produced large quantities of nanoparticles. The addition of sodium citrate allowed for the synthesis of nanoparticles of diameter <100 nm. Increasing reaction temperatures allowed particle size to be increased to 200-300 nm. While ammonia was initially used, it was found to cause the formation of nanoflowers, similar to the work in Section 3.2.1. It was therefore decided to remove ammonia from future synthesis attempts. An example of the products of these reactions is given in Figure 3.4.

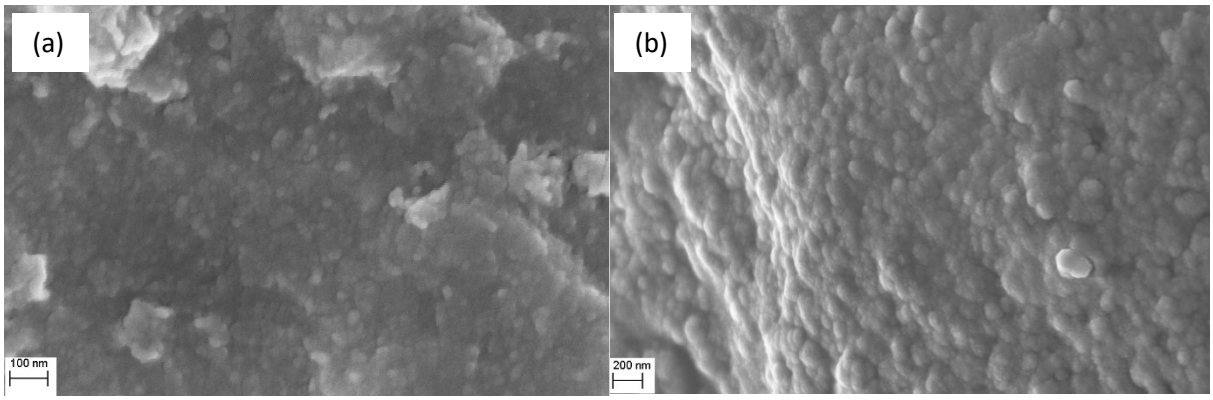


Figure 3.4 a) SEM micrograph of nickel hydroxide produced using hydrothermal synthetic methods and sodium citrate surfactant at 80°C b) SEM micrograph of nickel hydroxide produced using hydrothermal synthetic methods at 80°C with no surfactant

3.2.5 Comparison of Synthesis Methods

After consideration of all the methods listed above and the preliminary results obtained, it was decided that hydrothermal synthesis was the most useful method for $Ni(OH)_2$ synthesis. As well as producing a high yield, particularly compared to sonochemical and mixed phase syntheses, the particle sizes were consistent between multiple batches and had a low dispersity. Wet chemical precipitation using ammonium hydroxide base also produced large yields and repeatable results. The product morphology however, large aggregates comprised of nanoparticles, was unsuitable for the experiment. A summary of the results of the initial experiments can be seen in Table 3.1.

3.3 Synthesis Method

After the initial hydrothermal syntheses, adjustments were made to produce the sizes and morphologies desired for this experiment. Potassium hydroxide was used in the place of sodium hydroxide, since later electrochemical characterisation would use potassium hydroxide as the electrolyte. The concentration of the base was also reduced as it was found this produced a lower dispersity of particles. The ethanol initially used in the literature was found to play no role in the reaction and was replaced with water.

A reducing agent was also introduced to some of the syntheses to further decrease particle sizes. Sodium borohydride was selected as it had previously been shown to reduce particle sizes in $Ni(OH)_2$ nanoparticle formation.[5] These two synthesis routes, with and without $Na(BH)_4$, are termed non-Reductant Assisted (nRA) and Reductant Assisted (RA) routes respectively.

Table 3.1: Initial results of synthesis methods to produce $Ni(OH)_2$ nanoparticles

Synthesis Method	Reaction Conditions	Product Yield	Product Morphology	Particle size	Necessary Reproducibility
Wet Chemical Precipitation	0.4 mol dm^{-3} KOH base, 60 min stirring at 80^{O}C	High	Mixed flakes and particles	50-2000 nm	No
Wet Chemical Precipitation	0.4 mol dm^{-3} ammonium hydroxide base, 60 min stirring at 80^{O}C	High	Nanoflowers of aggregated particles	>1000 nm aggregate of ~50 nm	Yes
Mixed Phase	Sodium acetate and sodium ethoxide, stirring at 80^{O}C, 3.0 mol dm^{-3} KOH base added to pH 12.	Low	Continuous non-particulate domain	N/A	Yes
Mixed Phase	15 ml of 1 mmol Ni^{2+} dispersed in an emulsion of CTAB (1 g), glycerol (10 ml) and cyclohexane (15 ml). Then allow to react at 200^{o}C for 2 hours in autoclave	low	Mixed flakes and particles	1000 nm flakes and particles < 50 nm.	No
Sonochemical	0.02 mol dm^{-3} ammonium hydroxide base, 5 min in ultrasonic bath	Very Low	Nanoplates	100 nm	Yes
Hydrothermal	Stir with 2 mol dm^{-3} NaOH and an amount of ammonium hydroxide for 10 mins then allow to react at 100^{o}C for 24 hours in autoclave	High	Nanoplates	100-150 nm	Yes

Syntheses were carried out using a stainless-steel autoclave vessel with an 80 cm^3 PTFE liner produced by the Parr Instrument Company (USA). In a typical hydrothermal synthesis, 20 cm^3 of aqueous solution containing 20 mmol dm^{-3} of nickel nitrate hexahydrate (>95.0%) was stirred with either 200 mmol dm^{-3} or 2.00 mol dm^{-3} sodium citrate dehydrate (ACS ≥ 99.0%). For RA syntheses, the solution was then stirred with 10.0 cm^3 of 1.0 mol dm^3 sodium borohydride (> 99%) solution for 8 hours at 35 ^{o}C. For nRA syntheses, the solution was simply

diluted further with another 10.0 cm^3 of water and left to stir for 10 minutes. In both cases, the solution was then rapidly injected with 5.0 cm^3 of 2.0 mol dm^{-3} potassium hydroxide (VWR > 85%) and left to stir for another 10 minutes. The solution, now in some cases containing a precipitate, was transferred to the autoclave vessel, sealed and placed in the oven. A calculation using the ideal gas law was performed to find the maximum possible pressure generated during the reaction. This calculation assumed full vapourisation of the reaction solution in the minimum possible free space in the vessel (50 cm^3). The pressure found was still far below the recommended manufacturers safety limits. A full set of experimental conditions for each hydrothermal sample can be found in the Table 3.2.

Table 3.2: Full list of reaction conditions for hydrothermal syntheses of nickel hydroxide nanoplates.

Sample	Reaction temperature / ^oC	Reaction time / hours	Reduction assisted?	Surfactant concentration / mol dm^{-3}
1	60	24	Y	2.00
2	80	24	Y	2.00
3	100	24	Y	2.00
4	60	24	N	2.00
5	150	24	Y	2.00
6	60	24	N	0.20
7	60	72	N	0.20
8	80	24	N	0.20
9	100	24	N	0.20
10	120	24	N	0.20
11	150	24	N	0.20

Once the reaction was complete, the vessel was removed from the oven and left to cool for 3 hours. The precipitate was collected and washed at least three times with water until the run off pH was below 8. Between each washing, the product was centrifuged at 5600 rpm for 20 minutes.

The final product was dried in an oven at 60 ^oC for 24 hours. Where required, surfactant removal by ozonolysis was performed using a Novascan PSD series digital UV/Ozone system, further discussed in Section 3.5.1.

3.4 Materials Characterisation

3.4.1 Synthesis Mechanism

Nanoplates of $Ni(OH)_2$ were synthesised using hydrothermal processing between 60 ^oC and 150 ^oC. The aqueous nickel salt was reacted in a strong base in the presence of citrate as a surfactant. Excess surfactant was removed from the particles at the end of the reaction by ozonolysis. A reducing agent, $Na(BH)_4$, was added in some cases before hydrothermal processing to reduce final particle size. To discern the reaction mechanism with the reducing agent added, EDX analysis was performed on the intermediate formed before the addition of KOH, shown in Figure 3.5. The spectrum of the intermediate formed in the RA reaction shows a very low oxygen content compared to the final $Ni(OH)_2$ nanoparticles, shown in Figure 3.6. This suggests the intermediate products are $Ni_{(s)}$ particles, which then go on to act as the seeds for the formation of the $Ni(OH)_2$ nanoparticles.

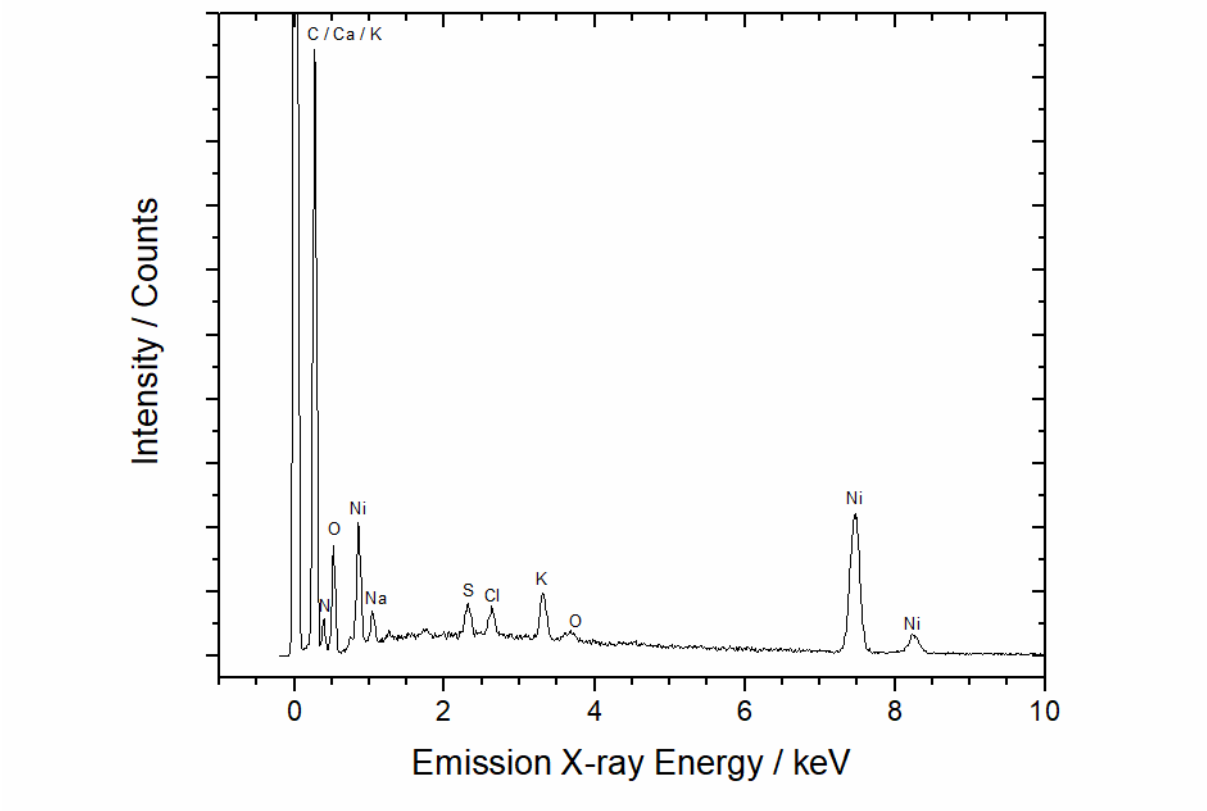


Figure 3.5 Energy dispersive X-ray spectroscopy of the intermediate of reduction assisted synthesis. Samples drop-cast directly onto aluminium stub for analysis. EDX performed at 10 kV accelerating voltage.

These findings support the mechanism reported previously in the literature.[5] Further study would be required to confirm this reaction mechanism, potentially using XRD, XPS, or *in-situ* measurements. It was not possible to separate the intermediate from the natant solution

using centrifugation, so the analysis was potentially in the presence of all reactants, which may make the results unreliable.

3.4.2 Chemical Composition of Hydrothermal Products

EDX spectra were taken for all samples and a typical example of one of these is shown in Figure 3.6. Elemental atomic ratios were measured using the methodology set out in Section 2.2.3. Analysis showed an expected Ni:O ratio of 0.5 ± 0.1 for both synthesis procedures. This is a significantly higher oxygen ratio than that found for the intermediate product, shown in Figure 3.5. It is also much higher than would be expected for NiO if the nickel had been fully oxidised.

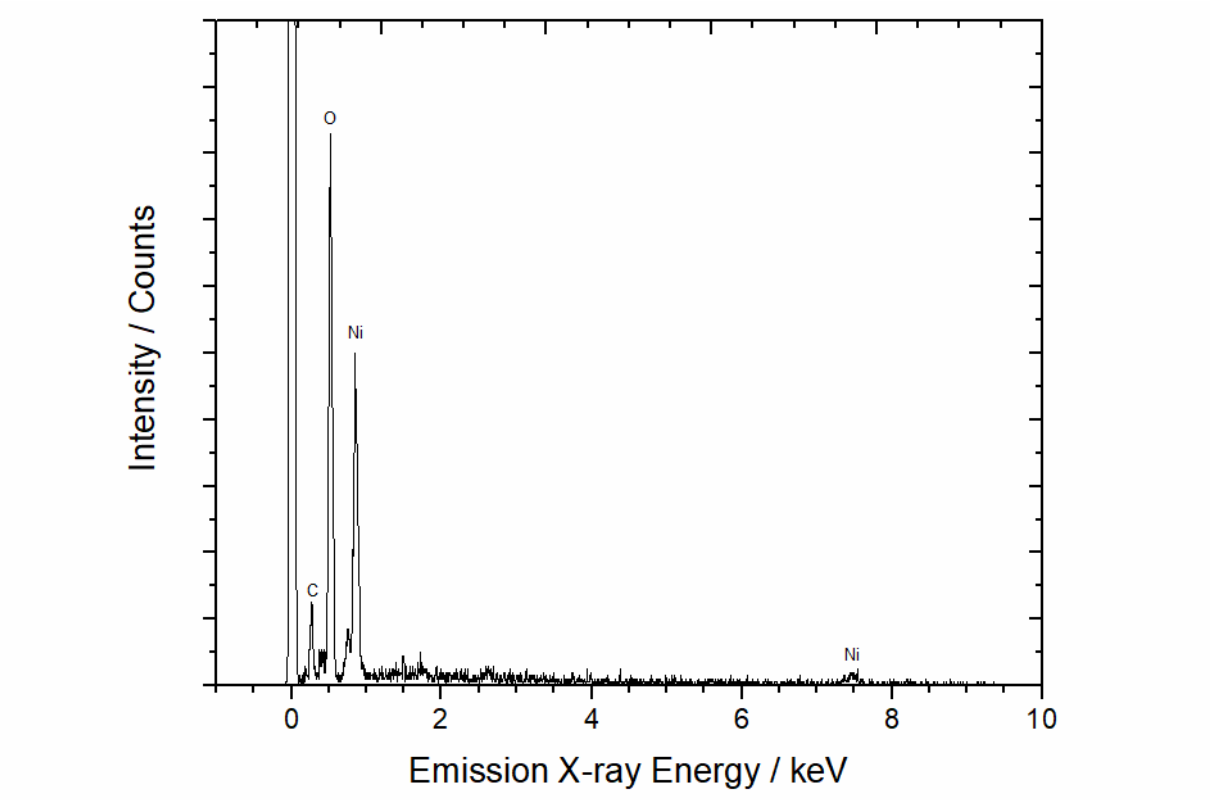


Figure 3.6 Energy dispersive X-ray spectroscopy of final product of hydrothermal reactions. Samples drop-cast directly onto aluminium stub for analysis. EDX performed at 10 kV accelerating voltage.

XPS analysis for the Ni 2P peak shows two major peaks with binding energies at 873.6 and 856.0 eV, which correspond to $Ni2p_{1/2}$ and $Ni2p_{3/2}$, respectively, with a spin-energy separation of 17.6 eV. These results, shown in Figure 3.7, are characteristic of $Ni(OH)_2$ and in good agreement with previously reported data within machine error.[3, 28]

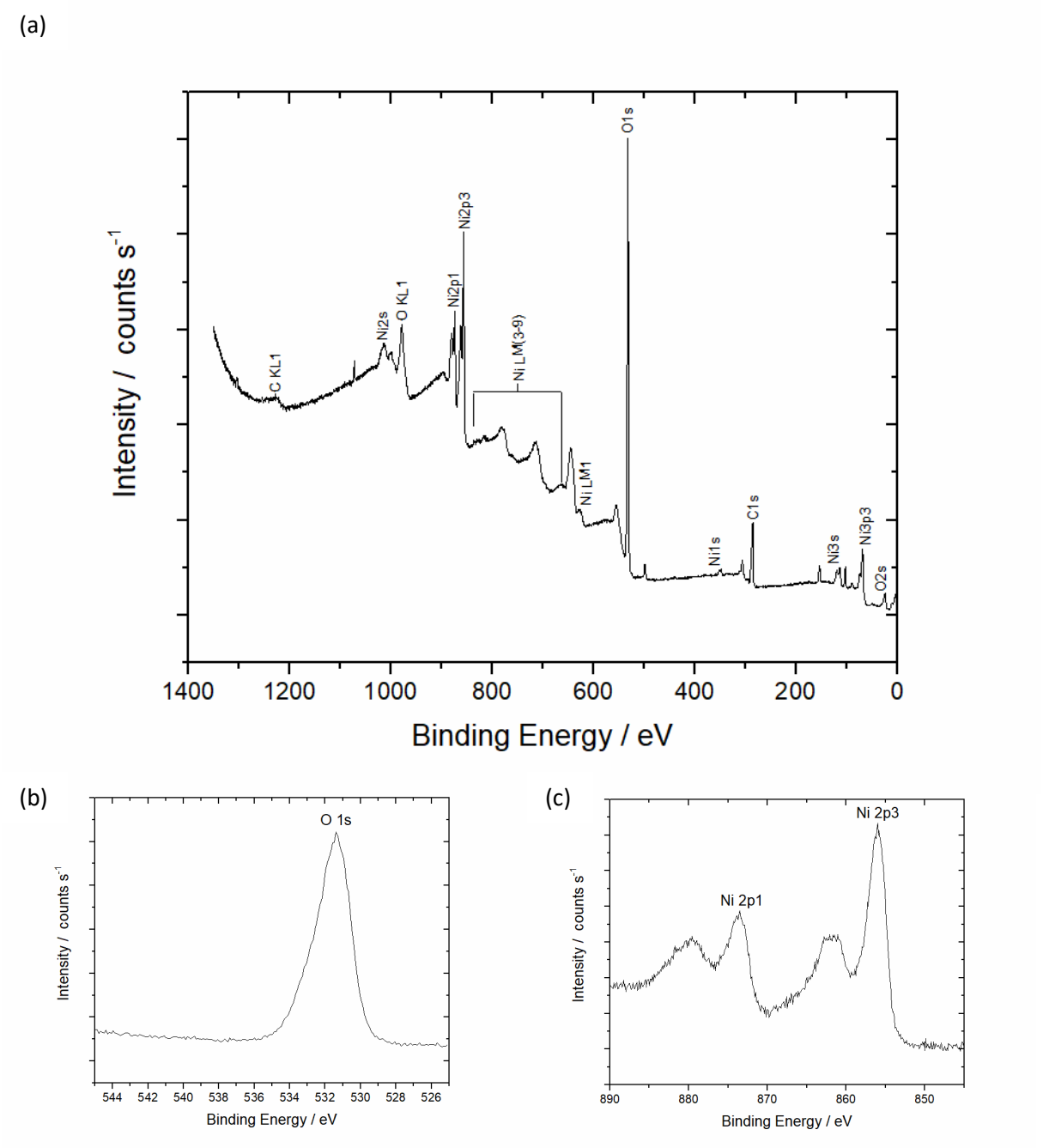


Figure 3.7 X-ray photoelectron spectra of $Ni(OH)_2$ samples using Al Kα X-rays (hν = 1486.86 eV) with C1s peak set to a binding energy of 285 eV (a) Survey spectrum (pass energy 200 eV, dwell time 25 ms) (b) O 1s and (c) Ni 2P spectra. The high-resolution Ni(2p) and O(1s) spectra were obtained at a pass energy of 20 eV, and a dwell time of 50 ms.

3.4.3 Phase, Size and Morphologies of $Ni(OH)_2$ Particles

In agreement with previous studies, the largest $Ni(OH)_2$ product exhibits a nanoplatelet morphology, as shown in SEM micrographs Figure 3.8a.[6] The more crystalline domains show a hexagonal structure, which is expected given the unit cell.[6, 9] As the size reduces, the shape becomes more spherical. Variation in reaction time, temperature and surfactant concentration allowed growth of batches of particles with defined average diameters

between 3 nm and 450 nm; higher reaction temperatures and lower surfactant concentrations leading to larger particles; see Figure 3.8 and Table 3.3. Increasing reaction times from 24 to 72 hours was shown to have a negligible effect on the resulting particle size, compare samples 6 and 7. The particle sizes for the RA syntheses were significantly smaller than those *via* nRA syntheses at the same temperature and surfactant concentration.

Table 3.3: List of particle diameters as measured by SEM/TEM for hydrothermal syntheses of nickel hydroxide nanoplates. Standard error in particle diameter was calculated using the method laid out in Section 2.2.1.

Sample	Average particle diameter measured by electron microscopy / nm	Standard Error in Particle diameter / nm
1	3	1
2	4	1
3	8	2
4	11	3
5	17	4
6	56	8
7	63	3
8	130	10
9	250	20
10	300	30
11	450	60

For particles <10 nm in diameter, TEM was used to measure the particle size. TEM micrographs are shown in Figure 3.9 and 3.10. Before ozonolysis, particles were observed to be separated after high vacuum drying, as shown in Figure 3.9a, suggesting that a layer of surfactant remains on the particle surface even after washing. After ozonolysis, the particles were observed to be aggregated, as shown in Figure 3.9b, suggesting the surfactant layer has now been removed. An edge-on nanoplate synthesised at 60^{o}C without the use of a reducing agent is shown in Figure 3.10. This shows the nanoplate thickness of around 5 nm and an interlayer spacing of around 0.5 nm. This agrees well with the expected c-direction of the unit cell of β-$Ni(OH)_2$.[9]

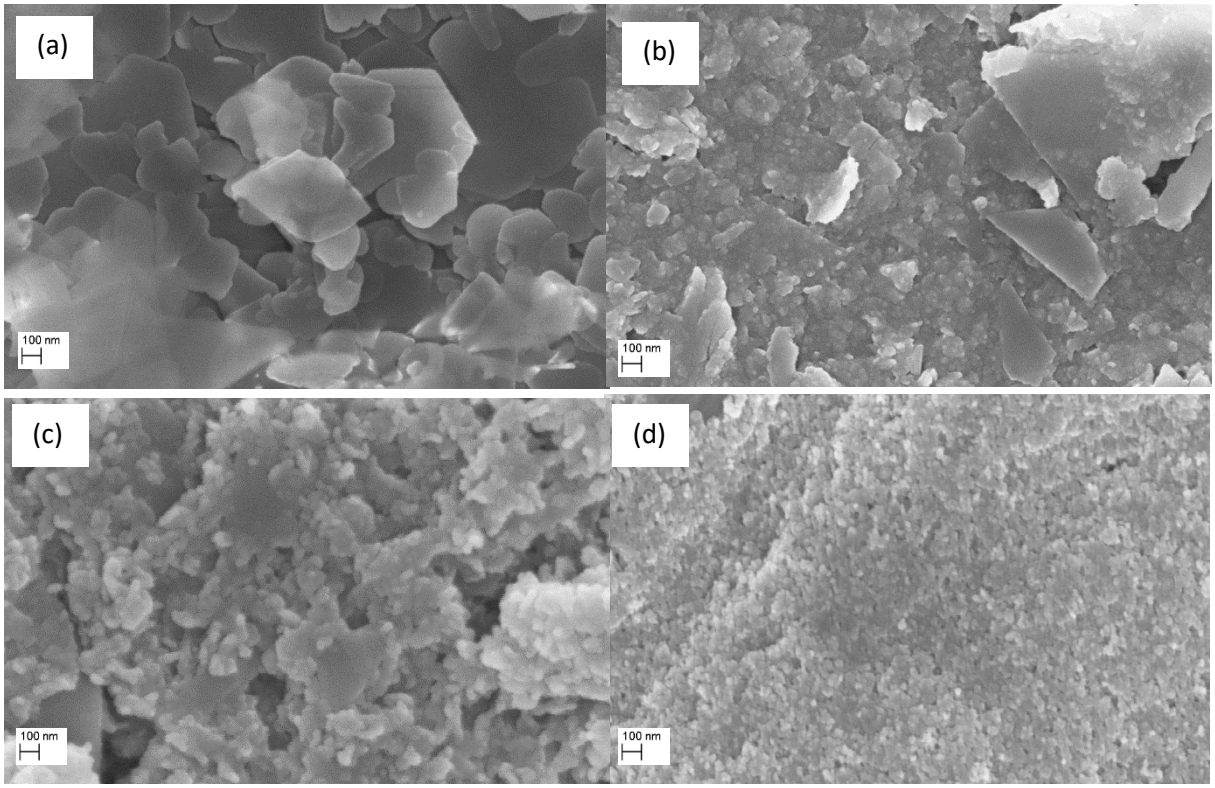


Figure 3.8 Scanning Electron Microscopy (a-d) SEM images of $Ni(OH)_2$ synthesised at various temperatures (150^{O}C, 120^{O}C, 80^{O}C, 60^{O}C) using 0.2 M surfactant and non-reduction assisted syntheses (samples 11,10,8,6). Images taken by directly drop-casting onto aluminium stub with no further metal coating

In addition to SEM/TEM, DLS was also used to size the nanoparticles, according to the methodology laid out in Section 2.2.7. DLS indicates the hydrodynamic radius of the particles, due to the timescales of the measurement and molecular rotation being similar. In this case, the hydrodynamic radius is determined by the diameter of the largest face of the nanoplates.

Results of initial DLS experiments, shown in Figure 3.11 and Table 3.4, show good agreement in the relative sizing of the particles compared to SEM. The magnitude of the sizing however is much larger compared to that observed using SEM/TEM. This is particularly seen in the sizing for larger particles, which are orders of magnitude larger. This is due to the instability of the larger particles in solution, as well as the effect of aggregation of the particles.

Zeta potential measurements for 3 nm particles was found to be as high as +35 mV, while this dropped to as low as +0.5 mV for sample 6, which had a diameter of around 56 nm according to SEM. Experiments using increased levels of surfactant after synthesis to aid dispersion proved unsuccessful due to the formation of surfactant micelles in solution. These factors made DLS ineffective at sizing across the whole range of particles.

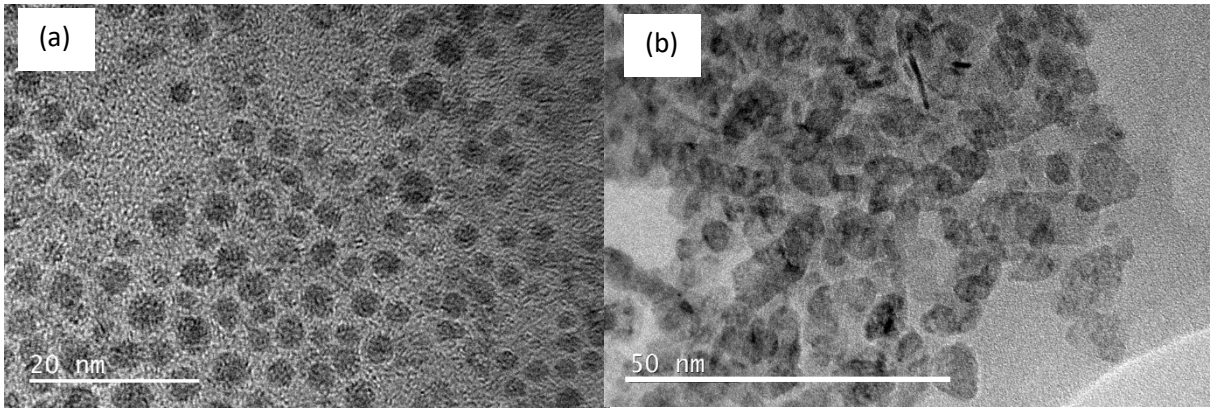


Figure 3.9 TEM images of particles synthesised at 60^{O}C using 2.0 M surfactant and reductant assisted synthesis (a) before ozonolysis and (b) after ozonolysis. Images taken by dispersing in methanol and drop casting onto carbon grid.

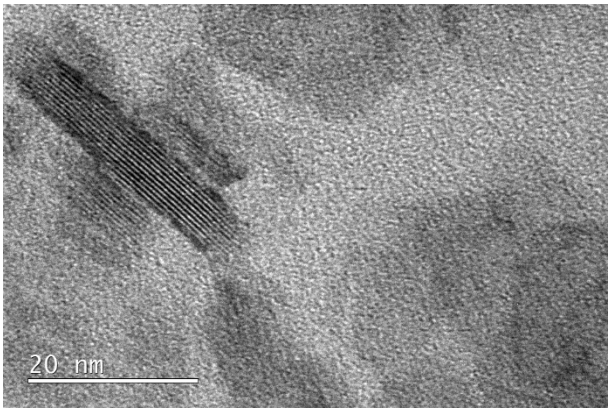


Figure 3.10 TEM image of edge on particles synthesised at 60^{O}C using 0.2 M surfactant in a non-reductant assisted synthesis. Images taken by dispersing in methanol and drop casting onto carbon grid.

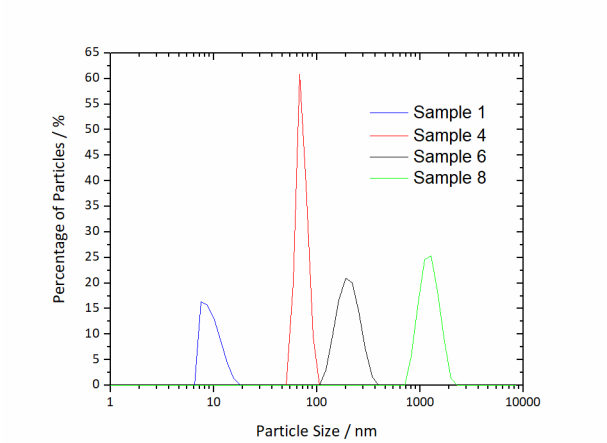


Figure 3.11 DLS results for hydrothermally synthesised samples of $Ni(OH)_2$ nanoparticles using different experimental conditions. Samples shown; (1) 60^{O}C + RA + 2 M surfactant (4) 60^{O}C + nRA + 2 M surfactant (6) 60^{O}C + nRA + 0.2 M surfactant (8) 80^{O}C + nRA + 0.2 M surfactant. All samples collected while dispersed in water at room temperature with no further surfactant to aid dispersion.

Table 3.4: List of particle diameters as measured by DLS for hydrothermal syntheses of nickel hydroxide nanoplates. Standard error in particle diameter was calculated using the Zetasizer software.

Sample	Average particle diameter measured by DLS / nm	Standard Error in Particle diameter / nm
1	8.7	0.4
4	65	4
6	290	70
8	1270	90

The XRD patterns for the $Ni(OH)_2$ particles are shown in Figure 3.12 and 3.13. For low syntheses with low concentration of surfactant, Figure 3.12, the α-$Ni(OH)_2$ (001) peak is the dominant peak at 60 and 100 °C. The β-$Ni(OH)_2$ (001) peak then becomes more prevalent above this temperature, with no discernible α-$Ni(OH)_2$ peaks above a reaction temperature of 120 °C.[29]

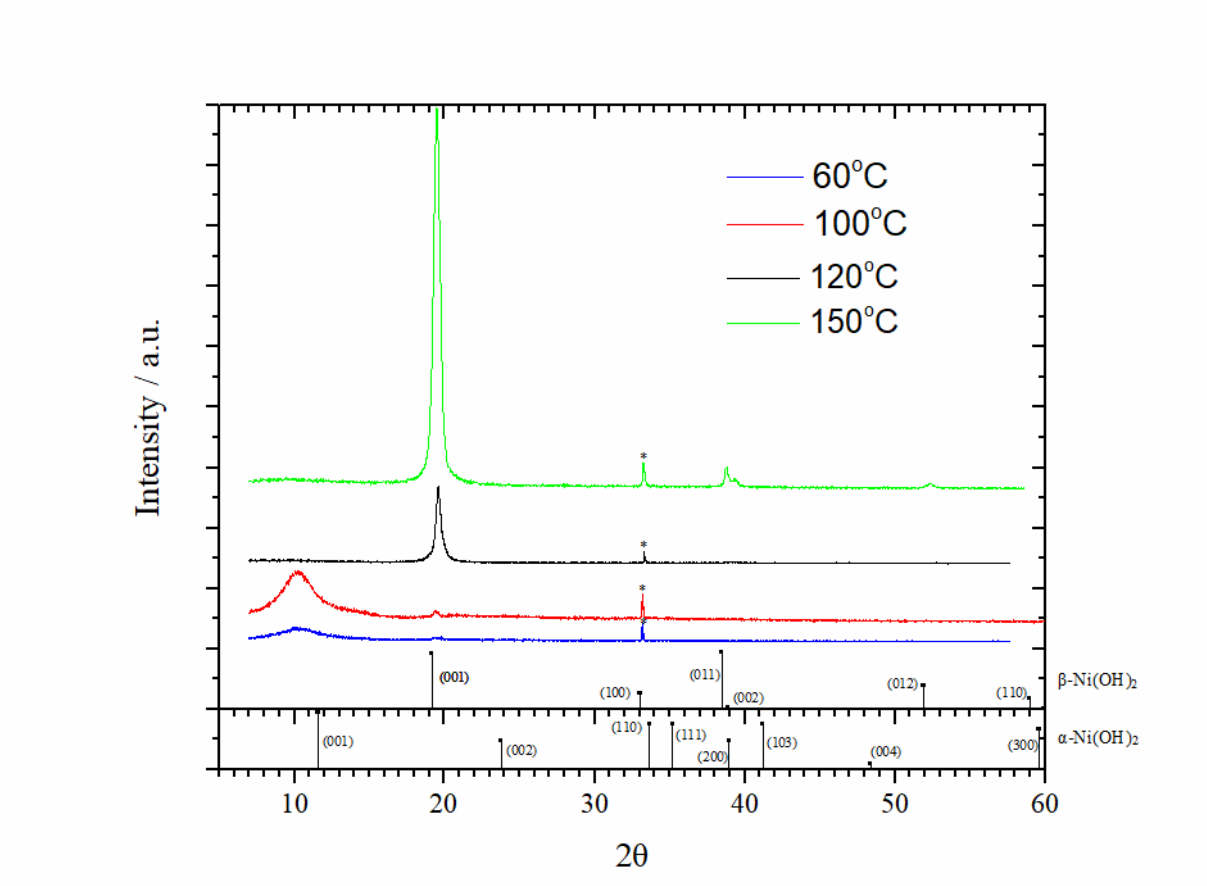


Figure 3.12 X-ray diffractograms of nickel hydroxide samples deposited on to Si wafer produced using low surfactant syntheses. Analysis conditions described in section 2.2.5

Samples formed using high concentrations of surfactant, Figure 3.13, show less well-defined peaks at all temperatures. Once again, the β-$Ni(OH)_2$ peaks begin to show at 100 °C but the small particle size means these peaks are much broader. The (001) peaks are significantly more intense when compared to the stick pattern. This is expected, since the particles have a platelet morphology shown in Figure 3.8a, the preferred orientation during drying will lead to a stacking of plates.

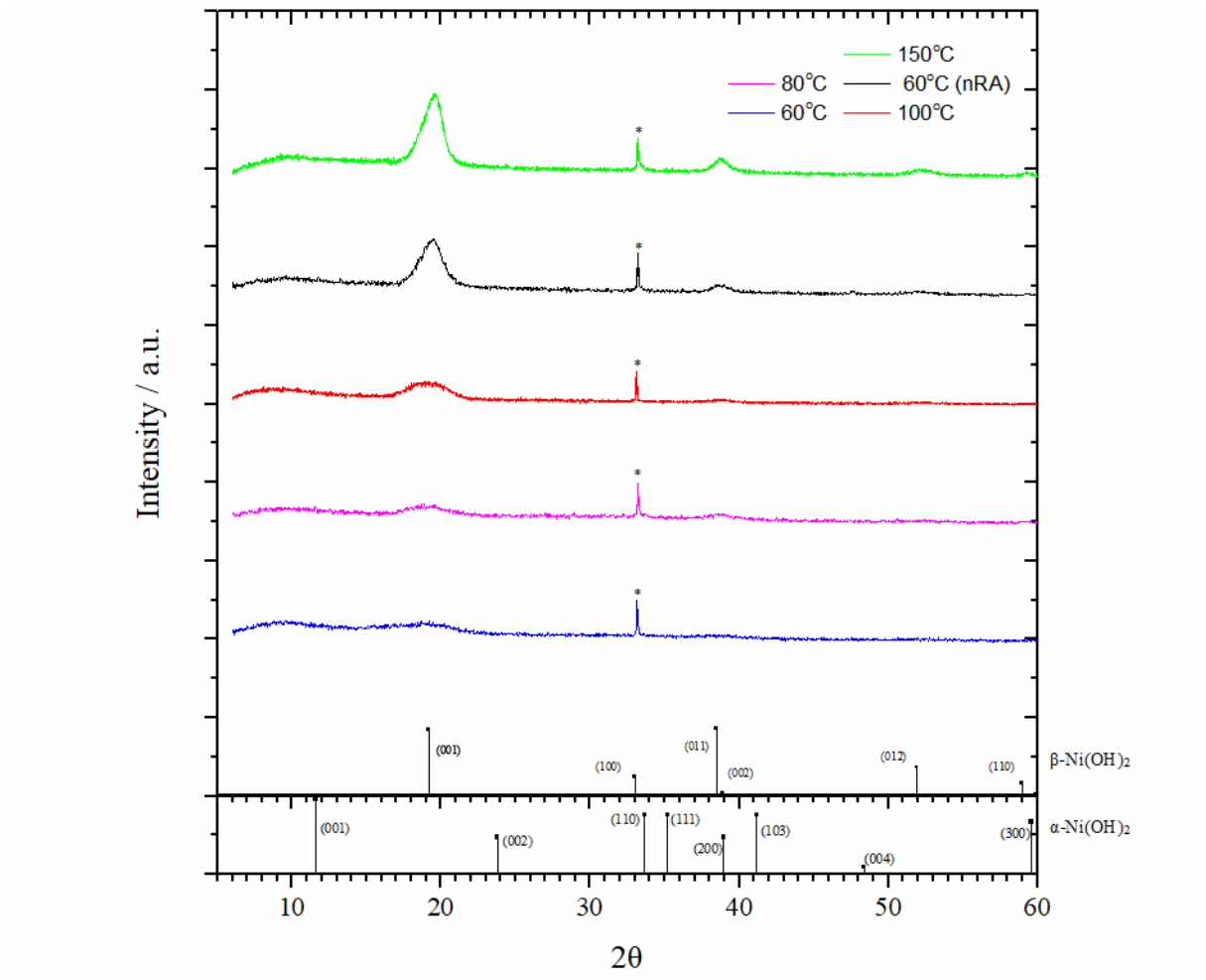


Figure 3.13 X-ray diffractograms of nickel hydroxide samples deposited on to Si wafer produced using high surfactant syntheses. Analysis conditions described in section 2.2.5

The α-$Ni(OH)_2$ phase has been shown to age on cycling in alkaline electrolyte to yield β-$Ni(OH)_2$.[30] To compare the electrochemical behaviour of samples with different *initial* phases, the capacitance measurement used were taken once the current had stabilised and the phase remained constant, as determined by *ex-situ* XRD. [30] This electrochemical aging is shown in Figure 3.14.

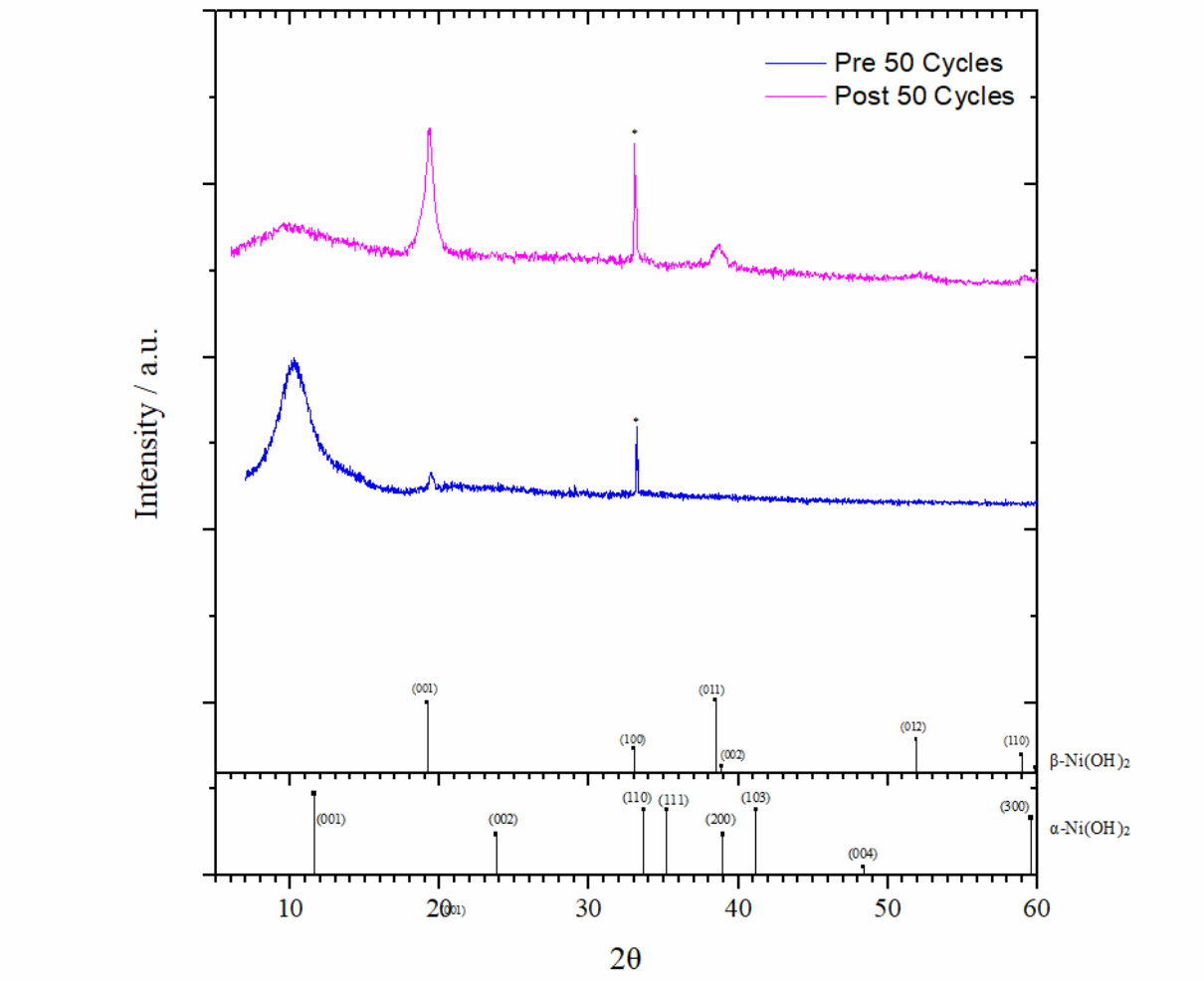


Figure 3.14 XRD diffractogram of Sample (9) produced at 100°C using nRA low surfactant synthesis before and after 50 cycles of cyclic voltammetry between 0.0 V and 0.7 V at a scan rate of 50 mV s^{-1}. Samples deposited onto Si wafer before analysis.

Particle sizing can also be achieved using XRD and the Scherrer Equation (3.5);

$$\tau = (K\lambda)/(\beta\cos\theta) \quad (3.5)$$

where τ is the mean size of the crystalline domains in m, *K* is the dimensionless shape factor, λ is the X-ray wavelength in m (Cu-Kα = 1.54 Å), β is the peak broadening at the FWHM in radians, and θ is the Bragg angle in degrees. A full methodology for the calculation of particle sizes and errors using XRD data can be found in Section 2.2.5. The results of this Scherrer sizing for the low surfactant syntheses, samples 6 and 9-11, can be seen in Table 3.5.

Table 3.5: List of particle diameters as measured by XRD for hydrothermal syntheses of nickel hydroxide nanoplates. Standard error in particle size was calculated using the three largest peaks in each diffractogram.

Sample	Average particle diameter determined from XRD / nm	Standard Error in Particle diameter / nm
6	4	2
9	18	2
10	70	6
11	91	6

While there is an internal consistency in the relative sizes of the samples, the magnitude of the particle sizing is much smaller than observed using SEM. This could be due to many factors, such as an incorrect assumption with respect to the shape factor used in Equation (3.5), discussed in Section 2.2.5. Alternatively, the defects in the crystal structure could lead to the particles appearing as polycrystalline in the XRD.

Table 3.6: List of particle diameters as measured by SAXS for hydrothermal syntheses of nickel hydroxide nanoplates. Error in particle size was calculated using PANalytical software and the interquartile range.

Sample	Average particle diameter determined from SAXS / nm	Error in Particle diameter (±) / nm
1	2	1
2	4	2
3	7	4
4	9	5
5	11	6

For samples with particle diameters suspected to be <50 nm, the particle sizes were confirmed using SAXS. SAXS analysis gives very good agreement with the sizes observed using SEM/TEM. This type of analysis is not possible over all particle sizes, so was only used to confirm the sizes of the particles with diameter <50 nm. The results of SAXS analysis are shown in Table 3.6. A summary table of all particle size measurements is given in Appendix 9.

3.4.4 Nanoparticle Specific Surface Area

Specific surface areas for the $Ni(OH)_2$ nanoplate modified electrodes were determined using N_2 adsorption. Adsorption/desorption isotherms are shown in Figure 3.15 for both extremes of particle size. The large particles show very little surface area and give a type I isotherm typical of a microporous solid. The small particles show a more complex type IV isotherm, indicating a mesoporous structure and capillary condensation.[31] DFT analysis, which yielded consistent results between multiple samples from the same synthesis, was chosen to calculate surface areas. A chemically cleaned blank Ni foil electrode showed negligible N_2 adsorption indicating that the areas measured relate to the particles only. The as-calculated surface areas are provided in Table 3.7, with the specific surface area increasing from 5.9 m^2 g^{-1} to 413 m^2 g^{-1} as the particle diameter decreases from 450 nm to 3 nm.

Table 3.7: Comparison of particle sizes measured by electron microscopy and specific surface areas for hydrothermal syntheses of nickel hydroxide nanoplates. Standard error in particle diameter was calculated using the method laid out in Section 2.2.8. Error in specific surface area is given as error in DFT analysis provided by Quantachrome software.

Sample	Average particle diameter / nm	Standard Error in Particle diameter / nm	Calculated Specific Surface Area / m^2 g^{-1}	Calculated error in specific surface area / m^2 g^{-1}
1	3	1	410	30
2	4	1	340	20
3	8	2	300	30
4	11	3	270	10
5	17	4	221	6
6	56	8	168	7
7	63	8	130	10
8	130	10	75	7
9	250	20	35	3
10	300	30	20	6
11	450	60	5.9	0.4

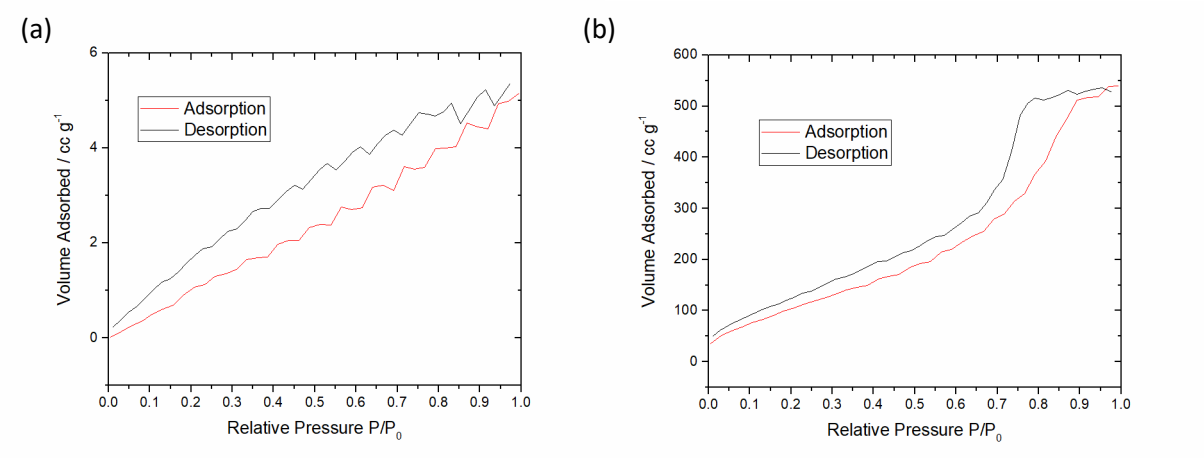


Figure 3.15 N_2 Adsorption/Desorption analysis of $Ni(OH)_2$ samples (a) 450 nm diameter particles (b) 3 nm diameter particles

The measured specific surface area can also be used to check consistency with the particle diameters calculated from electron microscopy. If spherical geometry is assumed, the relation between the volume and surface area of the sphere can be used to calculate an approximate density for a given surface area and diameter measurement. This is shown in Equation (3.6);

$$SA = n \times A_p = [m / (\rho(4/3\pi r^3)]*[4\pi r^2] = [(3m) / (\rho * r)] \quad (3.6)$$

where SA is the surface area measured, n is the number of particles in the sample, A_p is the surface area per particle, m is the mass of the sample measured, ρ is the density of the sample, r is the radius of the particle.

Taking sample mass as 1 g, the density is consistent over all particle sizes to within an order of magnitude. This suggest that both sets of experimental observations, made independently, are consistent with each other. This analysis assumes a spherical particle shape, which does not hold, especially at large particle diameters. It is, however, a good indication that no major errors have been made during particle sizing.

3.5 Electrochemical Characterisation of $Ni(OH)_2$ Nanoparticles

The aim of the electrochemical analysis in this experiment was to investigate the charging behaviour of the $Ni(OH)_2$ nanoparticles, and not to maximise the capacity of the materials. The electrochemical properties of the deposited $Ni(OH)_2$ nanoparticles were studied using CV and GCD techniques. Full details of the cell set up for electrochemical analysis can be found in Section 2.4.

3.5.1 Optimisation of Electrodes

To ensure a fair comparison of the capacity of the various particle sizes of $Ni(OH)_2$, it was important to standardise the preparation of the working electrodes. Unlike many works in the literature, no binders or conducting additive *e.g.* carbon black or PTFE were used during electrode preparation.[3, 32-33] This was to ensure there was no contribution from these elements to the capacity of the working electrode.

In many works, it has also become the standard to use Ni foam or another high surface area current collector to maximise the specific capacity/specific capacitance of deposited active materials.[10, 32-33] This was undesirable in this work however as the goal was to study the capacity of the $Ni(OH)_2$ alone. Ni foil was chosen as the current collector to simplify analysis and prevent further contribution to the charge storage. The nickel foil collector was found to have negligible capacitance and capacity, < 1 F g^{-1} / 0.1 mA h g^{-1}, see Figure 3.16.

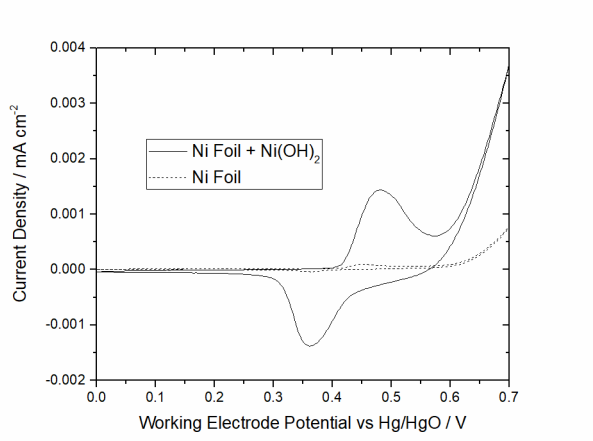


Figure 3.16 Comparison of Ni foil prior to deposition vs lowest capacity sample, sample 11, at a mass loading of 1 mg cm^{-2}. Both scans taken at 100 mV s^{-1}

Smaller particle sizes of $Ni(OH)_2$ were produced using high concentrations of the surfactant sodium citrate. This surfactant is a problem post synthesis as it forms a resistive layer and reduces the C_s of the sample. To prevent this layer from interfering in electrochemical

analysis, it was removed post synthesis using UV generated ozone. The ozone radicals react with organics, producing CO_2. XPS before and after ozonolysis showed no change in the Ni 2p spectrum, suggesting the $Ni(OH)_2$ is unaffected. The ozonolysis was performed for 15, 30, 60, and 120 minutes and the results were compared, see Figure 3.17a. It can be seen from the CV curve that there is no further improvement to the specific capacity in high surfactant samples after the ozonolysis has been allowed to run for 60 minutes. For comparison, samples produced using low surfactant concentrations were also treated, see Figure 3.17b. The specific capacitance was found not to increase to the same extent in these cases, with some samples giving lower specific capacity after long ozone exposure. Therefore, it was resolved to treat all samples produced using high surfactant synthesis methods for 60 minutes prior to

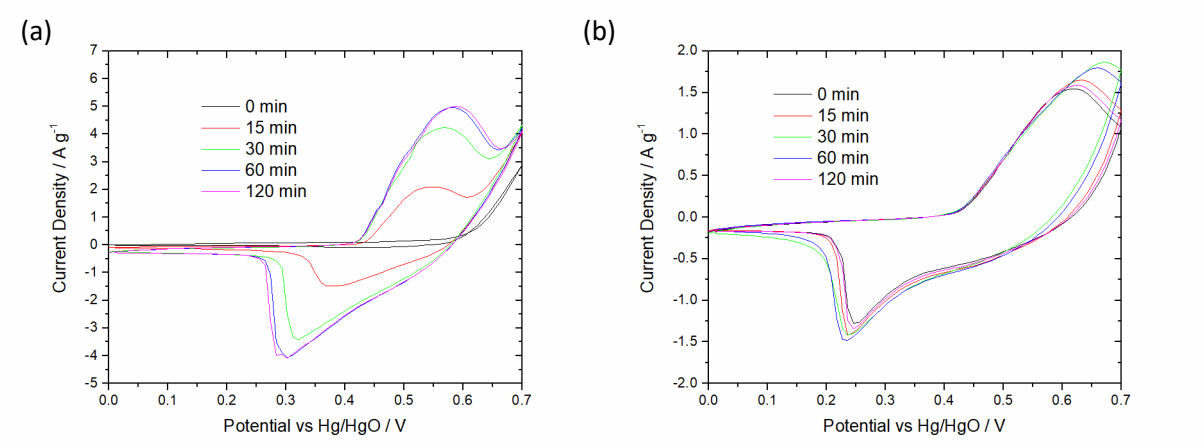


Figure 3.17 CV comparison of the effect of ozonolysis on $Ni(OH)_2$ nanoparticles. (a) Sample 2 - product of synthesis using high concentration of surfactant (b) Sample 8 -Product of synthesis using low concentration of surfactant. CV taken at a scan rate of 50 mV s^{-1}.

electrochemical analysis.

In addition to surfactant coatings on samples, another factor which must be controlled is the mass loading of the sample on the electrode surface. It is well documented that very low levels of mass loading are not representative of the capacity of the electroactive material.[34] A study of the specific capacity at various mass loadings was conducted to ensure that the results were representative of the true capacity of the sample. This can be seen in Figure 3.18. At low mass loadings, < 1 mg cm^{-2}, there is a large increase in specific capacity. It was therefore resolved that no electrochemical characterisation would be considered for samples with less than 1 mg cm^{-2} of active material on the electrode surface.

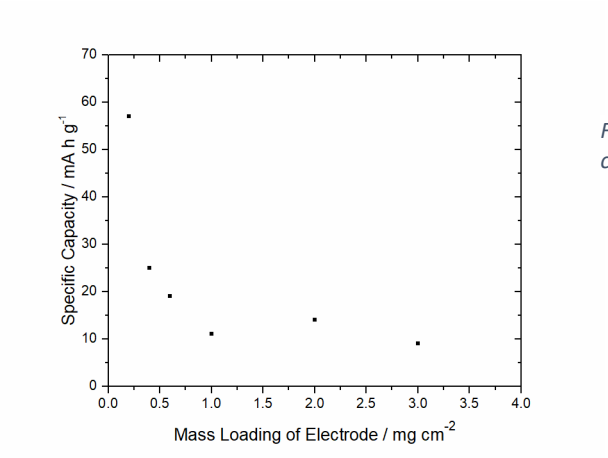


Figure 3.18 Effect of mass loading of sample 6 on specific capacity measured using CV at a scan rate of 10 mV s^{-1}.

3.5.2 Cyclic Voltammetry of $Ni(OH)_2$ Nanoparticles

Typical CV traces for three different particle sizes between 0.0 V and 0.7 V at various scan rates between 1 and 100 mV s^{-1} are shown in Figure 3.19-3.21. The potential window was determined to cover the expected redox peaks of Ni^{2+} and was limited by the stability of the electrolyte, in this case 1.0 mol dm^{-3} KOH.

The $Ni(OH)_2$ nanoparticles show strong peaks relating to the Faradaic oxidation/reduction of the $Ni(OH)_2$. The anodic and cathodic peak potentials are consistent with those published for the oxidation of the hydroxide and the reduction of the oxyhydroxide respectively.[1, 7, 9] These strong redox peaks are typical of a battery-type material.[12] The smaller particle CV shows broader redox peaks and a more rectangular shape, indicative of an increased contribution to charge storage from non-Faradaic electrical double layer capacitance. This effect is more prominent in the smaller particles and is often seen when nanosizing a battery material due to their increased surface area.[1, 5, 12]

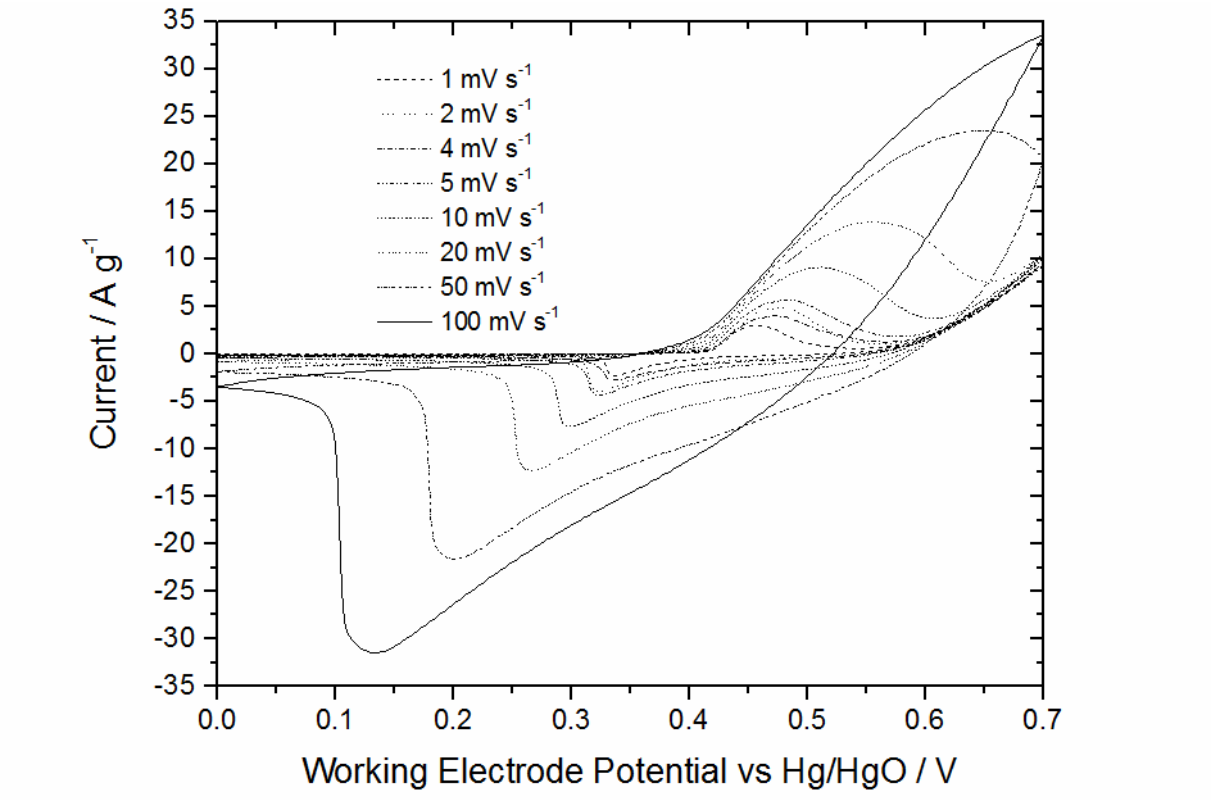


Figure 3.19 Cyclic Voltammogram of product of synthesis 1, 3 nm diameter $Ni(OH)_2$ nanoparticles at various scan rates. Full methodology for electrochemical analysis can be found in section 2.4.2.

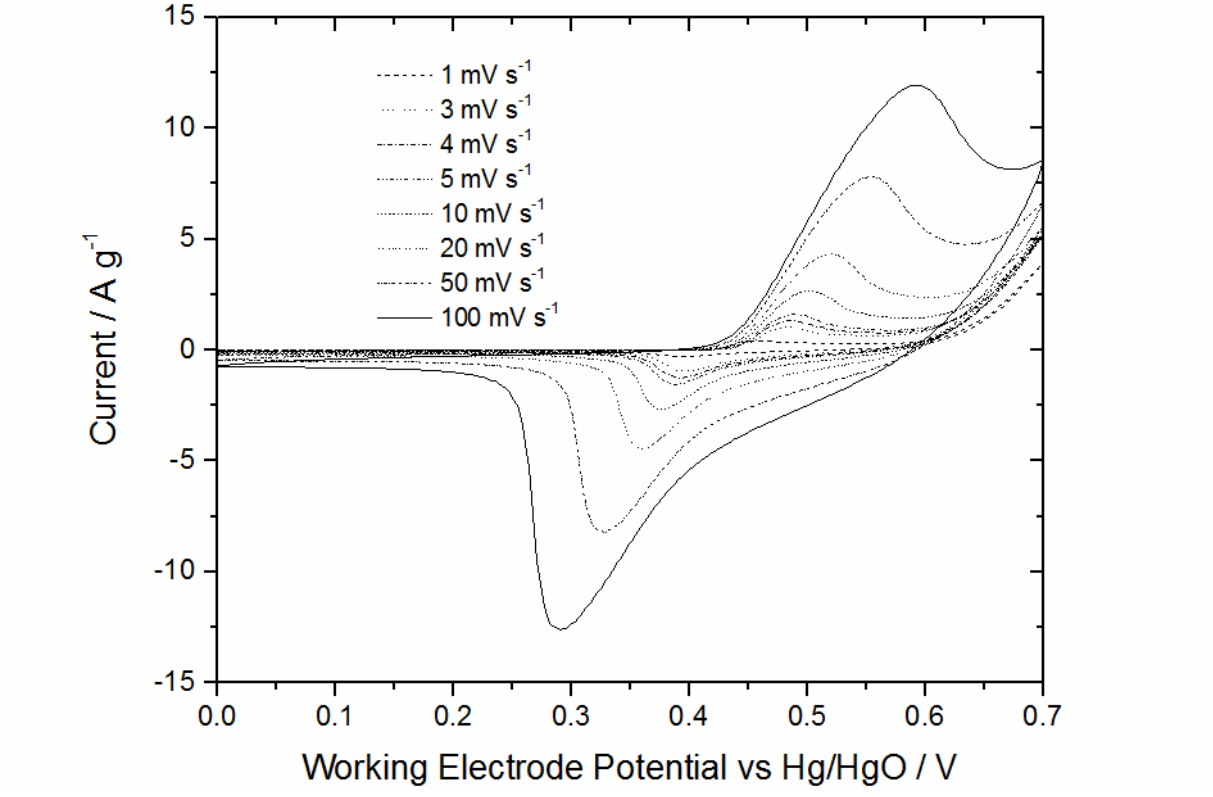


Figure 3.20 Cyclic Voltammogram of product of synthesis 6, 56 nm diameter $Ni(OH)_2$ nanoparticles at various scan rates. Full methodology for electrochemical analysis can be found in section 2.4.2.

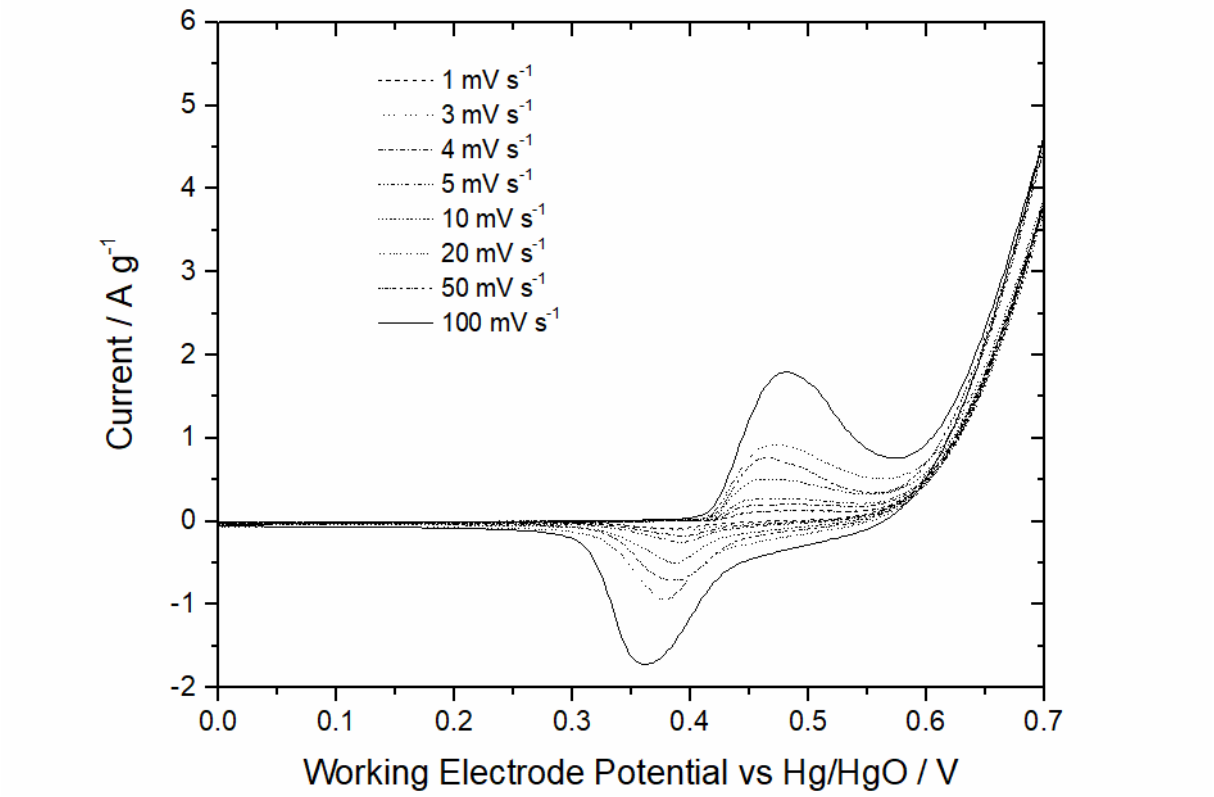


Figure 3.21 Cyclic Voltammogram of product of synthesis 11, 300 nm diameter $Ni(OH)_2$ nanoparticles at various scan rates. Full methodology for electrochemical analysis can be found in section 2.4.2.

The peak currents for oxidation and reduction are linear with the square root of the scan rate as shown in the Randles-Sevcik plots, Figure 3.22. This is expected for a material in which the electron transfer process is fast, and current is diffusion limited, again typical of a battery electrode.[12] It is worth noting that there is some deviation from this behaviour at low scan rates, as seen in Figure 3.22a and 3.22c.

It was noted that the separation of the peaks increases with increasing scan rate, suggesting the redox process is only quasi-reversible.[35] The peak current ratio of the anodic:cathodic currents also increases with scan rate. This suggests that at low scan rates, a portion of the oxidised material does not reduce back to $Ni(OH)_2$. Faster scan rates mean that less of the bulk material has time to react, and a more reversible system is seen. This effect is observed for all particle sizes.

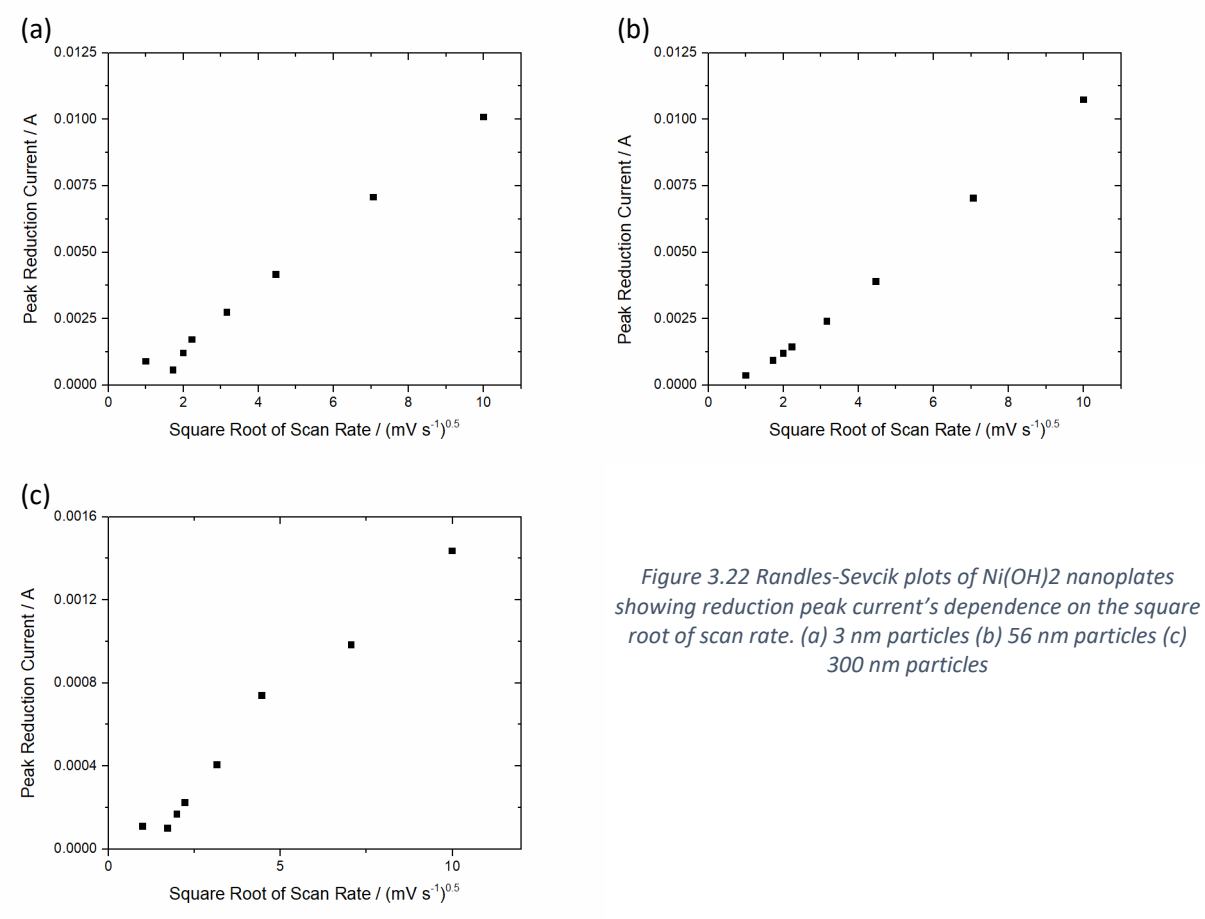


Figure 3.22 Randles-Sevcik plots of Ni(OH)2 nanoplates showing reduction peak current's dependence on the square root of scan rate. (a) 3 nm particles (b) 56 nm particles (c) 300 nm particles

3.5.3 Galvanostatic Charge/Discharge of $Ni(OH)_2$ Nanoparticles

The charging of the $Ni(OH)_2$ nanoparticles at various current densities is shown in Figure 3.23a. Even at relatively low current densities, the charging of the $Ni(OH)_2$ nanoparticles is rapid compared to charging rates expected for batteries. Comparative charging profiles for micro (300 nm) and nano-sized (3 nm) $Ni(OH)_2$ at 2 A g^{-1} are shown in Figure 3.23b.

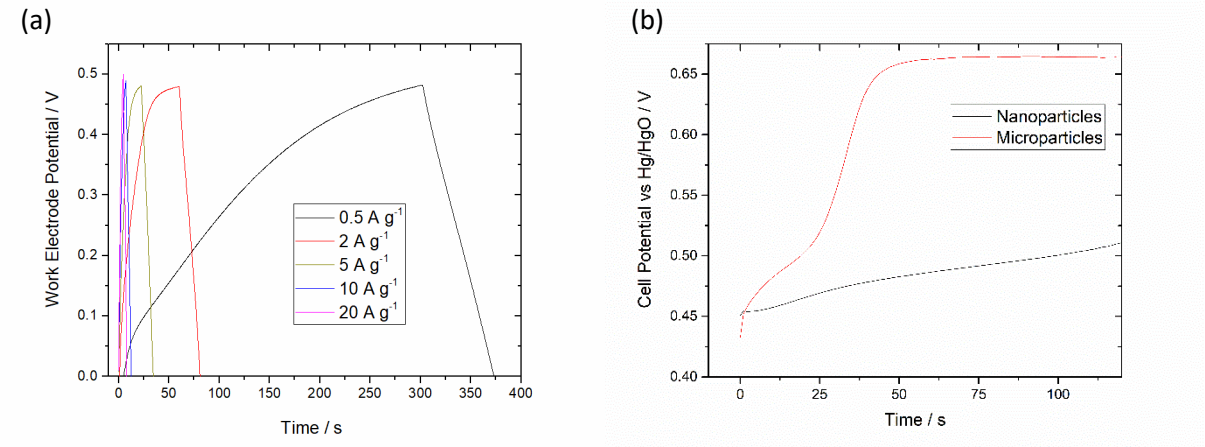


Figure 3.23 Galvanostatic charging of $Ni(OH)_2$ nanoparticles (a) sample 3 at various current densities (b) comparison of charging behaviour for extreme particle sizes, sample 1 and sample 10.

The nanoparticle coated electrodes showed constant potential increase during charging over the redox window, 0.45-0.50 V. In contrast the microparticle coated electrodes showed a reduction in gradient with respect to potential in this range, before the potential rapidly began to increase. The nano-sized particles appeared to give a lower charging potential, although this was due to the charging not going to completion on the same time scale as the microparticles. The increased amount of electroactive material and capacity in the nanoparticles compared to the microparticles was consistent with CV measurements.

3.6 Specific Capacity and Capacitance of $Ni(OH)_2$ Nanoparticles

The calculations for specific capacitance, Cap_s in F g^{-1} and the specific capacity, C_s in mA h g^{-1}, of the $Ni(OH)_2$ nanoparticles are discussed in Section 2.4.5 using Equations (2.4) and (2.5). [36-37]

For every particle size, the calculated value of C_s decreases with increasing scan rate, see Figure 3.24. This is indicative of limited charging of the electrode at fast scan rates. The dependence of C_s on scan rate is less pronounced for 3 nm diameter particles than the 300 nm diameter particles, particularly up to scan rates of 50 mV s^{-1}.

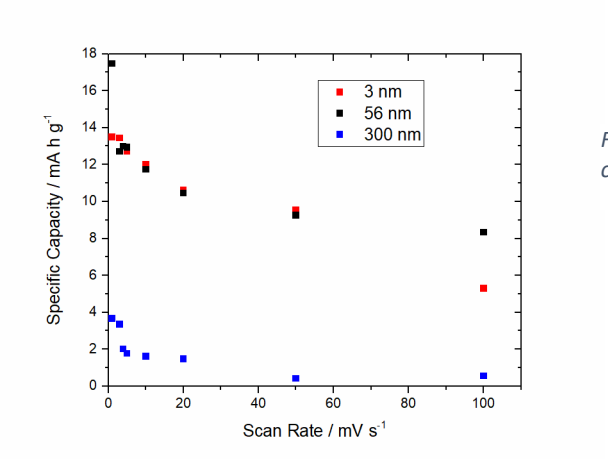


Figure 3.24 Comparing the effect of scan rate on specific capacitance on particles of various diameters.

Even at a scan rate of 1 mV s^{-1}, the specific capacity of the 300 nm sized particles is much lower than the 3 nm particles, suggesting there is a large amount of the material not able to react. The values of C_s determined at a scan rate of 10 mV s^{-1} varies with particle size, Figure 3.25.

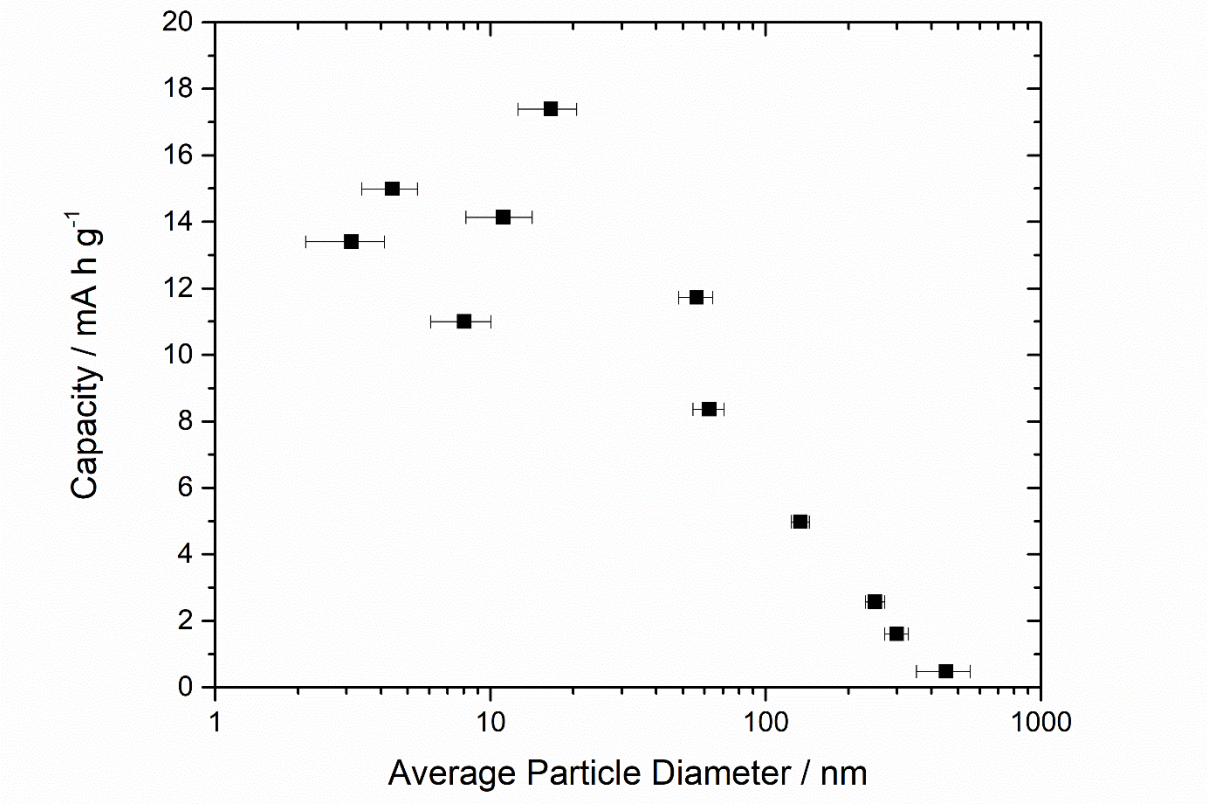


Figure 3.25 Variation of specific capacity, as calculated from CV data at 10 mV s^{-1}, with particle diameter. Calculation of particle size from SEM data and error calculation can be found in section 2.2.1.

All particles synthesised in the presence of high concentrations of surfactant initially showed very low values of C_s. Ozonolysis of electrodes modified with $Ni(OH)_2$ particles prepared in the presence of high concentrations of surfactant results in the removal of surfactant, as evidenced by the previously mentioned TEM and an increase in the measured value of C_s, see Figure 3.26.

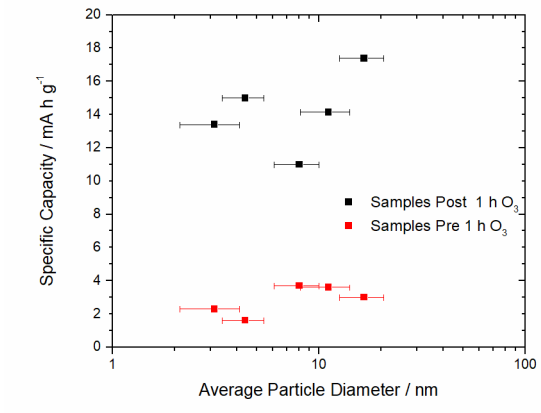


Figure 3.26 Variation in specific capacity after 1 hours of UV generated ozone treatment

Comparing surfactant free electrodes, C_s increases with decreasing particle size in the range 450 nm to 20 nm, consistent with a higher maximum surface area per gram and a psuedocapacitive charge storage mechanism. If the entirety of the particle was redox active, a constant specific capacity across all particle sizes would be expected.

For particles smaller than 20 nm diameter, C_s no longer increases with decreasing particle size. It can be argued that either the C_s remains constant below this diameter, or it decreases from a maximum around 20 nm. The reasons for this are unclear, but several alternative theories have been considered.

The maximum in C_s at 20 nm suggests the Debye length for charging of $Ni(OH)_2$ is *ca.* 10 nm. This would mean that as the particle diameter decreases from micron size, this charged 10 nm layer would act as a pseudo-surface reaction, explaining the change in C_s at diameters 450 nm to 20 nm. This charging "skin" mechanism is illustrated in Figure 3.27.

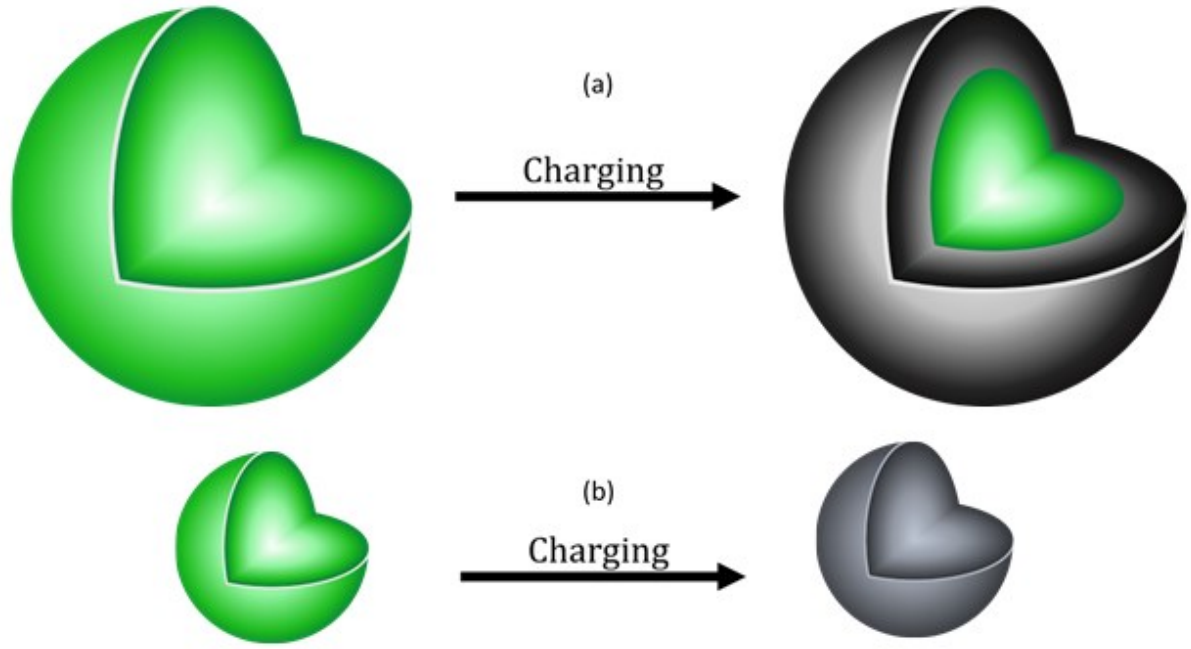


Figure 3.27 Proposed schematic of nickel hydroxide nanoparticle charging, showing electrochemically active material in black and inactive/unreacted material in green. (a) Large particles with diameter >20 nm and (b) Nanoparticles with diameter 20 nm or below.

Below 20 nm, this 10 nm charged layer may begin to interact and repel. This could explain the reduction in C_s below 20 nm diameter. Even if the charged layer does not interact with the charged layer from the opposite side of the particle, the particle is still fully charged so there can be no further increase in C_s through this model. This agrees well with what has been observed here.

A reduction of charge stored below this critical radius could also be due to increased resistance of sample due to unreacted surfactant or an increase in the contact resistance between more particles per unit volume.

Since there is still ongoing debate as to the pseudocapacitive or battery-like nature of $Ni(OH)_2$ charging, both models have been studied. The variation of Cap_s with particle diameter is shown in Figure 3.28. A similar peak is observed in Cap_s compared to the C_s, at a particle diameter of 20 nm.

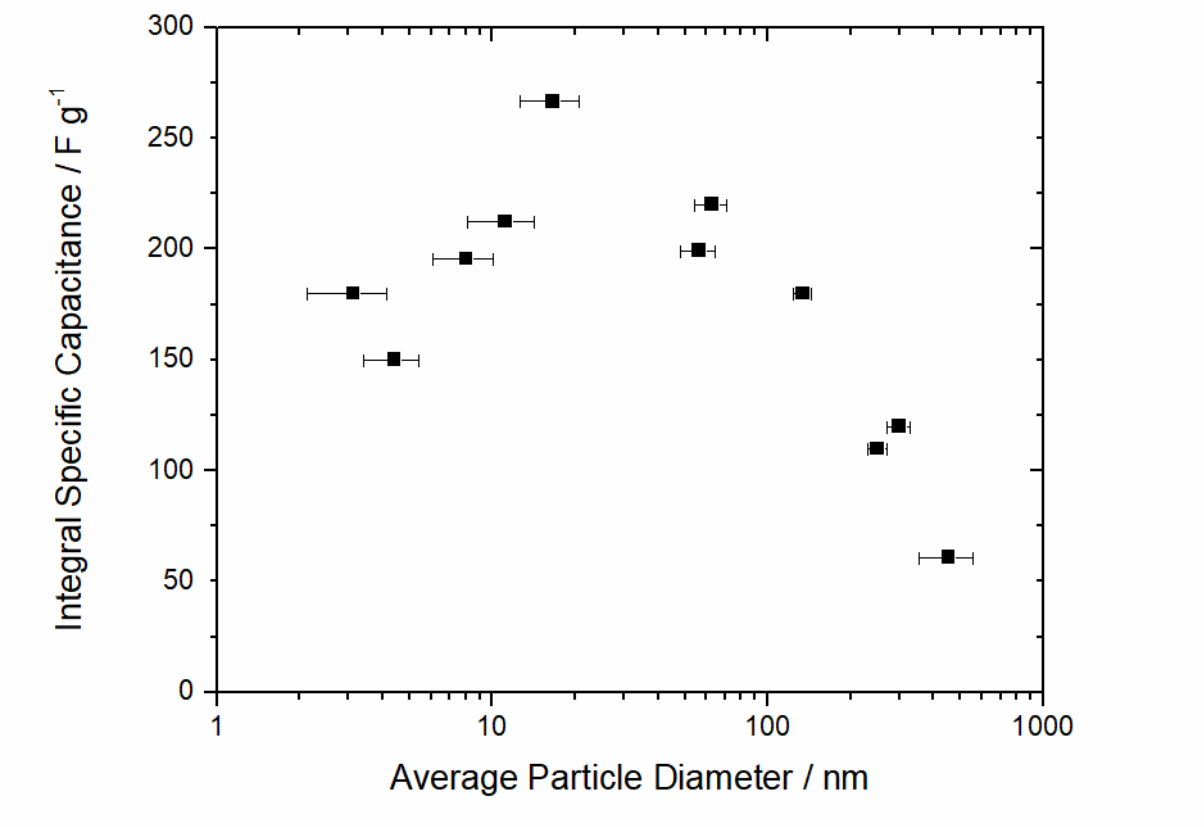


Figure 3.28 Variation of specific capacitance, as calculated from CV data at 10 mV s^{-1}, with particle diameter. Calculation of particle size from SEM data and error calculation can be found in section 2.2.1.

3.7 Capacity Per Unit Area of $Ni(OH)_2$ Nanoparticles

Capacity per unit area, C_A, as measured by N_2 adsorption and DFT analysis, is plotted in Figure 3.29. C_A varies with particle size, an observation that is *inconsistent* with purely pseudocapacitor type charging that is entirely a surface process. At large particle diameters from 450 nm down to 20 nm, the C_A is constant. Once the particle diameter falls below 20 nm, there is a sharp decrease in the C_A which continues down to 3 nm diameter particles. This is consistent with the observations of the C_s.

While the particle diameter is much larger than the charging layer, reducing the particle size results in more active material per gram of $Ni(OH)_2$. Reducing particle size also results in a higher *specific* surface area, as shown in Table 3.7. The net effect is a constant C_A. Once the critical diameter of 20 nm is reached however, whilst the specific surface area continues to increase, the active surface volume (surface area x charging layer depth) no longer increases resulting in a decrease in the value of C_A for particles of diameter less than 20 nm.

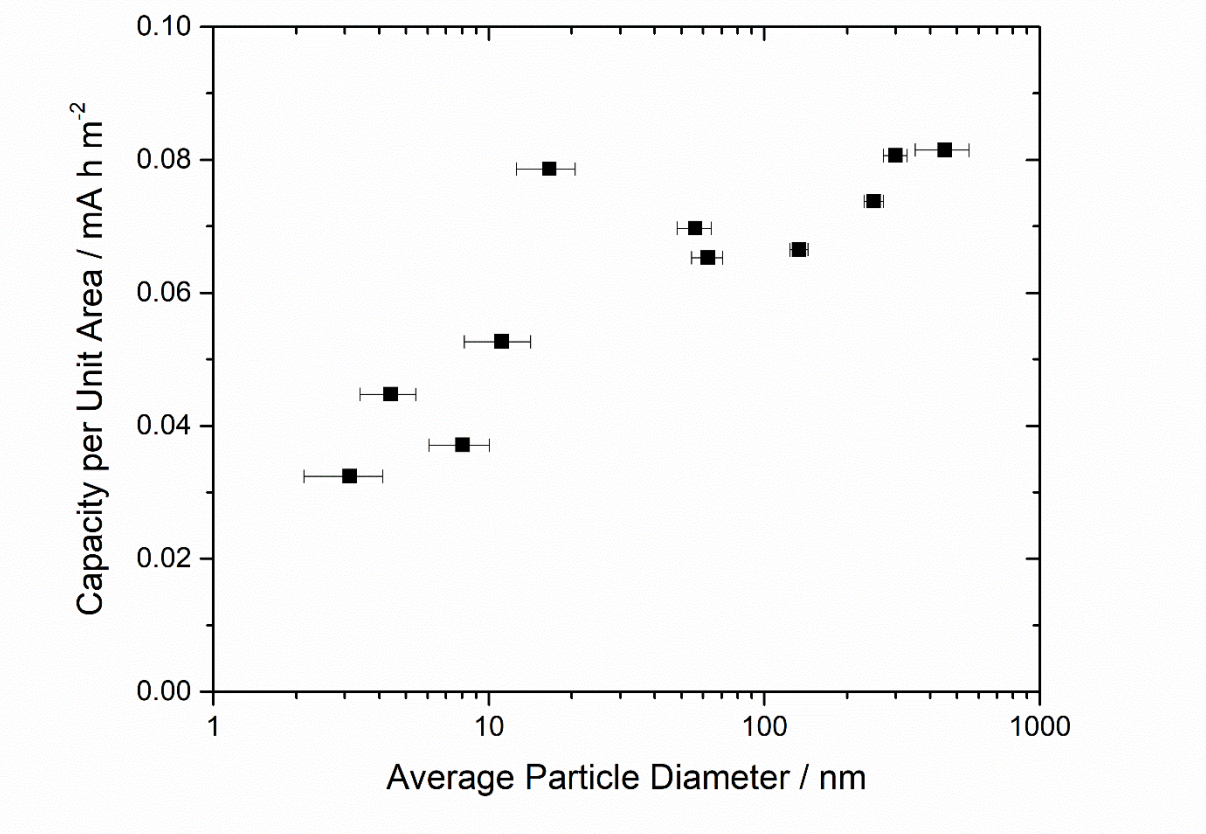


Figure 3.29 Variation of capacity per unit area, as calculated from CV data at 10 mV s^{-1}, with particle diameter. Calculation of particle size from SEM data and error calculation can be found in section 2.2.1.

As already discussed, while this is a working theory, there are alternative explanations for the behaviour observed. Electron microscopy indicates that the as-prepared $Ni(OH)_2$ has a platelet morphology, whilst in the XRD plots the (001) peak dominates, suggesting some texturing. In discussing the change in C_A with particle size, isotropic crystal growth has been assumed. In the case of anisotropic growth, C_A will increase with particle size if a more active charge storage crystal face dominates and decrease with particle size if the main crystal face suppresses charge storage.

The observation that an increase in C_A with particle size is only seen for particles up to 20 nm in diameter, however, suggests texturing does not have a significant influence on the charge stored per unit surface area. Further work, such as detailed textural analysis and density functional theory calculations on charge storage at the different crystal faces of $Ni(OH)_2$ are required to fully resolve the potential issue of anisotropy, discussed in Chapter 6.

An alternate explanation of the fall in C_A when particles are less than 20 nm is due to a change in porosity with particle size, leading to inaccessibility of the electrolyte. It has been reported that the size of pores in a material structure has a large effect on the capacity or capacitance of that system.[37] As the particle size decreases, the average pore size was also found to decrease. These nanosized pores in the electrode material may become inaccessible to electrolyte anions due to a large solvation shell. DFT analysis was found to be unreliable in measuring the pore sizes in these materials, so no numerical analysis of the variation of specific capacity with pore size was done in this work.

3.8 Conclusions

To study the charging behaviour of a model extrinsic psuedocapacitive system at different length scales, $Ni(OH)_2$ nanoplates ranging from 3 – 450 nm in diameter were synthesised. Several synthesis methods were trialled; most were rejected due to failings in reproducibility, unusable morphology or yield. Eventually, hydrothermal methods were chosen as the syntheses of choice, using temperature, reducing agents and sodium citrate surfactants to produce a wide size range of particles. Ozonolysis was used to remove surfactant from particles produced by syntheses using a high concentration of surfactant to allow a fair comparison between methods.

The chemical composition of the materials was characterised using EDX and XPS. The phase of the $Ni(OH)_2$ particles was studied using XRD, while the morphology was characterised using SEM/TEM. Particle sizing initially proved difficult, with methods using SEM/TEM, XRD, and DLS all being trialled. Eventually, SEM/TEM was found to be the most reliable method for particle sizing, with SAXS confirming particle sizes for particles in the < 50 nm size range.

Electrochemical characterisation of the $Ni(OH)_2$ nanoparticles on a Ni foil electrode was by CV and GCD. The traces showed the expected behaviour for $Ni(OH)_2$, corroborating the material structural characterisation.

The Cap_s and C_s of the particles were found to increase with decreasing particle size until a critical diameter of around 20 nm, at which C_s was approximately 20 mA h g^{-1} and Cap_s was around 250 F g^{-1}. Further decreases in particle size resulted in reduction in Cap_s and C_s. C_A was found to stay constant with decreasing particle diameter until a diameter of 20 nm was achieved, after which point the C_A also decreased with particle size. This phenomenon can be attributed to a surface charging layer within the $Ni(OH)_2$ of around 10 nm in depth, as shown in Figure 3.27. Alternate explanations for the fall in C_s / C_A when particle diameter is less than 20 nm have been offered, but further experiments are required to unambiguously establish the depth of the charging layer at the $Ni(OH)_2$ surface. Direct observation of charging layers require a depth sensitive technique which can identify different chemical species, such as XPS or ToF-SIMS.

3.9 References

1. Kiani, M. A.; Mousavi, M. F.; Ghasemi, S., Size effect investigation on battery performance: Comparison between micro- and nano-particles of β-Ni(OH)2 as nickel battery cathode material. *Journal of Power Sources* **2010,** *195* (17), 5794-5800.
2. Augustyn, V.; Simon, P.; Dunn, B., Pseudocapacitive oxide materials for high-rate electrochemical energy storage. *Energy & Environmental Science* **2014,** *7* (5), 1597-1614.
3. Li, Z.; Han, J.; Fan, L.; Guo, R., In-situ controllable growth of α-Ni(OH)2 with different morphologies on reduced graphene oxide sheets and capacitive performance for supercapacitors. *Colloid and Polymer Science* **2016,** *294* (4), 681-689.
4. Xiao, H.; Qu, F.; Wu, X., Ultrathin NiO nanoflakes electrode materials for supercapacitors. *Applied Surface Science* **2016,** *360, Part A*, 8-13.
5. Wang, R.; Lang, J.; Liu, Y.; Lin, Z.; Yan, X., Ultra-small, size-controlled Ni(OH)2 nanoparticles: elucidating the relationship between particle size and electrochemical performance for advanced energy storage devices. *NPG Asia Mater* **2015,** *7*, e183.
6. Zhang, J.; Liu, H.; Shi, P.; Li, Y.; Huang, L.; Mai, W.; Tan, S.; Cai, X., Growth of nickel (111) plane: The key role in nickel for further improving the electrochemical property of hexagonal nickel hydroxide-nickel & reduced graphene oxide composite. *Journal of Power Sources* **2014,** *267*, 356-365.
7. Li, H. B.; Yu, M. H.; Wang, F. X.; Liu, P.; Liang, Y.; Xiao, J.; Wang, C. X.; Tong, Y. X.; Yang, G. W., Amorphous nickel hydroxide nanospheres with ultrahigh capacitance and energy density as electrochemical pseudocapacitor materials. *Nature Communications* **2013,** *4*, 1894.
8. Brousse, T.; Bélanger, D.; Long, J. W., To Be or Not To Be Pseudocapacitive? *Journal of The Electrochemical Society* **2015,** *162* (5), A5185-A5189.
9. Oliva, P.; Leonardi, J.; Laurent, J. F.; Delmas, C.; Braconnier, J. J.; Figlarz, M.; Fievet, F.; Guibert, A. d., Review of the structure and the electrochemistry of nickel hydroxides and oxy-hydroxides. *Journal of Power Sources* **1982,** *8* (2), 229-255.
10. Lu, Z.; Chang, Z.; Zhu, W.; Sun, X., Beta-phased Ni(OH)2 nanowall film with reversible capacitance higher than theoretical Faradic capacitance. *Chemical Communications* **2011,** *47* (34), 9651-9653.
11. Zhu, Y.; Cao, C.; Tao, S.; Chu, W.; Wu, Z.; Li, Y., Ultrathin Nickel Hydroxide and Oxide Nanosheets: Synthesis, Characterizations and Excellent Supercapacitor Performances. *Scientific Reports* **2014,** *4*, 5787.

12. Gogotsi, Y.; Penner, R. M., Energy Storage in Nanomaterials – Capacitive, Pseudocapacitive, or Battery-like? *ACS Nano* **2018,** *12* (3), 2081-2083.
13. Cabanas-Polo, S.; Suslick, K. S.; Sanchez-Herencia, A. J., Effect of reaction conditions on size and morphology of ultrasonically prepared Ni(OH)2 powders. *Ultrasonics Sonochemistry* **2011,** *18* (4), 901-906.
14. Cheng, J.; Cao, G.-P.; Yang, Y.-S., Characterization of sol–gel-derived NiOx xerogels as supercapacitors. *Journal of Power Sources* **2006,** *159* (1), 734-741.
15. Xing, S.; Wang, Q.; Ma, Z.; Wu, Y.; Gao, Y., Controlled synthesis of mesoporous β-Ni(OH)2 and NiO nanospheres with enhanced electrochemical performance. *Materials Research Bulletin* **2012,** *47* (9), 2120-2125.
16. Guan, X. Y.; Deng, J. C., Preparation and electrochemical performance of nano-scale nickel hydroxide with different shapes. *Materials Letters* **2007,** *61*, 621-625.
17. Coudun, C.; Grillon, F.; Hochepied, J.-F., Surfactant effects on pH-controlled synthesis of nickel hydroxides. *Colloids and Surfaces A: Physicochemical and Engineering Aspects* **2006,** *280* (1–3), 23-31.
18. Song, Q.; Tang, Z.; Guo, H.; Chan, S. L. I., Structural characteristics of nickel hydroxide synthesized by a chemical precipitation route under different pH values. *Journal of Power Sources* **2002,** *112* (2), 428-434.
19. Sun, D.; Zhang, J.; Ren, H.; Cui, Z.; Sun, D., Influence of OH− and SO42− Anions on Morphologies of the Nanosized Nickel Hydroxide. *The Journal of Physical Chemistry C* **2010,** *114* (28), 12110-12116.
20. Rajamathi, M.; N. Subbanna, G.; Vishnu Kamath, P., On the existence of a nickel hydroxide phase which is neither alpha nor beta. *Journal of Materials Chemistry* **1997,** *7* (11), 2293-2296.
21. Soler-Illia, G. J. d. A. A.; Jobbágy, M.; Regazzoni, A. E.; Blesa, M. A., Synthesis of Nickel Hydroxide by Homogeneous Alkalinization. Precipitation Mechanism. *Chemistry of Materials* **1999,** *11* (11), 3140-3146.
22. Vidotti, M.; Salvador, R. P.; de Torresi, S. I. C., Synthesis and characterization of stable Co and Cd doped nickel hydroxide nanoparticles for electrochemical applications. *Ultrasonics Sonochemistry* **2009,** *16* (1), 35-40.
23. Meyer, M.; Bee, A.; Talbot, D.; Cabuil, V.; Boyer, J. M.; Repetti, B.; Garrigos, R., Synthesis and dispersion of Ni(OH)2 platelet-like nanoparticles in water. *Journal of Colloid and Interface Science* **2004,** *277*, 309-315.
24. Wu, Z.; Xu, C.; Chen, H.; Yu, H.; Wu, Y.; Gao, F., α-Nickel hydroxide 3D hierarchical architectures: Controlled synthesis and their applications on electrochemical determination of H2O2. *Materials Research Bulletin* **2013,** *48* (6), 2340-2346.
25. Wu, M.; Gao, J.; Zhang, S.; Chen, A., Synthesis and characterization of aerogel-like mesoporous nickel oxide for electrochemical supercapacitors. *Journal of Porous Materials* **2006,** *13* (3), 407-412.
26. Kunjara Na Ayudhya, S.; Tonto, P.; Mekasuwandumrong, O.; Pavarajarn, V.; Praserthdam, P., Solvothermal Synthesis of ZnO with Various Aspect Ratios Using Organic Solvents. *Crystal Growth & Design* **2006,** *6* (11), 2446-2450.
27. Zare, M.; Namratha, K.; Byrappa, K.; Surendra, D. M.; Yallappa, S.; Hungund, B., Surfactant assisted solvothermal synthesis of ZnO nanoparticles and study of their antimicrobial and antioxidant properties. *Journal of Materials Science & Technology* **2018,** *34* (6), 1035-1043.
28. Liang, J.; Dong, B.; Ding, S.; Li, C.; Li, B. Q.; Li, J.; Yang, G., Facile construction of ultrathin standing α-Ni(OH)2 nanosheets on halloysite nanotubes and their enhanced electrochemical capacitance. *Journal of Materials Chemistry A* **2014,** *2* (29), 11299-11304.
29. McEwen, R. S., Crystallographic studies on nickel hydroxide and the higher nickel oxides. *The Journal of Physical Chemistry* **1971,** *75* (12), 1782-1789.
30. Bernard, M. C.; Bernard, P.; Keddam, M.; Senyarich, S.; Takenouti, H., Characterisation of new nickel hydroxides during the transformation of α Ni(OH)2 to β Ni(OH)2 by ageing. *Electrochimica Acta* **1996,** *41* (1), 91-93.
31. Li, C.; Liu, S., Preparation and Characterization of Ni(OH)2 and NiO Mesoporous Nanosheets. *Journal of Nanomaterials* **2012,** *2012*, 6.

32. Ortiz, M. G.; Castro, E. B.; Real, S. G., Electrochemical performance comparison of MWCNTs/Ni (OH)2 composite materials by two preparation routes. *Journal of Solid State Electrochemistry* **2017**, 1-9.
33. Aghazadeh, M.; Ghaemi, M.; Sabour, B.; Dalvand, S., Electrochemical preparation of α-Ni(OH)2 ultrafine nanoparticles for high-performance supercapacitors. *Journal of Solid State Electrochemistry* **2014,** *18*, 1569 –1584.
34. Brisse, A.-L.; Stevens, P.; Toussaint, G.; Crosnier, O.; Brousse, T., Ni(OH)2 and NiO Based Composites: Battery Type Electrode Materials for Hybrid Supercapacitor Devices. *Materials* **2018,** *11* (7), 1178.
35. Bard, A. J.; Faulkner, L. R., *Electrochemical Methods: Fundamentals and Applications*. Wiley: 2000.
36. Conway, B. E., *Electrochemical Supercapacitors: Scientific Fundamentals and Technological Applications*. Springer US: 1999.
37. Simon, P.; Gogotsi, Y., Materials for electrochemical capacitors. *Nat Mater* **2008,** *7* (11), 845-854.

Chapter 4 – ToF-SIMS Depth Profiling of Nickel Hydroxide

Following on from the results obtained in Chapter 3, this chapter is concerned with further analysis of the charging depth electrochemically identified in nanosized $Ni(OH)_2$. This chapter presents another method of analysing this charging surface layer, using time of flight secondary ion mass spectrometry. Since the $Ni(OH)_2$ exchanges protons with the electrolyte on charging and discharging in alkaline media, deuterated solvents were used to load the charging layer with deuterium, which could then be analysed using a depth profile. For this method to be effective, the $Ni(OH)_2$ must be of a sufficient density that the deuterated solvent can not diffuse into the bulk of the deposited material. Electrodeposition was chosen as the synthesis method due to the speed of the synthesis. Varying multiple parameters also gave easy control of film thickness and density. Despite improvements in the film density, however, it was clear that the material was too porous. Conditions could not be found which allowed a dense enough layer to prevent electrolyte ingress to be deposited. An alternative method was then used to block the porosity, using a wax layer. Low melting point paraffin wax was used to fill all pores in the material, preventing electrolyte ingress. The surface was then ground down to allow electrolyte access to the top face of the electrodeposited $Ni(OH)_2$ only. Time of flight secondary ion mass spectrometry after potential cycling in deuterated aqueous alkaline electrolyte was performed on the samples before and after the wax deposition. It was found that despite an expected substantial deuterium background signal from the wax, a noticeable increase in deuterium was observed after cycling. This increase was proportional to the theoretical 50% exchange per cycle, suggesting the experiment was successful. Measuring the sputter crater depth using AFM allowed the decay with depth to be measured. It was found that the increase in deuterium only occurred over the first 20-30 nm, which agreed well with observations of a charging surface “skin” from Chapter 3.

4.1 Introduction

As already discussed in Chapter 3, a deeper understanding of the mechanisms of energy storage in devices is required to further improve the performance of charge storage devices. Renewable energy sources, which do not continuously produce power, rely on charge storage devices to hold excess energy when supply is high and provide energy when demand is high. Traditional batteries are currently fulfilling this role. Material toxicity, low power densities

and short cycling lifetimes mean that current battery technology is limited.[1-2] Supercapacitors are a potential replacement for traditional batteries, with better cyclability and power densities. The specific energy of EC devices must be improved however to bridge the gap between intercalation batteries and EC devices, as discussed in Section 1.3.[3]

Increasing the specific energy and power of charge storage devices has led to the development of porous high surface area nanostructured electrode materials.[4] The largest specific capacities/capacitances have used redox active materials such as electroactive polymers[5] and metal oxides/nitrides.[2, 5-6]

In Chapter 3, the charging behaviour of nanostructured nickel hydroxide was examined at various particle diameters. The results suggested that a charging "skin" of around 10 nm existed. This was in contradiction to the traditional view of the material, as an intercalation battery material. While the intercalation battery and the pseudocapacitor both store energy via redox processes, the defining feature of the pseudocapacitor is the site of the redox active process. Typically, the redox active process in a pseudocapacitor is at the surface of the material only, compared to a bulk redox reaction in a battery.[1, 7]

While the charging process in supercapacitor materials such as ruthenium oxide has been confirmed to be a surface only process, conflicting evidence exists for other redox active materials such as $Ni(OH)_2$.[8] The development of high surface area porous structures to maximise capacity has made this charging "skin" hard to study. Highly porous and open structures will yield results similar to an active bulk.

It is necessary to clarify whether the entire structure is participating in the redox behaviour due to electrolyte diffusion into the pores, or if the ion exchange into the bulk occurs through the charge storage material. While the methodology in the previous chapter did allow the charging behaviour to be studied, optimising the synthesis for a wide range of particle sizes was time consuming and difficult. A more direct and easier to apply method would make quantifying the charging depths of other redox active materials a less laborious task. A direct method would also allow for a more accurate determination of charging depth.

In a different approach to the one taken in the previous chapter, the redox behaviour of the $Ni(OH)_2$ was used to study charging depth, rather than the electrochemical response. On

charging, the nickel hydroxide oxidises to the oxyhydroxide form, as shown in Equation (4.1);[9-10]

$$Ni(OH)_2 + OH^- \rightarrow NiOOH + H_2O + e^- \quad (4.1)$$

The exchange of H^+ between the $Ni(OH)_2$ with the OH^- electrolyte has been used to determine which part of the material is charging. By charging then discharging electrodeposited $Ni(OH)_2$ in deuterated electrolyte, Ni(OH)(OD) and $Ni(OD)_2$ can be introduced into the electrode structure.

The deuterium ion uptake and distribution has been analysed using time of flight secondary ion mass spectrometry (ToF-SIMS). ToF-SIMS allows for resolution of trace elements on the order of ppm to ppb. Unlike other surface sensitive techniques, such as XPS which requires an electronic transition, ToF-SIMS can detect hydrogen and deuterium ions which is key for this work.[11]

Analysing a charge storage material using ToF-SIMS can be difficult due to charge build up, and these problems were addressed as the work progressed. The ingress of OD^- into the material has been studied with respect to sputter time. AFM analysis of the sputter crater at various sputter times was used to convert sputter time to sputter depth. Measuring the decay time of the D^- signal in the depth profile will allow the depth of charging to be identified. To confirm that the deuterium uptake is dependent on the electrochemical cycling, the effect of multiple cycles and the self-exchange of deuterium has also been studied.

Prior to charging and analysis by ToF-SIMS, first a non-porous $Ni(OH)_2$ layer was required. As already discussed, a highly porous structure will allow electrolyte to diffuse into the entirety of the structure, making it impossible to study a single charging layer. Since all the structures created by the deposition of nanoparticles in Chapter 3 were unsuitable in this respect, electrodeposition based synthesis techniques were investigated. As well as being fast and easy to repeat, the porosity of electrodeposited layers has been shown to be controllable.

4.2 Electrochemical Deposition Rational

Rather than precipitate the nickel hydroxide material in solution and then deposit onto an electrode surface, the material can be formed on the surface directly through electrodeposition.[12-14] The electrode is placed into a nickel salt solution and then held at a

constant potential. For a negative potential, a cathodic current reduces water to form hydroxide ions. Reduction of nickel salt counter ions will also contribute to hydroxide production.[12]

In the case of the synthesis used, the cathodic deposition reaction proceeded *via* the reduction of the nitrate ion to ammonia, see Equation (4.2).[12]

$$NO_3^- + 6H_2O + 8e^- \rightarrow NH_3 + 9OH^- \quad (4.2)$$

This high local concentration of hydroxide ions reacts with the aqueous Ni^{2+} to form the insoluble $Ni(OH)_2$ which will precipitate on the electrode surface, shown in Equation (4.3). This step is the same as seen in the wet chemical/hydrothermal syntheses, with the exception of taking place on a solid surface.

$$Ni^{2+} + 2OH^- \rightarrow Ni(OH)_{2(s)} \quad (4.3)$$

Thin layers of α- or β-$Ni(OH)_2$ have been shown to form using anodic[15-16] or cathodic[14] potentiostatic deposition. Layer thickness can be easily tuned by altering the deposition time. The phase has been shown to be potential and temperature dependant. Larger potentials, causing higher current densities, produce mixed phases, whereas low current densities result in purely α phase materials.[17] As was seen with the nanoparticles, higher temperatures favour the β phase.[14] Increasing the temperature has also been shown to increase porosity of the layers, giving a much higher specific capacitance of around 3000 F g^{-1} when deposited onto nickel foam support.[14] Porosity can also be increased by reducing the deposition potential, with the film morphology changing from a densely packed particle-like array to a porous flaky structure.[16]

The Faradaic efficiency of nickel hydroxide deposition at low concentrations of Ni^{2+} is around 100%.[12] At higher concentrations however (> 0.2 mol dm^{-3}) this efficiency decreases. This is due to the formation of solution stable species such as $NiOH^+$ which can diffuse away from the electrode surface without reacting.[12]

4.3 Determination of Reaction Parameters

Since the products of electrodeposition have been shown to be greatly affected by the synthesis conditions, it was important to tune the process to create the highest density film

possible. Alternative thin film deposition methods, such as chemical vapour deposition, were considered, however, a simple method to produce a hydrated $Ni(OH)_2$ was not found.

4.3.1 Selection of Starting Conditions

Initial electrodeposition synthesis procedures were based on the work of Wang *et al*.[14] In the most of the literature, increasing the porosity of the deposited $Ni(OH)_2$ is *desired* to achieve a higher specific surface area. This made finding an acceptable synthesis procedure difficult. The synthesis chosen yielded products which exhibited very low specific surface areas in the literature, so it was hoped this was due to high density.

The starting conditions based on this synthesis procedure were using a 0.100 mol dm^{-3} $Ni(NO_3)_{2(aq)}$ electrolyte and depositing at -0.7 V vs Hg/HgO at room temperature. The initial synthesis procedure was run for 300 s. The electrodes were held approximately 1 cm apart. Initial SEM micrographs of the product are shown in Figure 4.1.

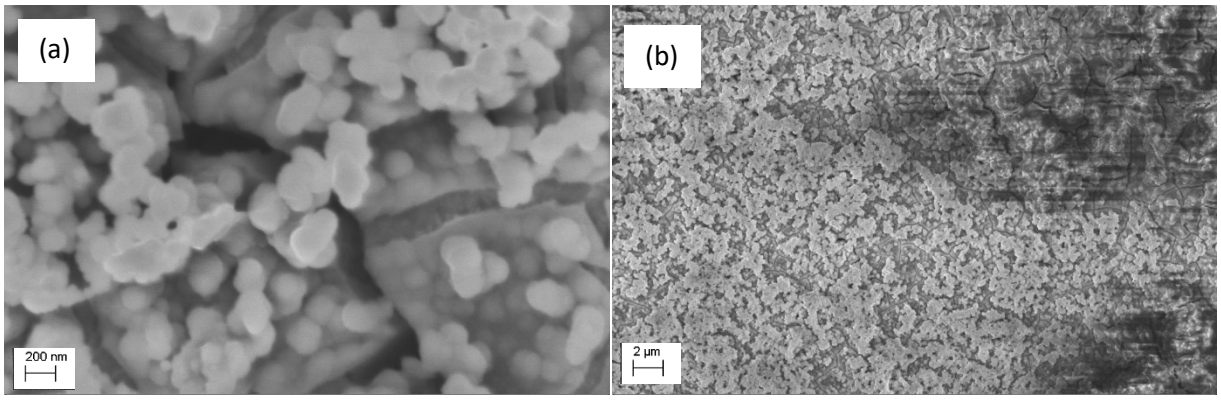


Figure 4.1 SEM micrographs of electrodeposited $Ni(OH)_2$ on Ni foil. Deposition run at -0.7 V for 5 mins at room temperature. Electrolyte was 0.100 mol dm^{-3} $Ni(NO_3)_2$. Full details of electrochemical set up can be found in Section 2.4.1.

The product showed good even distribution over the entire electrode surface and the particle sizes were around 200-250 nm in diameter. It was noted however there were several cracks in the deposited layer, which would allow for electrolyte to penetrate into the structure. It was also noted that the deposited layer was highly unstable and flaked off on removal from the electrochemical cell.

4.3.2 Substrate Selection

Nickel foil was initially used as the substrate for electrodeposition, since it was previously used to good effect in Chapter 3. It became clear however that the surface roughness of the

Ni foil, as well as substrate flexing, may lead to roughness and cracking in the sample. A more rigid and smooth substrate was therefore needed.

Gold electrodes were prepared on (100) Si wafer by sputtering a 10 nm Cr adhesion layer using a Quorum Q150T sputter coater, followed by a 20 nm Au layer using a Quorum Emitech K575X sputter coater. The structure of this substrate is shown in Figure 4.2.

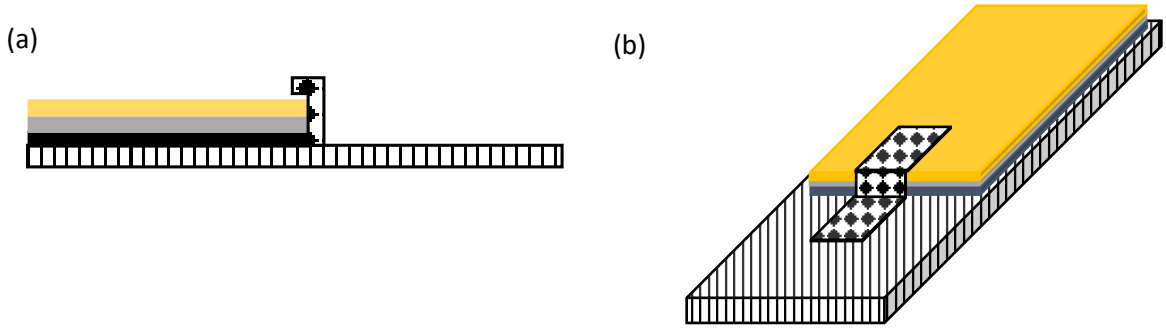


Figure 4.2 Structure of flat smooth substrate, (a) side view (b) isometric view, showing Ni current collector (stripes), Si (100) wafer (black), Cr layer (grey), Au layer (gold), and conductive silver paint (diamond) (layer thicknesses not to scale)

To ensure the new substrate would not have an effect on the morphology of the electrodeposited sample, the initial synthesis was repeated, shown in Figure 4.3.

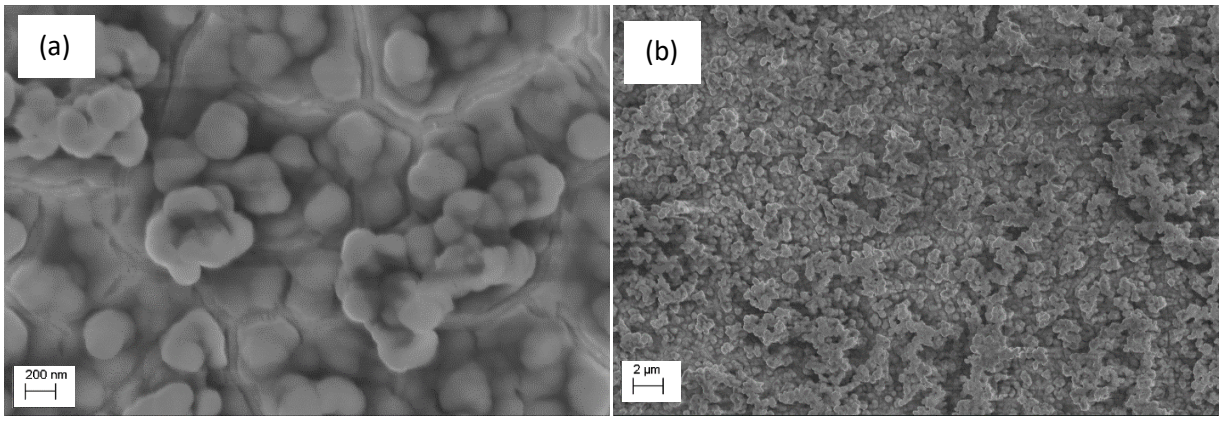


Figure 4.3 SEM micrographs of electrodeposited $Ni(OH)_2$ on Au/Cr sputter coated Si (100) wafer. Deposition run at -0.7 V for 5 mins at room temperature. Electrolyte was 0.100 mol dm^{-3} $Ni(NO_3)_2$. Full details of electrochemical set up can be found in Section 2.4.1.

The particle sizes found were similar to the deposition run on the Ni foil. The cracking of the deposited layer was less severe; however, cracks can still be seen at the nanoscale in Figure 4.3a. The sample charging was less of an issue, see Figure 4.2b and Figure 4.3b. This suggested better particle connectivity and contact with the metal surface.

4.3.3 Effect of Deposition Time

By varying deposition time, it was hoped that the cracks observed in the initial samples would be filled with additional deposited material and the layer could become denser. It was also important that the mass deposited could be controlled easily for reasons discussed in Section 3.5.1.

Electrodeposition was performed for 600 s using the same conditions described in Section 4.3.1. see Figure 4.4.

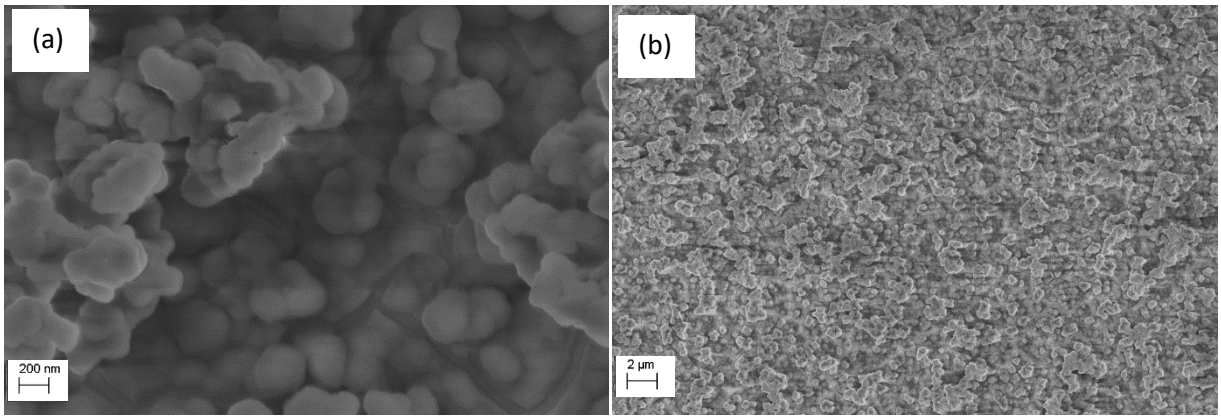


Figure 4.4 SEM micrographs of electrodeposited $Ni(OH)_2$ on Au/Cr sputter coated Si (100) wafer. Deposition run at -0.7 V for 10 mins at room temperature. Electrolyte was 0.100 mol dm^{-3} $Ni(NO_3)_2$. Full details of electrochemical set up can be found in section 2.4.1.

The longer deposition time did yield a higher deposited mass; however, the cracking the sample still remained. The deposition was run for 1, 2, 5, and 10 minutes in order to produce calibration curve of the desired mass, shown in Figure 4.5.

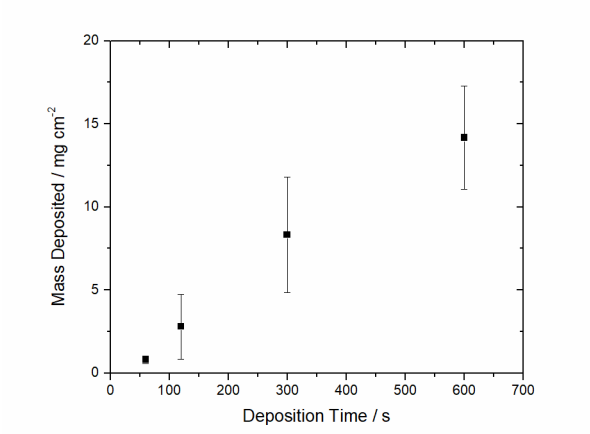


Figure 4.5 Dry mass of deposited $Ni(OH)_2$ on Au/Cr sputter coated Si (100) wafer electrode vs deposition time. Deposition run at -0.7 V at room temperature. Electrolyte was 0.100 mol dm^{-3} $Ni(NO_3)_2$. Full details of electrochemical set up can be found in Section 2.4.1. Error bars were calculated as the standard error of 3 experiments at the same deposition time.

In Section 3.5.1, a minimum mass loading of 1 mg cm^{-2} was shown to be sufficient to give a representative electrochemical analysis. It was noted for deposition times less than 300 s that

the coverage of the electrode surface was not complete. As shown in Figure 4.4a, the increase in deposition time did not eliminate cracking in the sample. It was therefore decided to keep the standard deposition time of 300 s as depositing for longer did not offer any benefit.

4.3.4 Effect of Deposition Temperature

Increasing the temperature of the deposition has been shown to lead to an increase in specific surface area measured.[14] While this was undesirable, an increase in reaction temperature was attempted to confirm those results, shown in Figure 4.6.

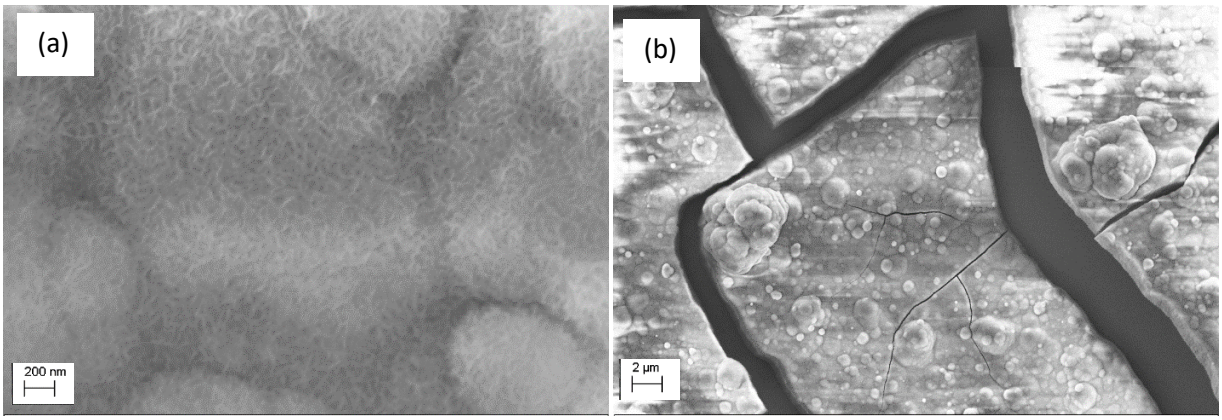


Figure 4.6 SEM micrographs of electrodeposited $Ni(OH)_2$ on Au/Cr sputter coated Si (100) wafer. Deposition run at -0.7 V for 5 mins at 60°C. Electrolyte was 0.100 mol dm^{-3} $Ni(NO_3)_2$. Full details of electrochemical set up can be found in Section 2.4.1.

Contrary to the literature findings, the deposited $Ni(OH)_2$, shown in Figure 4.6a, appeared significantly denser than the samples deposited at low temperatures. Depositing at an elevated temperature caused a significant increase in macroscale cracking across the sample. The increased cracking may have been the source of the increased surface area found in previous studies.

This cracking may be due to either the more rapid contraction of the deposited layer on drying. Alternatively, it could be due to the mismatch between the thermal expansion coefficient of the $Ni(OH)_2$ and that of the metal. Further work would need to be done to find a conductive substrate which could expand and contact with the $Ni(OH)_2$ to prevent this, however this was beyond the scope of this work.

4.3.5 Effect of Ni^{2+} Concentration

As already stated in Section 4.2, increasing the concentration of Ni^{2+} was expected to decrease the Faradaic efficiency of the reaction due to the formation of other soluble stable nickel

species. No reference could be found however for the effect of Ni^{2+} concentration on the morphology of the deposits.

The pH of the solution was also varied, however this caused precipitation of the Ni^{2+} from solution at high pH and dissolving of the $Ni(OH)_2$ product at low pH and so was discounted from the investigation.

The concentration of the Ni^{2+} in the electrolyte was varied from 0.100 mol dm^{-3} in the initial syntheses to 0.200 mol dm^{-3}, 0.300 mol dm^{-3} and finally 0.400 mol dm^{-3}, see Figure 4.7.

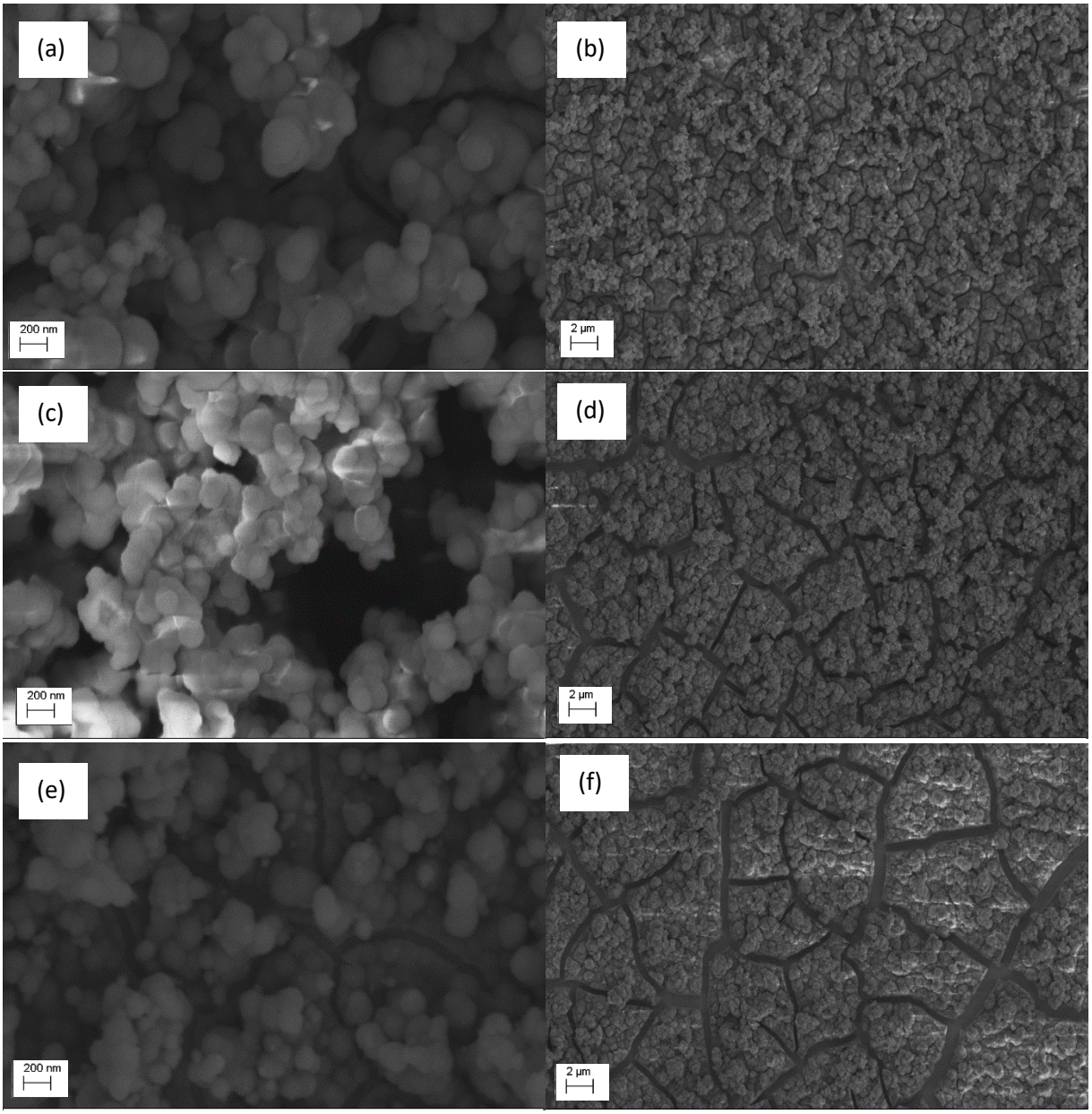


Figure 4.7 SEM micrographs of electrodeposited $Ni(OH)_2$ on Au/Cr sputter coated Si (100) wafer. Deposition run at -0.7 V for 5 mins at room temperature. $Ni(NO_3)_2$ electrolyte concentration was varied (a/b) 0.200 mol dm^{-3} (c/d) 0.300 mol dm^{-3} (e/f) 0.400 mol dm^{-3}. Full details of electrochemical set up can be found in section 2.4.1.

At all concentrations, a particle-like morphology is seen. The particle size decreases with increasing Ni^{2+} concentration. A similar effect has been seen in other electrodeposited metal oxides.[18] At low concentrations, the concentration of Ni^{2+} after the initial nucleation of $Ni(OH)_2$ will not be high enough for further nucleation, resulting in the growth at the initial nucleation sites only. This will lead to fewer and larger particles. In contrast to this at higher concentrations, it is expected that the growth will no longer be limited by the diffusion of Ni^{2+} to the surface. This will allow for multiple nucleation events and smaller but more numerous particles being formed, as well as a larger dispersity of particle sizes.

The formation of smaller particles into a denser film was beneficial for this work, however higher concentrations of $Ni(NO_3)_2$ in the electrolyte did also lead to large decrease in the mass deposited per coulomb transferred over 300 s. This can be attributed to the lower Faradaic efficiency discussed in Section 4.2. These thinner films were highly unstable, and it would found to be very difficult to transfer the films out of the synthesis cell. The increase in microscale film cracking can be seen in Figures 4.7b/d/f.

4.3.6 Effect of Deposition Potential

The deposition potential has been shown to have a large effect on the morphology of electrodeposited metal oxide thin films.[15, 18] The deposition potential was limited by the stability of the electrolyte, as well as the reduction potential of the nitrate in solution.

It was found that potentials more positive than -0.7 V produced no obvious deposition, even when left in excess of 1200 s. The focus was therefore moved to more negative potentials. The effect of deposition potential was studied between -0.7 V and -1.3 V at 0.2 V intervals. The products from these syntheses can be seen in Figure 4.8.

Once again, a particle like morphology is retained. The average particle diameter of the $Ni(OH)_2$ decreases from -0.7 V to -1.1 V and then remains consistent. The mass deposited increases with decreasing potential, as does film thickness. The films electrodeposited at -0.9 V and below are much more robust than those deposited at -0.7 V. This can be seen by the lack of microscopic film cracking in Figure 4.8b/d/f.

As the deposition potential becomes more negative, the porosity of the film can be seen to increase. This is possibly due to cathodic reduction of water in the aqueous electrolyte. The

hydrogen gas produced forms bubbles in the structure and prevents a dense layer from forming. Previous studies have found a sharp increase in the hydrogen evolution reaction (HER) at potentials below -0.9 V.[19] As already stated, this is undesirable in this experiment since a large porosity will allow electrolyte penetration into the bulk. Despite creating thicker and more stable films, deposition at potentials more negative than -1.0 V is unsuitable for this work.

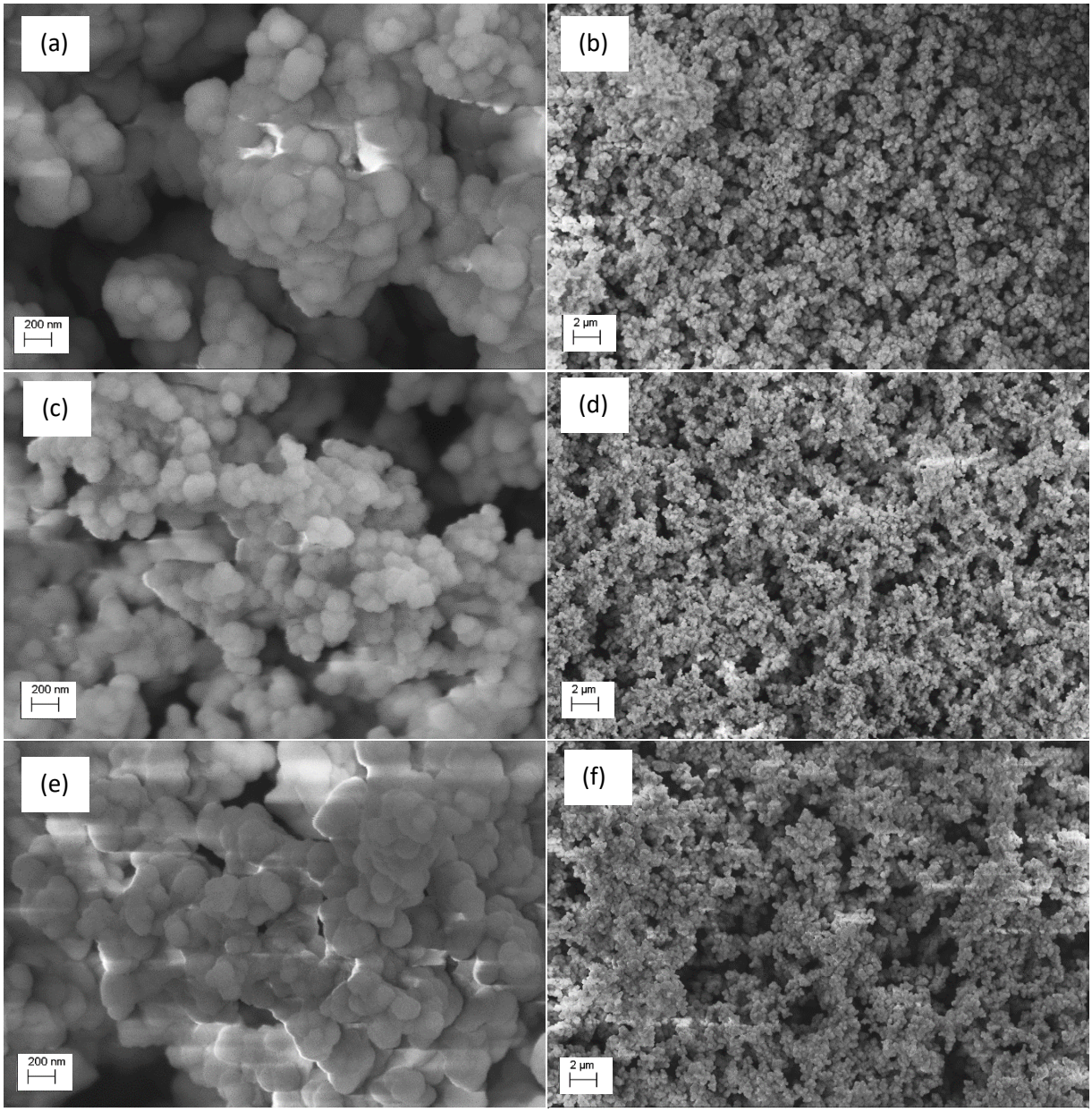


Figure 4.8 SEM micrographs of electrodeposited $Ni(OH)_2$ on Au/Cr sputter coated Si (100) wafer. Deposition was run for 5 mins at room temperature. $Ni(NO_3)_2$ electrolyte concentration was 0.100 mol dm^{-3}. Deposition potential was varied (a/b) -0.9 V (c/d) -1.1 V (e/f) -1.3 V. Full details of electrochemical set up can be found in section 2.4.1.

4.3.7 Final Synthesis Procedure

After studying the effects of electrolyte concentration as well as deposition temperature, time, and potential; the following experimental conditions were determined to be the most suitable.

Increasing deposition time had shown to not improved the stability of the continuity of the films, however it did make for an easy method to control mass loading. It was determined that 300 s was long enough to deposit a film of the desired mass loading (> 1 mg cm^{-2}) which covered the entirety of the electrode surface.

Increasing deposition temperature was found to cause substantial micro and macroscale cracking on cooling, so it was resolved to perform all further syntheses at room temperature.

Increasing the concentration of $Ni(NO_3)_{2(aq)}$ was also shown to cause micro-scale cracking in the sample, as well as reduce the Faradaic efficiency significantly. Therefore, all further syntheses were performed using 0.100 mol dm^{-3} $Ni(NO_3)_{2(aq)}$ electrolyte.

Finally, decreasing the working electrode deposition potential did lead to smaller particles and a thicker and more stable deposited layer. An increase in porosity, possibly due to the formation of gas bubbles at the electrode surface, made any syntheses using a deposition potential of < -1.0 V unsuitable for this work. It was therefore decided to use a deposition potential of -0.9 V for the remainder of this work.

4.4 Structural Characterisation of Electrodeposited $Ni(OH)_2$

The deposition current *vs* time plots show an initial plateau for deposition onto the metal substrate, followed by deposition onto the initial $Ni(OH)_2$ monolayer at a slightly higher current. This suggests depositing onto the $Ni(OH)_2$ is more favourable and explains why a continuous film was so difficult to produce. The deposition current then slowly decreases due to the increasing resistivity of the metal hydroxide layer as further deposition takes place, see Figure 4.9.

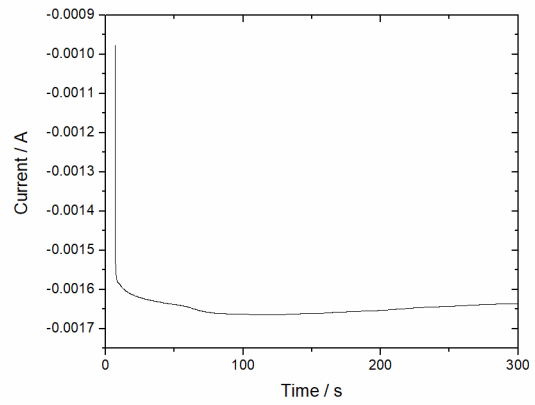


Figure 4.9 Typical current vs time plot of deposition procedure. Deposition was run for 5 mins at room temperature. $Ni(NO_3)_2$ electrolyte concentration was 0.100 mol dm^{-3}. Deposition potential was -0.9 V. Full details of electrochemical set up can be found in section 2.4.1.

XPS and EDX were used to confirm the composition of the deposited layer as $Ni(OH)_2$. A typical survey spectrum is shown in Figure 4.10.

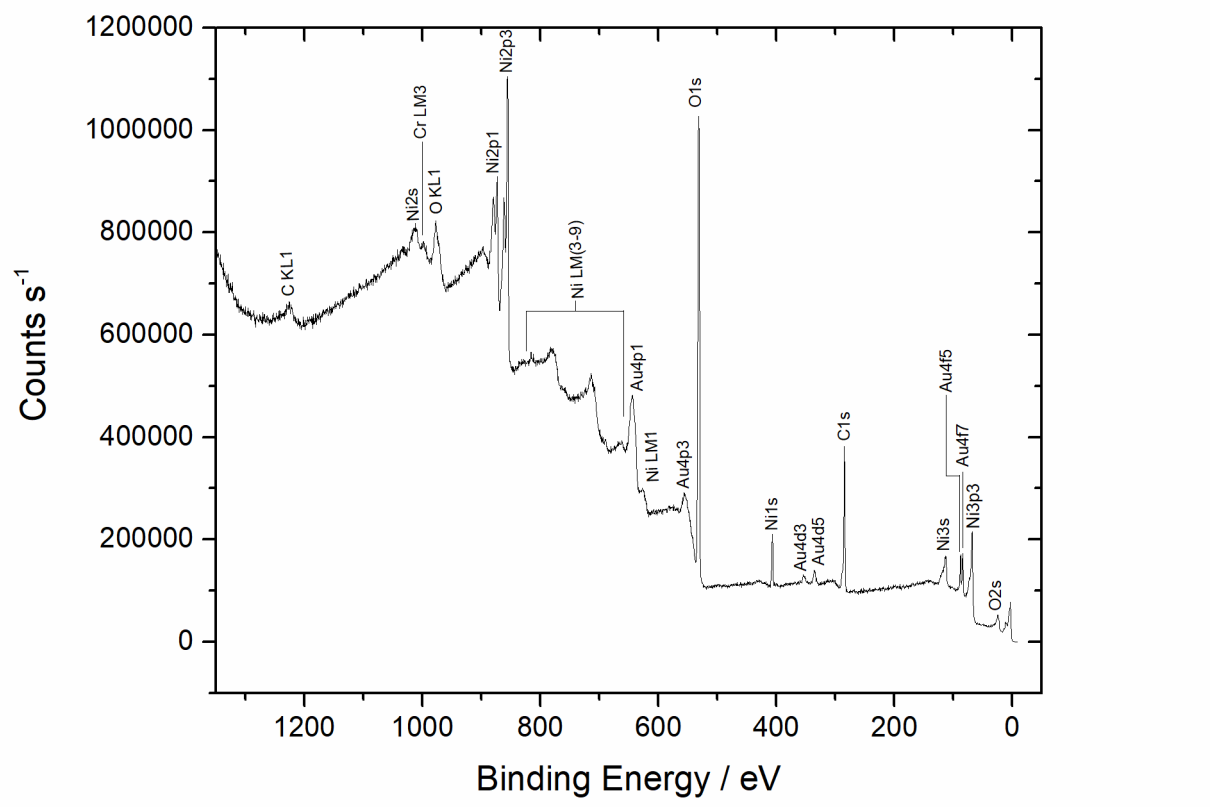


Figure 4.10 XPS survey spectrum of electrodeposited $Ni(OH)_2$ on Au/Cr coated Si wafer. Deposition was run for 5 mins at room temperature. $Ni(NO_3)_2$ electrolyte concentration was 0.100 mol dm^{-3}. Deposition potential was -0.9 V. Full details of electrochemical set up can be found in section 2.4.1.

The high-resolution spectrum of the Ni2P, shown in Figure 4.11b, shows two major peaks with binding energies at 873.2 eV and 855.6 eV, which correspond to $Ni2p_{1/2}$ and $Ni2p_{3/2}$, respectively, with a spin-energy separation of 17.6 eV. These binding energies were relative

to a carbon peak at 285.0 eV, as shown in Figure 4.11a. These peaks are characteristic of $Ni(OH)_2$ and in good agreement with previously reported data.[20]

In addition, Figure 4.11c shows the O1s spectrum with a strong peak at 531.1 eV, consistent with bound hydroxide groups.[20-21] There is a strong shoulder on this O1s spectrum, which could be due to mixed oxidation states or bound counter ions between the layers of $Ni(OH)_2$.

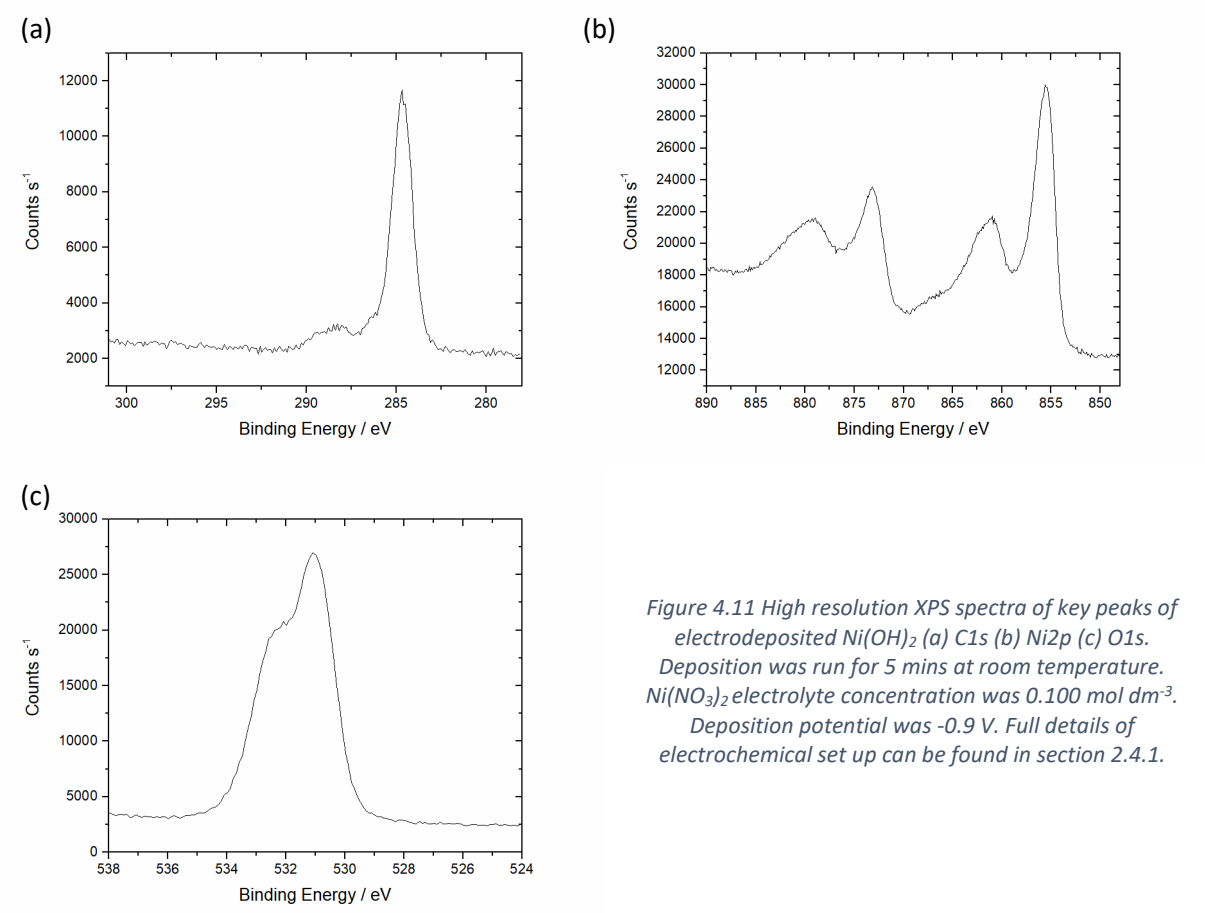


Figure 4.11 High resolution XPS spectra of key peaks of electrodeposited $Ni(OH)_2$ (a) C1s (b) Ni2p (c) O1s. Deposition was run for 5 mins at room temperature. $Ni(NO_3)_2$ electrolyte concentration was 0.100 mol dm^{-3}. Deposition potential was -0.9 V. Full details of electrochemical set up can be found in section 2.4.1.

The XPS analysis indicates that the as-synthesized sample is $Ni(OH)_2$. This is further supported by the elemental ratios calculated by EDX, giving an approximate atomic ratio of Ni:O of 0.5 ± 0.1, Figure 4.12.

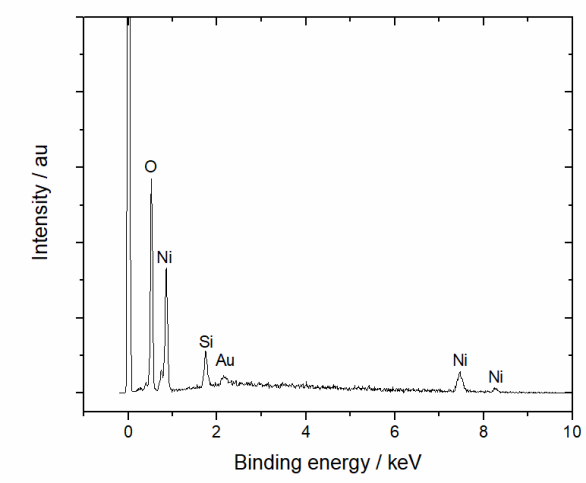


Figure 4.12 EDX analysis of electrodeposited $Ni(OH)_2$. Deposition was run for 5 mins at room temperature. $Ni(NO_3)_2$ electrolyte concentration was 0.100 mol dm^{-3}. Deposition potential was -0.9 V. Full details of electrochemical set up can be found in section 2.4.1.

Scanning electron micrographs, shown in Figure 4.8, exhibit a highly porous particulate structure, with connected particles of around 100 nm in size. This size could not be confirmed with XRD. No clear peaks are shown, other than those attributed to the metal coated substrate, see Figure 4.13. Since crystalline $Ni(OH)_2$ should show clear peaks at this mass loading for particles of this size.[22] The lack of peaks is attributed to the material being highly amorphous. This is also shown by the increase in the amorphous background at low 2θ, and the masking of the substrate peaks at 2θ of 44° and 52°.

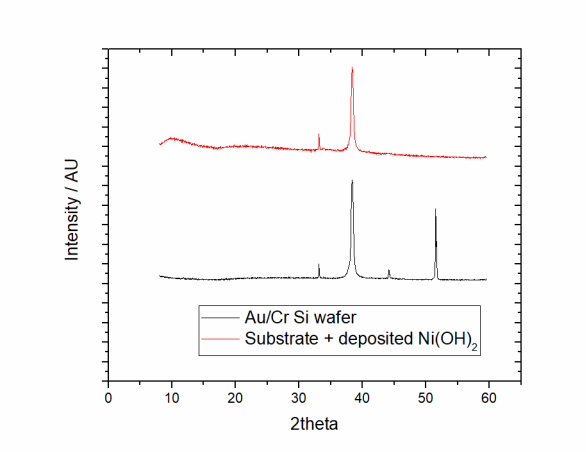


Figure 4.13 X-ray diffractogram of Au/Cr coated Si (100) wafer before and after electrodeposition of $Ni(OH)_2$. Deposition was run for 5 mins at room temperature. $Ni(NO_3)_2$ electrolyte concentration was 0.100 mol dm^{-3}. Deposition potential was -0.9 V. Full details of electrochemical set up can be found in section 2.4.1.

The porous nature of the $Ni(OH)_2$ is also shown using N_2 adsorption/desorption. The BET analysis shows a type IV isotherm typical of mesoporous solids, giving a surface area of 165.6 $m^2\ g^{-1}$, as shown in Figure 4.14a. The hysteresis between adsorption and desorption is due to capillary condensation in the mesopores.[20] The mesoporous structure was not analysable by DFT calculation, with only the nanopores < 10 nm width showing in the analysis, see Figure 4.14b.

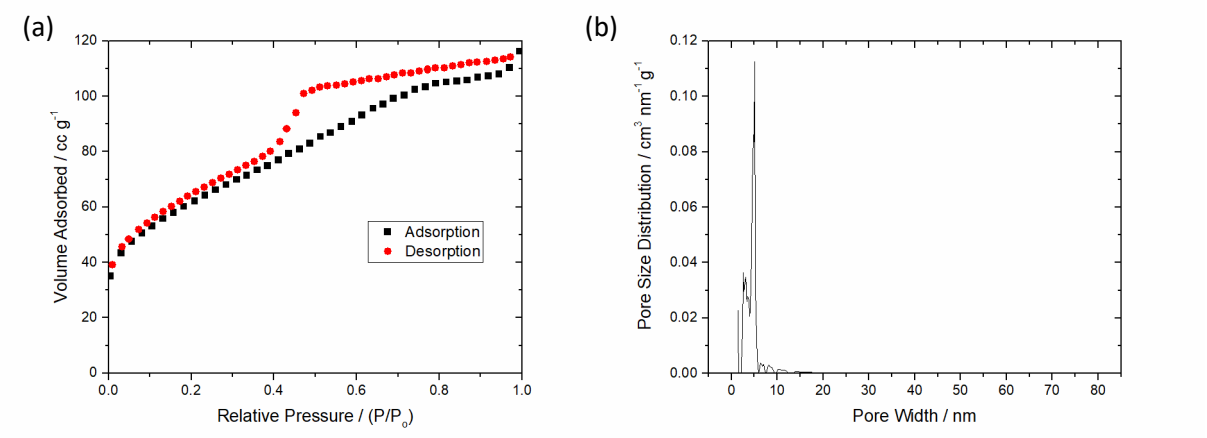


Figure 4.14 (a) N_2 Adsorption/Desorption analysis of electrodeposited $Ni(OH)_2$ samples (b) Pore size distribution by DFT analysis. Full BET analysis conditions can be found in section 2.2.8. Deposition was run for 5 mins at room temperature. $Ni(NO_3)_2$ electrolyte concentration was 0.100 mol dm^{-3}. Deposition potential was -0.9 V. Full details of electrochemical set up can be found in section 2.4.1.

AFM of the samples was also attempted; however, the samples were too rough to produce an image. This is discussed further in Section 4.6.3.

4.5 Electrochemical Characterisation of Electrodeposited $Ni(OH)_2$

For full details of the electrochemical cell set-up and analysis conditions, see Section 2.4. The electrochemical behaviour of the deposited $Ni(OH)_2$ matches that previously reported in the literature.[10, 21] CV traces, Figure 4.15, show the expected shape and peaks for nickel hydroxide,[4, 9] with specific capacity found to be *ca.* 20 mA h g^{-1} at 10 mV s^{-1} scan rate. Calculations for specific capacity can be found in Section 2.4.5. Redox peaks are visible in the trace, with oxidation to oxyhydroxide at *ca*. 0.40-0.50 V and reduction in the range of 0.25-0.30 V.

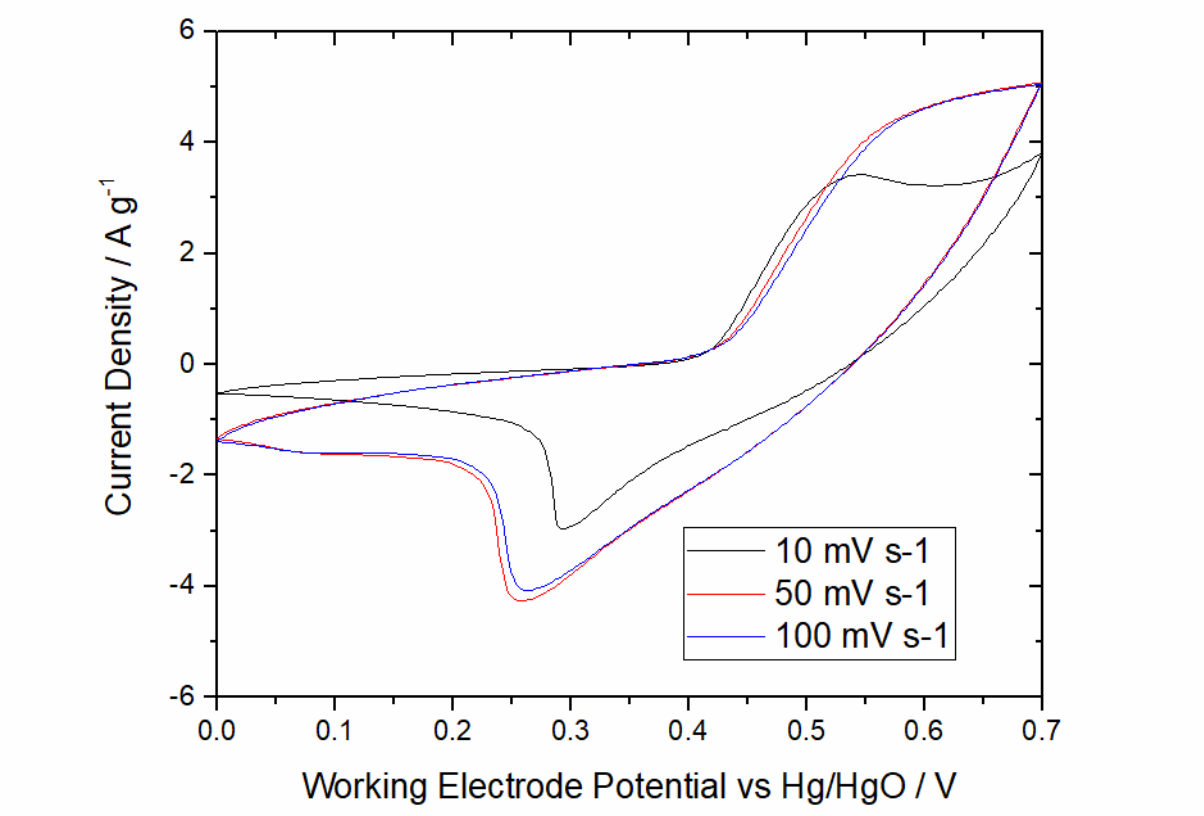


Figure 4.15 Cyclic voltammetry of electrodeposited $Ni(OH)_2$ film at various scan rates. Deposition was run for 5 mins at room temperature. $Ni(NO_3)_2$ electrolyte concentration was 0.100 mol dm^{-3}. Deposition potential was -0.9 V. Full details of electrochemical set up can be found in section 2.4.1. All electrochemical measurements made using a three-cell set up and in 1.0 M KOH, see section 2.4 for full conditions.

Figure 4.16 shows the GCD trace of the deposited $Ni(OH)_2$ at 1 A g^{-1} with current switching every 60 seconds. The GCD shows the expected charging behaviour.[20-21, 23] There is a charging plateau around 0.5 V, which matches well with the peaks observed in the CV. This plateau is

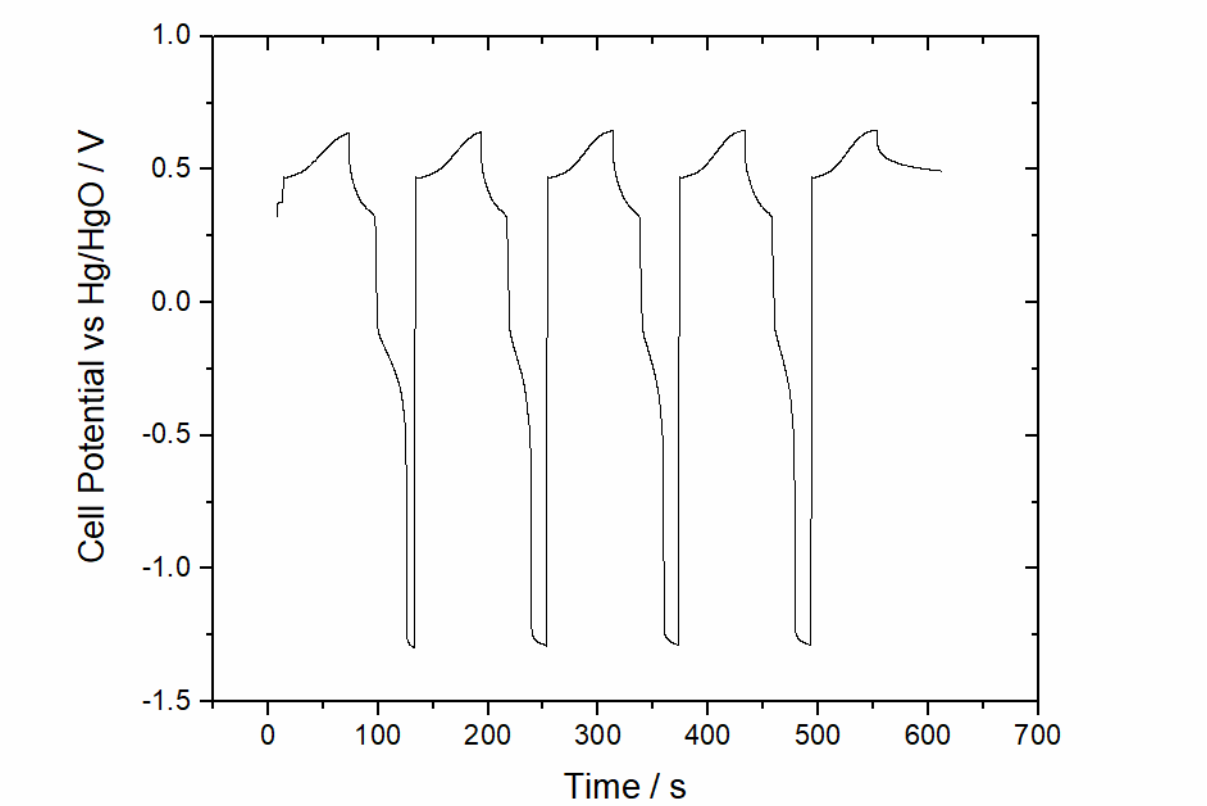


Figure 4.16 Galvanostatic charge/discharge of the electrodeposited $Ni(OH)_2$ film at 1 A g^{-1}. Deposition was run for 5 mins at room temperature. $Ni(NO_3)_2$ electrolyte concentration was 0.100 mol dm^{-3}. Deposition potential was -0.9 V. Full details of electrochemical set up can be found in section 2.4.1. All electrochemical measurements made using a three-cell set up and in 1.0 M KOH, see section 2.4 for full conditions.

usually associated with battery behaviour. The discharge trace however is more linear, as expected for a pseudocapacitor.

4.6 Manufacture of Non-Porous $Ni(OH)_2$ Electrode

Despite optimisation, the electrodeposited $Ni(OH)_2$ still exhibited a high surface area and appeared to be highly porous in SEM micrographs, see Figure 4.8a/b and Figure 4.14. It was decided that if a dense $Ni(OH)_2$ layer was not achievable through electrodeposition alone, an alternative method to prevent electrolyte ingress into the sample was needed. The method chosen was to use wax to block the pores in the $Ni(OH)_2$.

4.6.1 Wax Deposition

Low melting point (56-60 ^oC) paraffin wax (Sigma, UK) was chosen since it would be possible to fully melt the wax without exposing the samples to high temperatures which may cause dehydration or calcination of the $Ni(OH)_2$.

To ensure full ingress of the wax into the structure, a small deposition plate was constructed, see Figure 4.17. By applying pressure through tightening the screws, the wax was forced into the $Ni(OH)_2$ structure. The set-up also had the added benefit of containing all the wax within the O-ring and prevent it leaking out of the sample while liquid.

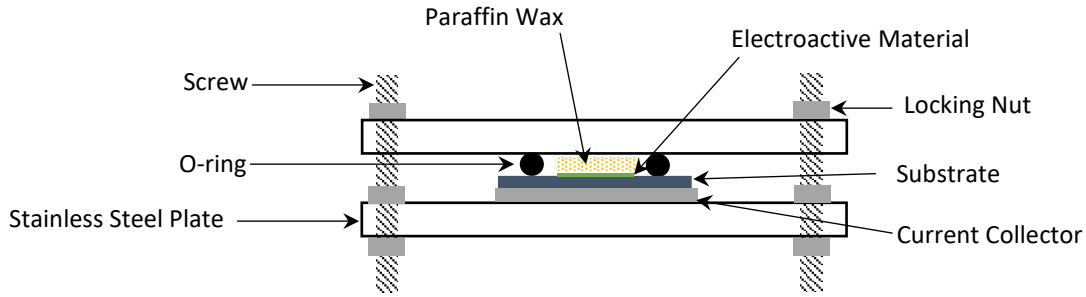


Figure 4.17 Wax deposition set up, prepared in house for this work.

To prepare the wax coated electrode, approximately 100 mg of shredded wax was placed on top of the electrode within the O-ring. The top plate was then screwed down until finger tight. Any tighter would cause cracking of the Si wafer substrate. The set-up was then placed in an oven at 80 ^{o}C for 30 minutes and allowed to melt. This ensured full melting of the wax while still being well below the smoke point of the wax, around 200 ^{o}C. Following melting, the set-up was removed from the oven and left to cool to room temperature for at least 1 hour. On removal, the $Ni(OH)_2$ was fully wax covered.

4.6.2 Wax Grinding

After wax coating, no electrodeposited $Ni(OH)_2$ was exposed. To expose the $Ni(OH)_2$ and create a flat surface for the reaction to occur, the electrodes were ground flat.

Wax grinding was performed using 4000 grit silicon carbide paper on a Streuers Rotoforce-1. The sample and pad were co-rotated, the pad at 64 rpm and the sample at 200 rpm. Faster rotation was attempted, however this led to a rapid degradation of the sample. 10 N constant pressure was applied for 20 second periods until the desired finish was achieved, typically <10 iterations.

The samples were imaged using light microscopy before grinding and after each 20 second period of grinding. An example of the surface before and after grinding can be seen in Figure 4.18. Immediately post wax deposition, the wax layer is rough with no visible nickel hydroxide.

After grinding however, small “islands” of exposed $Ni(OH)_2$ account for between 1-2% of the surface area, as measured using the method outlined in Section 2.2.10.

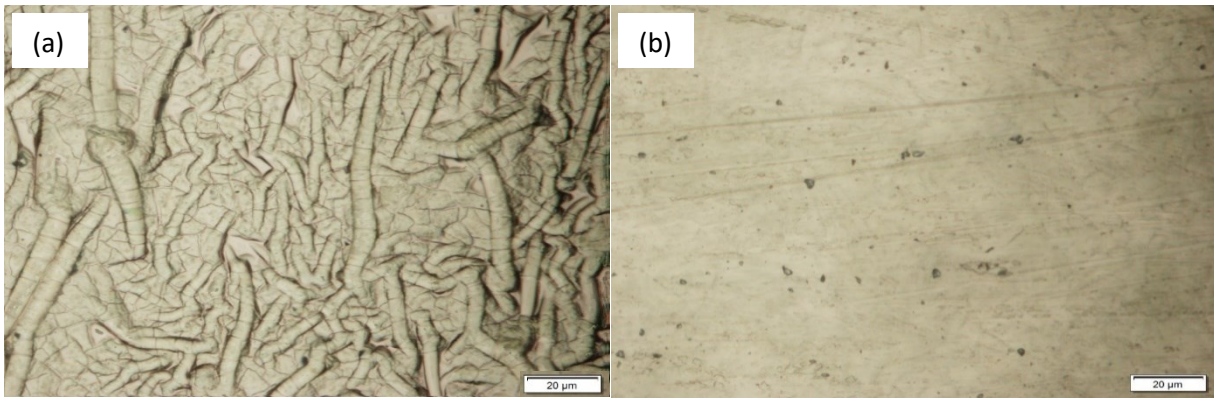


Figure 4.18 Light Microscopy of wax coated electrodeposited $Ni(OH)_2$ electrodes (a) before grinding and (b) after grinding

4.6.3 Structural Characterisation

Post wax deposition and grinding, the specific surface area decreases and becomes too low to accurately measure using nitrogen adsorption/desorption, see Figure 4.19. In contrast to the high surface area measured before wax deposition, see Figure 4.14a, this suggests that the porosity has been successfully blocked by the wax layer.

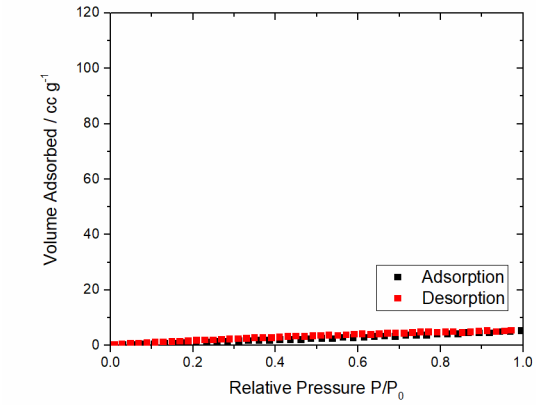


Figure 4.19 N_2 Adsorption/Desorption analysis of electrodeposited $Ni(OH)_2$ samples after paraffin wax deposition and grinding. Full BET analysis conditions can be found in section 2.2.8. Deposition was run for 5 mins at room temperature. $Ni(NO_3)_2$ electrolyte concentration was 0.100 mol dm^{-3}. Deposition potential was -0.9 V. Full details of electrochemical set up can be found in section 2.4.1.

AFM of the $Ni(OH)_2$ surface before wax deposition was not possible for the system available without signal fluctuation due to the sample being too rough. After wax deposition, a micrograph could be produced; however, there was still major signal fluctuation, see Figure 4.20. Post wax deposition and grinding, the surface is still rough. The roughness, however, was reduced to around +/- 1 µm and was now measurable. The surface roughness of the waxed sample was low enough to allow the measuring of the sputter crater used in Section 4.7 to study the depth of charging.

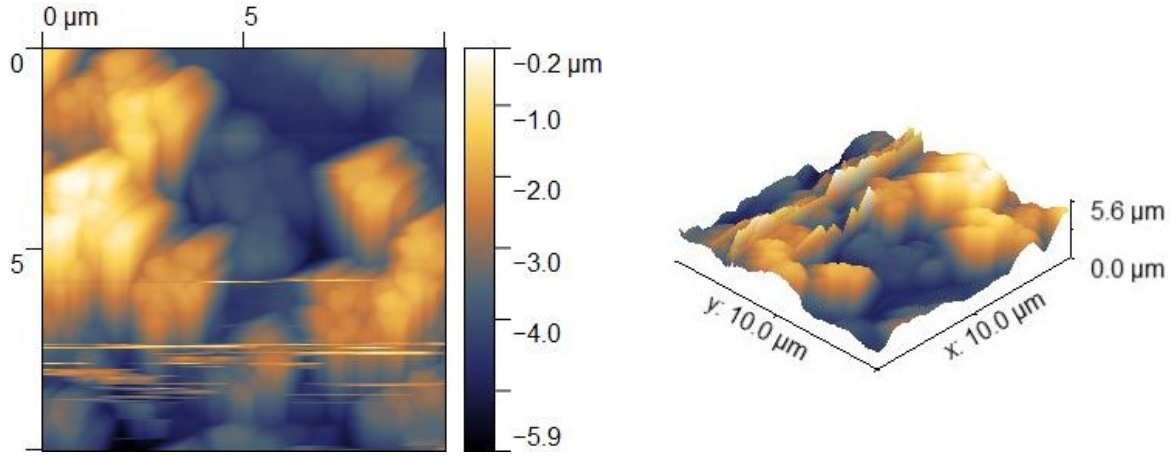


Figure 4.20 Atomic force micrograph of the electrodeposited $Ni(OH)_2$ electrode after wax coating, but prior to grinding.

4.6.4 Electrochemical Characterisation

After the deposition of the paraffin wax layer, no electrochemical response could be recorded due to the high resistance of the sample. Post wax grinding, a similar electrochemical response to the one found in Section 4.5 can be found. CV traces show the same redox peaks, only with a much lower current density, as shown in Figure 4.21. As expected, the current density is around 1% of that of the unwaxed sample. This corresponds to the amount of sample protruding from the wax, as observed by light microscopy in Figure 4.18b.

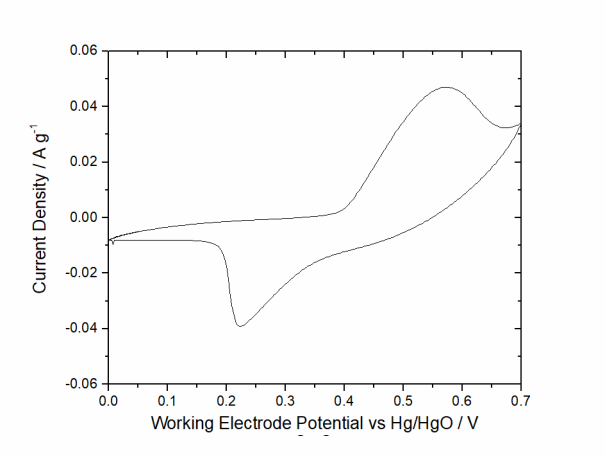


Figure 4.21 Cyclic voltammetry of electrodeposited $Ni(OH)_2$ film at 10 mV s^{-1} after wax deposition and grinding. Full details of electrochemical set up can be found in section 2.4.1. All electrochemical measurements made using a three-cell set up and in 1.0 M KOH, see section 2.4 for full conditions.

GCD traces at the same current density show a similar profile, with a change in gradient around 0.46 V due to the onset of the oxidation of the $Ni(OH)_2$. The wax covered sample shows a higher maximum potential due to the increased resistivity of the sample. The GCD shows a much faster charge time, due to the limited amount of material available for charging, see Figure 4.22.

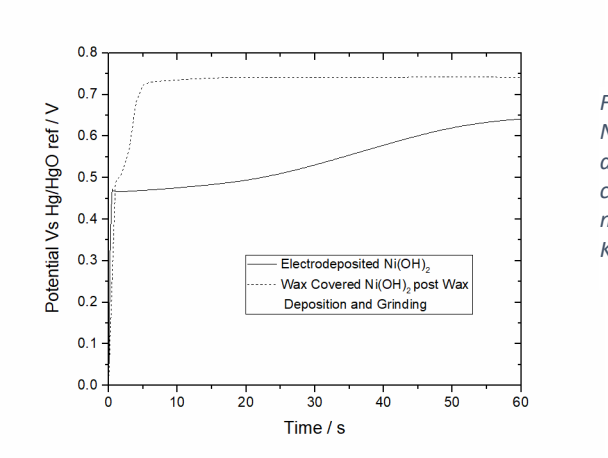


Figure 4.22 Galvanostatic charging of electrodeposited $Ni(OH)_2$ film at 1 A g^{-1} of active material, before and after wax deposition and grinding. Full details of electrochemical set up can be found in section 2.4.1. All electrochemical measurements made using a three-cell set up and in 1.0 M KOH, see section 2.4 for full conditions.

4.7 Time of Flight Secondary Ion Mass Spectrometry

On charging, the $Ni(OH)_2$ loses a proton to form the oxyhydroxide. The material then takes up D^+ during reduction back to the starting material, see Equation 4.4 and 4.5.

$$Ni(OH)_2 + OD^- \rightarrow NiOOH + HOD + e^- \quad (4.4)$$

$$NiOOH + D_2O + e^- \rightarrow NiODOH + OD^- \quad (4.5)$$

After samples were charged and discharged in deuterated alkaline electrolyte, they were analysed using ToF-SIMS. Full experimental details can be found in Section 2.3.

The deuterium ion (D^-) signal is normalised across different samples using a reference signal, in this case $NiOH^-$. This is done to ensure that the effects of different sputter currents and the amount of sample available are removed. Since deuterium is found at 0.0115% of all hydrogen naturally,[24] there is a background signal expected for all samples.

4.7.1 ToF-SIMS of Porous Electrodeposited $Ni(OH)_2$

Initial results of studying pure $Ni(OH)_2$, with no wax to block pores, showed consistent deuterium levels at all sputter times. This is expected as the porous structure will allow the whole electrode to undergo redox reactions through solvent diffusion into the pores, see Figure 4.23. The signal for H^- is excluded from Figure 4.23 as it is orders of magnitude stronger than the other signals ~10^5 counts. This was expected to give a D^- signal of the order of 10^1 counts, which is what is observed in Figure 4.23.

The signal is shown to be stable over both short and long sputter times.

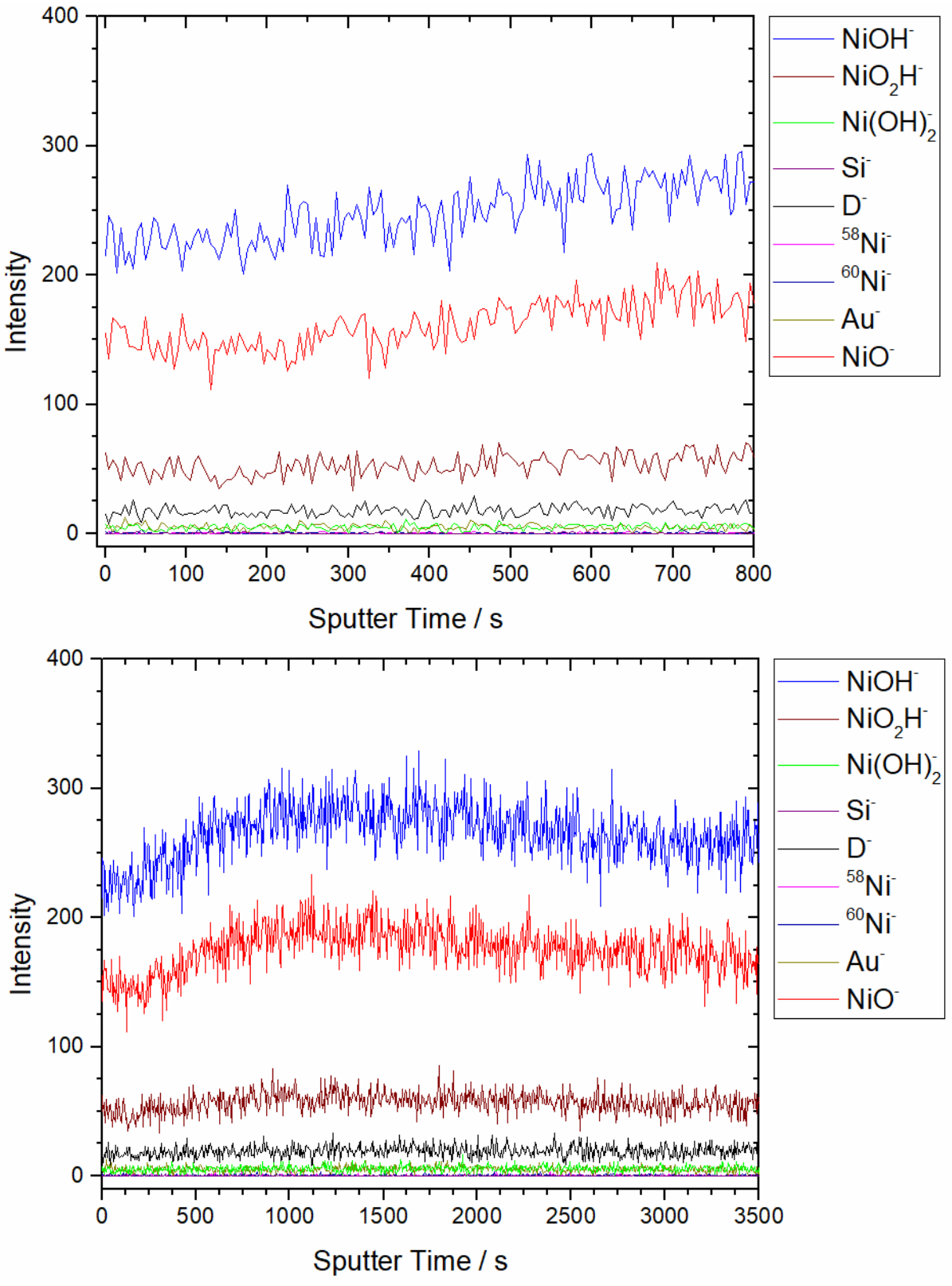


Figure 4.23 ToF-SIMS analysis of electrodeposited $Ni(OH)_2$ film on Au/Cr coated Si (100) wafer (a) short time scale (b) long time scale. Traces taken using analysis conditions described in section 2.3. H^- not shown due to large magnitude of signal, around 10^5 counts.

Before progressing to the wax coated samples, it was important to ensure that the deuterium uptake being studied was dependent on electrochemical cycling, rather than adsorption or self-exchange with the electrolyte. Initially, a sample was not cycled but exposed to deuterated electrolyte for two minutes as a control. The normalised deuterium intensity count for the uncycled sample did not exceed that expected for the background level.

The normalised deuterium level was then studied after multiple cycles, as shown in Figure 4.24.

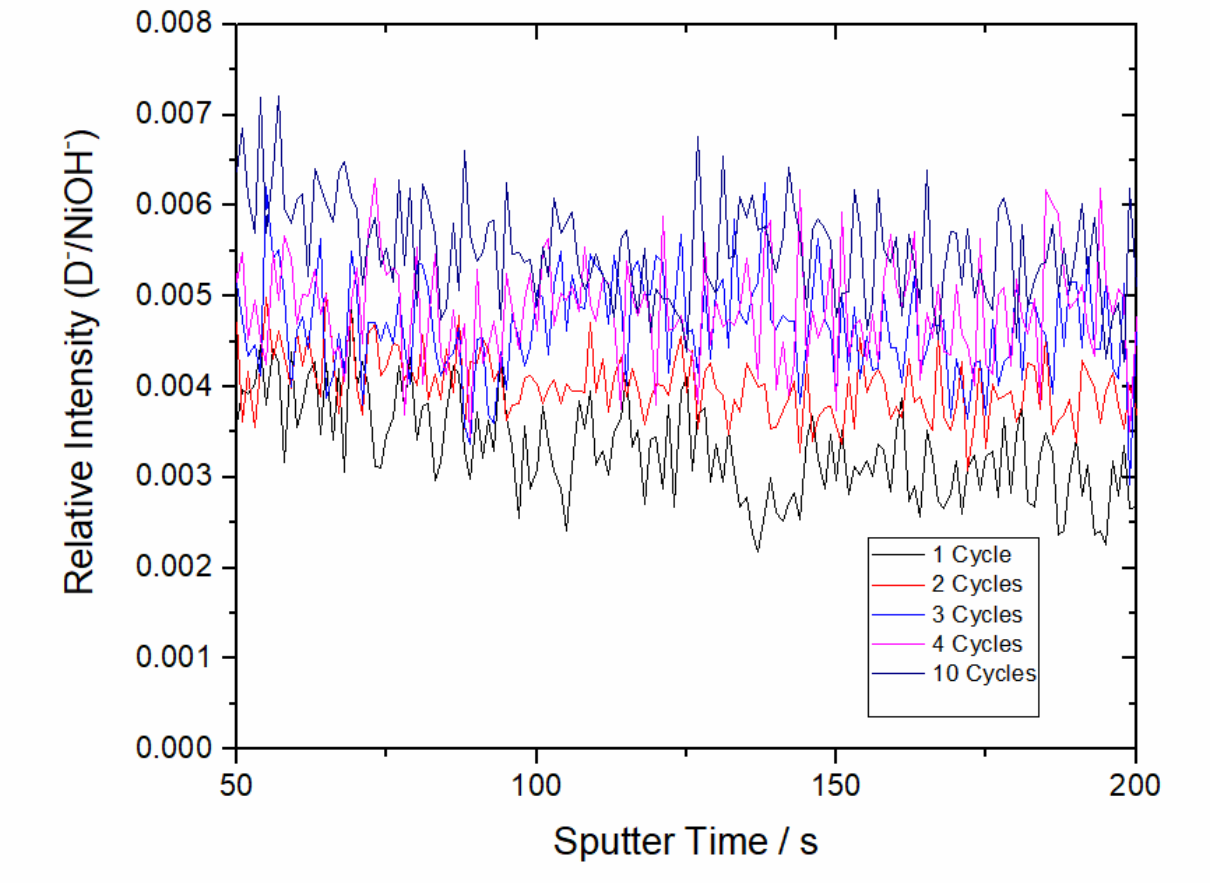


Figure 4.24 Relative measured intensity of D^- in electrodeposited $Ni(OH)_2$ electrode vs sputter time after various cycle numbers in deuterated alkaline electrolyte at 10 mV s^{-1}. Signal is normalised to $NiOH^-$.

On cycling, the uptake of deuterium was expected to increase. From Equation (4.4) and (4.5), there will be a single proton/deuterium exchanged per Ni during each charge/discharge cycle. Therefore, after cycle one, it can be expected that 50% of the protons in the $Ni(OH)_2$ sample will have exchanged with deuterium, assuming that the $[H^+] << [D^+]$ in the deuterated alkaline electrolyte. On the second cycle, either the deuterium can be exchanged, or the second proton can be exchanged. This gives 75% exchanged over the whole sample at the end of the second charge/discharge cycle. This will continue over each charge/discharge cycle, approaching 100% deuterium exchange after a high number of cycles, see Figure 4.25.

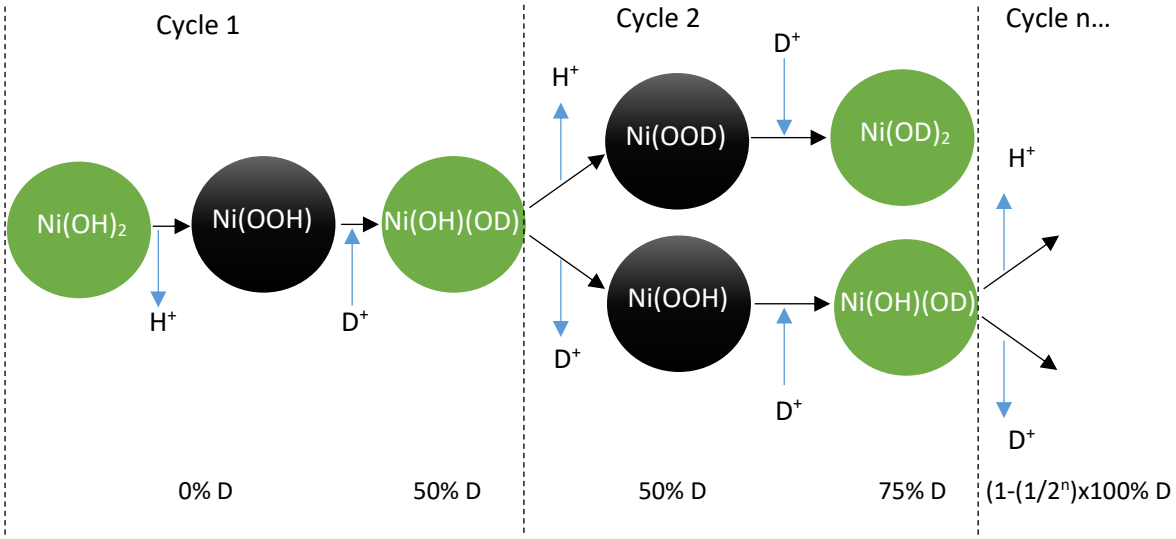


Figure 4.25 Reaction schematic for the charging and discharging of $Ni(OH)_2$ in deuterated electrolyte. Deuterium loading into the sample is given as % D.

An average was calculated for the deuterium relative intensity with sputter time at various cycle numbers, shown in Figure 4.24. This average is plotted against cycle number, see Figure 4.26.

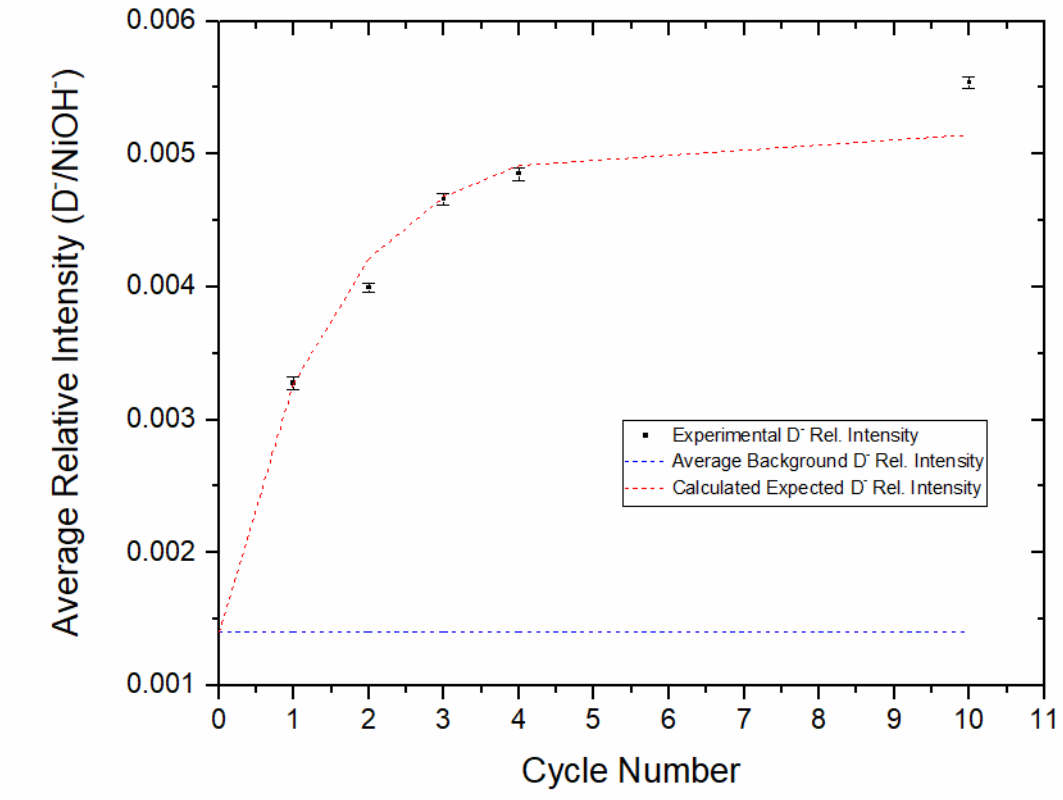


Figure 4.26 Variation of relative deuterium ion intensity with cycle number. Average value calculated from Figure 4.24 is plotted along with theoretically derived uptake based on mechanism shown in Figure 4.25. Error bars calculated as standard error in intensity between 50 and 200 sputter seconds.

The predicted change using the uptake after one cycle and the exchange % above is shown along with the experimentally found change in intensity. There is very good agreement with the experimentally measured deuterium ion intensity and the predicted values for the first 5 cycles. The intensity increases more than expected after 10 cycles, however this agrees well with the observed increase in current density over multiple cycles seen in Chapter 3.

4.7.2 ToF-SIMS of Non-Porous Electrodes

Once the wax layer is added to the sample, there is a large increase in the background intensity of D^- due to the signal produced by the hydrocarbon wax. There is also a large decrease in the intensity of ions based on the $Ni(OH)_2$ due to such a small percentage of the metal hydroxide being exposed.

Unlike the depth profiles produced using the cycled uncoated electrodes, this deuterium level is not consistent over the whole depth profile. The depth profiles produced using these wax-covered samples shows a much higher deuterium level at early sputter times. The high deuterium level rapidly decreases over the first 20-30 sputter seconds, as shown in Figure 4.27.

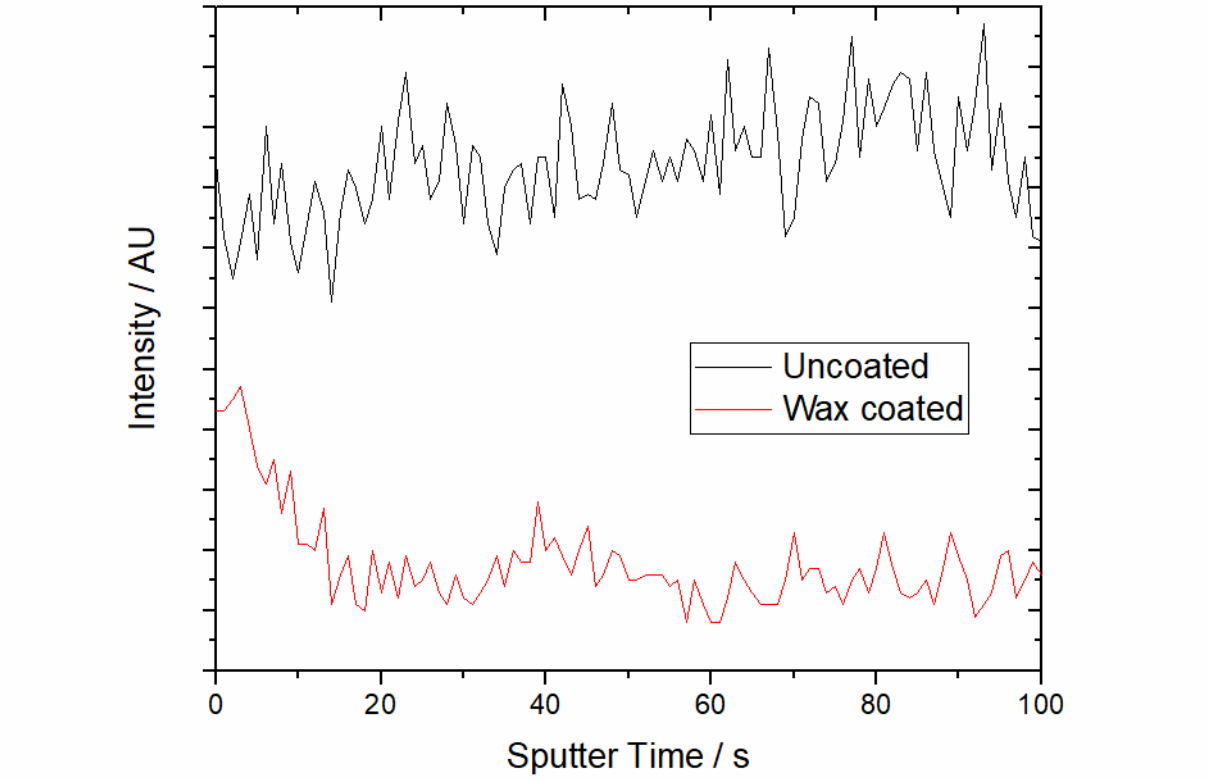


Figure 4.27 ToF-SIMS plots of deuterium ion intensity (normalised to $NiOH^-$) verses sputter time for waxed and unwaxed samples after 1 cycle of charging and discharging at 10 mV s^{-1}. The uncoated sample is much nosier due to lower overall deuterium ion intensity. Full procedural details for ToF-SIMS analysis can be found in section 2.3

In order to convert the measured decay in deuterium signal into a charging depth, the relationship between the sputter crater depth and the sputter time was found. The sputter craters were measured using AFM, an example is shown in Figure 4.28.

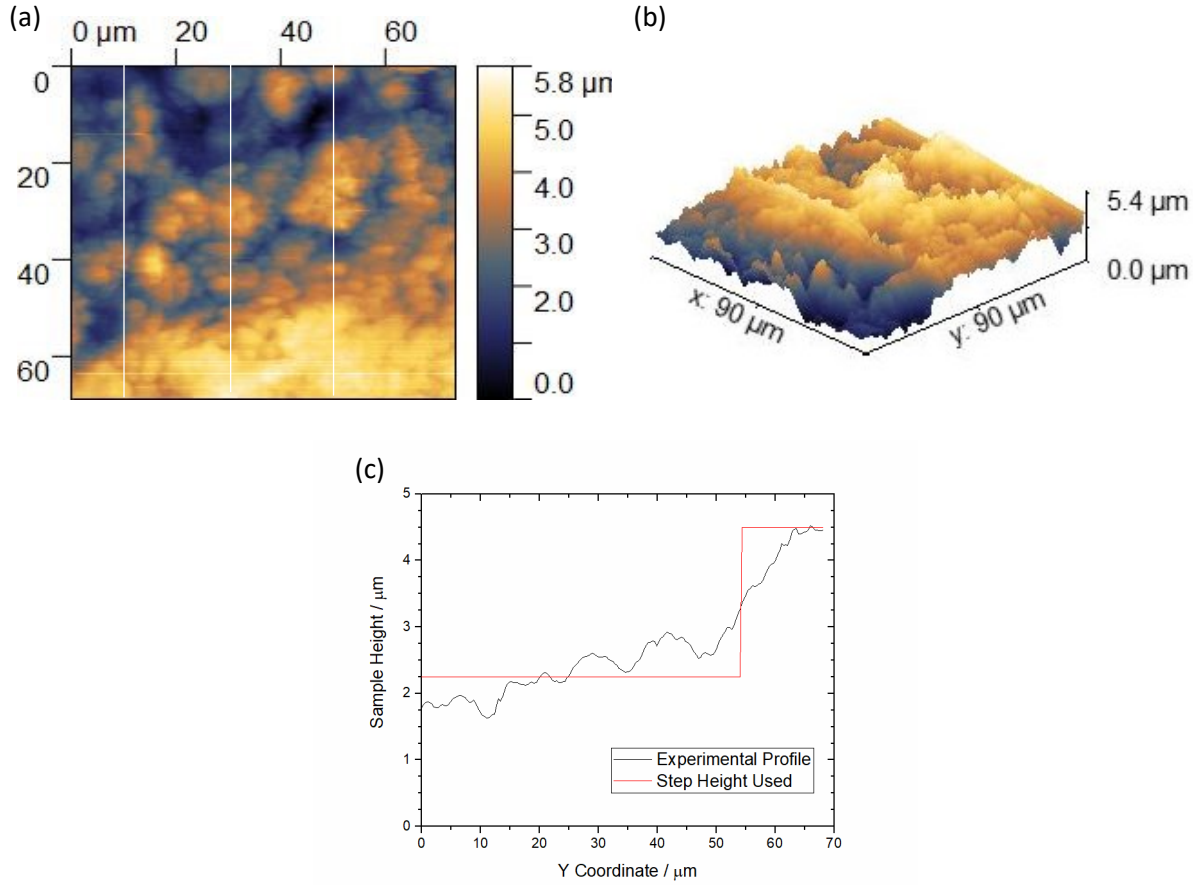


Figure 4.28 AFM studies of ToF-SIMS sputter crater (a/b) AFM of sputter crater, showing 10-pixel linear profiles used to calculate crater depth (white) spaced every 10 µm. (c) Average heights across three linear profiles shown in (a) giving experimental profile and step height calculated from data.

The crater depth calculated varied sample to sample; however, this is expected with varying sputter currents and sputter times. The sputter depth was found to be proportional to sputter time, giving an approximate sputter rate of 1 nm per sputter second.

After converting sputter time to sputter depth, a drop in the intensity of D^- can be observed in the first 20-30 nm of sputtering, see Figure 4.29. This suggests that the charging surface of the $Ni(OH)_2$ is approximately 20 nm into the material. This concurs well with the findings in Chapter 3. To ensure these findings were repeatable beyond the two instances shown in Figures 4.27 and 4.29, further D^- spikes are shown in Appendix 3.

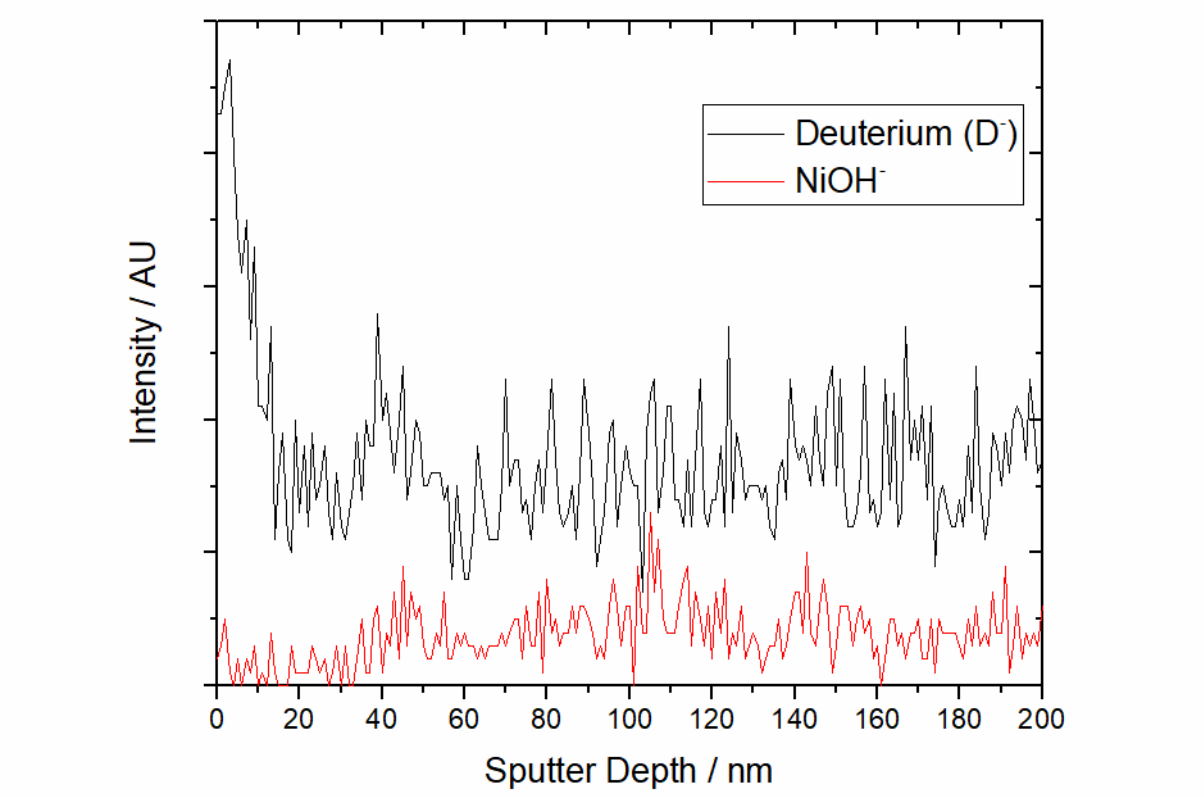


Figure 4.29 ToF-SIMS plots of deuterium ion intensity verses sputter depth. Comparison of D^- ion intensity and $NiOH^-$ ion intensity in a wax coated and ground sample after 1 cycle of charging and discharging at 10 mV s^{-1}. Full procedural details for ToF-SIMS analysis can be found in section 2.3

This demonstrates an empirical method for measuring the charging depth of the charge storage material, without relying on complex *in-situ* methods. It also shows the charging nature of $Ni(OH)_2$ is dependent on a surface "skin", not the entire bulk as assumed for the case of a battery material. The depth of this skin may be dependent on charging rate and requires further investigation.

4.8 Conclusions

Further improving the performance of charge storage devices requires a better understanding of the mechanism through which they store charge. The charging "skin" of $Ni(OH)_2$ has been studied using ToF-SIMS after charging in deuterated solvent. To prevent solvent from entering the bulk of the electrode material through diffusion, a dense non-porous layer is required. Multiple synthesis parameters for electrodeposition were tuned, however a dense enough layer could not be produced. Porosity blocking paraffin wax was then used to prevent electrolyte ingress and the surface was ground flat to expose the electroactive $Ni(OH)_2$.

ToF-SIMS was successfully used to study the deuterium uptake in the samples, giving an insight into the charging mechanism and depth. The relative intensity of deuterium in the sample has been shown to follow the expected increase for single hydrogen or deuterium exchange per nickel ion per charge/discharge cycle. Wax covered samples have also shown deuterium uptake in the first 20 nm of sputtering, suggesting this is the depth of the charging "skin" in the material. Further work is required to improve the signal to noise ratio in the measurement and determine whether the depth of the charging skin is scan rate dependent.

4.9 References

1. Conway, B. E., *Electrochemical Supercapacitors: Scientific Fundamentals and Technological Applications*. Springer US: 1999.
2. Arico, A. S.; Bruce, P.; Scrosati, B.; Tarascon, J.-M.; van Schalkwijk, W., Nanostructured materials for advanced energy conversion and storage devices. *Nat Mater* **2005,** *4* (5), 366-377.
3. Roldan, S.; Barreda, D.; Granda, M.; Menendez, R.; Santamaria, R.; Blanco, C., An approach to classification and capacitance expressions in electrochemical capacitors technology. *Physical Chemistry Chemical Physics* **2015,** *17* (2), 1084-1092.
4. Zhu, Y.; Cao, C.; Tao, S.; Chu, W.; Wu, Z.; Li, Y., Ultrathin Nickel Hydroxide and Oxide Nanosheets: Synthesis, Characterizations and Excellent Supercapacitor Performances. *Scientific Reports* **2014,** *4*, 5787.
5. Yang, M.; Xia, H., Exploration and progress of high-energy supercapacitors and related electrode materials. *Science China Technological Sciences* **2015,** *58* (11), 1851-1863.
6. Shi, F.; Li, L.; Wang, X.-l.; Gu, C.-d.; Tu, J.-p., Metal oxide/hydroxide-based materials for supercapacitors. *RSC Advances* **2014,** *4* (79), 41910-41921.
7. Brousse, T.; Bélanger, D.; Long, J. W., To Be or Not To Be Pseudocapacitive? *Journal of The Electrochemical Society* **2015,** *162* (5), A5185-A5189.
8. Wang, P.; Liu, H.; Xu, Y.; Chen, Y.; Yang, J.; Tan, Q., Supported ultrafine ruthenium oxides with specific capacitance up to 1099 F g−1 for a supercapacitor. *Electrochimica Acta* **2016,** *194*, 211-218.
9. Bode, H.; Dehmelt, K.; Witte, J., Zur kenntnis der nickelhydroxidelektrode—I.Über das nickel (II)-hydroxidhydrat. *Electrochimica Acta* **1966,** *11* (8), 1079-IN1.
10. Aguilera, L.; Leyet, Y.; Padrón-Hernández, E.; Passos, R. R.; Pocrifka, L. A., Understanding electrochemical performance of Ni(OH)2 films: a study contributions to energy storage. *Journal of Solid State Electrochemistry* **2018,** *22* (5), 1621-1628.
11. Vickerman, J. C.; Briggs, D., *ToF-SIMS: Materials Analysis by Mass Spectrometry*. SurfaceSpectra: 2013.
12. Streinz, C. C.; Hartman, A. P.; Motupally, S.; Weidner, J. W., The Effect of Current and Nickel Nitrate Concentration on the Deposition of Nickel Hydroxide Films. *Journal of The Electrochemical Society* **1995,** *142* (4), 1084-1089.
13. Jiang, H.; Guo, Y.; Wang, T.; Zhu, P.-L.; Yu, S.; Yu, Y.; Fu, X.-Z.; Sun, R.; Wong, C.-P., Electrochemical fabrication of Ni(OH)2/Ni 3D porous composite films as integrated capacitive electrodes. *RSC Advances* **2015,** *5* (17), 12931-12936.
14. Wang, Y.-M.; Zhao, D.-D.; Zhao, Y.-Q.; Xu, C.-L.; Li, H.-L., Effect of electrodeposition temperature on the electrochemical performance of a Ni(OH)2 electrode. *RSC Advances* **2012,** *2* (3), 1074-1082.
15. Wu, M.-S.; Huang, Y.-A.; Jow, J.-J.; Yang, W.-D.; Hsieh, C.-Y.; Tsai, H.-M., Anodically potentiostatic deposition of flaky nickel oxide nanostructures and their electrochemical performances. *International Journal of Hydrogen Energy* **2008,** *33* (12), 2921-2926.

16. Wu, M. S.; Huang, Y. A.; Yang, C. H., Capacitive Behavior of Porous Nickel Oxide/Hydroxide Electrodes with Interconnected Nanoflakes Synthesized by Anodic Electrodeposition. *Journal of The Electrochemical Society* **2008,** *155* (11), A798-A805.
17. McEwen, R. S., Crystallographic studies on nickel hydroxide and the higher nickel oxides. *The Journal of Physical Chemistry* **1971,** *75* (12), 1782-1789.
18. Illy, B. N.; Cruickshank, A. C.; Schumann, S.; Da Campo, R.; Jones, T. S.; Heutz, S.; McLachlan, M. A.; McComb, D. W.; Riley, D. J.; Ryan, M. P., Electrodeposition of ZnO layers for photovoltaic applications: controlling film thickness and orientation. *Journal of Materials Chemistry* **2011,** *21* (34), 12949-12957.
19. Chen, L.; Dong, X.; Wang, Y.; Xia, Y., Separating hydrogen and oxygen evolution in alkaline water electrolysis using nickel hydroxide. *Nature Communications* **2016,** *7*, 11741.
20. Li, Z.; Han, J.; Fan, L.; Guo, R., In-situ controllable growth of α-Ni(OH)2 with different morphologies on reduced graphene oxide sheets and capacitive performance for supercapacitors. *Colloid and Polymer Science* **2016,** *294* (4), 681-689.
21. Li, H. B.; Yu, M. H.; Wang, F. X.; Liu, P.; Liang, Y.; Xiao, J.; Wang, C. X.; Tong, Y. X.; Yang, G. W., Amorphous nickel hydroxide nanospheres with ultrahigh capacitance and energy density as electrochemical pseudocapacitor materials. *Nature Communications* **2013,** *4*, 1894.
22. Wang, X.; Luo, H.; Parkhutik, P. V.; Millan, A.-C.; Matveeva, E., Studies of the performance of nanostructural multiphase nickel hydroxide. *Journal of Power Sources* **2003,** *115* (1), 153-160.
23. Yang, G.-W.; Xu, C.-L.; Li, H.-L., Electrodeposited nickel hydroxide on nickel foam with ultrahigh capacitance. *Chemical Communications* **2008,** (48), 6537-6539.
24. Lide, D. R., *CRC Handbook of Chemistry and Physics, 89th Edition*. Taylor & Francis: 2008.

Chapter 5 - Impedance Analysis of Electrodeposited Nickel Hydroxide

Moving away from methods to discern the charging depth in nickel hydroxide, this chapter is concerned with analysis of the charge storage mechanisms themselves. The deconvolution of different charge storage processes is normally impossible using electrochemical analysis such as CV or GCD. However, using electrochemical impedance spectroscopy, the different time scales of the processes can be separated.

The impedance behaviour of the $Ni(OH)_2$ coated electrodes produced by electrochemical deposition in Chapter 4 has been investigated. First an appropriate perturbation potential had to be established. Following this, the impedance at 0.0 V DC potential was studied. This DC potential was then varied to study the changes in behaviour across the potential window used in previous CV analysis. An equivalent circuit model has been proposed, and the fitting of that model to the experimental data has also been reported. The capacitance response to frequency during charging was found and the different mechanisms of charge storage active have been identified based on their different time scales.

Finally, the change in response moving from porous electrodes, such as those normally studied in the literature, to flat wax coated electrodes has been studied. The capacitance response was studied under the same conditions as the porous electrodes and found to no longer exhibit bulk charge storage. The response of the porous electrodes was treated using a semi-infinite pore model, but it was found the data would not map onto the flat electrode data, showing the diffusion into the pores does not follow a semi-infinite model as often assumed in literature.

5.1 Introduction

The ability of nickel hydroxide to exhibit behaviour of both a battery and an electrochemical capacitor material during charge/discharge creates an exciting opportunity. If the charging behaviour can be fully understood, then optimising the materials for either high power or high energy density becomes possible.

In the previous two chapters, the charge stored in nickel hydroxide has been dealt with as a single value. Deconvolution of the contributions of the non-Faradaic electrical double layer and Faradaic redox reactions to the charge stored will aid device optimisation.

Electrochemical impedance spectroscopy (EIS) is the ideal technique to do this. Altering the frequency of analysis allows the different capacitive processes to be studied due to their different time constants. By varying the DC potential applied during the analysis, the dominating capacitive effect will change, allowing the different mechanisms of charge storage to be studied.

To properly describe EIS data, a circuit model based on the understanding of the system must be built. EIS has frequently been utilised in the literature for the study of energy storage materials.[1-3] The energy storage processes, as well as the resistance and diffusion elements of the electrode must be considered.

The most commonly used equivalent circuit for a simple electrochemical process is the simplified Randles circuit, Figure 5.1a.[3] The series Ohmic resistances can be represented by a single resistor, R_S. This includes the bulk resistance of the electrolyte and the electrode, as well as the contact resistance of the electrode and the electrolyte.[4]

The energy storage processes are then represented by a capacitive circuit element parallel to a second resistor, R. The physical meaning of the capacitor varies depending on the energy storage process. In the case of a double layer capacitance, C_{EDL}, this capacitive element is a combination of the Helmholtz and diffuse layer capacitances. For a semiconductor, the space-charge capacitance will dominate. See Section 1.4 for further details. The resistor in parallel to the double layer capacitance is known as the leakage resistance or the charge transfer resistance, R_{CT}.

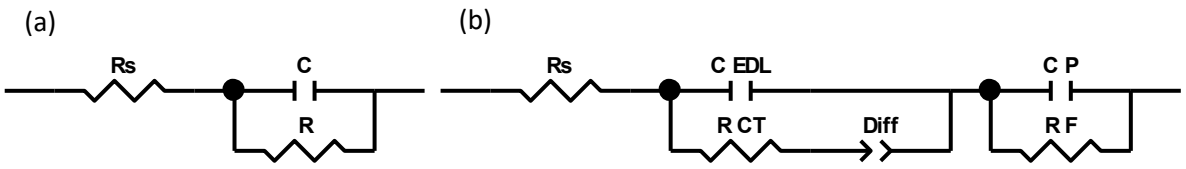


Figure 5.1 Equivalent circuit diagrams used in the characterisation of energy storage materials (a) Randles Cell (b) Combined EDL and Faradaic capacitances

In the case of Faradaic pseudocapacitance, the redox reaction can be represented by a second capacitive element, C_P, in parallel to a Faradaic resistance, R_F. Since both Faradaic and non-Faradaic energy storage mechanisms will be in effect to some extent, both must be included in the representative circuit model, see Figure 5.1b. An extra circuit component is also added

in parallel to the double layer capacitance. This is to represent the diffusion of the reacting ions to the electrode surface. The nature of the component is dependent on the relative size of the diffusion length to the length of concentration perturbation at the electrode surface. This is further discussed in Section 5.6.

The mechanisms of the Faradaic redox reactions and non-Faradaic EDL contributions to charge storage are explained in Section 1.4. In the specific case of $Ni(OH)_2$ coated electrodes, the Faradaic contribution to the charge stored is due to the oxidation of the nickel hydroxide to the oxyhydroxide. This oxidation occurs at approximately 0.3 V - 0.5 V *vs* Hg/HgO reference electrode. The subsequent reduction occurs at a slightly lower potential. The electrochemical activity of nickel hydroxide is fully discussed in Section 1.6.2.

When analysing EIS data for energy storage materials, care must be taken to ensure the design of the equivalent circuit is not chosen to maximise fit, at the expense of physical meaning. In addition, the impedance is often studied at a single DC potential, rather than varying across the potential range typically studied in other techniques such as cyclic voltammetry. This chapter will present a systematic study of the impedance of an electrodeposited $Ni(OH)_2$ electrode at various DC potentials in order to understand the changing contribution of charge storage effects during charge and discharge.

To fully elucidate the effect of the electrode structure on the electrochemical response, both porous and flat electrodes are required. A method for producing non-porous flat $Ni(OH)_2$ coated electrodes was introduced in Chapter 4 and is used again in this work.

5.2 Synthesis Method and Preparation of Impermeable $Ni(OH)_2$ Films

After studying various synthesis methods, see the previous two chapters, it was decided that the electrodeposition method was the most suitable for this study. Aside from consistently producing nanostructured films with the same particle size and morphology, the porosity and film thickness were already shown to be easily controllable, as shown in Section 4.3.4.

The same synthesis method to the one used in Section 4.3.7 was employed. Conditions for syntheses were chosen with consideration of film thickness and to ensure stable growth. This involved using a deposition potential at the low end of the successful experiments from the previous chapter, in this case -0.9 V. A deposition time of 5 minutes was selected as this was

shown in Section 4.3.4 to produce thick films of around a micron with no visible bare electrode. These conditions were selected to ensure that no large gaps formed in the deposited layer, and the entire electrode surface was covered in $Ni(OH)_2$. To produce non-porous electrodes, the same wax coating and grinding procedure used in Section 4.6 was utilised.

As with the previous chapter, the electrochemical deposition was shown to be multilayer. This was demonstrated by the thickness of the film and the current steps in the deposition current vs time plot, Figure 4.9.

5.3 Structural Characterisation of Electrodeposited $Ni(OH)_2$

Before attempting to understand the electrochemical behaviour of the material, it is important to confirm the chemical composition and structure of the samples. Understanding the particle nature and the microstructure is also key in determining the expected circuit model in the analysis of EIS data.

The full structural characterisation of the electrodeposited $Ni(OH)_2$ using SEM, XPS, EDX, XRD, and BET is discussed in Section 4.4. The full analysis will not be repeated in this chapter; however, a brief summary of findings is presented.

SEM micrographs show the films produced under the selected experimental conditions are formed of spherical particles of around 100-150 nm in diameter. The structure is highly porous, allowing for electrolyte ingress into the bulk, see Figure 4.8a/b. The porous nature of the electrodeposited films was confirmed using BET, with specific surface areas for the $Ni(OH)_2$ deposited electrodes of around 150 $m^2\ g^{-1}$.

EDX and XPS analyses was performed to confirm the identity of the film as $Ni(OH)_2$. EDX analysis showed a Ni:O ratio of 0.5 for all samples, a typical spectrum can be seen in Figure 4.12. Binding energies found using XPS analysis were characteristic of $Ni(OH)_2$ and in good agreement with previously reported data, see Figures 4.10 and 4.11.

As with the previous electrodeposited samples in Chapter 4, the amorphous nature of the particles meant no strong peaks could be observed in the X-ray diffractogram. This is despite the sample mass loading being higher than samples successfully measured using the same methodology in Chapter 3. An example diffractogram is shown in Figure 4.13.

5.4 Electrochemical Characterisation of Electrodeposited $Ni(OH)_2$

The initial electrochemical characterisation of the electrodeposited $Ni(OH)_2$ electrode is discussed in Section 4.5. Cyclic voltammograms show the expected shape and peaks for nickel hydroxide, as shown in Figure 4.15.[5-6] The deposition time of 5 minutes ensured that the film deposited with sufficient thickness that the mass loading was suitable. As shown in Figure 3.18, a minimum mass loading of 1 mg cm^{-2} is necessary to achieve a representative specific capacitance / capacity.

Using "*b*-value" analysis, the dynamics of the charge storage in the $Ni(OH)_2$ can be analysed by comparing the peak currents in the CV to the scan rate, v. This is similar to Randles-Sevcik analysis shown in Section 3.5.2. The peak current I_{max} obeys the relation shown in Equation (5.1);

$$I_{max} = a v^b \tag{5.1}$$

where *a* and *b* are constants. A *b*-value of 1 is indicative of Faradaic surface reactions expected in capacitive charge storage, where as a value of 0.5 is indicative of semi-infinite diffusion controlled processes, such as intercalation reactions used in battery-type electrodes.[7] By

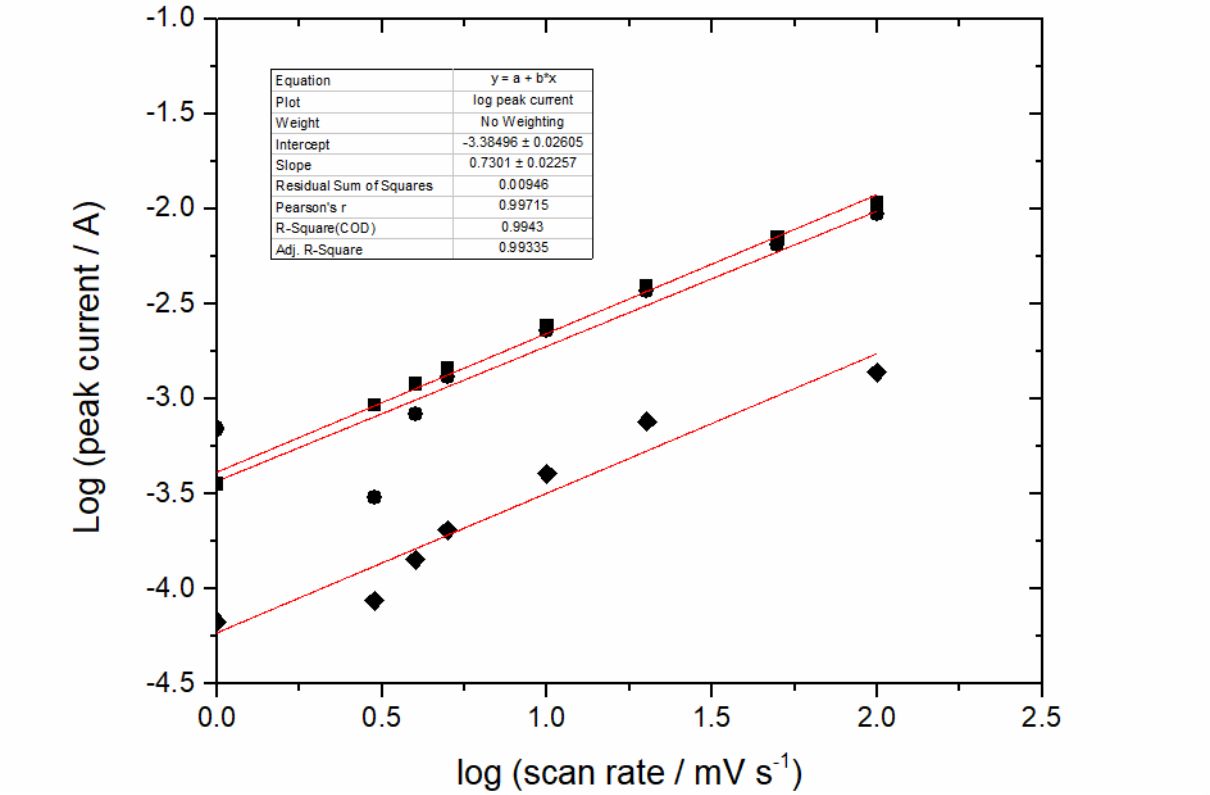


Figure 5.2 The b-value analysis of $Ni(OH)_2$ coated electrodes over multiple syntheses. Samples produced using the standard potentiostatic electrodeposition procedure at -0.9 V, -1.1 V and -1.3 V. Different syntheses shown using different shaped points. Inset is fitting parameters for one of the data sets.

plotting the log of the scan rate vs the log of the peak current, the *b*-value for the $Ni(OH)_2$ coated electrodes was found to be around 0.72 ± 0.01 over multiple samples, Figure 5.2.

The *b*-value for the $Ni(OH)_2$ coated electrodes has shown to be intermediate to the two extremes. This is usually indicative of finite diffusion-controlled behaviour within the time scales of the analysis. The intermediate *b*-value is an indicator that both a mass transport limited intercalation, and a diffusion-independent Faradaic surface reaction are contributing to charge storage.[7-8]

5.5 Determination of Perturbation Potential

For EIS analysis, a linear response between the applied potential and the current is assumed. AC impedance theory was originally based on electronic components such as resistors and capacitors. These components give a linear current response to potential. If the most common potential input $E(t)$, a sine wave, is used then the current output *I(t)* should also follow a sine wave. This is shown in Equations (5.2) and (5.3). This allows the impedance to be calculated according to Equation (5.4);[9]

$$E(t) = E^0\sin(\omega t) \tag{5.2}$$

$$I(t) = i^0\sin(\omega t+\theta) \tag{5.3}$$

$$Z(\omega) = |Z(\omega)|e^{i\theta} \tag{5.4}$$

where ω is angular frequency, *t* is time in seconds, and θ is the phase difference. This linear relationship is not always followed however, as is often the case for electrochemical systems where the current (I) is typically exponentially dependant on the change in potential (ΔE), as described by the Butler-Volmer Equation, Equation (5.5);[10]

$$I = I^0[\exp((\alpha_a zF/RT)(\eta+\Delta E)- \exp((\alpha_c zF/RT)(\eta+\Delta E)] \tag{5.5}$$

where I^0 is the exchange current density, $\alpha_{a/c}$ are dimensionless anodic and cathodic charge transfer coefficients respectively, z is the number of electrons transferred in the reaction, η is the overpotential, F is the Faraday constant (96485 C mol^{-1}), R is the universal gas constant (8.314 J mol^{-1} K^{-1}), and T is the temperature in K.

When ΔE is small, the Equation of quasi-linearization, Equation (5.6), can be used.

$$e^x \approx 1 + x \tag{5.6}$$

Following this assumption, the current is now proportional to the potential, restoring the linear behaviour required for AC impedance analysis. Therefore, when choosing the perturbation potential, it is important to choose a small enough potential that this assumption is valid. It is also necessary to choose the highest possible perturbation potential in order to minimise the signal to noise ratio.[9]

To decide on which perturbation potential to use, samples were initially run at an AC potential of 5 mV, 10 mV, 15 mV, and 20 mV, with a DC potential of 0 V. This allowed for the difference in the impedance response to be assessed and a suitable perturbation potential to be found. An example of the data obtained is shown in Figure 5.3.

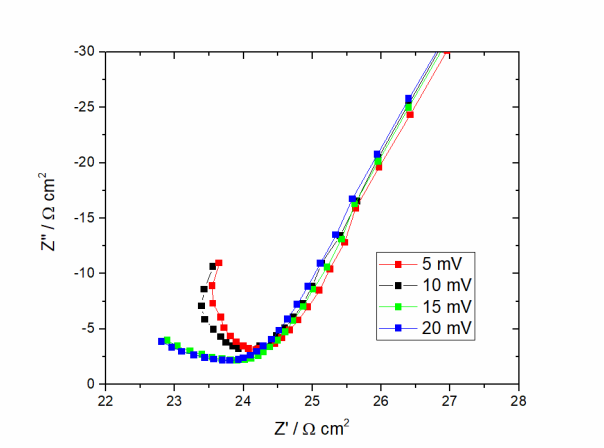


Figure 5.3 Nyquist plot at various perturbation potentials at 0.0 V DC potential.

The high frequency region was chosen for the analysis as it has the least noise, particularly at low AC potential. The Nyquist plot showed a similar response up to 10 mV, after which the measured impedance of the high frequencies deviated. At low frequencies, 10 mV perturbation offered significantly less noise than 5 mV. Therefore 10 mV perturbation was used throughout the following experiments.

5.6 Impedance of Porous $Ni(OH)_2$ Coated Electrodes at 0.0 V DC

The electrochemical cell schematic is shown in Section 2.4.1 while the experimental setup and methodology for EIS is fully described in Section 2.4.4. The resistance and reactance of the $Ni(OH)_2$ coated electrode at a DC potential of 0 V are plotted, Figure 5.4a/b. The data points are connected as a guide to the order in which the data points were acquired.

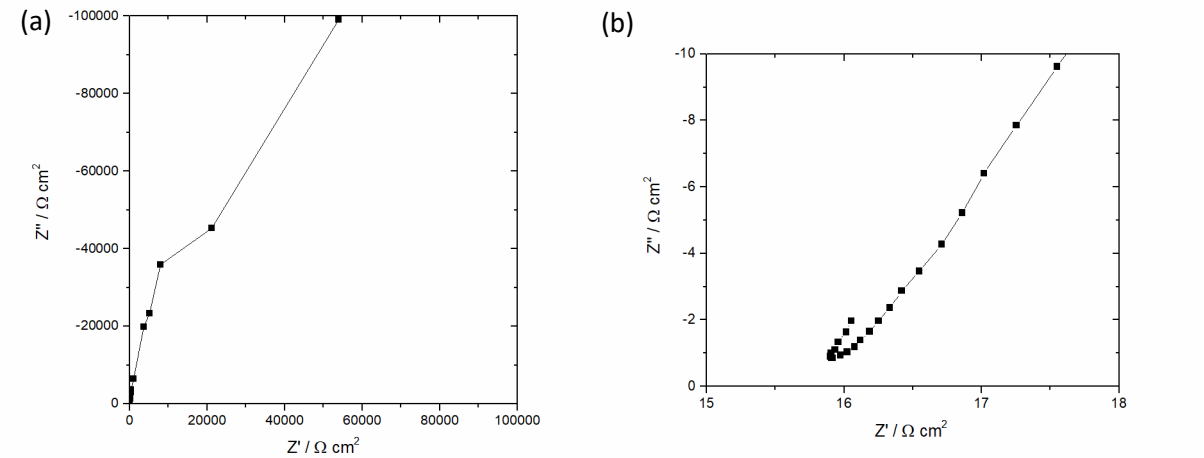


Figure 5.4 Nyquist plots of $Ni(OH)_2$ coated electrode at 0.0 V DC potential and a perturbation potential of 10 mV (a) Whole frequency range (b) High frequency range only

The plot is composed of two partial semi-circles in the higher frequency region, followed by a straight line in the lower frequency region. The extrapolated intercept of the plot with the real axis gives the series resistance, R_s, of around 16 Ω. This is a combination of the Ohmic resistances in the electrode, as discussed in Section 5.1. The diameter of the semi-circular regions yields the resistances associated with the capacitive processes due to the movement of electrons through the solid.

To analyse the EIS data, the equivalent circuit shown in Figure 5.1b was used. Modelling the diffusion of the reacting ions in the system requires a consideration of the type of diffusion occurring. The circuit component usually used in the modelling of charge carrier diffusion through a solid or liquid is known as a Warburg element.[9]

Typically, when modelling a system in which the electrode is immersed in a bulk electrolyte, the diffusion length of the ions from the bulk can be thought of as infinitely long when compared to the length of concentration perturbation at the electrode surface. Assuming the concentration perturbation ended in the bulk of the electrolyte, Fick's second law Equation can be solved to show the concentration perturbation at the interface of the electrode is 45° out of phase with the excitation current. This is seen in the Nyquist plot as a 45° line between

the real and imaginary components of impedance.[11] The element used to model this behaviour is known as an semi-infinite Warburg, W_{SI} .

The linear low frequency section of the Nyquist plot gives a phase angle significantly higher than the 45° expected for bulk diffusion represented by a semi-infinite Warburg. This is because the initial data was taken at 0.0 V with no Faradaic reaction, so there is no bulk diffusion occurring. The deviation from 90°, expected for a flat electrode, is due to the porosity of the $Ni(OH)_2$ coating. This is also shown in the Bode plot, Figure 5.5, which shows the change in phase angle with frequency.

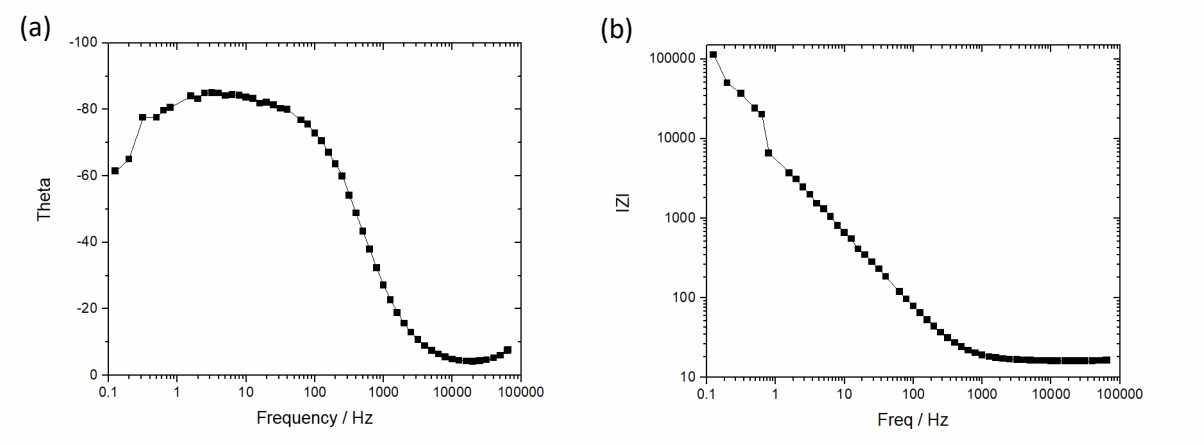


Figure 5.5 Bode Plots of $Ni(OH)_2$ coated electrodes at 0.0 V DC potential and 10 mV perturbation

For a nanoporous material, like the $Ni(OH)_2$ being studied, the assumption that the ion diffusion lengths involved are significantly longer than the concentration perturbation length may not hold. Diffusion of the charge carriers takes place in the electrode pores or in the solid phase of the electrode, giving short diffusion lengths.[9, 11]

In addition, the thin porous structure means that the charge carriers will penetrate into the entire thickness of the material during low frequency modulation. When the thickness of the material is large relative to the effective diffusion length in the active material, a typical semi-infinite Warburg type response can be expected.[11]

A finite Warburg can result in either an open circuit or short circuit terminus. If the thickness of the active material or the effective diffusion length is significantly shorter than the concentration perturbation length, the phase angle tends to 90° and behaviour similar to a pure capacitor is seen, giving an open circuit at low frequencies. If the effective diffusion and

concentration perturbation lengths are similar however, the phase will reduce with frequency and a semi-circle in the low frequency region will be seen in the Nyquist plot.[11]

In these studies, the Warburg short was selected as the layer deposited was thin, and it was expected that the ionic diffusion would penetrate the entire layer at low frequencies. The Warburg short (W_s), is defined by three parameters, which give the impedance (Z) according to Equation (5.7);

$$Z = R \tanh([IT\omega]^P) / (IT\omega)^P \quad (5.7)$$

where I is the current. The R parameter is the resistance of the medium at low frequency. The P parameter is the phase ratio between 0 and 1, with 0.5 being equal to a 45° phase shift. Finally, T is the ratio of effective diffusion thickness (L) and the diffusion coefficient in the medium (D), Equation (5.8).

$$T = L^2 / D \quad (5.8)$$

Using the finite Warburg circuit element, the new circuit model is shown in Figure 5.6. A table of values along with a percentage error for the circuit elements which best fit the experimental data is given in Table 5.1.

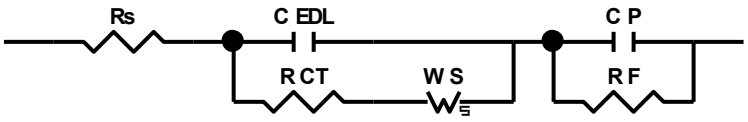


Figure 5.6 Equivalent circuit for the modelling of $Ni(OH)_2$ coated electrodes

The fit of the model to the experimental data is shown in Figures 5.7a/b. There is a small feature at high frequencies, shown in Figure 5.4b. This feature was discounted from the initial investigation due to the likelihood of it being a machine produced artefact. This was confirmed by the lack of variation in this feature over multiple measurements and is discussed further in Section 5.7. Due to this feature, the ohmic resistance R_s was fixed at 16 Ω for the circuit analysis.

The analysis was initially run without the C_P / R_F elements since there should be no oxidation of the $Ni(OH)_2$ at 0.0 V. The errors given matched those calculated with the elements added

back in; however, the error on the C_P / R_F elements is significantly higher than that of the C_{EDL} / R_{CT} elements since there is no oxidation occurring.

Table 5.1 Circuit component values for $Ni(OH)_2$ coated electrodes at 0.0 V DC potential and 10 mV perturbation potential calculated using equivalent circuit in Figure 5.6

Element	Freedom	Value	Error / %
R_s	Fixed	16 Ω cm^{-2}	N/A
C_{EDL}	Free	$1.7x10^{-2}$ F g^{-1}	2
R_{CT}	Free	15.8 Ω cm^{-2}	1
$W_s - R$	Free	490 Ω cm^{-2}	9
$W_s - T$	Free	1.98	0.05
$W_s - P$	Free	0.98	0.02
C_P	Free	$2.11x10^{-2}$ F g^{-1}	10
R_F	Free	12000 Ω cm^{-2}	9

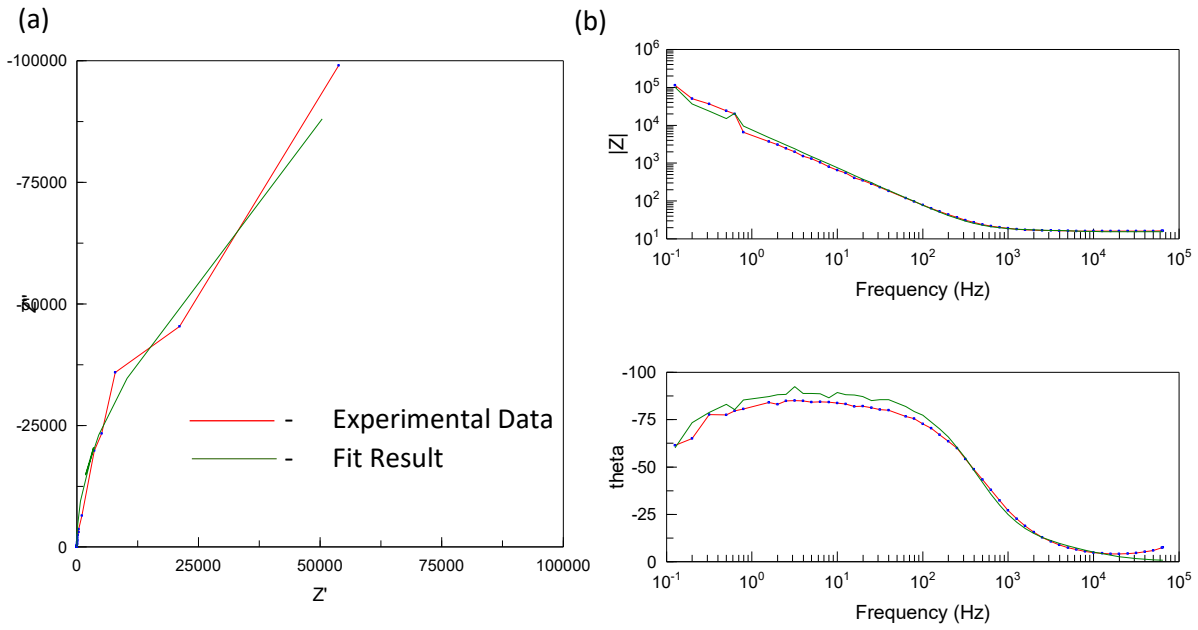


Figure 5.7 Fitting of equivalent circuit model to experimental data for $Ni(OH)_2$ coated electrodes at 0.0 V DC potential and 10 mV perturbation (a) Nyquist plot (b) Bode Plots

The Faradaic charge storage measurement for the material is very low, and the Faradaic resistance is very high. This is expected, however, due to the DC potential being well below the redox potential of the $Ni(OH)_2$.

5.7 Variation of Impedance with DC Potential in Porous $Ni(OH)_2$ Electrodes

As discussed in Section 2.4.4, the impedance of the $Ni(OH)_2$ coated electrodes was studied in the DC potential range of 0.0 V – 0.7 V with measurements taken at 0.1 V intervals. This was to simulate the cycling of the electrodes in alkaline electrolyte as in previous chapters. Impedance measurement at different DC potentials allowed the different mechanisms of charge storage to be studied by fitting to the equivalent circuit shown in Figure 5.6. The fitted results compared to the experimental data are shown in full in Appendix 4.

Initially, the high frequency region of the EIS spectra of the $Ni(OH)_2$ coated electrodes at 0.0 V – 0.7 V DC were analysed, see Figure 5.8. As expected, the series resistance is shown not to vary from 16 Ω when the DC potential increases from 0.0 V to 0.7 V, suggesting there is no major change in the series resistance with DC potential. The high frequency tail, discussed in Section 5.6, is also unchanged on the increase in DC potential. This suggests that it is a feature caused by the machine set-up and not a feature of the working electrode.

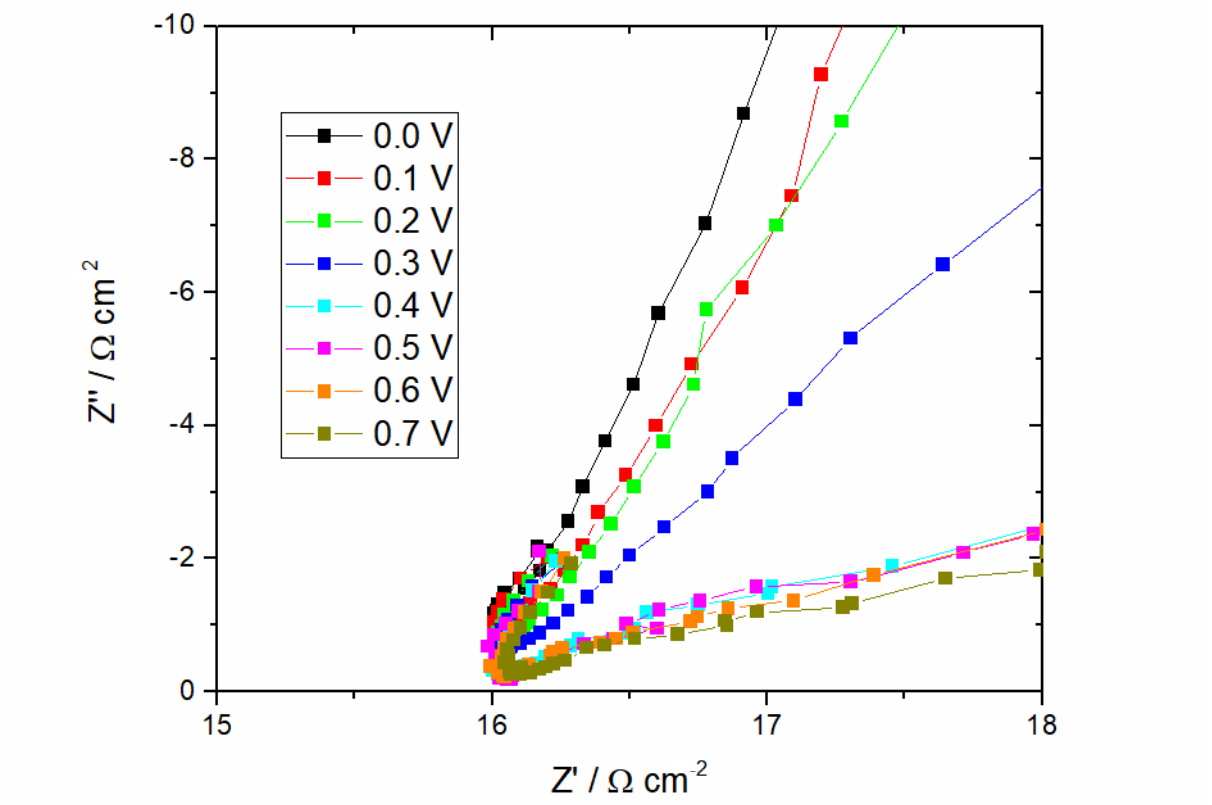


Figure 5.8 Nyquist plot of $Ni(OH)_2$ coated electrodes at various DC potentials and 10 mV AC perturbation, high frequency region only

Full Nyquist plots of the $Ni(OH)_2$ coated electrodes at 0.1 V – 0.7 V DC are shown in Figures 5.9a/b. For full data set at 0.0 V, refer back to Figure 5.4a.

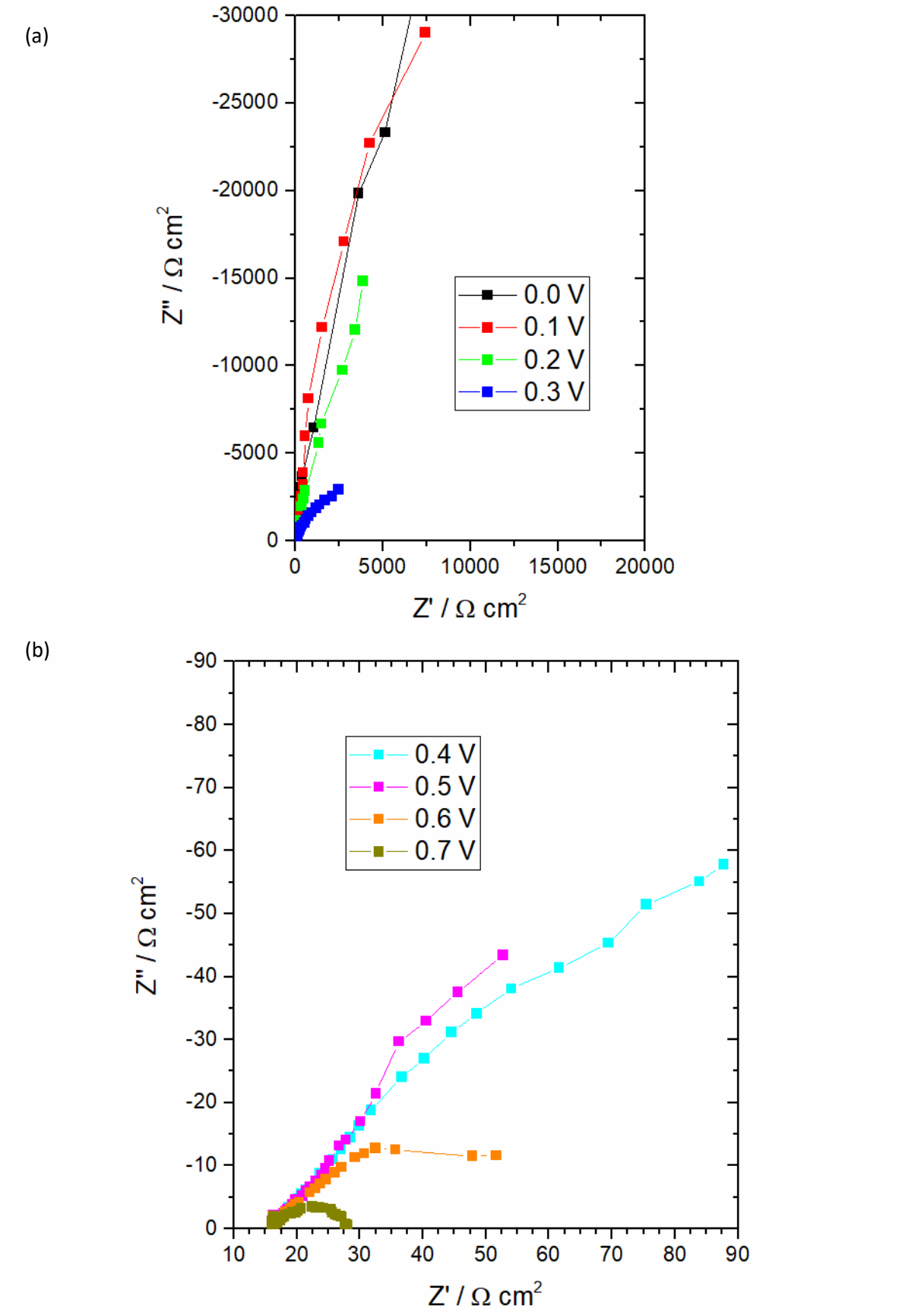


Figure 5.9 Nyquist plot of $Ni(OH)_2$ coated electrodes at various DC potentials and 10 mV AC perturbation (a) 0.0 V – 0.3 V (b) 0.4 V – 0.7 V.

To ensure the circuit model shown in Figure 5.6 is still valid, an example of the fitted data at 0.7 V DC potential is shown in Figure 5.10a/b with the best fitting values for the circuit components given in Table 5.2.

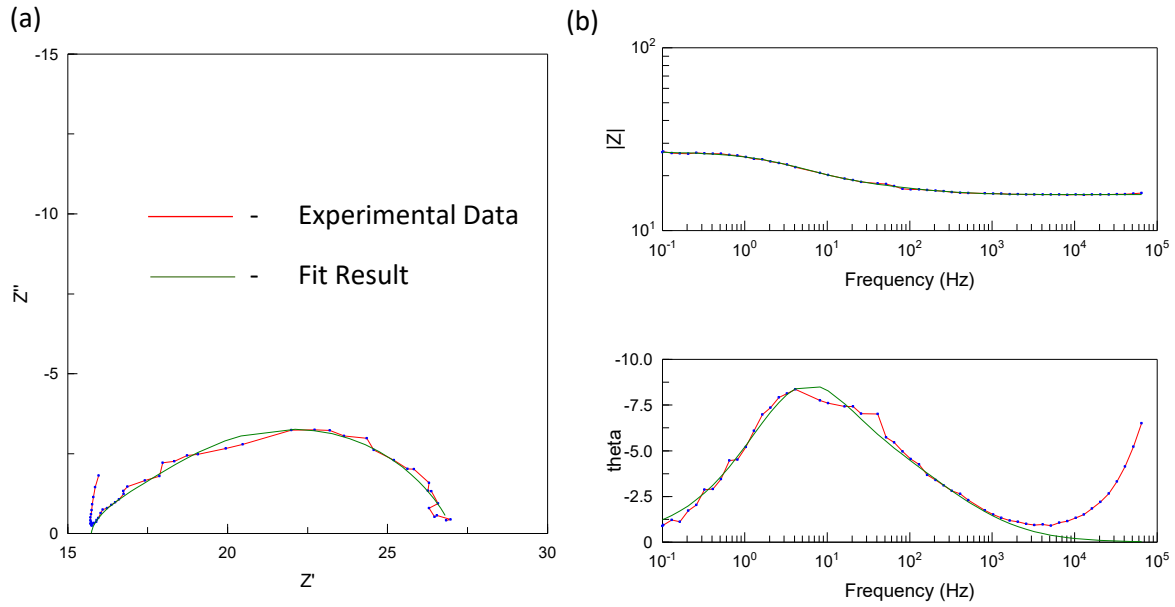


Figure 5.10 Fitting of equivalent circuit model to experimental data for $Ni(OH)_2$ coated electrodes at 0.7 V DC potential and 10 mV perturbation (a) Nyquist plot (b) Bode Plots

Table 5.2 Circuit component values for $Ni(OH)_2$ coated electrodes at 0.7 V DC potential and 10 mV perturbation potential calculated using equivalent circuit in Figure 5.6

Element	Freedom	Value	Error / %
R_S	Fixed	16 Ω cm^{-2}	N/A
C_{EDL}	Free	$5.4x10^{-1}$ F g^{-1}	10
R_{CT}	Free	5.9 Ω cm^{-2}	5
$W_S - R$	Free	12 Ω cm^{-2}	9
$W_S - T$	Free	0.16	10
$W_S - P$	Free	0.07	7
C_P	Free	7.5 F g^{-1}	10
R_F	Free	5.9 Ω cm^{-2}	7

The values of the fitted capacitor circuit elements with varying DC potential are shown in Figure 5.11. A full list of the values of the circuit elements that best fit the experimental data can be seen in Appendix 5.

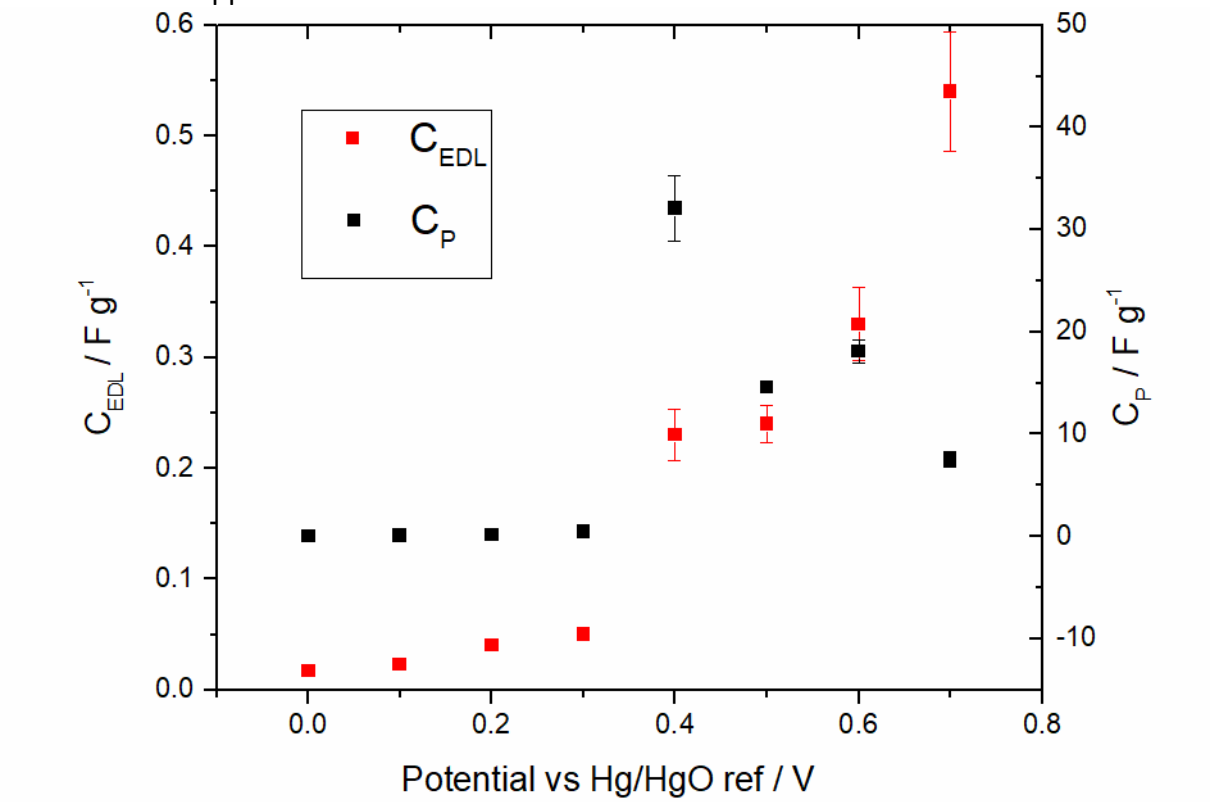


Figure 5.11 Variation in capacitive equivalent circuit component values with applied DC potential for $Ni(OH)_2$ coated electrodes charging from 0.0 V to 0.7 V and 10 mV AC perturbation potential calculated using equivalent circuit in Figure 5.6

As expected, there is a large increase in the capacitance of the circuit element representing the pseudocapacitive charge storage at around 0.4 V. This is due to the oxidation of the $Ni(OH)_2$ at this potential. This activity is still maintained at potentials above 0.4 V, suggesting there is still oxidation occurring. The capacitance is lower than the values measured in previous chapters, however this is due to the high mass loading of the electrodes.

As the DC potential increases from 0.0 V to 0.7 V, the low frequency depressed semi-circle becomes more pronounced. At 0.7 V, the semi-circle reaches back down to the real axis at low frequency, showing the system is acting as a perfect ohmic resistance at this DC potential. This shows the system is now shorting, and that charge carriers are now penetrating the entirety of the electrode at this low frequency. The capacitance of the circuit element representing the double layer capacitance also increases with the DC potential. This increase is represented in the plots by a decrease in the diameter of the high frequency semi-circle, which shows a decrease in R_{CT}. This increase in capacitance is also expected as the increase in polarisation of the electrode should increase the capacitance of the double layer formed at

the electrode surface according to Equation 1.5. The Bode plots of the variation of the magnitude of *Z* and the phase angle with frequency are shown in Figure 5.12a/b.

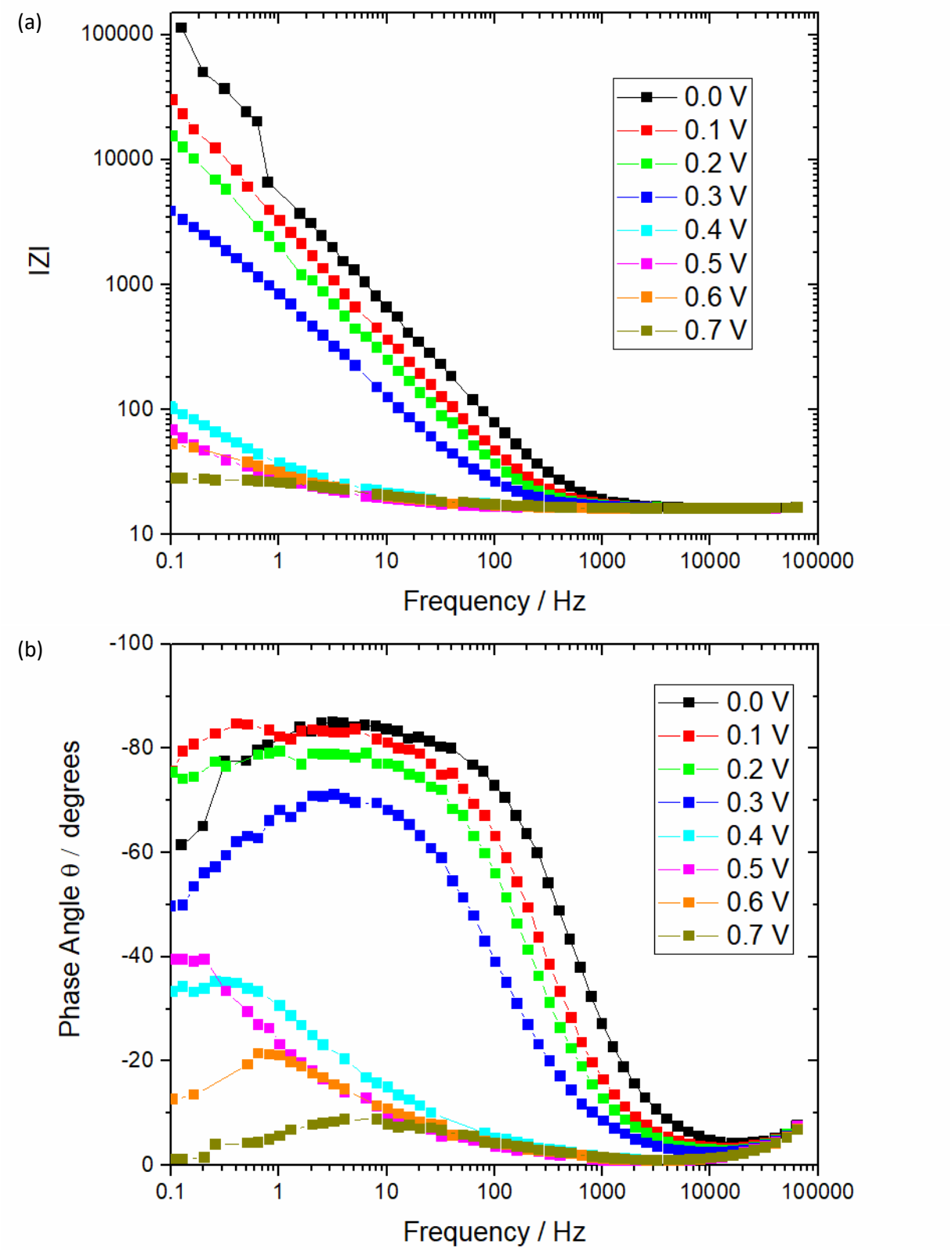


Figure 5.12 Bode plots of $Ni(OH)_2$ coated electrodes at various DC potentials 0.0 V – 0.7 V and 10 mV AC perturbation (a) variation of $|Z|$ (b) variation of θ

The magnitude of the impedance decreases by three orders of magnitude as the DC potential varies from 0.0 V to 0.7 V. The series resistance of the electrode does not change with the DC potential, as shown in Figure 5.8, which suggests the bulk resistance of the electrolyte and the electrode, as well as the contact resistance of the electrode and the electrolyte is also constant. The decrease in impedance with the DC potential is therefore due to the charge transfer processes occurring at the electrode surface.

For a more detailed analysis of the capacitance, the Bode representation of the impedance data can be used to separate the capacitive processes based on the time scales of the process. The real component of capacitance, *C'*, can be calculated from the imaginary component of impedance, *Z''*, using Equation (5.9);[7]

$$Z'' = \tfrac{1}{2}\pi f C' \tag{5.9}$$

where *f* is the frequency. The capacitive processes represented by *C'* are fast and reversible at the given frequency and perturbation potential. The change in *C'* with frequency at different potentials is shown in Figure 5.13.

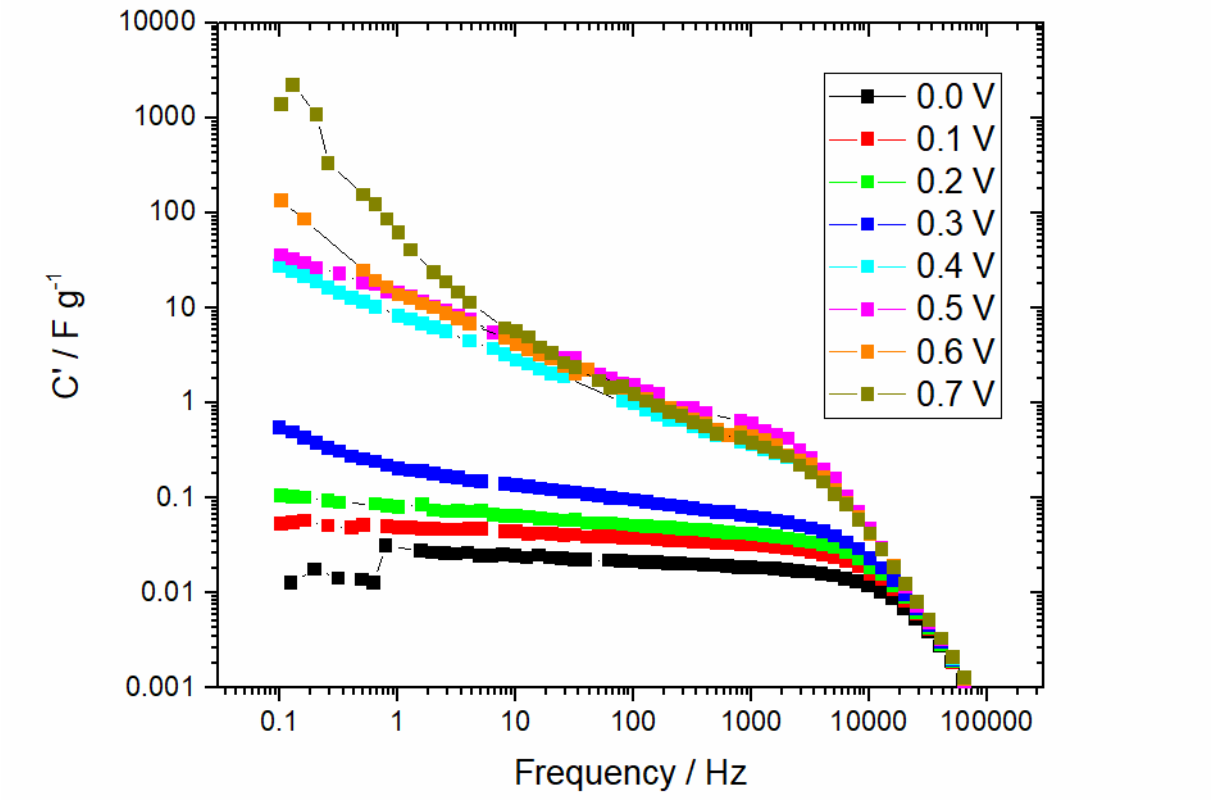


Figure 5.13 Capacitance analysis of $Ni(OH)_2$ coated electrodes at various DC potentials 0.0 V – 0.7 V and 10 mV AC perturbation vs frequency.

At high frequencies, down to $1x10^4$ Hz, the response of the capacitance to frequency at all potentials is similar. The capacitance increases with decreasing frequency, as expected for a porous electrode.[11]

Below 0.3 V DC potential, the capacitance remains constant below this frequency as the time scale of the formation of the double layer is much faster than the frequency of the perturbation. The measured capacitance is steady at each potential between 0.01 F g^{-1} at 0.0 V and 0.5 F g^{-1} at 0.3 V. These low capacitances are consistent with the capacitances measured using the circuit model given in Table 5.3. Even below the oxidation potential of the $Ni(OH)_2$, around 0.4 V, the Faradaic charge storage is still 10 x the capacitance of the non-Faradaic C_{EDL}.

Above 0.3 V, there is a 2-3 order of magnitude increase in *C'*. While this increase is consistent with the best fitting values predicted by the circuit model, the size of the increase is significantly larger than that given by the circuit model. At 0.4 V and 0.5 V DC potential, there is a steady increase in capacitance with frequency.

Above 0.5 V, there is another sharp deviation at a frequency of around 10 Hz. This could be indicative of a further charge storage process, with some insertion into the bulk of the material at these low rates. At 0.7 V, the capacitance is reaching around 1000-3000 F g^{-1}. This is consistent with the theoretical maximum and the highest measured pseudocapacitive charge storage of $Ni(OH)_2$ in previous studies.[6, 12]

Following the analysis of the impedance while charging from 0.0 V to 0.7 V, the impedance on discharge was also studied, as shown in Figure 5.14a-d. The shape of the Nyquist plots is retained after charging, showing the reversibility of the charge/discharge reactions, Figure 5.14a/b.

The phase behaviour, Figure 5.14d, also follows the same trend as on charging, with the exception of 0.3 V DC potential, where the phase falls to well below the phase measured on charging. This is due to the reduction reaction of Ni(OOH) back to $Ni(OH)_2$ occurring at a lower potential than the oxidation, as shown in cyclic voltammograms such as Figure 4.15. The phase angle at low frequency is closest to 45° at 0.4 V and 0.5 V DC potential for both charging and discharging. Since this is the potential at which the reduction of the $Ni(OH)_2$ or the oxidation of the Ni(OOH) is expected to occur, it is not surprising that this is the DC potential at which diffusion control dominates.

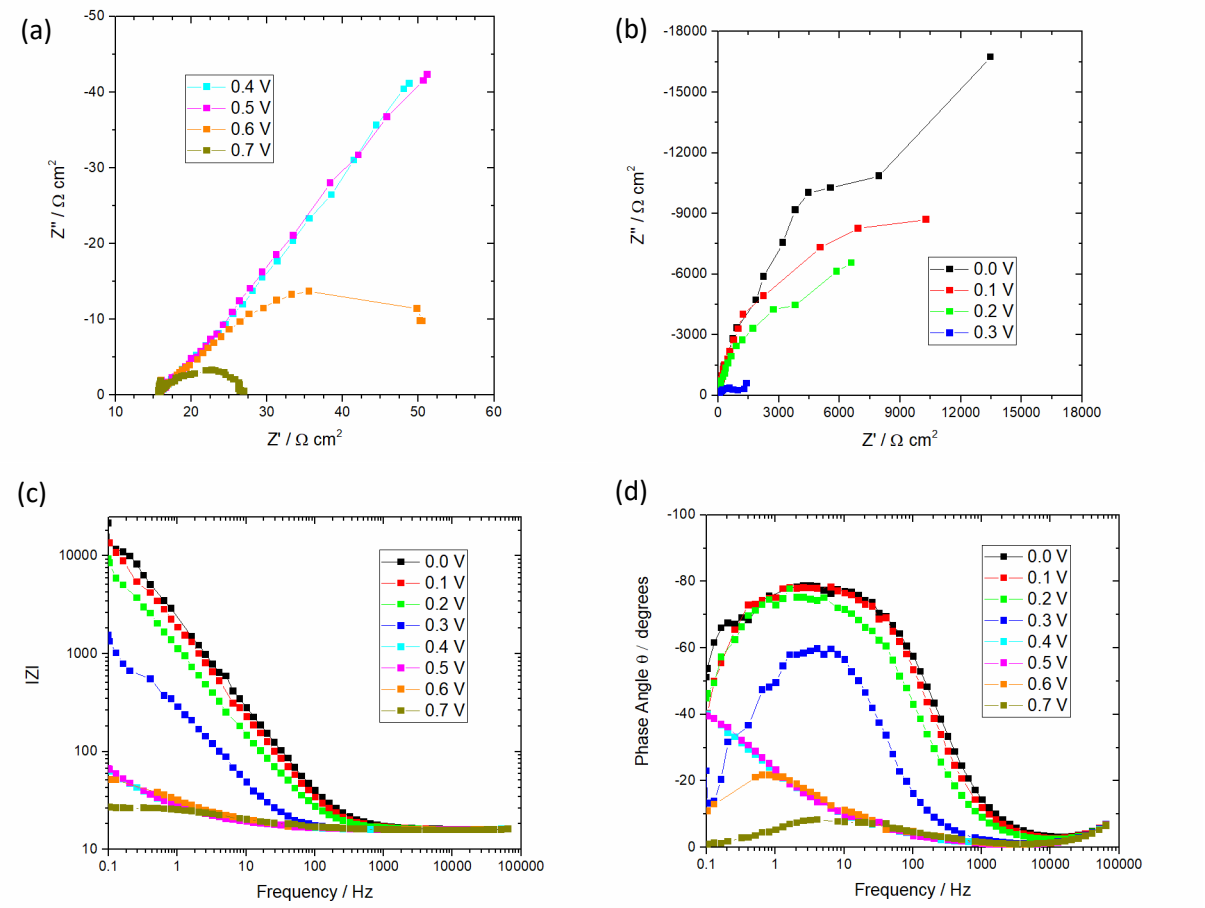


Figure 5.14 Impedance response of $Ni(OH)_2$ coated electrodes at various DC potentials and 10 mV AC perturbation (a) Nyquist plot 0.7 V – 0.4 V (b) Nyquist plot 0.3 V – 0.0 V (c) Bode plot showing variation of $|Z|$ with frequency (d) Bode plot showing variation of θ with frequency

The magnitude of the impedance, Figure 5.14c, is significantly lower on discharge compared to the original starting $Ni(OH)_2$ material. This is likely due to the introduction of defects after the first charging cycle. The capacitance values for the best fitting circuit elements on discharge is given in Table 5.3.

Table 5.3 Capacitive circuit component values for $Ni(OH)_2$ coated electrodes at various DC potentials discharging from 0.7 V to 0.0 V and 10 mV AC perturbation potential calculated using equivalent circuit in Figure 5.6

DC Potential / V	C_{EDL} / F g^{-1}	Error in C_{EDL} / %	C_P / F g^{-1}	Error in C_P / %
0.7	$8.1x10^{-1}$	8	8.8	10
0.6	1.4	7	20	10
0.5	1.5	6	20	9
0.4	1.7	4	15	20
0.3	$5.\ 1x10^{-1}$	20	7	10
0.2	$1.2x10^{-1}$	5	$2.0x10^{-1}$	9
0.1	$7.4x10^{-2}$	5	$1.8x10^{-1}$	10
0.0	$5.9x10^{-2}$	7	$1.4x10^{-1}$	10

While the best fit values for C_{EDL} were comparable to those calculated using charging data, the measured C_P values are an order of magnitude higher after a full charge and discharge cycle. This is consistent with CV findings, where a small increase in charge stored after the first few cycles was observed.

5.8 Impedance of Non-Porous $Ni(OH)_2$ Coated Electrodes

Moving from porous to flat electrodes offers insight into the system by reducing the complexity of the system. Most electrodes in energy storage are highly porous, like those studied in this chapter so far, so as to provide a large interfacial area for reactions to occur.[13]

Due to the dispersity in pore dimensions, this means that not all pores in the material become active over the same time scale. This results in even the double layer capacitance, which dominates at high frequency, being frequency dependant, see Figure 5.13. For a perfectly flat electrode, such as a Hg drop electrode, C_{EDL} is independent of frequency, see Figure 5.15a.[11]

A porous electrode can be described using the transmission line model (TML) equivalent circuit, see Figure 5.15b.[14] The TML described a pore as a network of connected *RC* elements. As the frequency of modulation decreases, the active surface area of the pore due to the penetration of current increases. This means more of the elements in the TML are "seen" and the capacitance varies with frequency.

The formation of flat $Ni(OH)_2$ electrodes in Chapter 4 by the application of wax and subsequent grinding to reveal a single face of $Ni(OH)_2$ gives a unique opportunity to study the impedance of the material without the complications of diffusion into the pores.

The circuit model used in the analysis was adapted to fit the new electrode set up. The wax coated electrode no longer exhibits a highly porous structure. It is therefore assumed that the electrolyte can no longer penetrate all the way through the deposited layer, as was the case in Section 5.6. The Warburg – short element is no longer representative of the system, so must be replaced with a Warburg – open, Figure 5.16. At low frequencies, the system tends towards a perfectly polarisable electrode rather than a short circuit.

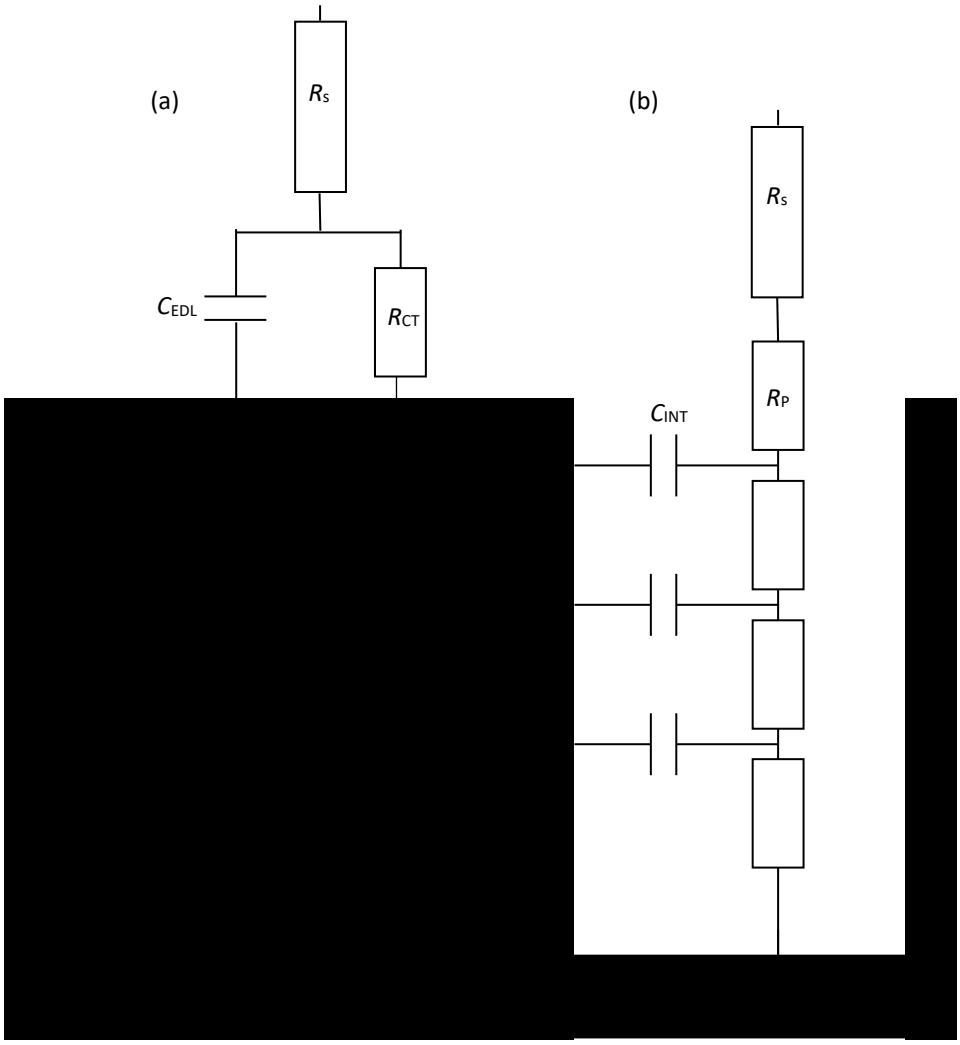


Figure 5.15 Representation of (a) flat and (b) porous electrodes using RC circuit elements C_{INT}, the interfacial capacitance and R_P, the pore resistance

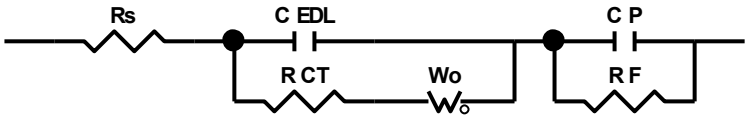


Figure 5.16 Equivalent circuit for the modelling of the $Ni(OH)_2$ coated electrodes after deposition and grinding of a porosity blocking wax layer

The Nyquist and Bode representations during charging and discharging for the $Ni(OH)_2$ coated electrodes after deposition and grinding of a porosity blocking wax layer can be seen in Figures 5.17a-d and 5.18a-d.

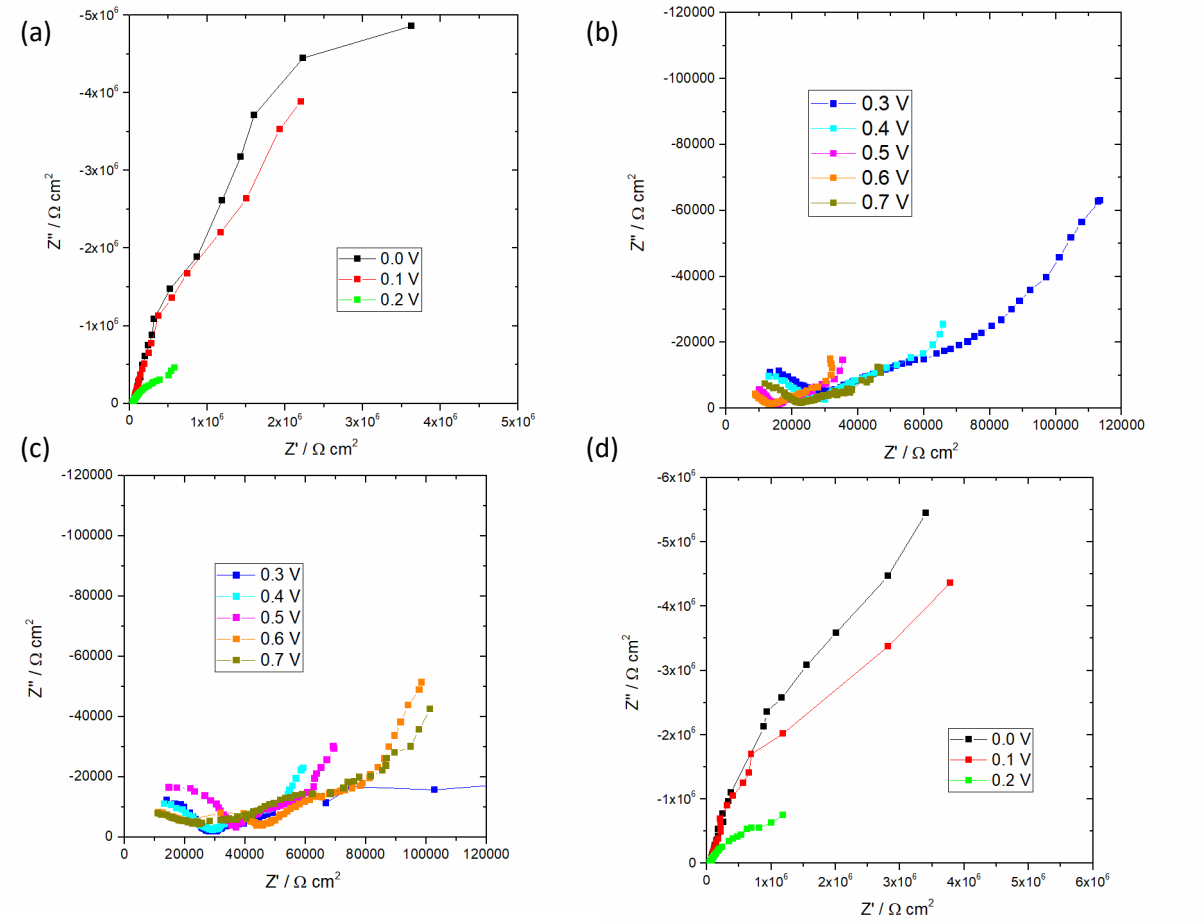


Figure 5.17 Nyquist representation of impedance data for $Ni(OH)_2$ coated electrodes after deposition and grinding of a porosity blocking wax layer at various DC potentials and 10 mV AC perturbation (a/b) charging (c/d) discharging

The Nyquist plots, Figure 5.17, show a different behaviour compared to the porous electrodes in Figure 5.9a/b and 5.14a/b. As predicted, there is no longer a semi-circle reaching back down to the real axis in the low frequency region at high potentials, as there was for the porous electrode. This shows the system is no longer shorting at low frequencies and is instead acting as a flat electrode.

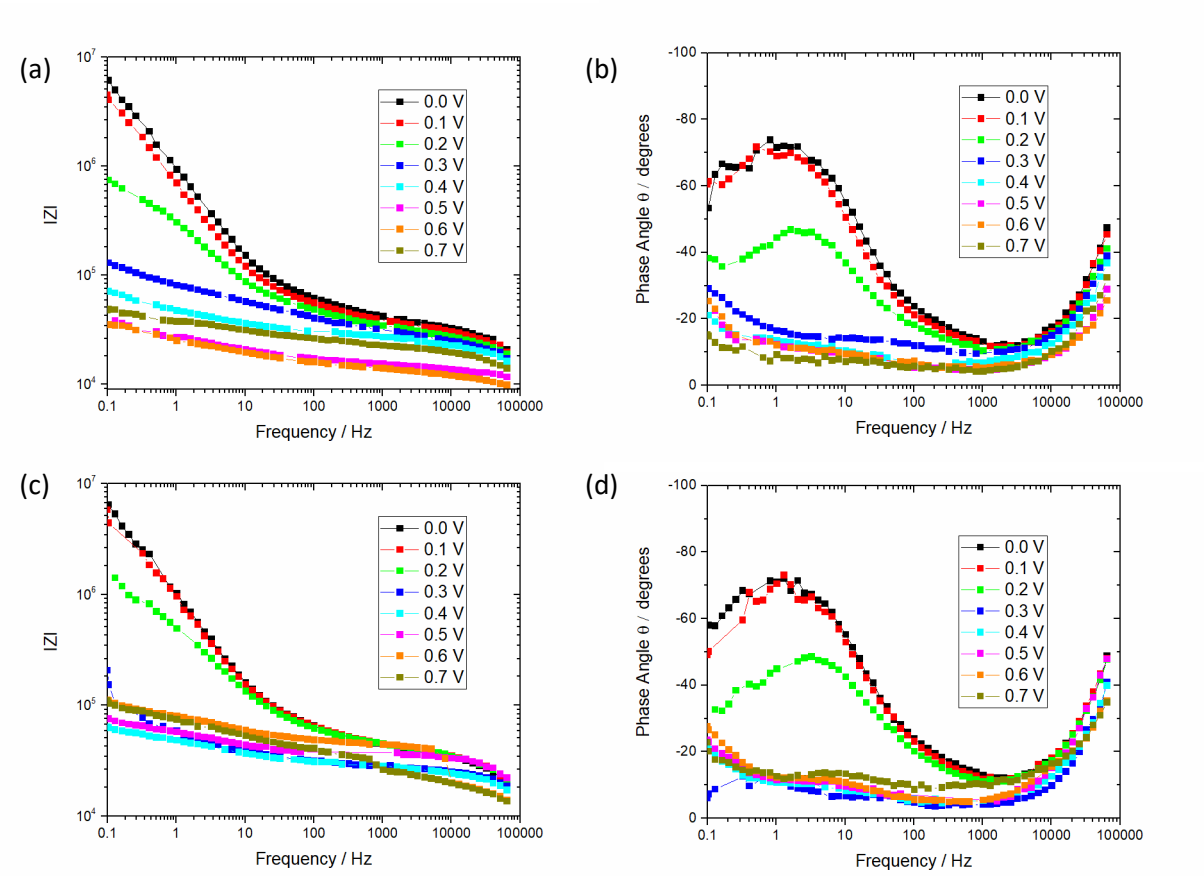


Figure 5.18 Bode representation of impedance data for $Ni(OH)_2$ coated electrodes after deposition and grinding of a porosity blocking wax layer at various DC potentials and 10 mV AC perturbation (a/b) charging (c/d) discharging

The magnitude of the impedance, Figure 5.18a/c, is significantly higher than the electrode prior to wax coating. The best fitting values of R_s, see Appendix 6, are also significantly higher. This is to be expected due to the low surface area of $Ni(OH)_2$ exposed by the wax coating. This resistivity is also the cause of the increased noise in the measurement. There is a large variation in the value of R_s calculated from the fitted circuit models, which is also due to the large noise in the measurement. The phase behaviour of the samples is similar at mid-range frequencies, although the phase is significantly higher at high frequencies for the flat electrodes compared to the porous equivalent.

Using the same method as used for the porous $Ni(OH)_2$ electrode in Section 5.7, the capacitance response to frequency during charging was plotted, Figure 5.19.

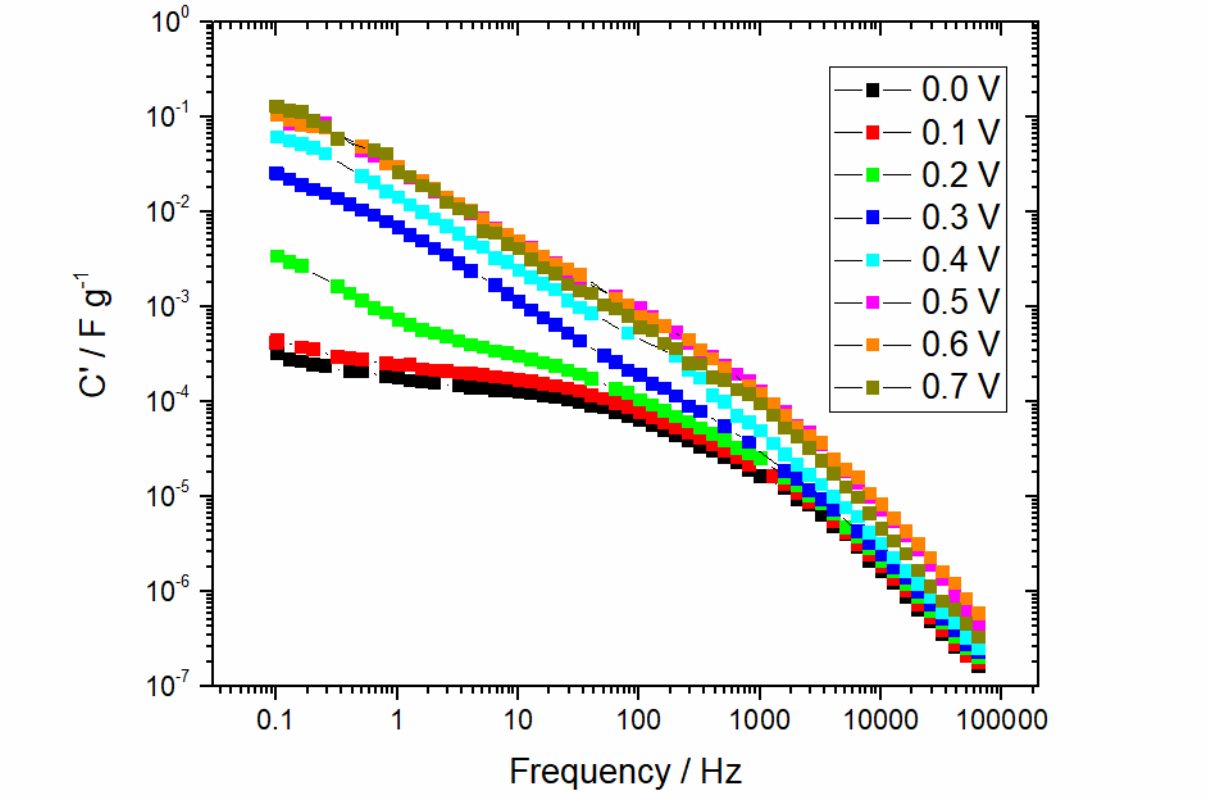


Figure 5.19 Capacitance analysis of $Ni(OH)_2$ coated electrodes after deposition and grinding of a porosity blocking wax layer at various DC potentials 0.0 V – 0.7 V and 10 mV AC perturbation vs frequency.

Unlike for the porous electrode, there is no large increase in capacitance at 0.4 V when the $Ni(OH)_2$ oxidation should occur. There is also no increase in capacitance at high potentials around 1 - 10 Hz, which suggests there is no longer intercalation of ions into the bulk of the structure as was seen for the porous electrode.

In contrast to the porous electrode, which showed no change in capacitance response with potential at high frequencies, there is a rough increase in capacitance with potential even at frequencies as high as 10^4 – 10^5 Hz.

5.9 Mapping of Porous Impedance Data onto Flat Impedance Data

When considering the circuit models for studying the impedance data of the porous $Ni(OH)_2$ electrode, it is important to consider whether diffusion into the pores can be considered finite or semi-infinite, as discussed in Section 5.6.

Using the impedance response of the flat electrode, the diffusion behaviour in the porous electrode can be confirmed. Considering the TML model of a pore shown in Figure 5.14b in more detail, an infinitesimally small section of the pore is shown in Figure 5.20.

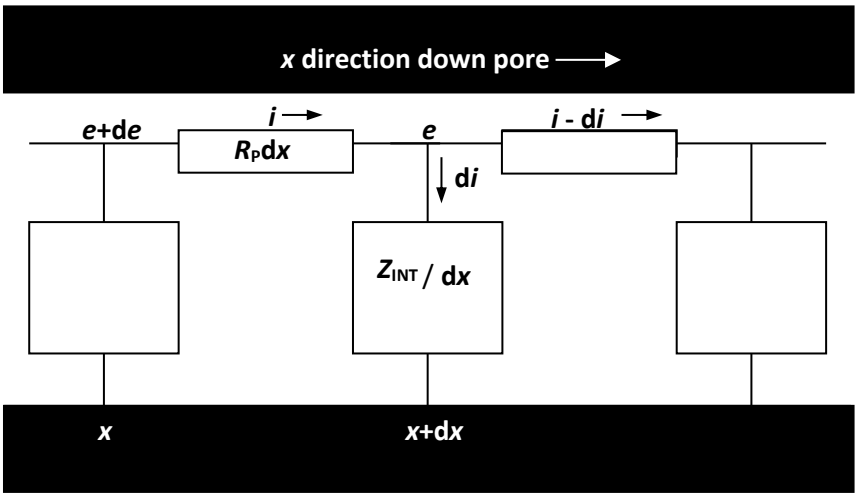


Figure 5.20 Equivalent circuit model of an infinitely small section of pore showing potential drop as current moves down pore in x direction.

The resistance per unit length in the pore is shown as R_P. The interfacial impedance, Z_{INT}, moving down the pore is related to the change in the potential at that point in the circuit, e, across the pore resistance and the current, i, by Equations (5.10) and (5.11) respectively.[16]

$$de = - iR_P dx \tag{5.10}$$

$$e = - (Z_{INT} / dx) di \tag{5.11}$$

Combining Equations (5.10) and (5.11), the second order differentials of the current and potential with respect to distance down the pore can be found, Equations (5.12) and (5.13).[16]

$$d^2i / dx^2 = (R_P / Z_{INT})i \tag{5.12}$$

$$d^2e / dx^2 = (R_P / Z_{INT})e \tag{5.13}$$

Using the boundary conditions of a semi-infinite pore, the applied potential at $e(0)$, E, tends to zero at $e(\infty)$. According to Equation (5.14) the current at the pore opening, $i(0)$, can be calculated.[16]

$$i(0) = E / (R_P Z_{INT})^{1/2} \tag{5.14}$$

The impedance of the semi-infinite porous electrode can be calculated using the square root of the impedance response of the interfacial impedance. In the case of a flat electrode, the impedance is entirely dominated by the interfacial impedance. Therefore, the impedance

response of the flat electrode should be reproducible by taking the square of the impedance of the porous electrode. It was decided to use the original data generated using the porous electrode in the analysis due to the lower noise levels in the data.

Since impedance, Z, is a complex number made up of the real Z' and imaginary parts Z'', Equation (5.15), the square of the impedance is calculated using Equation (5.16) where i is the square root of minus one.

$$Z = Z' + iZ'' \tag{5.15}$$

$$Z^2 = (Z' + iZ'')^2 = (Z'^2 - Z''^2) + i(2Z'Z'') \tag{5.16}$$

Nyquist representations of the porous electrode impedance response at 0.4 V – 0.7 V after squaring the real and imaginary components are shown in Figure 5.21. The shape of the plot does not change after squaring. Most notably the low frequency tail at almost 90^o phase angle which is observed in the impedance response for the flat electrode is missing.

This suggests that the assumptions made in the selection of the boundary conditions for the semi-infinite pore model do not hold. This supports the original hypothesis that the pore behaviour is finite and the current fully penetrates the deposited layer at low frequencies. This contradicts several literature sources which use semi-infinite diffusion models to characterise similar porous electrodes.[5, 15]

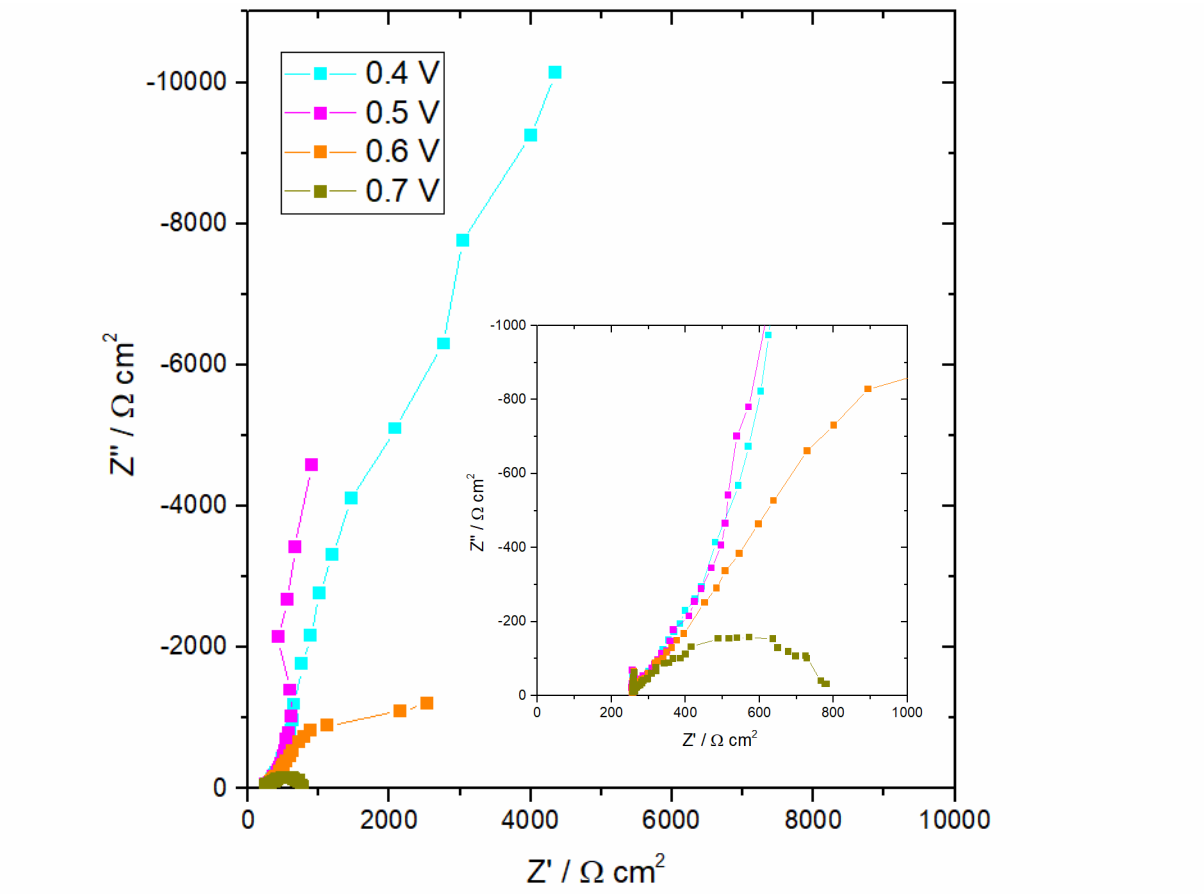


Figure 5.21 Nyquist representation of the impedance response of porous $Ni(OH)_2$ coated electrode at various DC potentials and 10 mV AC perturbation squared, high frequency region magnified in insert.

5.10 Conclusions

The impedance response of electrodes coated in $Ni(OH)_2$ has been studied to better understand the charging processes occurring. The porous $Ni(OH)_2$ coated electrodes were prepared by electrodeposition using the same method optimised in Section 4.3.7. The materials were already characterised using SEM, N_2 adsorption/desorption, XRD, EDX, and XPS, confirming their identity as $Ni(OH)_2$. The initial electrochemical characterisation using CV also supported the structural characterisation, as well as showing non-ideal behaviour in the *b*-value analysis.

The AC perturbation potential was varied, and it was found that 10 mV perturbation offered the best signal to noise ratio while not deviating from the linear current vs potential regime. Initially, the impedance of the electrodes was studied at 0.0 V DC. A circuit model including two sources of capacitance as well as a Warburg short diffusion element were needed to fit the data in a physically meaningful way.

The DC potential was then varied from 0.0 V to 0.7 V at 0.1 V intervals. The shaped of the Nyquist plot was observed to change, giving a third semi-circle in the low frequency region. This second intercept with the real axis is due to the current penetrating all the way into the pores of the material at low frequencies. The capacitance was found to be dependent on the frequency at all potentials. There was a change in capacitive regimes at around $10^3 – 10^4$ Hz indicating the onset of Faradaic charge transfer. There was a second change at 1- 10 Hz, which can be attributed to charge storage by intercalation into the bulk. The maximum capacitance approached the theoretical limit for $Ni(OH)_2$ at low frequencies. The impedance on discharge was also studied and the response was found to map well onto the chagrining response, although the final total impedance was significantly lower after charge cycling.

Porosity blocking paraffin wax was used to turn the porous $Ni(OH)_2$ coated electrodes into flat electrodes. The impedance response showed a large increase in resistance and a lower signal to noise ratio, as expected. The semi-circle at high potential was no longer observed, showing the current was no longer penetrating into the electrode layer. This was also supported by the lack of an increase in capacitance at high potential and low frequency.

The impedance response for the porous electrode was squared in order to compare it to the response of the flat electrode. This proved unsuccessful however, demonstrating the frequently used boundary conditions of diffusion into semi-infinite pores was unsuitable for analysis of these materials.

5.11 References

1. Kiran, G. K.; Munichandraiah, N.; Vishnu Kamath, P., Effect of non-stoichiometry on the charge storage capacity of NiO conversion anodes in Li-ion batteries. *Journal of Solid State Electrochemistry* **2018,** *22* (12), 3833-3843.
2. Babu, I. M.; William, J. J.; Muralidharan, G., Surfactant tuned morphology of mesoporous β-Co(OH)2/CMC nanoflakes: a prospective candidate for supercapacitors. *Journal of Solid State Electrochemistry* **2019**.
3. Saravanakumar, B.; Purushothaman, K. K.; Muralidharan, G., Interconnected V2O5 Nanoporous Network for High-Performance Supercapacitors. *ACS Applied Materials & Interfaces* **2012,** *4* (9), 4484-4490.
4. Chakrabarty, N.; Chakraborty, A. K., Controlling the electrochemical performance of β-Ni(OH)2/carbon nanotube hybrid electrodes for supercapacitor applications by La doping: A systematic investigation. *Electrochimica Acta* **2019,** *297*, 173-187.
5. Aguilera, L.; Leyet, Y.; Padrón-Hernández, E.; Passos, R. R.; Pocrifka, L. A., Understanding electrochemical performance of Ni(OH)2 films: a study contributions to energy storage. *Journal of Solid State Electrochemistry* **2018,** *22* (5), 1621-1628.

6. Li, H. B.; Yu, M. H.; Wang, F. X.; Liu, P.; Liang, Y.; Xiao, J.; Wang, C. X.; Tong, Y. X.; Yang, G. W., Amorphous nickel hydroxide nanospheres with ultrahigh capacitance and energy density as electrochemical pseudocapacitor materials. *Nature Communications* **2013,** *4*, 1894.
7. Ko, J. S.; Sassin, M. B.; Parker, J. F.; Rolison, D. R.; Long, J., Combining battery-like and pseudocapacitive charge storage in 3D MnOx@carbon electrode architectures for zinc-ion cells. *Sustainable Energy & Fuels* **2018,** *2* (3), 626-636.
8. Aoki, K.; Tokuda, K.; Matsuda, H., Theory of linear sweep voltammetry with finite diffusion space: Part II. Totally irreversible and quasi-reversible cases. *Journal of Electroanalytical Chemistry and Interfacial Electrochemistry* **1984,** *160* (1), 33-45.
9. Barsoukov, E.; Macdonald, J. R., *Impedance spectroscopy : theory, experiment, and applications*. 2 ed.; Wiley-Interscience: Hoboken, N.J., 2005.
10. Bard, A. J.; Faulkner, L. R., *Electrochemical Methods: Fundamentals and Applications*. Wiley: 2000.
11. Qu, D.; Wang, G.; Kafle, J.; Harris, J.; Crain, L.; Jin, Z.; Zheng, D., Electrochemical Impedance and its Applications in Energy-Storage Systems. *Small Methods* **2018,** *2* (8), 1700342.
12. Lu, Z.; Chang, Z.; Zhu, W.; Sun, X., Beta-phased Ni(OH)2 nanowall film with reversible capacitance higher than theoretical Faradic capacitance. *Chemical Communications* **2011,** *47* (34), 9651-9653.
13. Conway, B. E., *Electrochemical Supercapacitors: Scientific Fundamentals and Technological Applications*. Springer US: 1999.
14. de Levie, R., On porous electrodes in electrolyte solutions. *Electrochimica Acta* **1963,** *8* (10), 751-780.
15. Murugesamoorthi, K. A.; Srinivasan, S.; Appleby, A. J., AC impedance studies on nickel oxide electrodes to determine self-discharge characteristics of Ni-H2 batteries. *Journal of Applied Electrochemistry* **1991,** *21* (2), 95-98.
16. MacDonald, J. R., Barsoukov, E., Impdanace Spectroscopy: Theory, Experiment, and Applications., 2nd Ed, Wiley: 2005.

Chapter 6 – Conclusions and Outlook

6.1 Summary of Research Chapters

The initial work in this project was nanoparticle based and required the synthesis of a large size range of nanoparticles whilst maintaining the same morphology and phase. This was achieved, with $Ni(OH)_2$ nanoplates ranging from 3 – 450 nm in diameter synthesised using hydrothermal methods. With electrochemical cycling, the phase was shown to age to the thermodynamically stable β-$Ni(OH)_2$, removing the phase as variable. The electron micrographs showed a platelet morphology at all sizes, although there was some anisotropy which became more pronounced at larger particle diameters.

Electrochemical characterisation showed the charge stored per unit mass was much lower than the theoretical limit for $Ni(OH)_2$, at around 20 mA h g^{-1}. This was expected however for an unoptimised electrode with no binder or conductive additives.

The aim of the initial work was to study the charge stored per unit mass and per unit area, to compare the results to the theoretical outcomes for a bulk charge storage and surface only charge storage. This was successfully achieved, with particles showing surface-only dominated behaviour at large particle diameters. As particles became smaller however, the behaviour varied from that predicted for surface-only charging.

At a critical diameter of around 20 nm, further decreasing particle size resulted in reduction in Cap_s and C_s. C_A was found to stay constant with decreasing particle diameter until this same critical diameter was reached, after which point the C_A also decreased with particle size. This phenomenon was attributed to a surface charging layer, or "skin", within the $Ni(OH)_2$ of around 10 nm in depth.

This charging layer was of great interest, as it implies a lower limit on particle size in electrochemical energy storage. Moving the work forward required the confirmation of the observed charging layer. The synthesis method was changed to electrodeposition to decrease the time taken to prepare samples and produce more uniform electrodes.

ToF-SIMS was chosen as the method to further study this charging skin after charging/discharging in deuterated electrolyte. To the authors knowledge, observing a charging depth in $Ni(OH)_2$ using ToF-SIMS had never previously been achieved. This was due

in part to the highly porous nature of the electrodes which allowed electrolyte ingress into the bulk. This would cause a surface-only reaction to appear as a bulk reaction under ToF-SIMS analysis.

Electrodeposition was used to try to create a dense $Ni(OH)_2$ layer. Then to produce a flat electrode, porosity blocking paraffin wax was introduced yielding a surface in which a small amount of $Ni(OH)_2$ was exposed. This gave rise to problems of high resistivity, sample charging, and low signal to noise ratio.

In ToF-SIMS analysis, a peak in deuterium was observed over multiple experiments. Using AFM to measure the sputter crater, these peaks were shown to correspond to charging depths of around 20-30 nm. These results complemented the results found in Chapter 3 well and showed an empirical method for measuring charging depth without the use of complex *in-operando* methods.

To establish the nature of the charging, electrochemical impedance spectra for the samples during charging and discharging were collected. In addition, the development of the flat wax coated electrodes gave an opportunity for novel measurements on the material without diffusion into the porous structure.

Determination of the circuit model was based on the accepted model of two capacitive *RC* elements in series with an element representing diffusion in the bulk and the porous structure of the electrode in parallel to the double layer capacitance. It was decided the nature of the pore element for the porous electrode was a Warburg short element due to the expected permeation of the current through the entirety of the electrode at low frequencies. The Nyquist representations of the EIS data at high potentials confirmed this hypothesis.

The capacitance of the system during charging was studied, and was found to agree well with the redox behaviour observed using CV. The plot showed three clear charging regimes, with double layer formation, surface-only redox, and then charge intercalation causing a more rapid increase in the capacitance with decreasing frequency. This demonstrated a powerful method of determining when different charging mechanisms are accessible at different charging rates.

The impedance response of the porous electrode was modelled using a semi-infinite diffusion model, as is commonly done in the literature. The square of the porous electrode impedance should give a proportional response to that of the flat electrode. This was found to not be the case however, further supporting the hypothesis of finite diffusion in the pores of the $Ni(OH)_2$ coated electrode.

6.2 Future Work

6.2.1. Chapter 3

Further experiments are required to unambiguously establish the existence and depth of the charging layer at the $Ni(OH)_2$ surface. Alternative analysis techniques using *in-situ* and *in-operando* methods would allow the charging layer to be observed directly and without the added complication of removing the electrodes from the electrolyte and drying before analysis. *In-situ* measurements would be possible using an X-ray transmissive cell, which would allow observation of any phase changes without removal of the electrodes. *In-operando* measurements are further discussed in Section 6.2.4.

Further investigation of the anisotropy in the particle morphology of the nanoparticles of $Ni(OH)_2$ produced in Chapter 3 is necessary. In the XRD analysis of the nanoparticles, it was clear that certain peaks showed greater intensity than expected from the literature stick pattern. This is either due to crystal growth in certain planes being favoured, or it could be an artefact of the deposition method. The powder diffractometer will only show crystal faces which are parallel to the plane of the X-rays. While this is not normally a problem for powder diffraction due to the random orientation of particles, the carcinogenic nature of the nanoparticles meant that they had to be drop-cast onto an Si wafer. It is easy to see how the shape of the platelets could favour face to face stacking, giving an unrepresentative intensity in the diffractogram.

To deconvolute the effects of crystal growth and deposition stacking, texture analysis could be performed. This would require the angle of the mounting of the sample to be varied, to see if the relative intensity of the peaks varies. If it is found that the relative intensity does not vary with angle of mounting, then the anisotropy is an effect of anisotropic growth of a favoured crystal face.

In the case of anisotropic growth, the charge stored will increase if a crystal face which allows more rapid redox reactions or intercalation dominates. If the relative amount of this more active crystal face varies with particle size, this could be an alternative explanation for the increase and decrease in charge stored per unit mass and unit area with particle size.

If a more active crystal face is identified, it is important to understand why this face is more active. DFT could be used to study the approach and reaction of hydroxide ions at the various faces of $Ni(OH)_2$. Identifying the most reactive crystal face will allow future synthesis research to focus on producing materials which maximise the most reactive crystal faces.

6.2.2 Chapter 4

This work showed that the measurement of charging depth using a combination of ToF-SIMS and AFM is possible, even for porous materials such as $Ni(OH)_2$. Moving forward, further improvements must be made in order to improve the ease of sample preparation and the signal to noise ratio in the measurement.

The low signal to noise ratio in the measurement is currently limiting in terms of the resolution of the measurement. The low signal is due to the low amount of deuterated metal hydroxide exposed, as well as the high surface roughness. Further improving these experiments, samples with either larger amounts of metal hydroxide exposed, or lower surface roughness should be prepared.

To expose a larger amount of $Ni(OH)_2$, the original methodology employed in Chapter 4 needs to be revisited, producing dense thin films of $Ni(OH)_2$ with no wax coating. While potentiostatic electrodeposition was not promising, there are other methods which may be used. Thin film preparation techniques such as chemical vapour deposition[1] or pulsed laser deposition[2] may be employed to produce highly dense films. The equipment available at the time of writing was not suitable to produce metal hydroxide films, however work into deposition in hydrated atmospheres is ongoing. In other cases, chemical etching of deposited metal oxide thin films by strong base has been shown to produce mixed phase thin films of oxide and hydroxide.[2-3]

If synthesising dense thin films of nickel hydroxide does not prove to be successful, improving the wax deposition method will also be useful in reducing surface roughness. Using harder

waxes as porosity blockers will also allow for a much more rigorous polishing regime. This will reduce the surface roughness but leave the low amount of $Ni(OH)_2$ exposed.

These improvements would allow for a more accurate measurement of the charging depth in the material and lead to better understanding of the morphologies required to maximise energy density.

6.2.3 Chapter 5

The study of the impedance response of $Ni(OH)_2$ coated electrodes had already seen a fair amount of attention prior to this work. Further improving the understanding of the porous $Ni(OH)_2$ coated electrodes requires isolation of the different components of the impedance response, in a similar way to the porosity blocking used in Chapter 5.

Further study into the transport of ions through the bulk electrolyte and in the electrode, pores is necessary for tuning pore volume and size in future devices. Transport mechanisms and their dependence on electrolyte viscosity have already been studied in other aspects of energy storage such as ionic liquids[4-5] and lithium sulphur batteries.[6]

Further study of the diffusion component of the impedance response can be achieved by altering the viscosity of the electrolyte. An unreactive gelling agent, such as sodium gluconate, could be used to alter the viscosity of the electrolyte. By altering the viscosity of the electrolyte without directly interfering with the electrochemical reaction, the influence of diffusion can be separated.

6.2.4 *In-operando* Measurements

In addition to further *ex-situ* measurements, work could also progress in *in-operando* measurements using beam lines. Both synchrotron X-ray diffraction and neutron scattering experiments could be used to great effect when studying the charging and discharging of $Ni(OH)_2$ nanoscale materials.

Studies in chapters 3 and 4 have allowed the observation of a charging “skin”. These observations, however, are either indirect or *ex-situ* with no applied charging field at the time of measurement. To fully confirm the charging “skin” hypothesis, the phase change of the charging layer must be observed *in-situ* and *in-operando*. On charging, the phase change to NiOOH and the increase in interlayer spacing should be observable directly by XRD.

Experiments using traditional lab-based XRD instruments have showed difference in phase or spacing before and after charging. This is due in part to the lack of sensitivity of the instrument with the signal being dominated by the bulk. There is also the possibility of relaxation effects in *ex-situ* analysis.

Grazing angle XRD could be used to study the phase change and increase in interlayer spacing accompanying charging from α- or β-$Ni(OH)_2$ to γ- or β-NiOOH respectively. The observation of the expected phase change would confirm the charging "skin" hypothesis.

To observe the phase change localised to the surface, consistent with a core shell structure, a high flux X-ray source is necessary to study this thin 10 nm range with an acceptable signal to noise ratio; a synchrotron is therefore needed. In addition, *in-operando* measurements are necessary, not only to observe the expected surface phase change, but also to provide information on the kinetics of the reaction. Understanding the kinetics of the reaction is key to providing better power density in future device design.

Another *in-operando* techniques which would be useful in understanding the nature of charging in $Ni(OH)_2$ is neutron scattering. As already shown in Chapter 4, deuterium ion uptake can be used to follow the electrochemical reaction occurring in the charging/discharging $Ni(OH)_2$ electrode.

Using X-ray based techniques, such as XPS, deuterium uptake can not be analysed due to the low X-ray cross-section of the small deuterium ions. X-rays interact with the electron cloud surrounding the nucleus, and the diffraction intensity is therefore proportional to atomic number.[7]

Neutrons interact directly with the nucleus of the atom. This is beneficial since not only are neutrons scattered strongly by small atoms such as deuterium, but the scattering is also isotope dependant. This means the uptake of deuterium can be followed in the presence of hydrogen.[7]

Neutron scattering is already commonly used in the study of energy storage materials. The most common examples are hydrogen storage materials[8-9] and Li-ion batteries.[10-11] If the uptake of deuterium into the $Ni(OH)_2$ can be directly visualised with respect to potential at various scan rates, the question of charging mechanism could be definitively answered.

6.3 References

1. Maruyama, T.; Arai, S., The electrochromic properties of nickel oxide thin films prepared by chemical vapor deposition. *Solar Energy Materials and Solar Cells* **1993,** *30* (3), 257-262.
2. Birjega, R.; Vlad, A.; Matei, A.; Ion, V.; Luculescu, C.; Dinescu, M.; Zavoianu, R., Growth and characterization of ternary Ni, Mg–Al and Ni–Al layered double hydroxides thin films deposited by pulsed laser deposition. *Thin Solid Films* **2016,** *614*, 36-41.
3. Wang, Y.; Wang, H.; Wang, X., The cobalt oxide/hydroxide nanowall array film prepared by pulsed laser deposition for supercapacitors with superb-rate capability. *Electrochimica Acta* **2013,** *92*, 298-303.
4. Oldiges, K.; Diddens, D.; Ebrahiminia, M.; Hooper, J. B.; Cekic-Laskovic, I.; Heuer, A.; Bedrov, D.; Winter, M.; Brunklaus, G., Understanding transport mechanisms in ionic liquid/carbonate solvent electrolyte blends. *Physical Chemistry Chemical Physics* **2018,** *20* (24), 16579-16591.
5. Sillars, F. B.; Fletcher, S. I.; Mirzaeian, M.; Hall, P. J., Variation of electrochemical capacitor performance with room temperature ionic liquid electrolyte viscosity and ion size. *Physical Chemistry Chemical Physics* **2012,** *14* (17), 6094-6100.
6. Kolosnitsyn, V. S.; Kuzmina, E. V.; Karaseva, E. V.; Mochalov, S. E., A study of the electrochemical processes in lithium–sulphur cells by impedance spectroscopy. *Journal of Power Sources* **2011,** *196* (3), 1478-1482.
7. Lindner, P., *Neutron, X-ray and light scattering : introduction to an investigative tool for colloidal and polymeric systems*. North-Holland: Netherlands, 1991.
8. Fukunaga, T.; Itoh, K.; Orimo, S.; Aoki, K., Structural observation of nano-structured and amorphous hydrogen storage materials by neutron diffraction. *Materials Science and Engineering: B* **2004,** *108* (1), 105-113.
9. Ramirez-Cuesta, A. J.; Jones, M. O.; David, W. I. F., Neutron scattering and hydrogen storage. *Materials Today* **2009,** *12* (11), 54-61.
10. Senyshyn, A.; Mühlbauer, M. J.; Nikolowski, K.; Pirling, T.; Ehrenberg, H., "In-operando" neutron scattering studies on Li-ion batteries. *Journal of Power Sources* **2012,** *203*, 126-129.
11. Sharma, N.; Peterson, V. K.; Elcombe, M. M.; Avdeev, M.; Studer, A. J.; Blagojevic, N.; Yusoff, R.; Kamarulzaman, N., Structural changes in a commercial lithium-ion battery during electrochemical cycling: An in situ neutron diffraction study. *Journal of Power Sources* **2010,** *195* (24), 8258-8266.

Appendices

Appendix 1

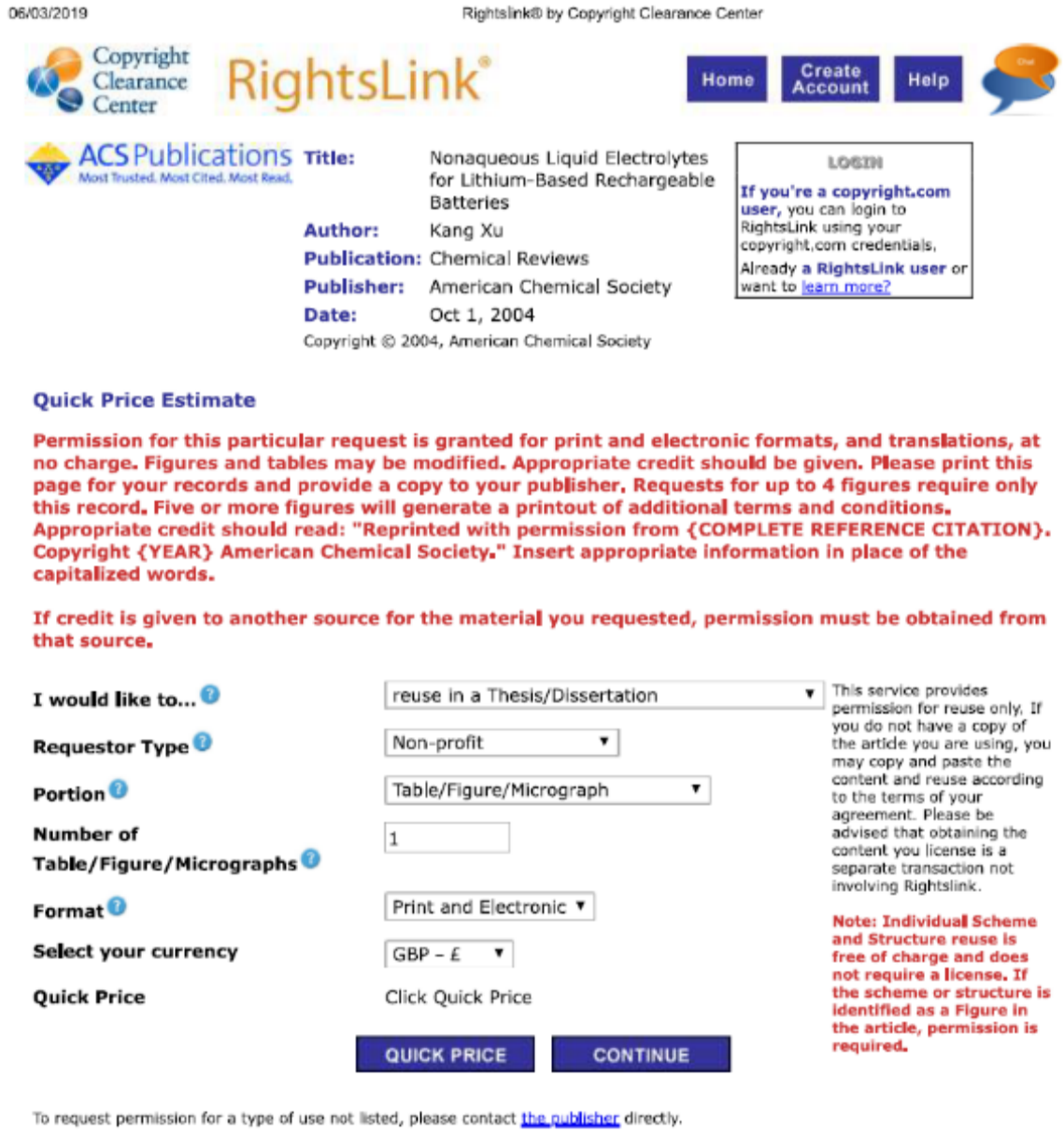


Figure A1 Permissions for the reuse of Figure 1.6) from Xu, K., Nonaqueous Liquid Electrolytes for Lithium-Based Rechargeable Batteries. Chemical Reviews 2004, 104 (10), 4303-4418. Copyright (2019) American Chemical Society.

Appendix 2



27/03/2019 Rightslink® by Copyright Clearance Center

Copyright Clearance Center RightsLink®

Home | Create Account | Help

Title: Examining the charging behaviour of nickel hydroxide nanomaterials

Author: Joseph H.L. Hadden,Mary P. Ryan,D. Jason Riley

Publication: Electrochemistry Communications

Publisher: Elsevier

Date: April 2019

© 2019 The Authors. Published by Elsevier B.V.

LOGIN

If you're a copyright.com user, you can login to RightsLink using your copyright.com credentials.

Already **a RightsLink user** or want to learn more?

Please note that, as the author of this Elsevier article, you retain the right to include it in a thesis or dissertation, provided it is not published commercially. Permission is not required, but please ensure that you reference the journal as the original source. For more information on this and on your other retained rights, please visit: https://www.elsevier.com/about/our-business/policies/copyright#Author-rights

BACK CLOSE WINDOW

Copyright © 2019 Copyright Clearance Center, Inc. All Rights Reserved. Privacy statement. Terms and Conditions.
Comments? We would like to hear from you. E-mail us at customercare@copyright.com

Figure A2 Permissions for figures and data used in Chapter 3 from J.H.L. Hadden, M.P. Ryan, D.J. Riley, Examining the charging behaviour of nickel hydroxide nanomaterials, Electrochemistry Communications, 101 (2019) 47-51. Copyright (2019) Elsevier B.V.

Appendix 3

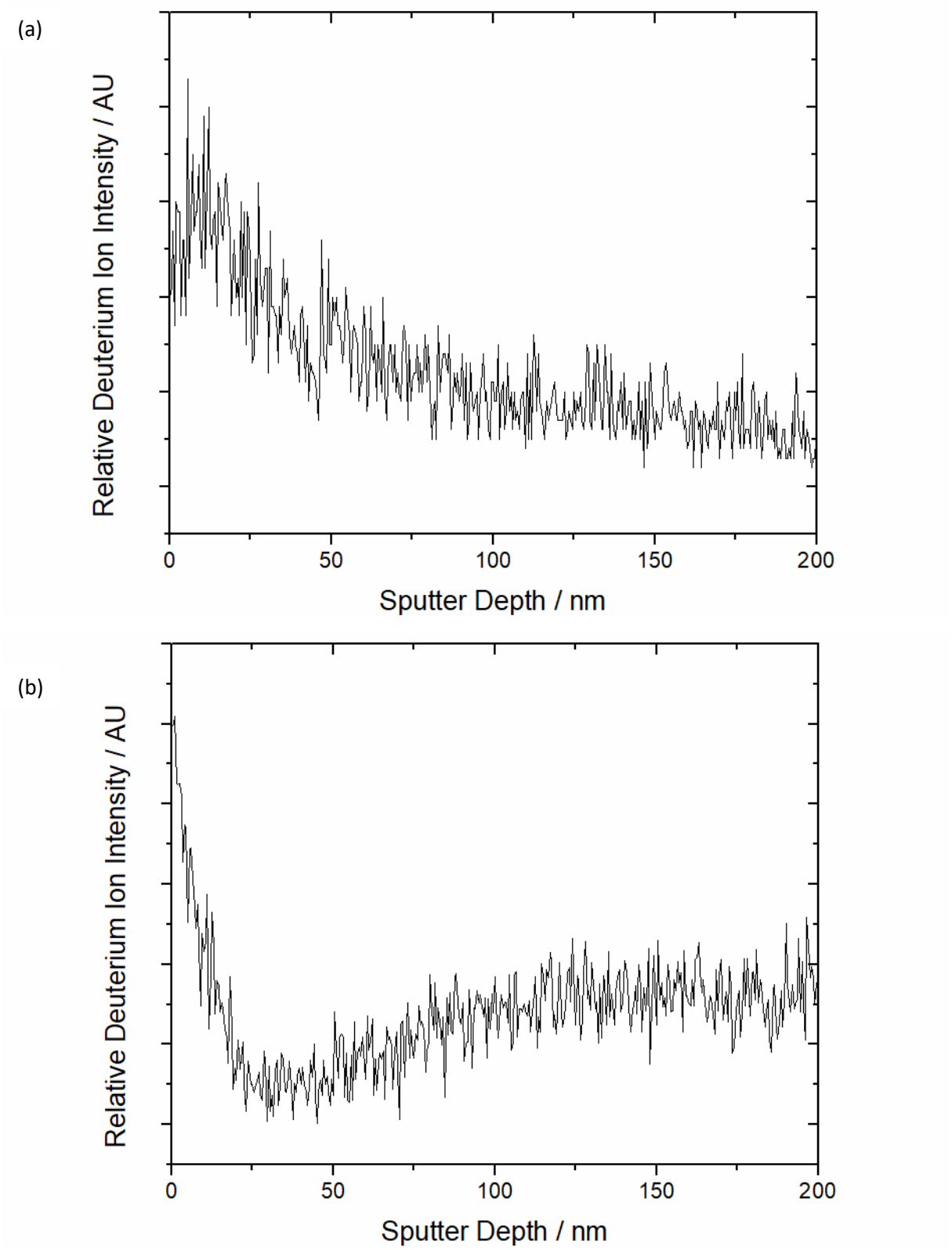


Figure A3 ToF-SIMS plots of deuterium ion intensity verses sputter depth. D^- ion intensity in a wax coated and ground samples after 1 cycle of charging and discharging at 10 mV s^{-1}. Full procedural details for ToF-SIMS analysis can be found in section 2.3. (a) After 20 seconds grinding at 500 rpm prior to cycling (b) after 4 x 20 seconds grinding at 200 rpm prior to cycling

Appendix 4

Impedance during charging of porous $Ni(OH)_2$ coated electrode

0.0 V in main body of text

0.1 V

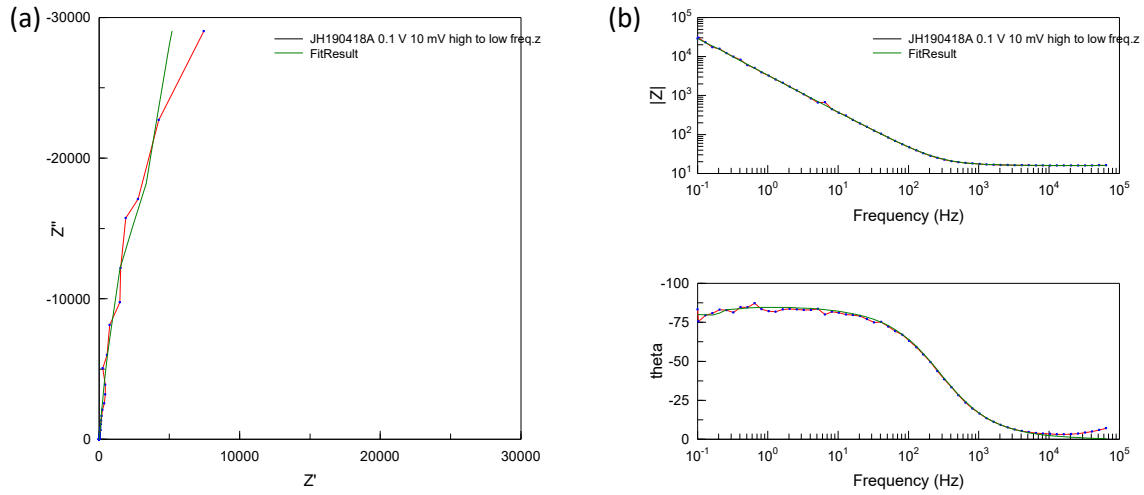


Figure A4 Fitting of equivalent circuit model to experimental data for $Ni(OH)_2$ coated electrodes during charging at 0.1 V DC potential and 10 mV perturbation (a) Nyquist plot (b) Bode Plots

0.2 V

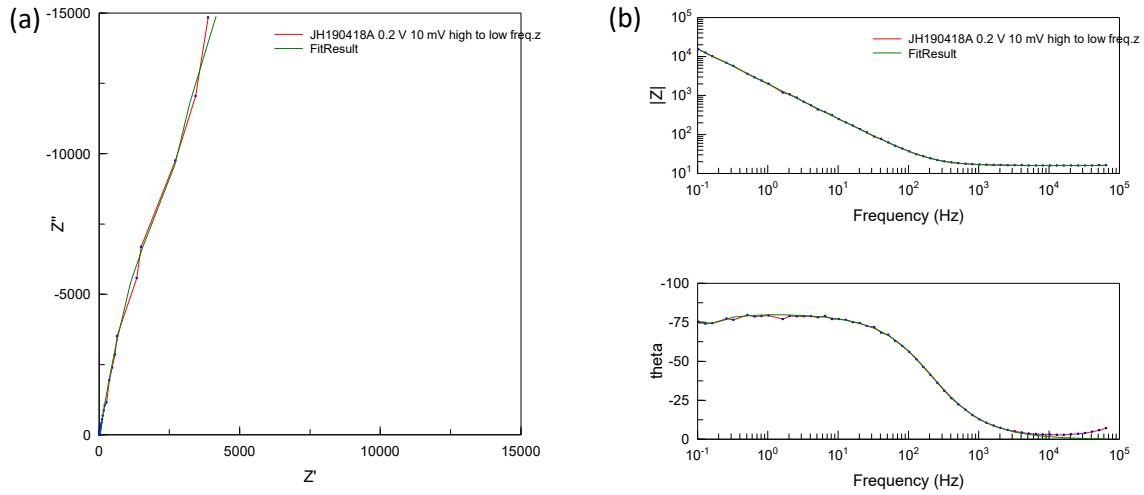


Figure A5 Fitting of equivalent circuit model to experimental data for Ni(OH)2 coated electrodes during charging at 0.2 V DC potential and 10 mV perturbation (a) Nyquist plot (b) Bode Plots

0.3 V

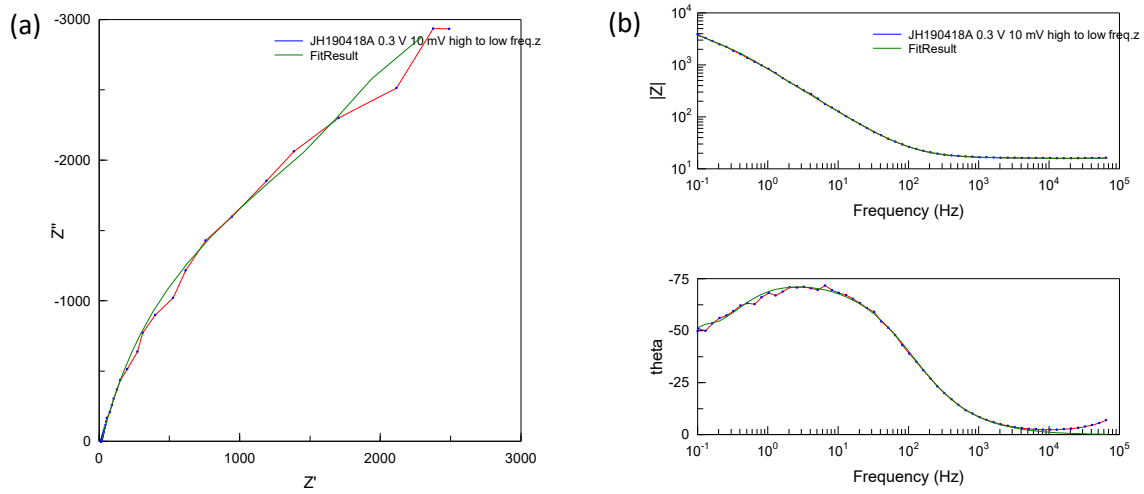


Figure A6 Fitting of equivalent circuit model to experimental data for $Ni(OH)_2$ coated electrodes during charging at 0.3 V DC potential and 10 mV perturbation (a) Nyquist plot (b) Bode Plots

0.4 V

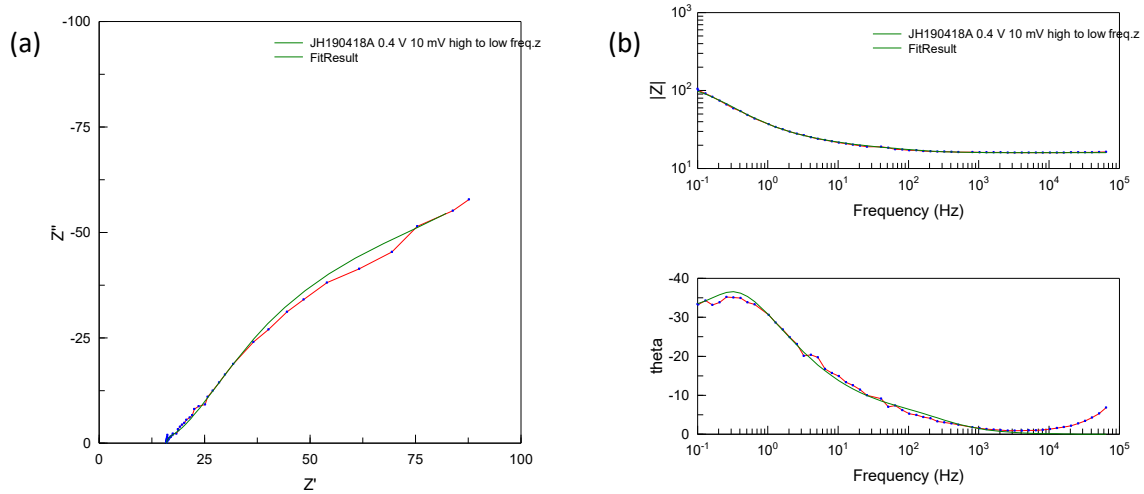


Figure A7 Fitting of equivalent circuit model to experimental data for $Ni(OH)_2$ coated electrodes during charging at 0.4 V DC potential and 10 mV perturbation (a) Nyquist plot (b) Bode Plots

0.5 V

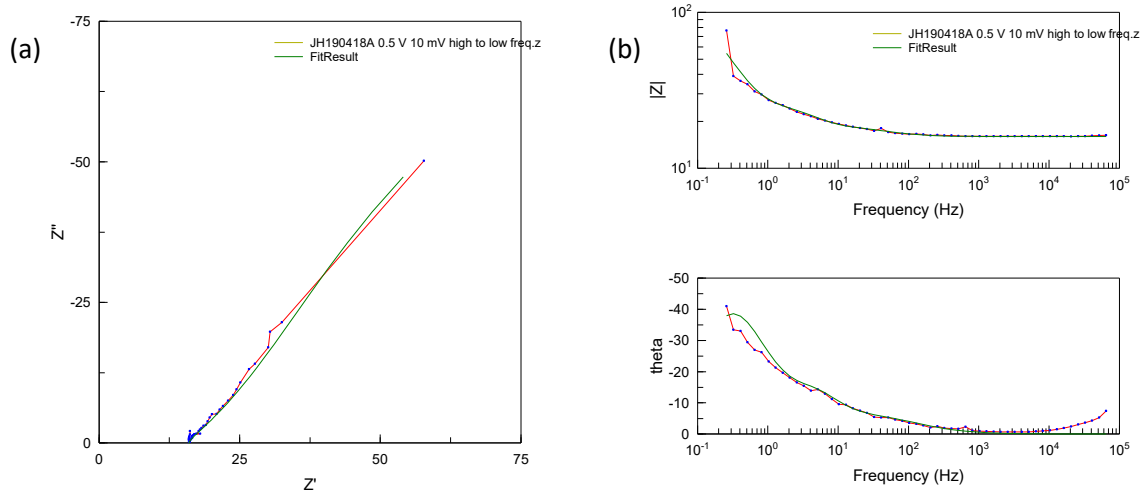


Figure A8 Fitting of equivalent circuit model to experimental data for $Ni(OH)_2$ coated electrodes during charging at 0.5 V DC potential and 10 mV perturbation (a) Nyquist plot (b) Bode Plots

0.6 V

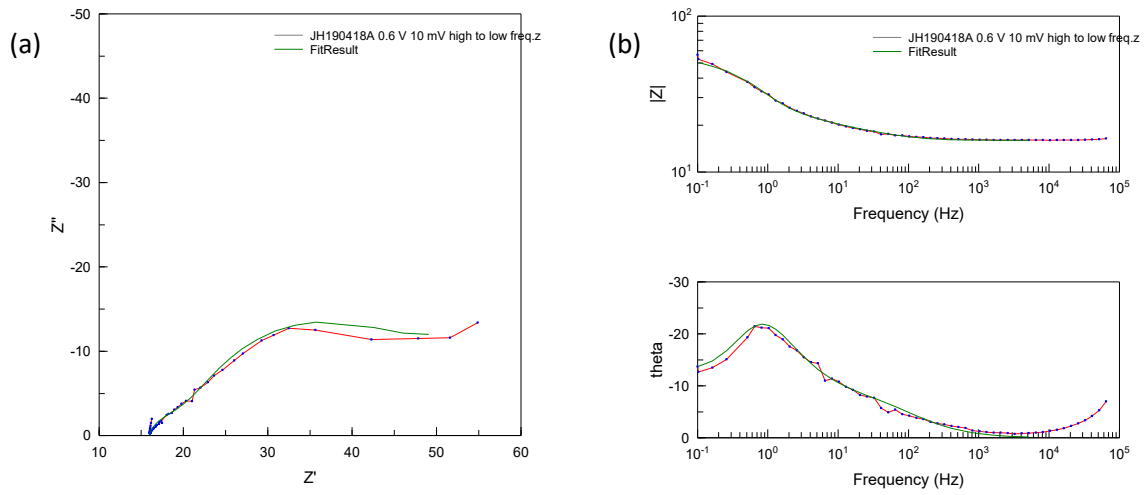


Figure A9 Fitting of equivalent circuit model to experimental data for $Ni(OH)_2$ coated electrodes during charging at 0.6 V DC potential and 10 mV perturbation (a) Nyquist plot (b) Bode Plots

0.7 V in main body of text

Impedance during discharging of porous $Ni(OH)_2$ coated electrode

0.7 V

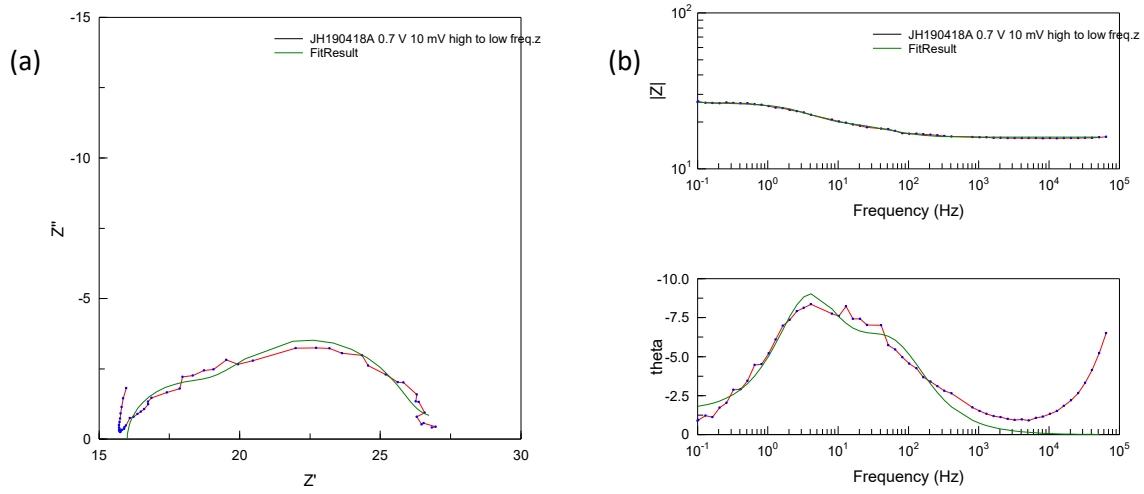


Figure A10 Fitting of equivalent circuit model to experimental data for $Ni(OH)_2$ coated electrodes during discharging at 0.7 V DC potential and 10 mV perturbation (a) Nyquist plot (b) Bode Plots

0.6 V

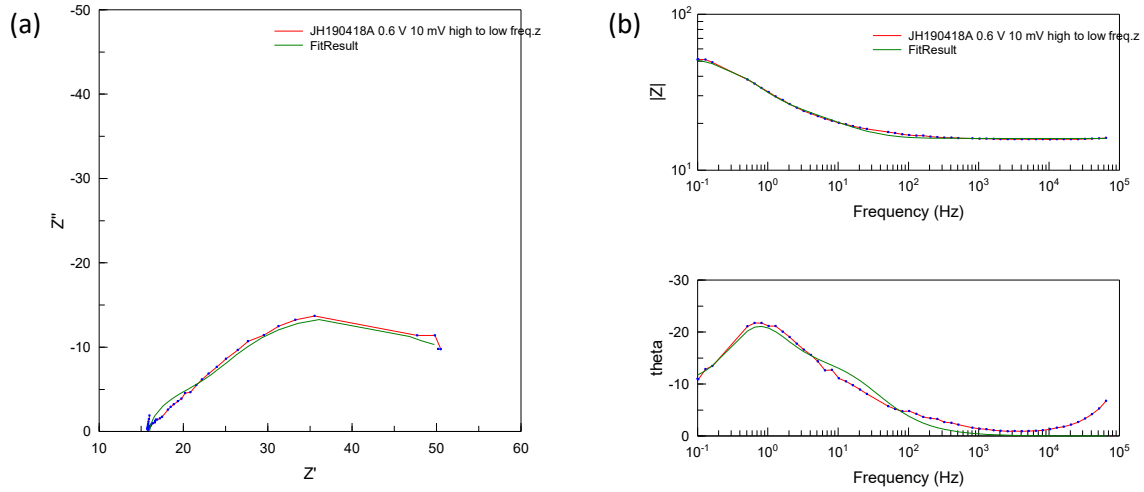


Figure A11 Fitting of equivalent circuit model to experimental data for $Ni(OH)_2$ coated electrodes during discharging at 0.6 V DC potential and 10 mV perturbation (a) Nyquist plot (b) Bode Plots

0.5 V

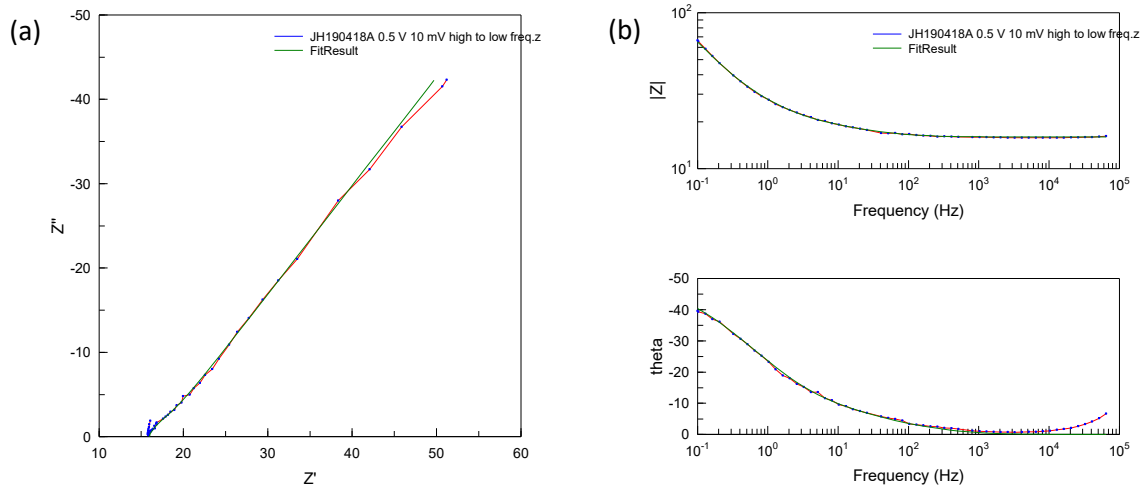


Figure A12 Fitting of equivalent circuit model to experimental data for $Ni(OH)_2$ coated electrodes during discharging at 0.5 V DC potential and 10 mV perturbation (a) Nyquist plot (b) Bode Plots

0.4 V

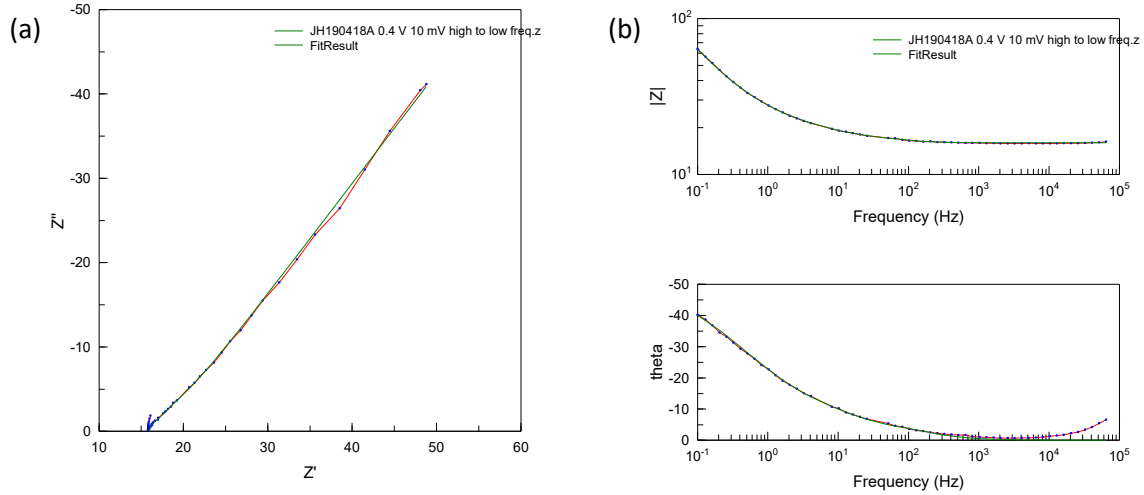


Figure A13 Fitting of equivalent circuit model to experimental data for $Ni(OH)_2$ coated electrodes during discharging at 0.4 V DC potential and 10 mV perturbation (a) Nyquist plot (b) Bode Plots

0.3 V

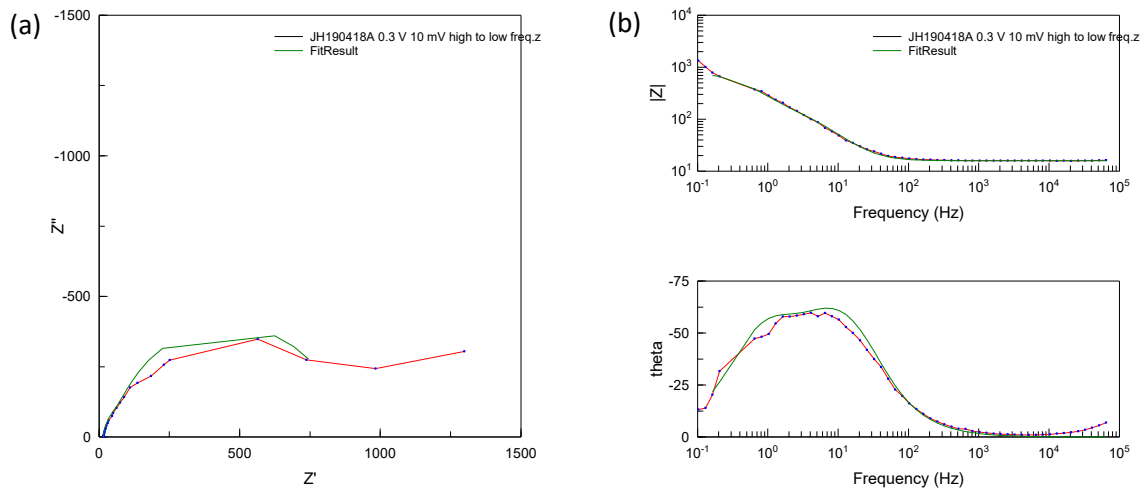


Figure A14 Fitting of equivalent circuit model to experimental data for $Ni(OH)_2$ coated electrodes during discharging at 0.3 V DC potential and 10 mV perturbation (a) Nyquist plot (b) Bode Plots

0.2 V

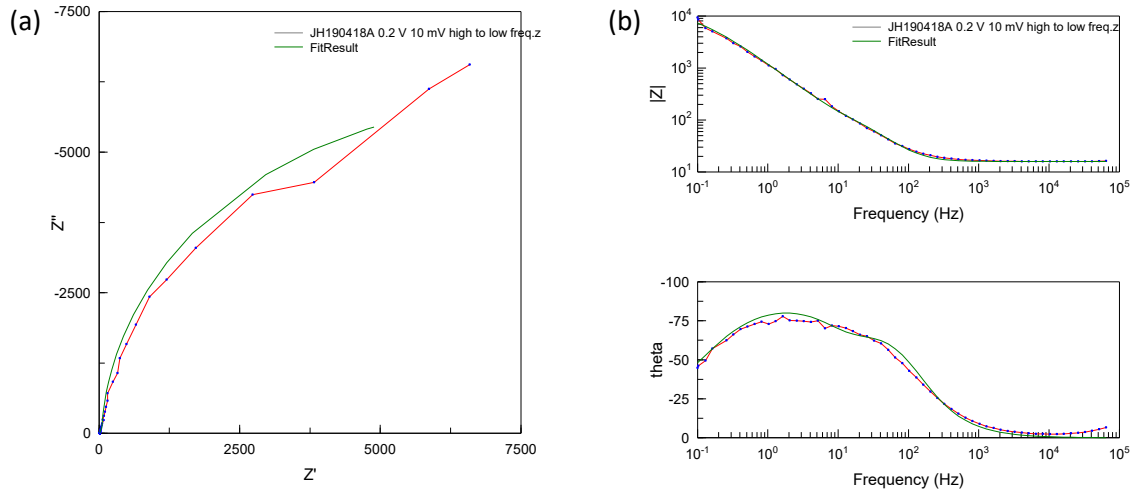


Figure A15 Fitting of equivalent circuit model to experimental data for $Ni(OH)_2$ coated electrodes during discharging at 0.2 V DC potential and 10 mV perturbation (a) Nyquist plot (b) Bode Plots

0.1 V

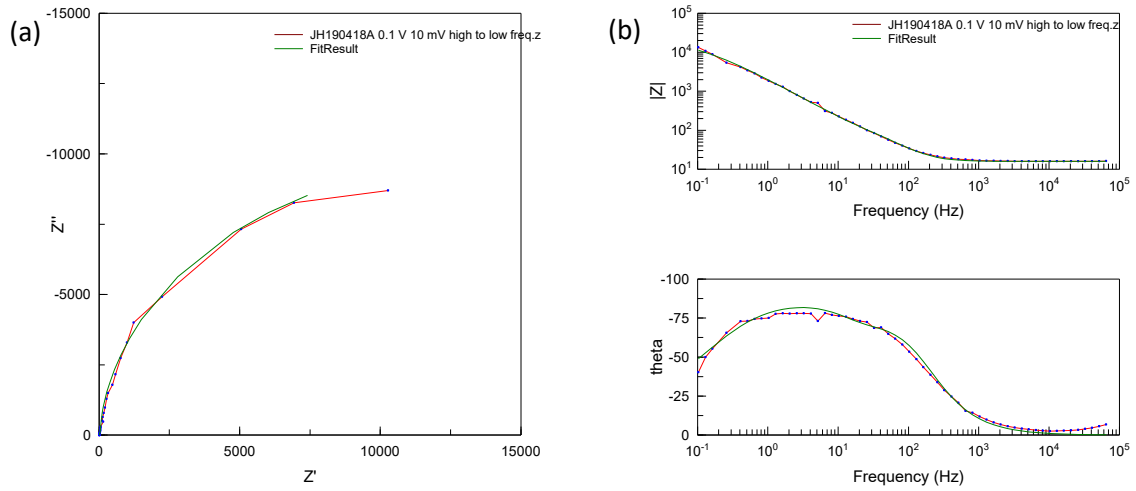


Figure A16 Fitting of equivalent circuit model to experimental data for $Ni(OH)_2$ coated electrodes during discharging at 0.1 V DC potential and 10 mV perturbation (a) Nyquist plot (b) Bode Plots

0.0 V

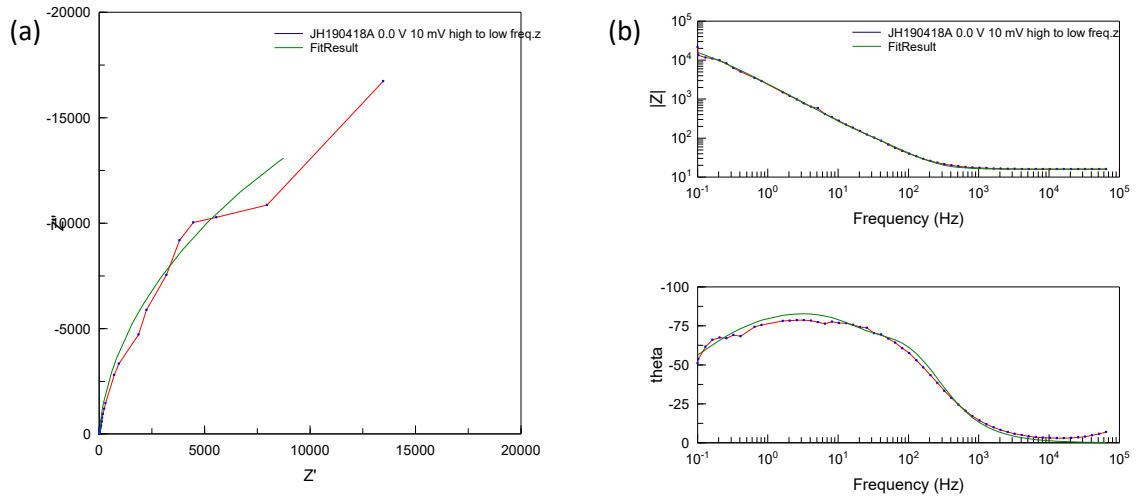


Figure A17 Fitting of equivalent circuit model to experimental data for $Ni(OH)_2$ coated electrodes during discharging at 0.0 V DC potential and 10 mV perturbation (a) Nyquist plot (b) Bode Plots

Appendix 5

Table A1 Values of the circuit elements that best fit the experimental data for electrochemical impedance spectroscopy of porous Ni(OH)2 coated electrodes during charging and discharging.

Element	Freedom	0.0 V		0.1 V		0.2 V	
		Value	Error / %	Value	Error / %	Value	Error / %
R_s / Ω cm^{-2}	Fixed	16	N/A	16	N/A	16	N/A
C_{EDL} / F g^{-1}	Free	1.7x10^{-2}	2	2.3x10^{-2}	3	4.0x10^{-2}	2
R_{CT} / Ω cm^{-2}	Free	15.8	1	0.65	7	1.7	10
W_s – R / Ω cm^{-2}	Free	490	9	14000	20	15000	10
W_s – T	Free	1.98	0.05	5.5	10	5.5	10
W_s – P	Free	0.98	0.02	0.78	3	0.73	3
C_P / F g^{-1}	Free	2.11x10^{-2}	10	6.3x10^{-2}	4	0.145	6
R_F / Ω cm^{-2}	Free	12000	9	12000	10	13000	20

Element	Freedom	0.3 V		0.4 V		0.5 V	
		Value	Error / %	Value	Error / %	Value	Error / %
R_s / Ω cm^{-2}	Fixed	16	N/A	16	N/A	16	N/A
C_{EDL} / F g^{-1}	Free	5.0x10^{-2}	10	2.3x10^{-1}	10	2.4x10^{-1}	7
R_{CT} / Ω cm^{-2}	Free	2.0	10	2.0	10	1.9	7
W_s – R / Ω cm^{-2}	Free	13000	9	840	10	5.5	4
W_s – T	Free	1.3	20	0.8	20	0.5	20
W_s – P	Free	0.70	2	0.46	1	0.53	2
C_P / F g^{-1}	Free	0.484	5	32.1	10	14.6	4
R_F / Ω cm^{-2}	Free	1135	7	30.7	1	76	10

Element	Freedom	0.6 V		0.7 V	
		Value	Error / %	Value	Error / %
R_s / Ω cm^{-2}	Fixed	16	N/A	16	N/A
C_{EDL} / F g^{-1}	Free	3.3x10^{-1}	10	5.4x10^{-1}	10
R_{CT} / Ω cm^{-2}	Free	3.4	10	5.9	5
W_s – R / Ω cm^{-2}	Free	30.4	7	12	9
W_s – T	Free	0.78	1	0.16	10
W_s – P	Free	0.43	2	0.07	7
C_P / F g^{-1}	Free	18.1	6	7.5	10
R_F / Ω cm^{-2}	Free	13.7	10	5.9	7

Element	Freedom	0.7 V		0.6 V		0.5 V	
		Value	Error / %	Value	Error / %	Value	Error / %
R_s / Ω cm^{-2}	Fixed	16	N/A	16	N/A	16	N/A
C_{EDL} / F g^{-1}	Free	8.1x10^{-1}	8	1.4	7	1.5	6
R_{CT} / Ω cm^{-2}	Free	4.5	7	16.3	3	2.5	10
W_s – R / Ω cm^{-2}	Free	2.6	8	18.2	8	5.6	2
W_s – T	Free	0.58	10	0.64	4	2.0	10
W_s – P	Free	0.047	2	0.11	3	0.25	5
C_P / F g^{-1}	Free	8.8	10	20	10	20	9
R_F / Ω cm^{-2}	Free	5.6	7	16	10	9.9	8

Element	Freedom	0.4 V		0.3 V		0.2 V	
		Value	Error / %	Value	Error / %	Value	Error / %
R_s / Ω cm^{-2}	Fixed	16	N/A	16	N/A	16	N/A
C_{EDL} / F g^{-1}	Free	1.7	4	5. 1x10^{-1}	20	1.2x10^{-1}	5
R_{CT} / Ω cm^{-2}	Free	3.9	5	5.1	3	7.8	5
W_s – R / Ω cm^{-2}	Free	5.2	10	84	10	106	4
W_s – T	Free	1.0	5	1.6	10	0.43	8
W_s – P	Free	0.289	2	0.36	4	0.78	2
C_P / F g^{-1}	Free	15	20	7	10	2.0x10^{-1}	9
R_F / Ω cm^{-2}	Free	10.7	5	960	20	65	10

Element	Freedom	0.1 V		0.0 V	
		Value	Error / %	Value	Error / %
R_s / Ω cm^{-2}	Fixed	16	N/A	16	N/A
C_{EDL} / F g^{-1}	Free	7.4x10^{-2}	5	5.9x10^{-2}	7
R_{CT} / Ω cm^{-2}	Free	7.4	5	12.6	5
W_s – R / Ω cm^{-2}	Free	313	20	168	10
W_s – T	Free	3.2	10	5.8	10
W_s – P	Free	0.84	2	0.91	5
C_P / F g^{-1}	Free	1.8x10^{-1}	10	1.4x10^{-1}	10
R_F / Ω cm^{-2}	Free	29.5	2	29.9	3

Appendix 6

Impedance during charging of $Ni(OH)_2$ coated electrode after the addition of a porosity blocking wax layer

0.0 V

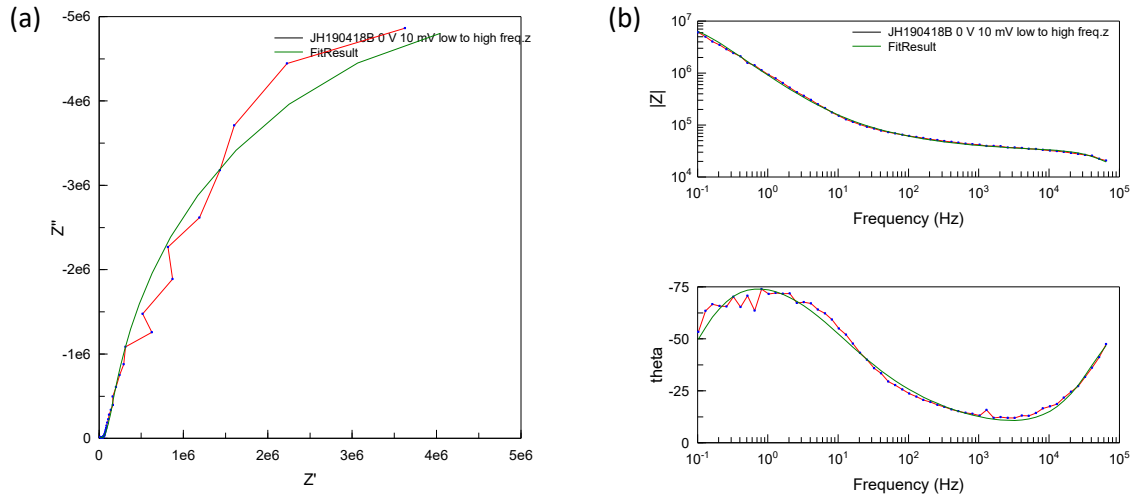


Figure A18 Fitting of equivalent circuit model to experimental data for $Ni(OH)_2$ coated electrodes after the application of porosity blocking paraffin wax during charging at 0.0 V DC potential and 10 mV perturbation (a) Nyquist plot (b) Bode Plots

0.1 V

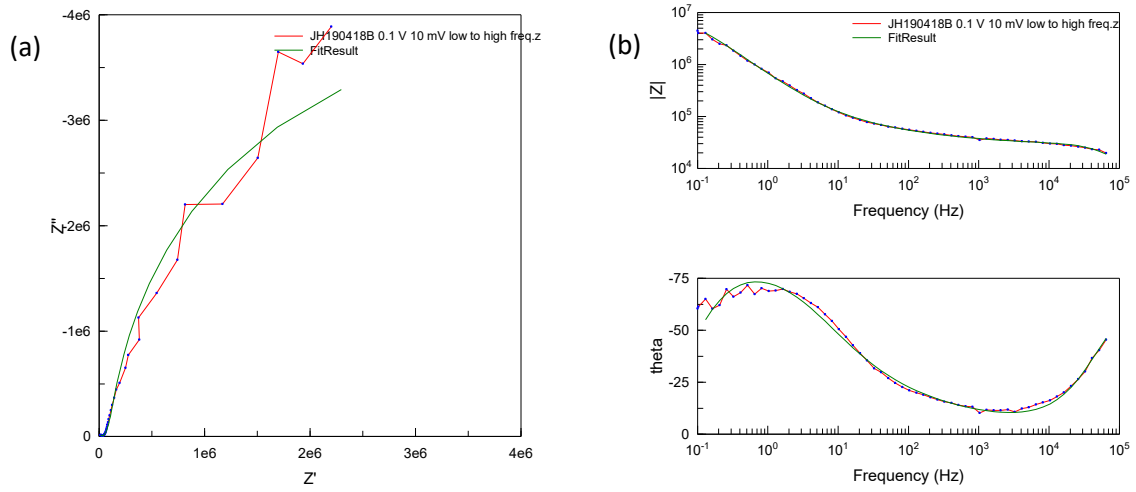


Figure A19 Fitting of equivalent circuit model to experimental data for $Ni(OH)_2$ coated electrodes after the application of porosity blocking paraffin wax during charging at 0.1 V DC potential and 10 mV perturbation (a) Nyquist plot (b) Bode Plots

0.2 V

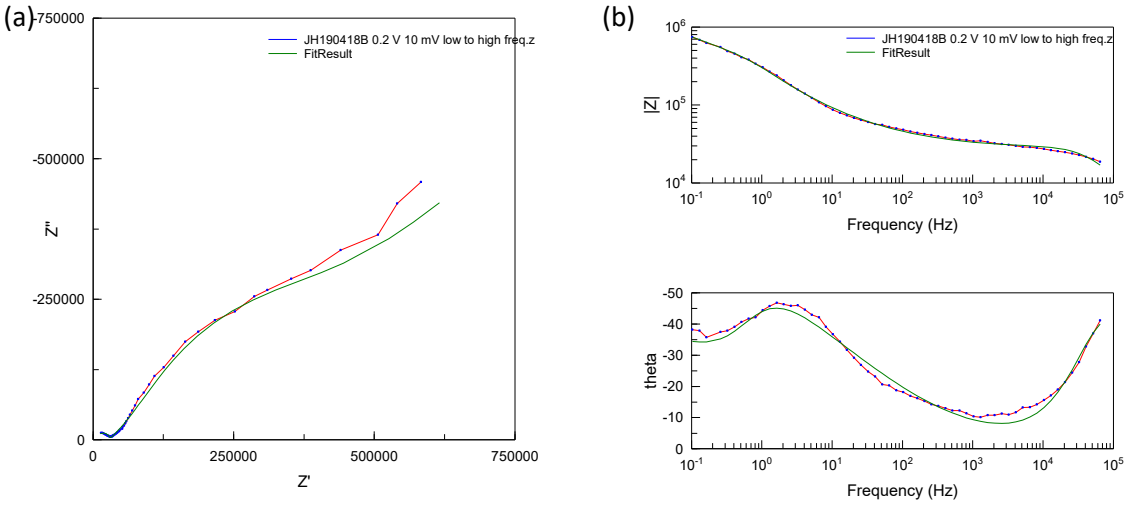


Figure A20 Fitting of equivalent circuit model to experimental data for $Ni(OH)_2$ coated electrodes after the application of porosity blocking paraffin wax during charging at 0.2 V DC potential and 10 mV perturbation (a) Nyquist plot (b) Bode Plots

0.3 V

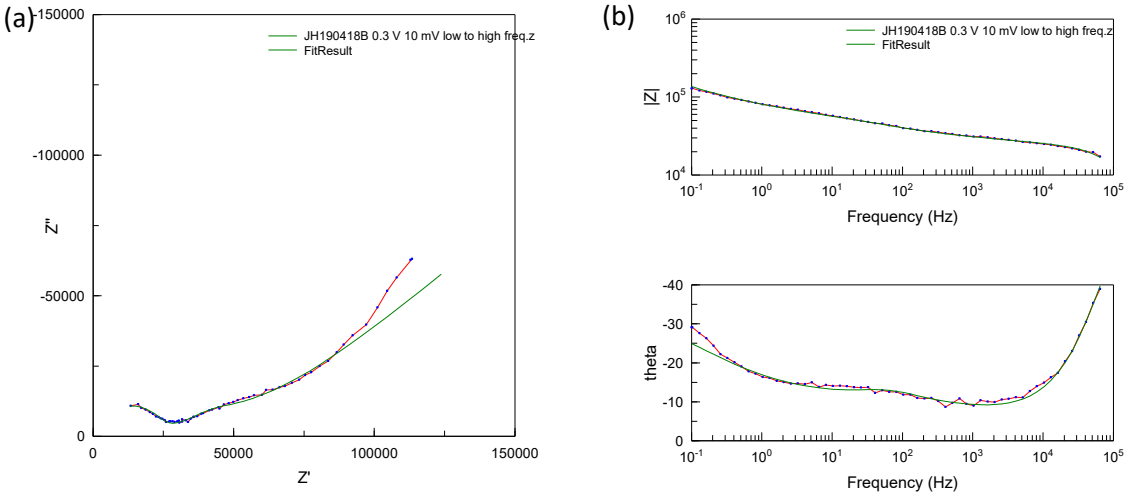


Figure A21 Fitting of equivalent circuit model to experimental data for $Ni(OH)_2$ coated electrodes after the application of porosity blocking paraffin wax during charging at 0.3 V DC potential and 10 mV perturbation (a) Nyquist plot (b) Bode Plots

0.4 V

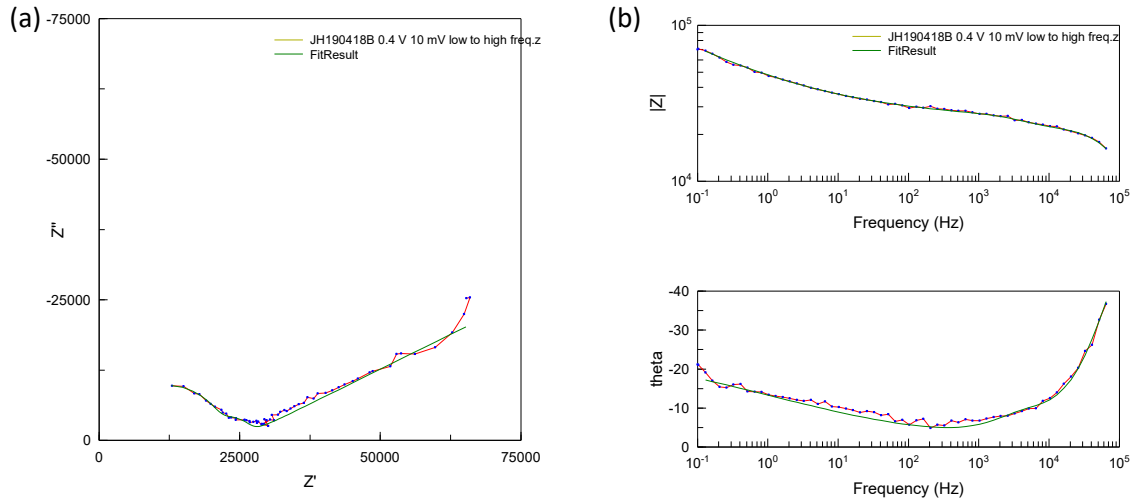


Figure A22 Fitting of equivalent circuit model to experimental data for $Ni(OH)_2$ coated electrodes after the application of porosity blocking paraffin wax during charging at 0.4 V DC potential and 10 mV perturbation (a) Nyquist plot (b) Bode Plots

0.5 V

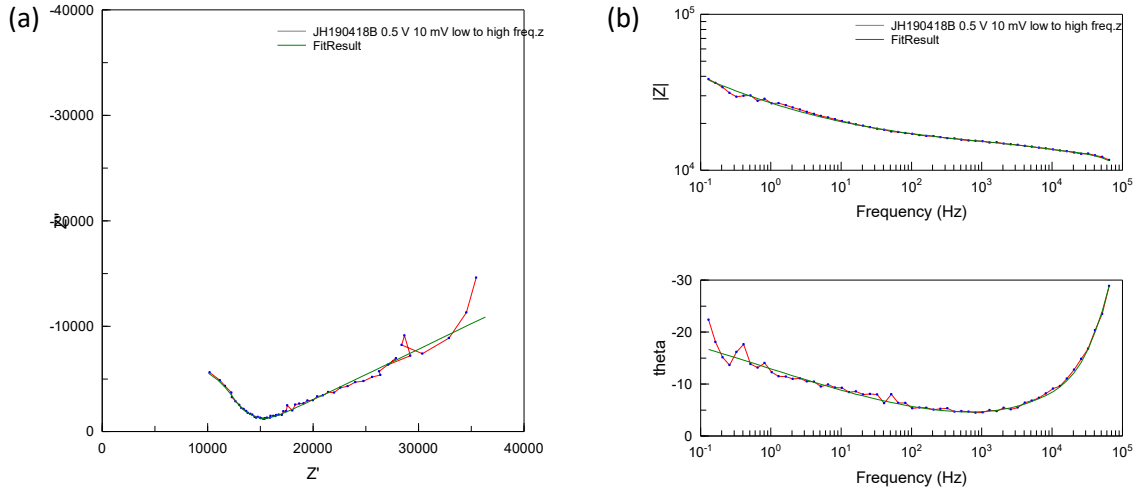


Figure A23 Fitting of equivalent circuit model to experimental data for $Ni(OH)_2$ coated electrodes after the application of porosity blocking paraffin wax during charging at 0.5 V DC potential and 10 mV perturbation (a) Nyquist plot (b) Bode Plots

0.6 V

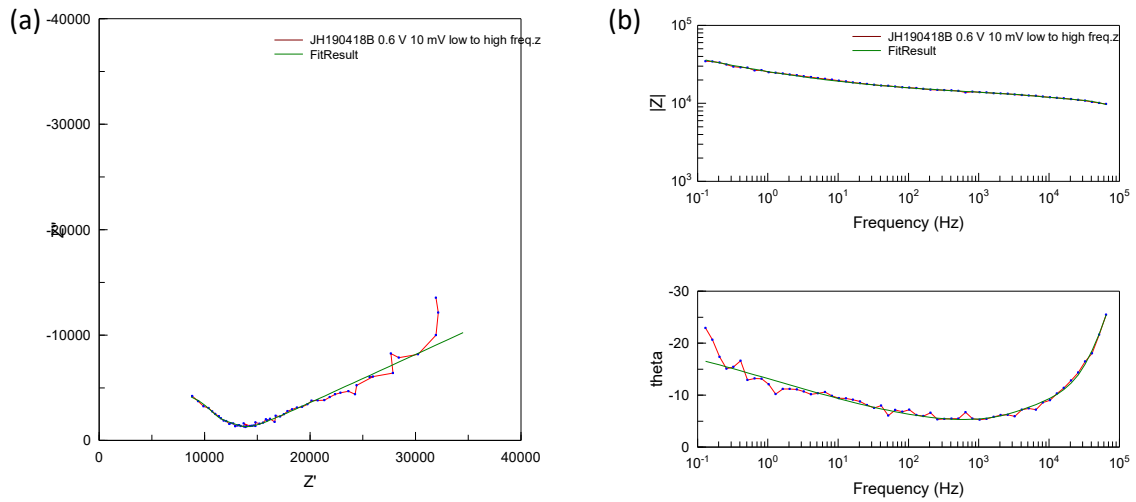


Figure A24 Fitting of equivalent circuit model to experimental data for $Ni(OH)_2$ coated electrodes after the application of porosity blocking paraffin wax during charging at 0.6 V DC potential and 10 mV perturbation (a) Nyquist plot (b) Bode Plots

0.7 V

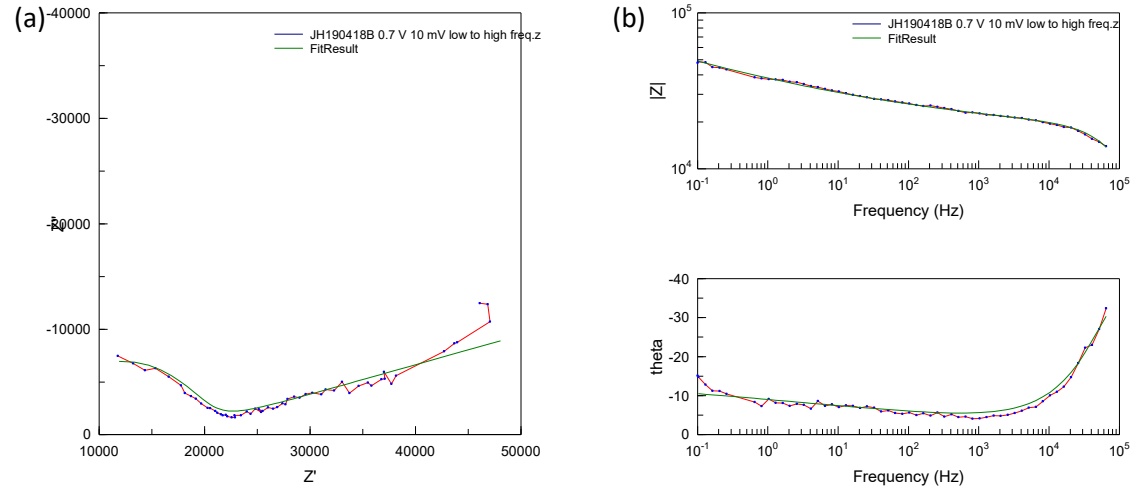


Figure A25 Fitting of equivalent circuit model to experimental data for $Ni(OH)_2$ coated electrodes after the application of porosity blocking paraffin wax during charging at 0.7 V DC potential and 10 mV perturbation (a) Nyquist plot (b) Bode Plots

Appendix 7

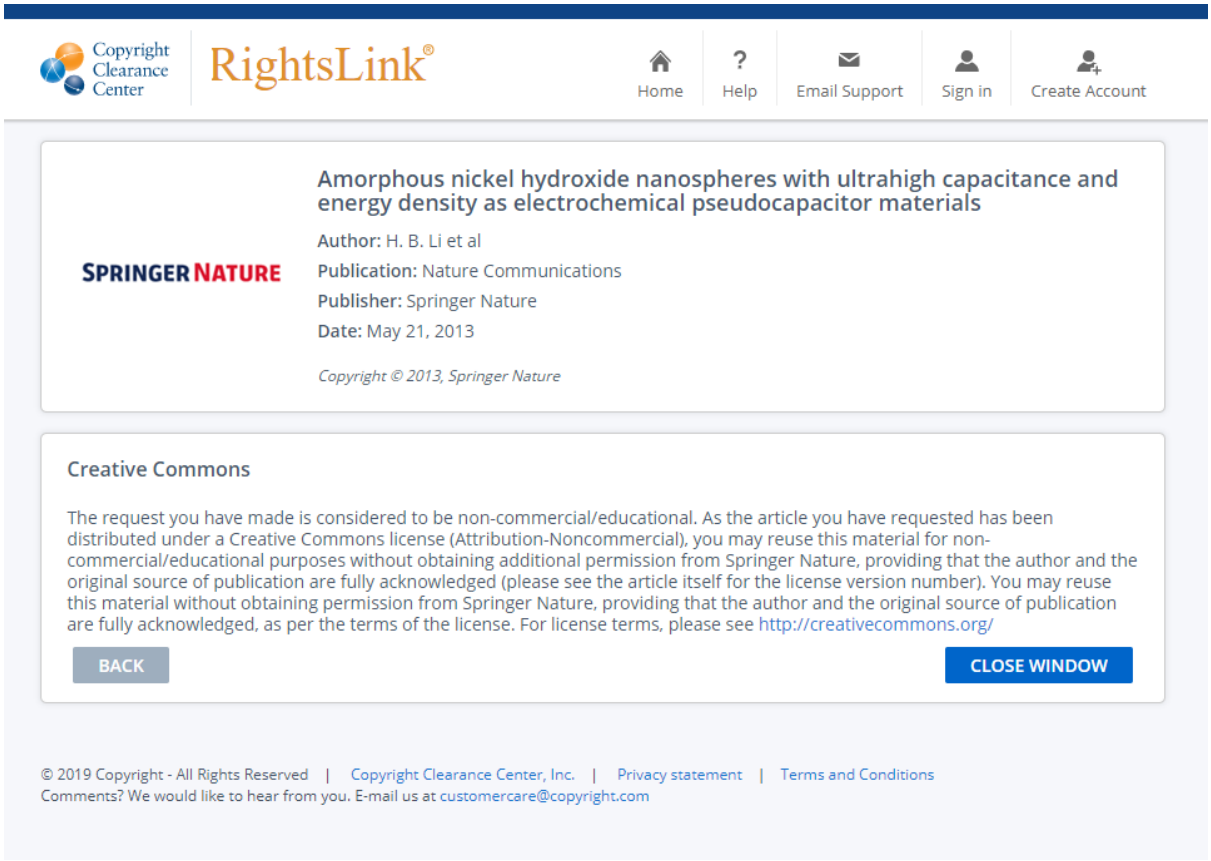


Figure A26 Permissions for the reuse of Figure 1.11 from Li, H. B.; Yu, M. H.; Wang, F. X.; Liu, P.; Liang, Y.; Xiao, J.; Wang, C. X.; Tong, Y. X.; Yang, G. W., Amorphous nickel hydroxide nanospheres with ultrahigh capacitance and energy density as electrochemical pseudocapacitor materials. Nature Communications 2013, 4, 1894. Copyright (2013) Macmillan Publishers Limited

Appendix 8

Table A2 Summary of $Ni(OH)_2$ nanoparticle size measurements from Chapter 3, using all particle size measuring techniques.

Sample	Average particle diameter measured by electron microscopy / nm	Standard Error in Particle diameter / nm	Average particle diameter measured by DLS / nm	Standard Error in Particle diameter / nm	Average particle diameter measured by XRD / nm	Standard Error in Particle diameter / nm	Average particle diameter measured by SAXS / nm	Error in Particle diameter / nm
1	3	1	8.7	0.4	-	-	2	1
2	4	1	-	-	-	-	4	2
3	8	2	-	-	-	-	7	4
4	11	3	65	4	-	-	9	5
5	17	4	-	-	-	-	11	6
6	56	8	290	70	4	2	-	-
7	63	3	-	-	-	-	-	-
8	130	10	1270	90	-	-	-	-
9	250	20	-	-	18	2	-	-
10	300	30	-	-	70	6	-	-
11	450	60	-	-	91	6	-	-

Dissemination of Research

Publications resulting from this work

J.H.L. Hadden, M.P. Ryan, D.J. Riley, Examining the charging behaviour of nickel hydroxide nanomaterials, *Electrochemistry Communications*, 101 (2019) 47-51.

J.H.L. Hadden, M.P. Ryan, D.J. Riley, Is Nickel hydroxide charging only skin deep?, *ACS Nano*, Under review.

Conferences Attended

(P)- Poster Presented *(T)*-Talk given

Electrochem 2015 – Durham University and 2016 – Leicester University *(P)*
STFC Batteries Early Careers Research Conference, Abingdon 2016
STFC Batteries Annual Meeting, Royal Institution London 2017
Imperial College Department of Materials PhD Research Day 2017 *(P)* 2018 *(T)*
MRS Summer Meeting in Phoenix, Arizona 2017 *(P)* and Fall Meeting in Boston, Massachusetts 2019 *(T)*